

# **Methane Production from Microalgae via Continuous Catalytic Supercritical Water Gasification: Development of Catalysts and Sulfur Removal Techniques**

THÈSE N° 6740 (2015)

PRÉSENTÉE LE 21 AOÛT 2015

À LA FACULTÉ DE L'ENVIRONNEMENT NATUREL, ARCHITECTURAL ET CONSTRUIT

GROUPE LUDWIG

PROGRAMME DOCTORAL EN ENERGIE

ÉCOLE POLYTECHNIQUE FÉDÉRALE DE LAUSANNE

POUR L'OBTENTION DU GRADE DE DOCTEUR ÈS SCIENCES

PAR

**Gaël PENG**

acceptée sur proposition du jury:

Prof. J.-L. Scartezzini, président du jury  
Prof. C. Ludwig, Prof. F. Vogel, directeurs de thèse  
Dr N. Boukis, rapporteur  
Dr D. Refardt, rapporteur  
Dr J. Van Herle, rapporteur



ÉCOLE POLYTECHNIQUE  
FÉDÉRALE DE LAUSANNE

Suisse  
2015

# Acknowledgements

I would like to thank Prof. Dr. Christian Ludwig for his continuous support, and precious advices over the last 4 years.

Many thanks to Prof. Dr. Frédéric Vogel for accepting me in his group, for his good supervision, and for his trust for developing my own ideas.

I thank Dr. Jan Van Herle, Dr. Dominik Refardt, and Dr. Nikolaos Boukis for co-refereeing this thesis. I would like to thank Prof. Dr. Jean-Louis Scartezzini for presiding over the jury.

I show my gratitude to the Competence Center Energy and Mobility (CEM-CH) and Swiss-electric Research for the financial support of this doctoral thesis.

I thank Prof. Dr. Alexander Wokaun for the fruitful discussions during our quarterly meetings.

My sincere thanks to the following people for their support: Erich de Boni (construction of KONTI-C, SEM-EDX, support during the gasification campaign, his help for the construction of the fixed-bed plug flow reactor, and his precious advices), Albert Schuler (ICP-OES analysis, CNS elemental analysis, support during the gasification campaign), Thanh-Binh Truong (analytics, support during the gasification campaign), Lorenz Bani (construction of KONTI-C, technical support, support during the gasification campaign), Timon Käser (analytics), Peter Hottinger (technical support), Marcel Hottiger (technical support), Dr. Jörg M. Wambach (XPS analysis), Dr. Fabian Gramm (STEM-HAADF), Martin Elsener (CO pulse chemisorption), Xiaoying Xu (GC-MS), Michael Schneider (elemental analysis), Gisela Herlein (administration), Cécile Taverney (administration), and Marie Sudki (administration).

And thanks to the people who contributed to the successful gasification campaign: Joachim Reimer, Christian Bährle, Dominik Gschwend, Franziska Mayr, Dr. Mariluz Bagnoud-Velásquez and Eya Damergi.

Dr. Mariluz Bagnoud-Velásquez, Per Christensen, Dr. Davide Ferri, Dr. Anastasios Kampolis, and Dr. Tilman Schildhauer many thanks for your scientific support and collaboration.



---

To my students: Matthias Steib, Jakob Breinl, and Markus Roth, I really appreciated your support and contribution to this doctoral thesis. Thanks a lot!

Special thanks to the following people for their friendship and the good moments at PSI: Adrian Marberger, Patrick S. Steiger, Dr. Arnim G. Eyssler, Andrey Petrov, Valentina Marchionni, Manasa Sridhar, and Dr. Katarzyna A. Michalow-Mauke.

Dr. Marian Dreher, I thank you a lot for all the good moments at PSI and in Basel, your scientific advices and technical support, your friendship, and of course to have been a so good climbing partner. I will never forget our ascensions of "La Dent Blanche" and "Nadelhorn".

Dr. Martin Brandenberger, thanks a lot for introducing me in this project and for the nice climbs in Jura.

A special thanks to all my family and friends who supported me during this doctoral dissertation.

Muchas gracias a Laura B. Gimenez para su apoyo, paciencia, y amor.

Je dédicace ce travail à ma maman qui m'a tant apportée durant toutes ces années d'étude. Merci pour tout!

# Abstract

This doctoral thesis aims at demonstrating the technical feasibility of methane production from microalgae via continuous catalytic supercritical water gasification (CSCWG). This work focuses on three different research approaches: (i) assessment and improvement of the catalytic performance of Ru/C catalysts, (ii) optimization of the salt separation, and (iii) continuous removal of sulfur. With all the acquired knowledge, a new process demonstration unit so called KONTI-C with a pumping capacity of  $1\text{-}2\text{ kg h}^{-1}$  was built in the frame of the SunCHem project.

The catalytic performance of Ru/C catalysts was assessed with isopropanol (IPA) at  $450\text{ }^{\circ}\text{C}$  and  $30\text{ MPa}$  in a fixed-bed plug flow reactor. Ru/C was able to convert efficiently IPA to a  $\text{CH}_4$ -rich gas (65 vol %) over a period of 96 h at a relatively low weight hourly space velocity ( $\text{WHSV}_{\text{gRu}}$ ). By working at a higher  $\text{WHSV}_{\text{gRu}}$ , a deactivation of the catalyst was observed. The decomposition of IPA over the carbon surface to coke that has progressively covered the Ru nanoparticles, was responsible for the loss of the catalytic activity. The Ru loading was found to be a crucial parameter for the improvement of the coking resistance. As a result, the stability of our standard catalyst was enhanced by increasing the Ru loading from 2 wt % to 5 wt %. When assessing the effect of some synthesis factors it was found that a higher Ru dispersion, the use of acetone during the catalyst impregnation, and the choice of a chloride free salt precursor ( $\text{Ru}(\text{NO})(\text{NO}_3)_3$ ) were needed for the improvement of the catalytic activity. Whereas the presence of carboxylic groups on the carbon support during the catalyst preparation did not improve the performance. The catalyst prepared with  $\text{Ru}(\text{NO})(\text{NO}_3)_3$  exhibited a better catalytic activity and stability than our standard commercial catalyst. By comparing the performance of a Ru/C catalyst with other Ru catalysts supported on metal oxides ( $\text{Ru}/\text{TiO}_2$ ,  $\text{Ru}/\text{ZrO}_2$ , and  $\text{Ru}/\text{Al}_2\text{O}_3$ ), Ru/C was found to be the most stable and active catalyst. Hence, Ru/C is the most suitable catalyst for CSCWG.

The design of the salt separator was improved by modifying the configuration of the feed entrance (feeding from the bottom of the salt separator). As a result, the salts and the inorganic sulfur ( $\text{SO}_4^{2-}$ ) were efficiently removed from the reactor effluent when processed with a model salt solution ( $\text{Na}_2\text{SO}_4/\text{K}_2\text{SO}_4$  in 10 wt % IPA).

---

A commercial ZnO adsorbent showed a high mechanical stability in supercritical water (SCW) (400 °C, 30 MPa). The adsorbent was able to adsorb sulfur ( $S^{2-}$ ) when processed with a model sulfur solution ( $Na_2S \cdot 9H_2O$ ) at 400 °C and 30 MPa. Characterization of the spent ZnO adsorbent confirmed that sulfur was adsorbed on ZnO to form ZnS.

The improved commercial catalyst (5% Ru/C<sub>BASF</sub>), the new design of the salt separator, and the commercial ZnO adsorbent were implemented in the development of KONTI-C. As a result, microalgae (*Chlorella vulgaris*) were successfully gasified (400 °C, 28 MPa) to a CH<sub>4</sub>-rich gas (55-60 vol %) over a period of 55 h during the gasification campaign performed in Wädenswil (CH). The low total organic carbon in the reactor effluent recorded over that period showed the good catalytic performance of the 5% Ru/C<sub>BASF</sub>. A brine effluent rich in nutrients (N, K, S, P, and Na) was obtained with the salt separator. The promising results obtained during the gasification campaign allowed to demonstrate the technical feasibility of continuous CSCWG of microalgae.

## Keywords

*Catalytic supercritical water gasification, Microalgae, Methane, Ru/C, Coking, Salt separator, Process demonstration unit, Separation techniques, Sulfur, Gasification campaign*

# Résumé

Cette thèse doctorale a pour objectif de démontrer la faisabilité technique de la production de méthane à partir de microalgues via la gazéification catalytique continue en eau supercritique (CSCWG). Ce travail se focalise sur trois différents axes de recherche : (i) évaluation et amélioration des performances catalytiques des catalyseurs Ru/C, (ii) optimisation de la séparation des sels, et (iii) élimination du soufre en continue. Avec toutes les nouvelles connaissances acquises, une nouvelle unité de démonstration du procédé appelée KONTI-C, ayant une capacité de pompage de 1-2 kg h<sup>-1</sup>, a été construite dans le cadre du projet SunCHem.

Les performances catalytiques des catalyseurs Ru/C ont été évaluées avec de l'isopropanol (IPA) à 450 °C et 30 MPa dans un réacteur à écoulement piston à lit fixe. Ru/C a été capable de convertir l'IPA en un gaz riche en CH<sub>4</sub> (65% vol) durant une période de 96 h à une vitesse spatiale horaire pondérale (WHSV<sub>gRu</sub>) relativement faible. En opérant à une WHSV<sub>gRu</sub> plus élevée, une désactivation du catalyseur a été observée. La décomposition de l'IPA à la surface du carbone en carbone solide (coke) qui a progressivement recouvert les nanoparticules de Ru, a été responsable de la perte de l'activité catalytique. La charge en Ru a été un paramètre crucial pour l'amélioration de la résistance à la cokéfaction. En conséquence, la stabilité de notre catalyseur standard a été améliorée en augmentant la charge de Ru de 2% m à 5% m. Lors de l'étude de certains facteurs de synthèse, il a été montré qu'une dispersion de Ru élevée, l'utilisation d'acétone pendant la préparation du catalyseur, ainsi que le choix d'un précurseur de sel ne contenant pas de chlorure (Ru(NO)(NO<sub>3</sub>)<sub>3</sub>) ont été nécessaires dans l'amélioration de l'activité catalytique. Alors que la présence de groupes carboxyliques sur le support de carbone lors de la préparation du catalyseur n'a pas été favorable. Le catalyseur préparé avec Ru(NO)(NO<sub>3</sub>)<sub>3</sub> a montré une meilleure activité catalytique et stabilité que notre catalyseur commercial standard. En comparant les performances d'un Ru/C avec d'autres catalyseurs de Ru sur support d'oxyde métallique (Ru/TiO<sub>2</sub>, Ru/ZrO<sub>2</sub>, and Ru/Al<sub>2</sub>O<sub>3</sub>), Ru/C a été le catalyseur le plus stable et le plus actif. Par conséquent, Ru/C est le catalyseur le plus adéquat pour CSCWG.

---

La conception du séparateur de sels a été améliorée en modifiant la configuration de l'entrée de l'alimentation (alimentation à partir du fond du séparateur de sels). En conséquence, les sels et le soufre inorganique ( $\text{SO}_4^{2-}$ ) ont été efficacement enlevés de l'effluent du réacteur lors du traitement d'une solution modèle de sels ( $\text{Na}_2\text{SO}_4/\text{K}_2\text{SO}_4$  in 10 wt % IPA).

Un adsorbent commercial de ZnO a montré une haute stabilité mécanique dans l'eau supercritique (SCW) (400 °C, 30 MPa). L'adsorbent a été capable d'adsorber le soufre ( $\text{S}^2$ ) lors du traitement d'une solution modèle contenant du soufre ( $\text{Na}_2\text{S}\cdot 9\text{H}_2\text{O}$ ) à 400 °C et 30 MPa. La caractérisation de ZnO usagé a confirmé que le soufre a été adsorbé sur ZnO pour former ZnS.

Le catalyseur commercial amélioré (5% Ru/C<sub>BASF</sub>), la nouvelle conception du séparateur de sels, et l'adsorbent commercial de ZnO ont été implémentés dans le développement de la KONTI-C. En conséquence, les microalgues (*Chlorella vulgaris*) ont été gazéifiées (400 °C, 28 MPa) avec succès en un gaz riche en  $\text{CH}_4$  (55-60% vol) pendant une période de 55 h lors de la campagne de gazéification effectuée à Wädenswil (CH). La réduction du carbone organique total dans l'effluent du réacteur enregistrée durant cette période a démontré les bonnes performances catalytiques du 5% Ru/C. Un effluent de saumure riche en nutriments (N, K, S, P, and Na) a été obtenu avec le séparateur de sels. Les promettants résultats obtenus durant la campagne de gazéification ont permis de démontrer la faisabilité technique de la CSCWG en continue de microalgues.

## Mots-clés

Gazéification catalytique en eau supercritique, Microalgues, Biométhane, Ru/C, Cokéfaction, Séparateur de sels, Unité de démonstration du procédé, Techniques de séparation, Soufre, Campagne de gazéification

# Contents

<b>Acknowledgements .....</b>	<b>iii</b>
<b>Abstract .....</b>	<b>v</b>
<b>Keywords.....</b>	<b>vi</b>
<b>Résumé.....</b>	<b>vii</b>
<b>Mots-clés.....</b>	<b>viii</b>
<b>Contents.....</b>	<b>ix</b>
<b>Notation .....</b>	<b>xiii</b>
<b>Chapter 1    Introduction.....</b>	<b>19</b>
1.1    The role of bioenergy.....	19
1.2    The role of biomass conversion technologies.....	20
1.3    Microalgae as a sustainable feedstock.....	20
1.4    Microalgae-to-biofuels.....	22
1.4.1    Thermochemical conversion.....	22
1.4.2    Biochemical conversion.....	25
1.4.3    Chemical conversion.....	26
1.5    Properties of supercritical water (SCW) .....	27
1.6    Phase behavior of salt-water mixtures.....	31
1.7    Biomass degradation to smaller molecules in sub- and supercritical water .....	32
1.7.1    Degradation of carbohydrates.....	33
1.7.2    Degradation of proteins.....	33
1.7.3    Degradation of lipids.....	35
1.7.4    Degradation of nucleic acids.....	35
1.8    Catalytic supercritical water gasification (CSCWG) .....	35
1.8.1    Heterogeneous catalysts for CSCWG .....	36
1.8.2    Effect of sulfur during CSCWG .....	39
1.8.3    Effect of salts .....	41
1.8.4    Tar and coke formation.....	44
1.9    The SunChem process .....	47
1.10    Continuous CSCWG of microalgae .....	49
1.11    Problem statement.....	54
1.12    Scope of the thesis.....	56
1.13    Structure of dissertation .....	57

<b>Chapter 2</b>	<b>Experimental Part .....</b>	<b>59</b>
2.1	Catalysts preparation.....	59
2.1.1	Pre-treatment of the catalyst support .....	59
2.1.2	Impregnation with the Ru salt precursor.....	59
2.2	Materials.....	60
2.3	Characterization and analytic methods.....	61
2.3.1	N <sub>2</sub> -physisorption.....	61
2.3.2	CO pulse chemisorption.....	61
2.3.3	H <sub>2</sub> temperature-programmed reduction (H <sub>2</sub> -TPR) .....	62
2.3.4	Temperature-programmed oxidation (TPO) .....	62
2.3.5	CO <sub>2</sub> /CO-temperature-programmed desorption (CO <sub>2</sub> /CO-TPD).....	62
2.3.6	Carbon, nitrogen, and sulfur elemental analysis (CNS) .....	62
2.3.7	Total carbon (TC), total organic carbon (TOC), and total inorganic carbon (TIC) analysis.....	63
2.3.8	TC, TOC, and TIC analysis measured on-line .....	63
2.3.9	Elemental composition of biomass samples.....	63
2.3.10	NH <sub>4</sub> <sup>+</sup> -determination .....	63
2.3.11	Ash content of biomass samples.....	63
2.3.12	Dry matter of the feed (microalgae) .....	64
2.3.13	pH-determination .....	64
2.3.14	Sulfide test paper.....	64
2.3.15	Off-line gas chromatograph (GC) .....	64
2.3.16	On-line micro gas chromatograph (microGC) .....	64
2.3.17	Gas chromatography-mass spectroscopy (GC-MS) .....	64
2.3.18	Boehm titration .....	65
2.3.19	Inductively coupled plasma optical emission spectroscopy (ICP-OES).....	65
2.3.20	Wavelength dispersive X-ray fluorescence (WDXRF) .....	66
2.3.21	X-ray photoelectron spectroscopy (XPS) .....	66
2.3.22	X-ray diffraction analysis (XRD).....	66
2.3.23	Scanning electron microscopy and energy dispersive X-ray spectroscopy (SEM-EDX) .....	66
2.3.24	Scanning transmission electron microscopy (STEM) .....	67
2.4	Experimental setups .....	67
2.4.1	Stability test of the carbon support in mini-batch reactor.....	67
2.4.2	Gasification and sulfur adsorption experiments in the continuous reactor setup (PFR).....	68
2.4.3	Salt separation experiments in the continuous reactor setup (KONTI-2) .....	69
2.4.4	Liquefaction and gasification experiments in the continuous reactor setup (KONTI-C) .....	72
2.4.5	General procedure for the experiments.....	76
2.5	Terms and definitions .....	77
2.5.1	Weight hourly space velocity (WHSV) .....	77
2.5.2	Total organic carbon conversion (X <sub>C</sub> ) .....	78

2.5.3	Carbon gasification efficiency ( $GE_C$ ) .....	78
2.5.4	Rate of coke deposition ( $R_{Coke\ dep.}$ ) .....	79
2.5.5	Turnover frequency (TOF) .....	79
2.5.6	Carbon, nitrogen, and sulfur recoveries .....	79
2.5.7	Chemical equilibrium gas composition .....	80
<b>Chapter 3</b>	<b>Assessment and Improvement of the Catalytic Performance of Ru/C Catalysts .....</b>	<b>81</b>
3.1	CSCWG of IPA .....	81
3.2	Stability of the physical structure of the carbon support in SCW .....	82
3.3	Blank SCWG experiment .....	83
3.4	Catalytic performance of Ru/C catalysts .....	86
3.5	Effect of the synthesis factors .....	91
3.5.1	Effect of the Ru dispersion .....	91
3.5.2	Effect of the solvent (water vs. acetone) .....	94
3.5.3	Effect of the salt precursor .....	97
3.5.4	Effect of the Ru loading .....	99
3.5.5	Effect of the surface functional groups of carbon .....	103
3.6	Comparison of the performance of Ru catalysts supported on carbon and different metal oxides .....	114
3.7	Summary .....	119
<b>Chapter 4</b>	<b>Optimization of the Salt Separator .....</b>	<b>121</b>
4.1	Performance of the salt separator .....	121
4.2	New design of the salt separator .....	124
4.3	Summary .....	128
<b>Chapter 5</b>	<b>Continuous Sulfur Removal in Supercritical Water Conditions .....</b>	<b>131</b>
5.1	Characteristics of the ZnO adsorbent ( <i>Katalco 32-5</i> ) .....	131
5.2	Stability in SCW .....	132
5.3	Performance of the ZnO adsorbent .....	133
5.4	Corrosion .....	136
5.5	Summary .....	140
<b>Chapter 6</b>	<b>Continuous Liquefaction and Catalytic Supercritical Water Gasification of Microalgae .....</b>	<b>143</b>
6.1	Assessment of the new salt separator with model salt solutions .....	143
6.2	Continuous liquefaction and CSCWG of microalgae .....	148
6.2.1	Continuous liquefaction of microalgae .....	148
6.2.2	Continuous CSCWG of microalgae .....	162
6.3	Summary .....	170
<b>Chapter 7</b>	<b>Gasification Campaign in Wädenswil (CH) .....</b>	<b>173</b>
7.1	Feedstock composition .....	173
7.2	Process parameters .....	173
7.3	Gas analysis .....	175
7.4	Analysis of the liquid effluents .....	177



7.5	Analysis of the solid residue .....	185
7.6	Characterization of the spent catalyst .....	187
7.7	Characterization of the spent ZnO adsorbent.....	191
7.8	Temperature and pressure profiles .....	195
7.9	Summary.....	200
<b>Chapter 8</b>	<b>Concluding Remarks and Recommendations for Further Research .....</b>	<b>203</b>
8.1	Achieved results .....	203
8.2	Recommendations for further research.....	206
<b>A. Appendix</b> .....		<b>209</b>
<b>A.1 Screenshots of the LabVIEW based software for KONTI-C</b> .....		<b>209</b>
<b>A.2 Process flow sheet of KONTI-C</b> .....		<b>212</b>
<b>A.3 List of all the experiments performed in this doctoral thesis</b> .....		<b>219</b>
<b>References</b> .....		<b>223</b>
<b>List of publications</b> .....		<b>237</b>
<b>Curriculum Vitae</b> .....		<b>239</b>

# Notation

## Greek letters

symbol	meaning	units
$\beta$	line broadening at half the maximum intensity	radians
$\theta$	Bragg angle	$^{\circ}$
$\lambda$	X-ray wavelength	$\text{\AA}$
$\rho$	density	$\text{kg m}^{-3}$
$\eta$	dynamic viscosity	$\text{mPa s}$
$\nu$	kinematic viscosity	$\text{m}^2 \text{s}^{-1}$
$\Delta H_{\text{vap.}}$	enthalpy of vaporization	$\text{kJ mol}^{-1}$
$\Delta_r H^{\circ}_{298}$	standard enthalpy of reaction	$\text{kJ mol}^{-1}$

## Roman symbols

symbol	meaning	units
D	diffusion coefficient	$\text{m}^2 \text{s}^{-1}$
T	temperature	$^{\circ} \text{C}$
P	pressure	MPa
V	volume	mL
C	concentration	$\text{mol kg}^{-1}$
K	shape factor	-
m	mass	mg or g or kg
$\text{GE}_c$	carbon gasification efficiency	%

$X_C$	total organic carbon conversion	%
$d_{at}$	atomic diameter	Å
$d_p$	particle diameter	mm
$d_{p,CO}$	particle diameter determined by CO-chemi-sorption	nm
$d_{p,STEM}$	particle diameter determined by STEM	nm
$d_{p,XRD}$	particle diameter determined by XRD	nm
$d_{reactor}$	reactor diameter	mm
$D_{CO}$	dispersion obtained by CO-chemisorption	-
$D_{STEM}$	dispersion obtained by STEM	-
$N_{ads}$	amount of gas adsorbed during pulse	mmol g <sup>-1</sup>
$F_s$	stoichiometric factor	moles of metal/moles of gas
$M_{met}$	metal atomic weight	g mol <sup>-1</sup>
$W_{met}$	metal loading on a mass basis	wt %
$n_{CSF}$	moles of carbon surface functionalities	mol
$\dot{m}$	mass flow rate	g min <sup>-1</sup> or mg min <sup>-1</sup> or kg h <sup>-1</sup>
$R_{Coke\ dep.}$	rate of coke deposition	mmol C min <sup>-1</sup>
$\dot{n}$	molar flow rate	mol min <sup>-1</sup> or mol s <sup>-1</sup>
wt %	weight percent	%
vol %	volume percent	%

---

## Acronyms used within the text

acronyms	meaning	units
APS	5'-adenylsulfate	-
ATP	adenosine triphosphate	-
BET SSA	Brunauer–Emmett–Teller specific surface area	m <sup>2</sup> g <sup>-1</sup>
CNS	carbon, nitrogen, and sulfur	-
CSCWG	catalytic supercritical water gasification	-
CSTR	continuous stirred tank reactor	-
DI	deionized	-
DMSO	dimethyl sulfoxide	-
EPFL	Ecole Polytechnique Fédérale de Lausanne	-
EREC	European Renewable Energy Council	-
ETHZ	Eidgenössische Technische Hochschule Zürich	-
FHWM	full width at half maximum intensity	-
GC	gas chromatograph	-
GC-MS	gas chromatography-mass spectroscopy	-
HAADF	high angle annular dark field	-
ICP-OES	inductively coupled plasma optical emission spectroscopy	-
IPA	isopropanol	-
LHSV	liquid hourly space velocity	L L <sub>cat</sub> <sup>-1</sup> h <sup>-1</sup>
microGC	micro gas chromatograph	-
MWCNTs	multi-walled carbon nanotubes	-

N.A.	not available	-
NDIR	non-dispersive infrared	-
PBR	photobioreactor	-
PDU	process demonstration unit	-
PFR	plug flow reactor	-
PSI	Paul Scherrer Institut	-
PUFAs	polyunsaturated fatty acids	-
RT	room temperature	-
Ru/C <sub>a</sub>	carbon supported Ru catalyst prepared with acetone	-
Ru/C <sub>w</sub>	carbon supported Ru catalyst prepared with water	-
SCW	supercritical water	-
SCWG	supercritical water gasification	-
SEM-EDX	scanning electron microscopy and energy dispersive X-ray spectroscopy	-
SLW	synthetic liquefied wood	-
STEM	scanning transmission electron microscopy	-
SWCNTs	single-walled carbon nanotubes	-
TAG	triacylglyceride	-
TC	total carbon	-
TCD	thermal conductivity detector	-
TGA	thermogravimetric analysis	-
TIC	total inorganic carbon	-
TOC	total organic carbon	-

TOF	turnover frequency	$\text{s}^{-1}$
TPD	temperature-programmed desorption	-
TPR	temperature-programmed reduction	-
WDXRF	wavelength dispersive X-ray fluorescence	-
WGS	water-gas shift	-
WHSV	weight hourly space velocity normalized to one gram of catalyst	$\text{g}_{\text{org}} \text{g}_{\text{cat}}^{-1} \text{h}^{-1}$
$\text{WHSV}_{\text{gRu}}$	weight hourly space velocity normalized to one gram of Ru	$\text{g}_{\text{org}} \text{g}_{\text{Ru}}^{-1} \text{h}^{-1}$
XPS	X-ray photoelectron spectroscopy	-
ZACHH	zinc aluminium carbonate hydroxide hydrate	-

---



# Chapter 1 Introduction

## 1.1 The role of bioenergy

The use of biomass as an energy source has been used by mankind since more than 400000 years for heating. Nowadays, its use remains the main source of energy in many developing countries where 35% of the energy needs of the three-quarters of the world are covered by bioenergy in its traditional form [1]. In the future, bioenergy will continue to be used for cooking or for heating by the population. In Figure 1.1, the current and the estimated global energy from 2001-2040 estimated by the European Renewable Energy Council (EREC) is depicted. The total consumption of renewable energy in 2001 represented 13.6% of the total energy consumption where 10.8% came from bioenergy. In 2040, this percentage may even reach 16%.

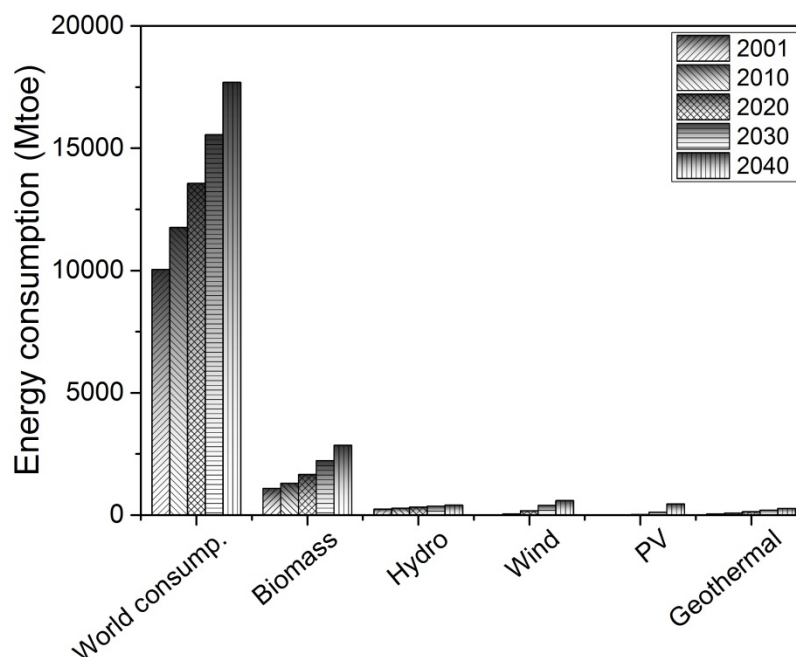


**Figure 1.1.** Current and estimated energy consumption from 2001-2040 (adapted from [1,2]).

One important aspect, which was not taken into account by the EREC, was the technological developments performed in the conventional energy sector (*e.g.* oil and gas). In fact, their study was only



based on technological developments carried out in the renewable energy sector. Therefore by considering the development in the conventional energy sector, which may have a significant impact on renewable energy development, the percentage of the renewable energy consumption may be even higher.

## 1.2 The role of biomass conversion technologies

The long-term future of bioenergy can only be possible if the people needs are satisfied in terms of cheap, clean, and efficient energy forms (*e.g.* electricity, liquid, and gaseous fuels). In order to reach this objective, the role of biomass conversion technologies is determinant. Currently, almost 90% of bioenergy is produced by combustion technologies, which consist at burning biomass in air (800-1000 °C) for generating heat, mechanical power or electricity. Any type of biomass containing a water content < 50 wt % can be burnt in practice. Although the scale of combustion plants is wide from the domestic heating up to large-scale plants (100-3000 MW), the overall thermal efficiency (biomass to electricity) is relatively low and often does not exceed 40% [3]. For the conversion of wet biomass (water content > 50 wt %) such as manure, household residues, sewage sludge, and marine algae, the anaerobic digestion for biogas production is the most developed and used technology. As for the combustion technologies, its overall thermal efficiency is rather low (25-50%) [4,5]. Its low efficiency is related to the incapacity for converting all the organic material to biogas. These two examples show that many efforts in the improvement of the biomass conversion efficiency should be undertaken. Hence, the optimization of current technologies by a better process integration such as the cogeneration (heat/power) and the development of new biomass conversion technologies combining fuels and chemicals production (biorefinery) are the key for ensuring the long-term future of the use of biomass as a feedstock.

## 1.3 Microalgae as a sustainable feedstock

The choice of the biomass feedstock for biofuel production is a crucial step in the determination of the biofuel sustainability. Actually, the use of crops such as corn, sugar cane, and sugar beet is subjected to polemic due to their high environmental impact (intensive use of the land) and their responsibility for competing with food crops. In the future, as the energy consumption will increase, biofuel production from crops in larger quantities will be not sustainable and not conceivable any-

more. Currently, biofuel production (biodiesel and bioethanol) requires about 1% (14 million hectares) of the world's available arable lands which provides only 1% of the global transport fuels [6]. In order to satisfy the increasing demand, there is a necessity to use sustainable feedstocks. At the moment, microalgae as feedstocks appear to be the only renewable way for producing biofuels since their use does not compete for agriculture land used for food production. Their main advantages over the conventional crops are [6]:

- a higher biomass productivity (yields per hectare per year)
- can be cultivated on marginal lands (*e.g.* seashore land) avoiding the competition with arable lands for food production
- a higher CO<sub>2</sub> sequestration capacity
- a lower environmental impact such as the deforestation
- production of value-added co-products or by-products (*e.g.* pigments, fertilizers)
- can be cultivated in salt and waste water streams reducing the use of freshwater
- Reduction of NO<sub>x</sub> emission

In line with all the benefits of microalgae, currently more than 150 companies worldwide show interest of generating biofuels from microalgae [7]. For instance, some companies such as ExxonMobil Corp and BP Amoco plc. ExxonMobil Corp or even Dow Chemical Co. have invested in microalgae research for biofuel production. Even the US Department of Energy has published a document of their "National Algal Biofuels Technology Roadmap" which promises a good future for microalgae [8]. As mentioned by Singh et al. [7] the future of microalgae-based biofuels will rely on a hybrid biofuel refinery concept where coproduction of both biofuels and chemical products should be coupled in which CO<sub>2</sub> and nutrients should be recycled for microalgae culture (see Figure 1.2).

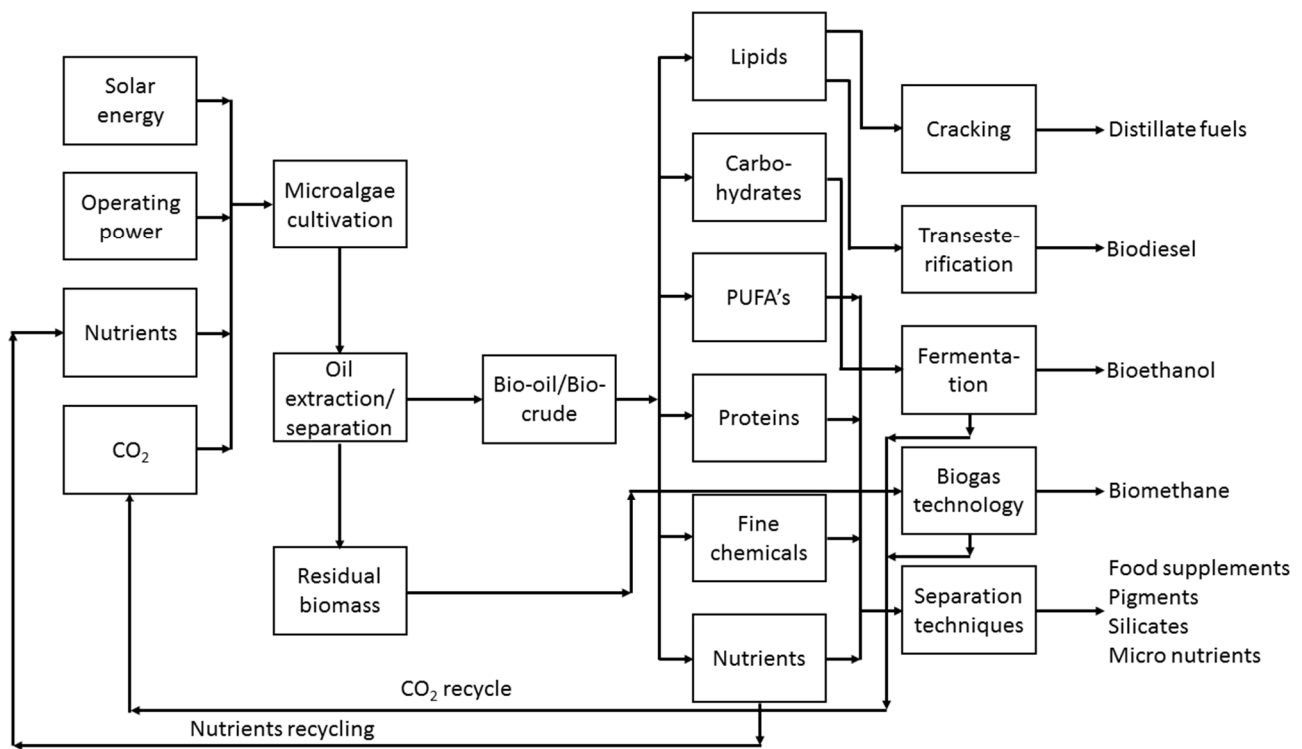


**Figure 1.2.** Proposed schematic flow sheet for microalgae biorefinery (adapted from [7]).

## 1.4 Microalgae-to-biofuels

The conversion technologies of microalgae to biofuels are mostly the same that those used for the 1<sup>st</sup> and 2<sup>nd</sup> generation biofuels. In Figure 1.3, the different conversion processes from microalgae to biofuels are shown. Note that the choice of the conversion technology depends on: the type and quantity of the feedstock; the desired form of energy; environmental standards; economic conditions; and project specific factors [9]. The conversion technologies can be classified in three categories: thermochemical conversion; biochemical conversion; and chemical conversion.

### 1.4.1 Thermochemical conversion

Thermochemical conversion involves all the processes that use the thermal decomposition of organic components in biomass for producing biofuels. These processes include the gasification, the hydrothermal gasification, the hydrothermal liquefaction, the hydrothermal carbonization, the pyrolysis, and the direct combustion.

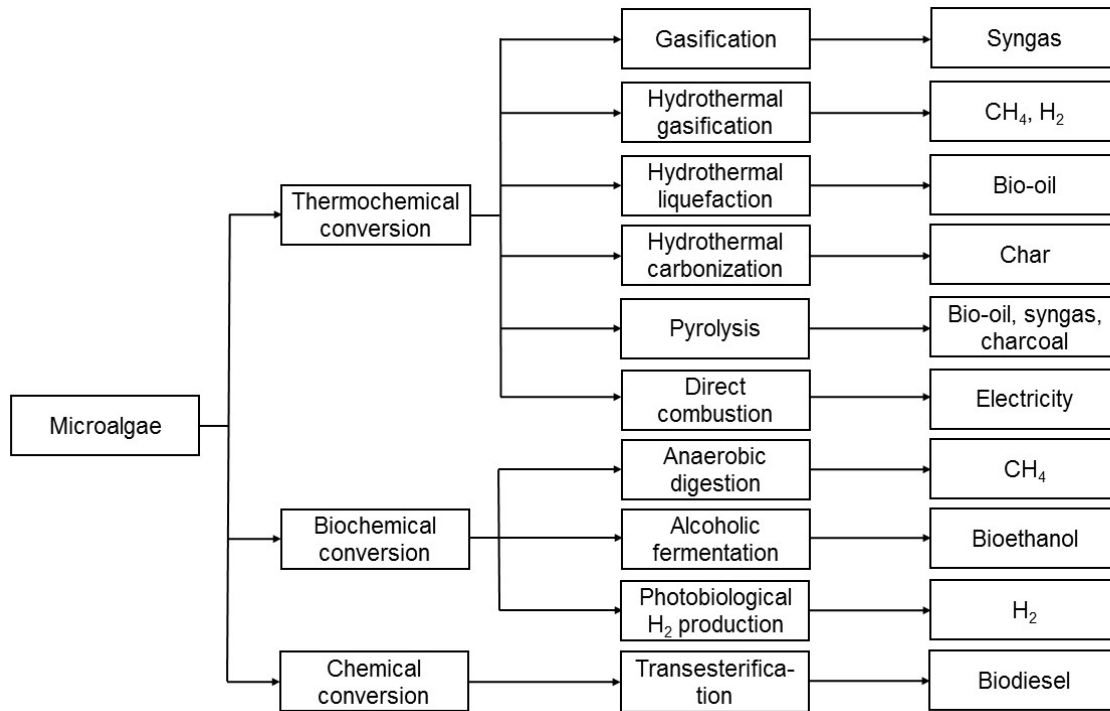


**Figure 1.3.** Microalgae conversion processes (adapted from [10]).

#### 1.4.1.1 Gasification

Gasification operates at high temperatures (800-1000 °C) where the biomass is partially oxidized by oxygen and steam to generate syngas (mixture of CO and H<sub>2</sub>), CO<sub>2</sub>, N<sub>2</sub>, and CH<sub>4</sub>. The main advantage is that syngas can be produced from a large variety of biomass feedstock [10]. Hirano et al. [11] have partially oxidized microalgae (*Spirulina*) at 850-1000 °C and measured the gaseous products. Based on the gas composition obtained, they calculated that the highest theoretical methanol yield was 0.64 g<sub>methanol</sub> g<sub>biomass</sub><sup>-1</sup> at 1000 °C. The energy balance, defined as the ratio between the energy of produced methanol to the total required energy, was estimated to 1.1. Note that most of the energy required was consumed during the microalgae cultivation.

#### 1.4.1.2 Hydrothermal gasification

Hydrothermal gasification (or supercritical water gasification) uses the unique properties of supercritical water (T > 374 °C, P > 22.1 MPa) for decomposing wet biomass into gaseous products (CH<sub>4</sub>, H<sub>2</sub>, CO<sub>2</sub>, and CO). According to the process temperature and the target products, we can differentiate three distinct categories:

1. High temperatures (500-700 °C) without catalysts or with homogeneous catalysts for H<sub>2</sub> production

2. Moderate temperatures (374-500 °C) with catalysts for CH<sub>4</sub> production
3. Low-moderate temperatures (< 374 °C, subcritical water) with catalysts for CH<sub>4</sub> production

This technology is well suited for processing microalgae since there is no need for a drying step allowing to reach high thermal efficiencies (70-77%) [12]. Moreover, wet biomass can be fully converted within short residence times (< 30 min) [4]. Many excellent reviews published over the last few years, reported about this novel technology [13–16]. Note that the latter is discussed in detail in the next sections. Concerning the hydrothermal gasification of microalgae, many studies were published with several microalgae species and were summarized by Brandenberger [17]. It should be mentioned that most of these studies were carried out in batch reactor where the main objective was to show how the catalyst affect the carbon conversion, the gas yield, and the gas composition.

#### 1.4.1.3 *Hydrothermal liquefaction*

Hydrothermal liquefaction aims at producing bio-oil from biomass in water at medium temperatures (280-370 °C) and high pressures (10-25 MPa). The main advantage of this process is that wet biomass can be converted to biofuels avoiding thus the drying step, which is energy intensive. Many papers have reported about thermochemical liquefaction of microalgae by operating under a wide variety of process conditions [18–26]. Most of these studies have investigated the effect of the temperature on the bio-oil yield and claimed that the optimum reaction temperature is in the range of 350-375 °C. Other parameters such as the reaction time or even the use of catalysts are also relevant regarding the optimization of the bio-oil yield. An excellent review on hydrothermal liquefaction of microalgae discussed in more detail the influence of the process parameters on the bio-oil yield [27].

#### 1.4.1.4 *Hydrothermal carbonization*

Hydrothermal carbonization aims at producing char products from wet biomass under mild conditions (~ 200 °C, < 2 MPa) [27]. During this process, two streams are obtained, one containing char products and another consisting of an aqueous phase. Heilmann et al. [28] reported that acceptable levels of char products can be achieved from diverse microalgae (*e.g. Chlamydomonas reinhardtii*,

*Synechocystis* sp., *Aphanizomenon flos-aquae*, *Spirulina* spp., and *Chlorella* spp.) under mild conditions (200 °C, < 2 MPa) and at short residence times (30 min). However, due to the low value of the char products, few studies were dedicated to the development of this technology.

#### 1.4.1.5 Pyrolysis

Pyrolysis consists in the conversion of biomass to bio-oil, syngas, and charcoal at moderate to high temperatures (350-700 °C) in absence of air. Note that if the conversion is performed at low temperatures (200-300 °C), the process is called mild pyrolysis or torrefaction [29]. Although this process is thought to have a potential for replacing petroleum based liquid fuels, the bio-oil products need to be upgraded by hydrogenation or catalytic cracking for reducing the oxygen content and the alkalis [10]. By contrast to slow pyrolysis performed at moderate temperature (400 °C) and very long residence times, fast pyrolysis is carried out at 500 °C with short hot vapor residence times allowing to enhance the bio-oil yield. For instance, Miao et al. [30] achieved bio-oil yields of 18% and 24% during fast pyrolysis of *Chlorella protothecoides* and *Microcystis aeruginosa* (500 °C, 0.1 MPa). Demirbas [31] pyrolyzed *Chlorella protothecoides* and found out that the bio-oil yield increased from 5.7% to 55.8% when the temperature rose from 254 °C to 502 °C.

#### 1.4.1.6 Direct combustion

During direct combustion, biomass is burnt in presence of air for producing hot gases in a furnace, boiler, or steam turbine at high temperatures (> 800 °C). Any type of biomass can be burnt but only if the water content is < 50 wt % [10]. As mentioned in section 1.2, the overall thermal efficiency of the process is rather low due to the pre-treatment of the feedstock (e.g. drying, grinding).

### 1.4.2 Biochemical conversion

Biochemical conversion processes are constituted by the anaerobic digestion, the alcoholic fermentation, and the photobiological hydrogen production.

#### 1.4.2.1 Anaerobic digestion

Anaerobic digestion is the conversion of organic waste to biogas such as CH<sub>4</sub> and CO<sub>2</sub> with traces of other gases such as H<sub>2</sub>S. During this process, organic compounds are hydrolyzed into sugars that are then fermented with the help of fermentative bacteria into soluble alcohol, acetic acid, volatile fatty acids, and a gaseous product containing H<sub>2</sub> and CO<sub>2</sub>. Finally, methanogens convert H<sub>2</sub> and CO<sub>2</sub> into

CH<sub>4</sub> (60-70%) and CO<sub>2</sub> (30-40%) [10]. Although biomass feedstocks containing a high water content (80-90 wt %) can be processed, the thermal efficiency is rather low (25-50%) and long residence times are needed (20-33 days) [4,5]. The reason for the low thermal efficiency is caused by the incomplete conversion of the biomass.

#### 1.4.2.2 *Alcoholic fermentation*

Alcoholic fermentation aims at producing bioethanol from biomass containing sugars, starch, and cellulose. Biomass is ground down and the starch transformed to sugars by enzymes. Then, the sugars are converted to ethanol with yeasts. The purification of ethanol by distillation is required. This step is the main drawback of this process due to the high amount of needed energy. The solid residue from the process can be either used as cattle-feed or as a fuel for boilers or for subsequent gasification [3]. The production of ethanol from the *Chlorococcum littorale* (marine green alga) by dark fermentation was reported by Ueno et al. [32]. They claimed a maximum productivity of 450  $\mu\text{mol}_{\text{ethanol}} \text{g}^{-1} \text{dry wt. at } 30^\circ\text{C}$ .

#### 1.4.2.3 *Photobiological hydrogen production*

Under anaerobic conditions, eukaryotic microalgae can produce H<sub>2</sub> during the photosynthesis. Briefly, microalgae convert the water molecules into H<sup>+</sup> and O<sub>2</sub> during the photosynthesis where hydrogenase enzymes subsequently metabolized H<sup>+</sup> into H<sub>2</sub> [10]. According to the sparse studies found in the literature, it seems that this process attracted few attentions.

#### 1.4.3 *Chemical conversion*

After a mechanical extraction of the lipid contained in microalgae, bio-oil is converted into biodiesel via the transesterification process. During this process, triglycerides react with alcohol to form mono-esters which represent the biodiesel. Due to the physical and chemical similarities of algal biodiesel with petroleum diesel, the latter seems to be a suitable substitute to fossil fuels. Moreover, algal biodiesel has other advantages over petroleum diesel: it is renewable (derived from biomass); it is almost carbon neutral under sustainable production; it is non-toxic; it contains a lower levels of particulates, CO, soot, hydrocarbons, and SO<sub>x</sub> [10].

## 1.5 Properties of supercritical water (SCW)

Supercritical water gasification (SCWG) uses the unique properties of water at high pressures and moderate temperatures for converting wet biomass into gaseous products. The phase diagram of pure water is depicted in Figure 1.4. The black line (saturation line) represents the vapor pressure of pure water. Below the critical point of water, two phases exist: liquid water in equilibrium with its vapor phase. Above the critical point of water, there is no clear phase distinction between the liquid and the gas phases, this is the so called supercritical phase of water.

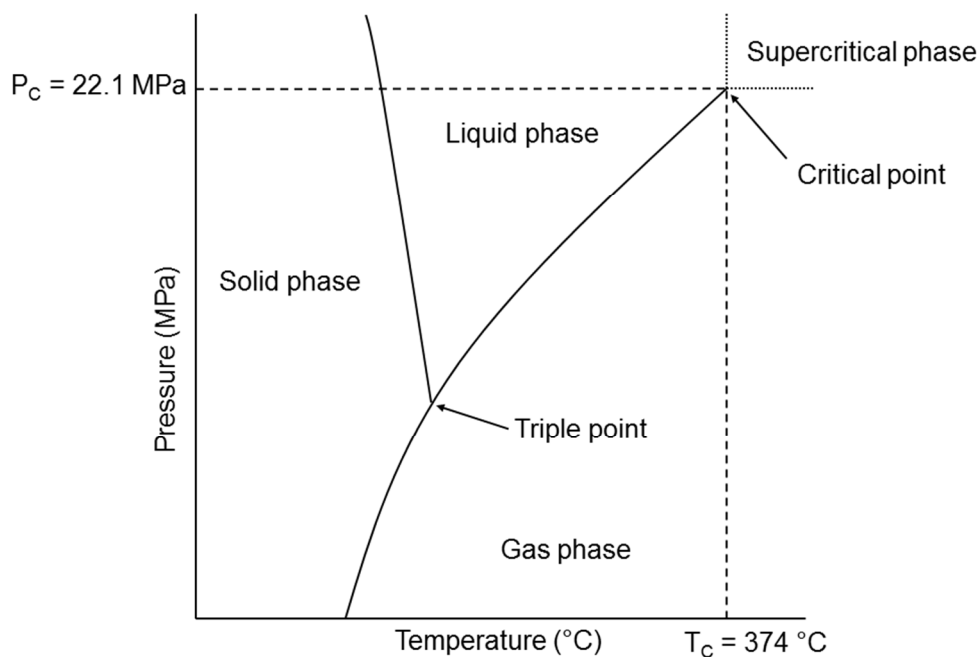


**Figure 1.4.** Phase diagram of pure water.

At these conditions, the properties of water offer an interesting environment to carry out chemical reactions. In Table 1.1, the physical properties of SCW are compared with those of liquid and gas.

**Table 1.1.** Comparison of the physical properties of liquids, gases and supercritical fluids (taken from [33]).

Physical quantity	Gas (ambient)	SCW ( $T_c$ , $P_c$ )	Liquid (ambient)
Density ( $\rho$ ), $\text{kg m}^{-3}$	0.6-2	200-500	600-1600
Dynamic viscosity ( $\eta$ ), mPa s	0.01-0.3	0.01-0.03	0.2-3
Kinematic viscosity ( $\nu^a$ ), $10^6 \text{ m}^2 \text{ s}^{-1}$	5-500	0.02-0.1	0.1-5
Diffusion coefficient ( $D$ ), $10^6 \text{ m}^2 \text{ s}^{-1}$	10-40	0.07	0.0002-0.002

[a] Estimated from dynamic viscosity and density ( $\nu = \eta/\rho$ ).



The density of SCW is slightly inferior than the one of liquid but higher than gas, whereas the dynamic viscosity of gas and SCW are very close to each other. The higher diffusivity of SCW compared to liquid and the inexistence of gas/fluid and fluid/fluid interphases reduce considerably the diffusion-controlled phenomena occurring in liquid phase. As illustrated in Figure 1.5, the high pressure-dependent density of SCW is another important characteristic that can be used to engineer the reaction environment. At 10 MPa the evaporation of water takes place around 310 °C and the density drops rapidly from 690 kg m<sup>-3</sup> to 55 kg m<sup>-3</sup>. By contrast, at 30 MPa (isobaric curve) there is no discontinuity from the liquid to the vapor phase. The reason is the absence of evaporation/condensation boundaries ( $\Delta H_{\text{vap}} = 0$ ). Therefore around the critical point, it is possible to adjust continuously either the pressure or the temperature in order to obtain a vast range of density.

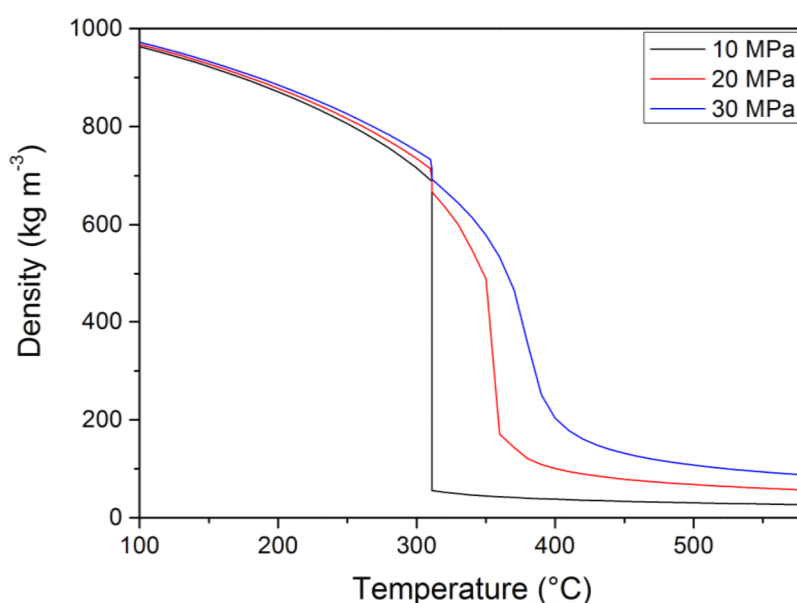


**Figure 1.5.** Variation of water density with pressure and temperature (calculated from NIST [34]).

Another interesting property of SCW is its low dielectric constant. As shown in Figure 1.6, the dielectric constant of water diminishes with increasing the temperature and falls drastically around the critical point. The decrease of the dielectric constant corresponds to a diminution of the water polarity. Hence, at SCW conditions, water behaves much more like an organic solvent having a high miscibility for weakly polar and non-polar organic compounds (*e.g.* fatty acids, naphthalene) and a low solubility for the salts.

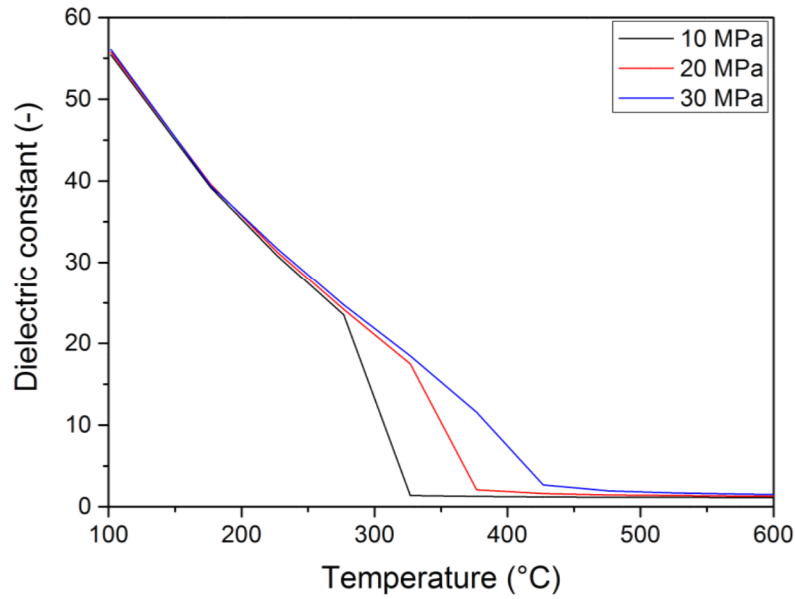
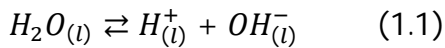


**Figure 1.6.** Influence of pressure and temperature on the dielectric constant of pure water (calculated from NIST [34]).

Figure 1.7 shows the effect of the temperature and pressure on the ionization constant of pure water defined as the product of the activities of the  $H^+$  and  $OH^-$  ions resulting from self-dissociation:



The ionization constant increases by approximately three orders of magnitude from 25 °C ( $10^{-14} \text{ mol}^2 \text{ kg}^{-2}$ ) up to 250-350 °C ( $10^{-11} \text{ mol}^2 \text{ kg}^{-2}$ ) and drops rapidly in the vicinity of the critical point by about 7 orders of magnitude ( $10^{-18}$ ). As shown in Figure 1.8, the phase change from liquid to vapor during heating of pure water at atmospheric pressure causes an abrupt increase of the enthalpy, while in the supercritical region the phase transition is smoother corresponding to a lower increase the enthalpy. Consequently, by operating at supercritical conditions, the process is less energy consuming in comparison to other superheated steam processes.

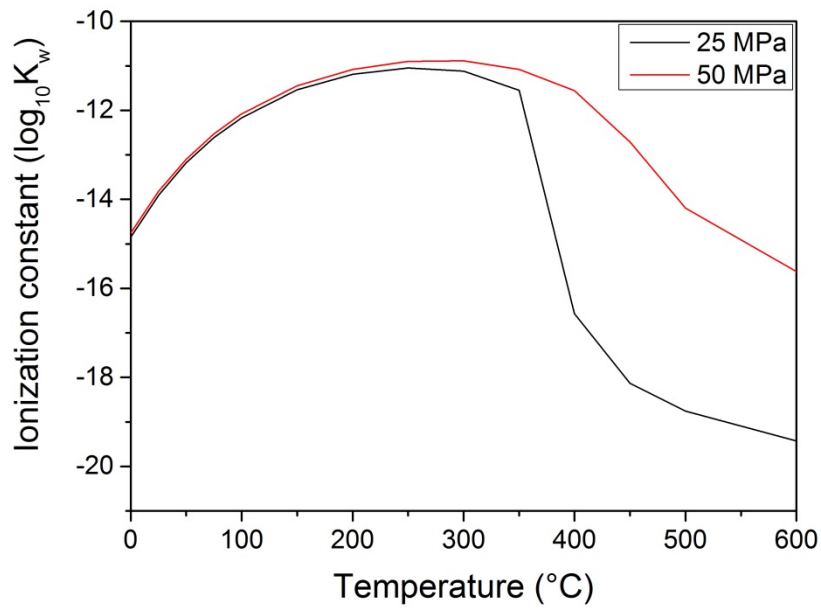


**Figure 1.7.** Influence of pressure and temperature on the ionization constant of pure water (adapted from [35,36]).

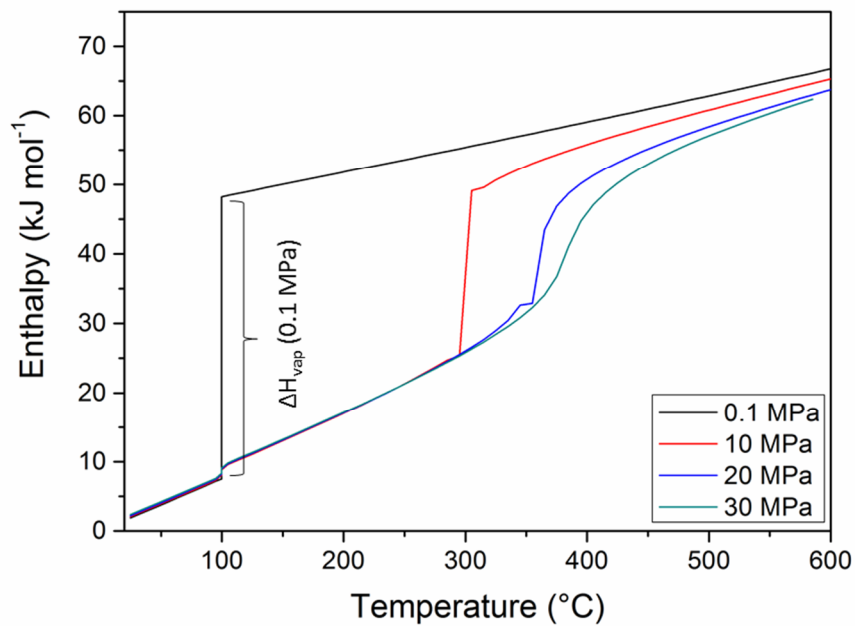


**Figure 1.8.** Enthalpy for pure water as a function of the temperature at different pressures (calculated from NIST [34]).

All these unique features of SCW offer several advantages during SCWG:

- The high effect of the temperature and pressure near the critical point of water allows the adjustment of the properties according to the process requirements [37].

- The low dielectric constant of water under SCW conditions results in low solubility of salts and improves the solubility of non-polar organic substances and gases [15,38]. As a result, tar and coke formation is reduced [16,39] and the salts can be removed by precipitation [40–43].
- The high density (compared to gases) and the low viscosity (compared to liquids) of SCW accelerate the heat and mass transfer [15,44].
- Enable to catalyze acid-base catalyze reactions such as hydrolysis or condensation reactions in sub-critical water due to the enhanced self-dissociation of water [37,45].

## 1.6 Phase behavior of salt-water mixtures

The phase behavior of salt-water mixtures at high temperatures and high pressures is highly specific, diverse, and differ considerably from the one at low temperatures and pressures. Usually, p-T-projections are used for the understanding of the phase behavior where the critical curve of the components (water and salt) and the three phases (S-L-V) can be visualized. Several types of binary water-salt mixtures exist but Valyashko has proposed a simplification by defining two basic categories of behavior, referred to as type 1 and type 2 phase behavior [46]. In Figure 1.9, a simplified p-T-projection of a type 1 and type 2 behavior is illustrated. For a type 1 phase behavior, the salt solubility increases continuously with the increasing of the temperature, even above the critical point of pure water. Note that the critical curve (V-L) does not intersect with the solubility curve (V-L-S<sub>s</sub>). Whereas for a type 2 phase behavior, an interruption of the critical curve occurs between the two critical endpoints where the solubility curve (V-L-S<sub>s</sub>) intersects the critical curve (V-L). Consequently, near the critical point of water, the solubility of salts decreases drastically with the increasing of the temperature. As a result, a solid phase is in equilibrium with a homogeneous supercritical fluid phase.

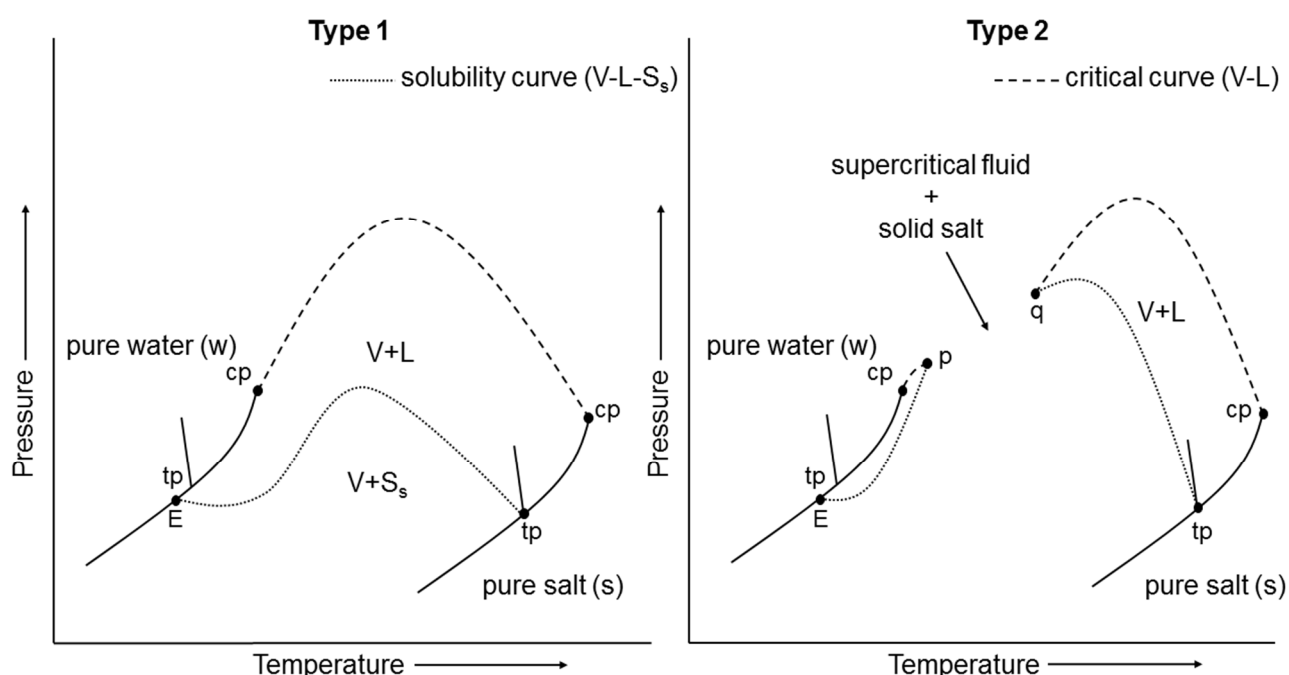


**Figure 1.9.** p-T phase diagrams for binary type 1 and 2 salt-water mixtures. cp: critical point of the pure components, tp: triple point of the pure components, p: lower critical endpoint, q: upper critical endpoint, E: eutectic point, V: vapor, L: liquid, S<sub>s</sub>: solid salt phase (adapted from [36], original version [47]).

In Table 1.2, a list of some salts classified in type 1 and type 2 phase behavior is given.

**Table 1.2.** Example of some salts classified as type 1 and type 2 phase behavior, according to Valyashko [48]. Note that some salts are listed twice, because different ion combinations for a particular cation or a particular anion are listed in a row.

Type 1 salts	Type 2 salts
KF (92 g 100 mL <sup>-1</sup> ) <sup>a</sup> , RbF (131 g 100 mL <sup>-1</sup> ) <sup>a</sup> , CsF	LiF (0.3 g 100 mL <sup>-1</sup> ) <sup>a</sup> , NaF (4 g 100 mL <sup>-1</sup> ) <sup>b</sup>
LiCl (84 g 100 mL <sup>-1</sup> ) <sup>c</sup> , LiBr (167 g 100 mL <sup>-1</sup> ) <sup>b</sup> , LiI	LiF
NaCl (36 g 100 mL <sup>-1</sup> ) <sup>c</sup> , NaBr, NaI	NaF
K <sub>2</sub> CO <sub>3</sub> (112 g 100 mL <sup>-1</sup> ) <sup>b</sup> , Rb <sub>2</sub> CO <sub>3</sub>	Li <sub>2</sub> CO <sub>3</sub> (1.3 g 100 mL <sup>-1</sup> ) <sup>b</sup> , Na <sub>2</sub> CO <sub>3</sub>
Rb <sub>2</sub> SO <sub>4</sub>	Li <sub>2</sub> SO <sub>4</sub> , Na <sub>2</sub> SO <sub>4</sub> , K <sub>2</sub> SO <sub>4</sub>
Na <sub>2</sub> SeO <sub>4</sub>	Na <sub>2</sub> SO <sub>4</sub> (19 g 100 mL <sup>-1</sup> ) <sup>b</sup>
K <sub>2</sub> SiO <sub>3</sub>	Li <sub>2</sub> SiO <sub>3</sub> , Na <sub>2</sub> SiO <sub>3</sub>
K <sub>3</sub> PO <sub>4</sub> (90 g 100 mL <sup>-1</sup> ) <sup>b</sup>	Li <sub>3</sub> PO <sub>4</sub> , Na <sub>3</sub> PO <sub>4</sub>
CaCl <sub>2</sub> (75 g 100 mL <sup>-1</sup> ) <sup>b</sup> , CaBr <sub>2</sub> , CaI <sub>2</sub>	CaF <sub>2</sub> (0.0016 g 100 mL <sup>-1</sup> ) <sup>b</sup>
SrCl <sub>2</sub> (54 g 100 mL <sup>-1</sup> ) <sup>b</sup> , SrBr <sub>2</sub>	SrF <sub>2</sub> (0.039 g 100 mL <sup>-1</sup> ) <sup>c</sup>
BaCl <sub>2</sub> (36 g 100 mL <sup>-1</sup> ) <sup>c</sup> , BaBr <sub>2</sub>	BaF <sub>2</sub> (0.16 g 100 mL <sup>-1</sup> ) <sup>b</sup>

Solubility in water at [a] 18 °C, [b] 20 °C, and [c] 25 °C at atmospheric pressure.

## 1.7 Biomass degradation to smaller molecules in sub- and supercritical water

Microalgae are complex eukaryotic organisms containing specialized vesicles (organelles) such as the chloroplasts. The latter play a major role for the human being, since they are responsible for

transforming solar energy, CO<sub>2</sub>, and water to oxygen via the photosynthesis. Although microalgae possess a high diversity of their biochemical composition, four main biochemical classes of molecules can be considered: carbohydrates, proteins, lipids, and nucleic acids. Additionally, they contain a large amounts of heteroatoms such as nitrogen (0.1 to > 10 wt %), sulfur (0.1 to > 1 wt %), chloride (0.1 to > 16 wt %), and phosphorus (0.1 to > 2 wt %) [17]. The decomposition of microalgae to smaller molecules in sub- and supercritical water proceeds through many complex reactions that can occur simultaneously resulting in a wide range of decomposition products. For the ease of the understanding, the following basic reaction mechanisms were described [13,49]:

- 1) Depolymerization of the biomass
- 2) Decomposition of biomass monomers by cleavage, dehydration, decarboxylation, and deamination
- 3) Recombination of reactive fragments

#### 1.7.1 Degradation of carbohydrates

Microalgae are constituted by carbohydrates mainly found as starch. Starch is a polysaccharide consisting of glucose monomers connected with  $\beta$ -(1  $\rightarrow$  4) and  $\alpha$ -(1  $\rightarrow$  6) [13]. In comparison to cellulose, starch is easily hydrolyzed to glucose or smaller oligomer units under hydrothermal conditions. These products undergo further degradation through a complex set of reactions including dehydration, retro-aldol, tautomerization, hydration, oxidation, and rearrangements. Glucose degrades mostly to fragmentation products such as glycolaldehyde, pyruvaldehyde, and glyceraldehyde. Nagamori et al. [50] investigated the decomposition products of starch (from sweet potato) at 180-240 °C in a batch reactor and found that glucose was the major product. The presence of other oligomers such as maltose, fructose, 5-hydroxymethylfurfural, and furfural was also reported.

#### 1.7.2 Degradation of proteins

Proteins are major components of microalgae representing 20-60 wt % of the cell content [51]. They consist of amino acid groups linked together by a peptide bond, which is a C-N bond between the carboxyl and amine groups. This bond is readily hydrolyzed in hydrothermal environment. Although amino acids have a different chemical structure, they degrade following decarboxylation and deamination reactions. Klingler et al. [52] studied the decomposition of alanine and glycine (250-450 °C,

24-34 MPa) in a continuous reactor. Both amino acids showed similar decomposition kinetic with an activation energy of  $160 \text{ kJ mol}^{-1}$ . No effect of the pressure was found between 24 MPa and 34 MPa. The decomposition products of alanine were mainly lactic acid and ethylamine. Whereas a high selectivity towards methylamine (84%) was found for the glycine decomposition at  $400^\circ\text{C}$  and 34 MPa. The degradation of bovine serum albumin was investigated by Rogalinski et al. [53] in a continuous reactor ( $310^\circ\text{C}$ , 25 MPa). The decomposition products were acetic acid, propanoic acid, n-butyric acid, iso-butyric acid, iso-valeric acid and the gaseous products were  $\text{CO}$ ,  $\text{CO}_2$ ,  $\text{H}_2$ , and  $\text{CH}_4$ .

During biomass degradation, amino acids and sugars are simultaneously formed and may react via the Maillard reaction (see Figure 1.10). The Maillard products are nitrogen containing cyclic organic compounds such as pyridines and pyrroles. These compounds act as free radical scavengers and inhibit free radical chain reactions which are relevant for gas formation at sub- and supercritical conditions [49].

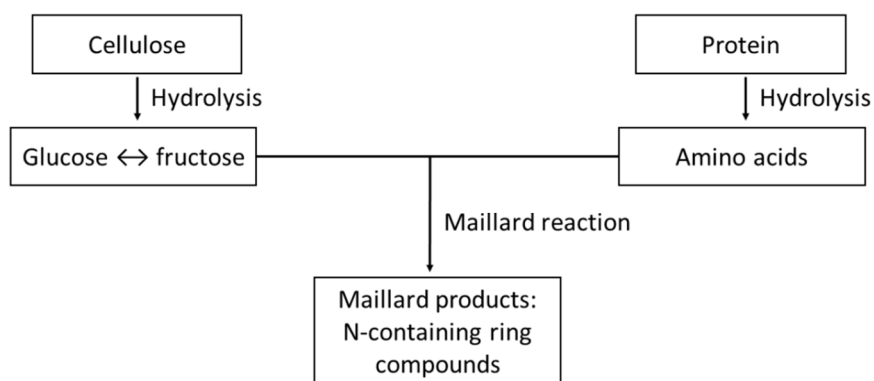


**Figure 1.10.** Reaction pathways of Maillard reaction during biomass degradation (adapted from [54]).

#### 1.7.2.1 Sulfur assimilation by microalgae

Microalgae, like most photolithotrophs, acquired sulfur as sulfate contained in the ocean and freshwater. After its uptake into the cytoplasm, sulfate is transported into the plasmids or stored in the vacuoles (in case of excess). Prior to its reduction, the sulfate anion must be activated to 5'-adenylsulfate (APS) by adenosine triphosphate (ATP). Then, APS is reduced to sulfite by APS reductase, which is further reduced to sulfide by sulfite reductase. Sulfide is rapidly integrated into cysteine

which is the first stable organic sulfur compound formed in the pathway [55]. Through this metabolic pathway, all reduced sulfur is incorporated into cysteine, which serves directly or indirectly as a precursor for the synthesis of all the compounds constituted with reduced sulfur. For instance, photosynthetic organisms (but not the animals) use cysteine as a precursor for the synthesis of methionine. Cysteine and methionine as amino acids are both the building blocks for all the proteins. Hence, the amount of sulfur contained in microalgae is directly related with the protein content.

### 1.7.3 Degradation of lipids

Microalgae are constituted mostly by fatty acid triacylglycerides (TAGs) and phospholipids/glycolipids. TAGs and phospholipids are easily hydrolyzed at 350 °C to glycerol, oleic acid, P-containing compounds, choline, and phosphoric acid in the case of phospholipids [56]. As one of the hydrolysis product, glycerol is rather converted to water-soluble compounds. Bühler et al. [45] investigated the decomposition products of glycerol in a continuous reactor (349-475 °C, 25-45 MPa). The conversion was 31% and the main products were methanol, acetaldehyde, propionaldehyde, acrolein, allyl alcohol, ethanol, formaldehyde, CO, CO<sub>2</sub>, and H<sub>2</sub>.

### 1.7.4 Degradation of nucleic acids

Nucleic acids provide the basis for microalgae division and growth. They constitute 3-5 wt % of the cell content, and are the major part of the phosphate in the cell as well as the second most important site of nitrogen [51]. According to the author's knowledge, no studies investigated the degradation products of nucleic acids. As mentioned by Brandenberger [17] due to their aromatic structure and high nitrogen content, they may prone to tar and char formation under sub- and SCW conditions.

## 1.8 Catalytic supercritical water gasification (CSCWG)

By contrast to SCWG performed at high temperatures (500-700 °C) where close to full conversion of biomass into a H<sub>2</sub>-rich product gas can be achieved without catalysts, CSCWG is carried out at low temperatures (below 374 °C, subcritical water) or moderate temperatures (374-500 °C). As the construction and operation of high pressure/high temperature equipment are high, by operating at milder conditions, the capital costs can be reduced [57]. At these conditions, in order to achieve full biomass conversion and a high selectivity towards H<sub>2</sub> or CH<sub>4</sub>, a catalyst is needed.



### 1.8.1 Heterogeneous catalysts for CSCWG

The choice of the catalyst relies mainly on the gaseous biofuel wished ( $\text{CH}_4$  or  $\text{H}_2$ ). In Figure 1.11, the desirable catalytic properties for  $\text{CH}_4$  production are described. Biomass is first hydrolyzed to small aliphatic molecules such as acetic acid, formic acid and acetaldehyde which can reach the catalytic active sites [15]. The decomposition of these intermediate molecules on the catalyst surface through C-C bond cleavage, results in the formation of  $\text{CO}$  and  $\text{H}_2$ , which are further upgraded to  $\text{H}_2$  and  $\text{CO}_2$  via the water-gas shift (WGS) reaction. If the catalyst favors the cleavage of C-O bonds, the produced  $\text{H}_2$  is used for the hydrogenation of the adsorbed species resulting in the formation of  $\text{CH}_4$ . Dreher [58] reported that methanation proceeds via direct hydrogenation of  $\text{CH}_x$  adsorbates on the Ru surface, instead of the classic methanation pathway via  $\text{CO}$  and  $\text{H}_2$ . In summary, for  $\text{CH}_4$  production, the catalyst should exhibit a high activity for the cleavage of C-C and C-O bonds and enhance the WGS. By contrast for  $\text{H}_2$  production, the catalyst should minimize C-O bond cleavage, besides favoring the C-C bond cleavage and the WGS [59,60].

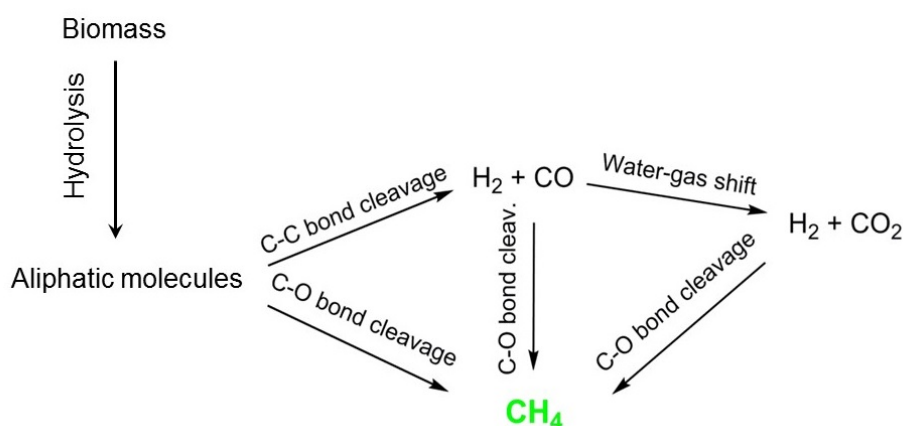


**Figure 1.11.** Reaction pathways for  $\text{CH}_4$  production during CSCWG of aliphatic molecules (adapted from [57,61]).

Ru has been found to be the most active and selective metal towards  $\text{CH}_4$  formation by facilitating also the C-O bond cleavage [15]. Osada et al. [62] investigated the catalytic performance of various supported metal catalysts (*e.g.* Ru, Rh, Pt, Pd, and Ni) during CSCWG of lignin at 400 °C and 37.1 MPa. The catalytic activity was in the following order: Ru > Pt > Rh > Pd > Ni demonstrating the better catalytic performance of supported Ru catalysts. Waldner [63] reported the good catalytic performance of a commercial Ru/C catalyst for CSCWG of synthetic liquefied wood (SLW) over a period of 220 h as well as its high  $\text{CH}_4$  selectivity. Apart from Ru-based catalysts, Ni-based catalysts were also widely studied for CSCWG [64]. Although the price of Ni is low in comparison to the one

of Ru, its main drawback, is its ability to sinter rather rapidly under SCW conditions [63,65]. Elliott et al. [14,66] evaluated also different Ni-based catalysts and observed their low stability due to either breakdown of the support or even sintering. Besides of the active metal, the role of the catalyst support under SCW conditions is crucial. Due to the harsh conditions of SCW, most of the conventional metal oxide supports such as SiO<sub>2</sub>, zeolites, *anatase*-TiO<sub>2</sub>, aluminosilicate, MgO, *cubic*-ZrO<sub>2</sub>,  $\gamma$ -Al<sub>2</sub>O<sub>3</sub>, and silica-alumina are not stable [64]. Among the catalyst supports, mainly *rutile*-TiO<sub>2</sub>,  $\alpha$ -Al<sub>2</sub>O<sub>3</sub>, *monoclinic*-ZrO<sub>2</sub> and carbon were reported to be promising supports for CSCWG [64,67–69]. The use of carbon has several advantages like a high specific surface area ( $> 500 \text{ m}^2 \text{ g}^{-1}$ ) allowing for a higher Ru dispersion, a high resistance to acidic and basic media, a good stability at high temperatures and in aqueous media, the possibility to modify its chemical surface properties by adding anchoring groups, the recovery of the active phase of the used catalyst by combustions (crucial if the active phase is a noble metal), and a low price. Elliott et al. [68] tested numerous Ru catalysts supported on different supports during continuous CSCWG of phenol (350 °C, 21 MPa). They reported a good long-term stability for the Ru/C, Ru/ZrO<sub>2</sub>, and *rutile*-TiO<sub>2</sub> catalysts by operating at full conversion. Zöhrer [36] investigated the stability of several Ru catalysts supported on metal oxides during continuous CSCWG of glycerol (400 °C, 28.5 MPa). Among the tested catalysts, Ru/*rutile*-TiO<sub>2</sub>, Ru/*monoclinic*-ZrO<sub>2</sub>, and a stabilized tetragonal Ru/ZrO<sub>2</sub> exhibited good catalytic performance by working at a low WHSV of  $0.6 \text{ g}_{\text{org}} \text{ g}_{\text{cat}}^{-1} \text{ h}^{-1}$  (full conversion). Other studies carried out in batch reactor compared the activity of Ru catalysts supported on different supports. For instance, Osada et al. [70] observed a higher activity and stability for Ru/TiO<sub>2</sub> compared to Ru/C during CSCWG of lignin (400 °C, 37.1 MPa). The decrease of the specific surface area of the Ru/C, which was due to a change of the pore structure, was believed to be the cause for the loss of activity. More recently, Yamaguchi et al. [71] reported a similar activity between Ru/C and Ru/TiO<sub>2</sub> during CSCWG of lignin (400 °C, 37.1 MPa).

The current status on catalyst development for CSCWG shows that most of the tested catalysts are commercial catalysts. Non-noble metal catalysts that are used for hydrogenation (e.g. Raney Ni), steam reforming (e.g. Ni/Al<sub>2</sub>O<sub>3</sub>), and also noble metal catalysts (e.g. Ru/C, Ru/Al<sub>2</sub>O<sub>3</sub>, Pt/Al<sub>2</sub>O<sub>3</sub>) are the most commonly employed catalysts. As mentioned by Azadi et al. [64] most of the research is mainly focused on the potential application of SCWG process for converting diverse types of biomass into H<sub>2</sub>, CH<sub>4</sub>, and syngas. Although most of these applications use catalysts for improving the gasification rate, up to now only few studies concentrate solely on the catalyst design. In fact, there

is still a lack of knowledge about the interdependence between the catalyst formulation and its structure related to its catalytic performance. For instance, by investigating systematically the effect of the synthesis factors (e.g. metal dispersion, catalyst preparation method) on the catalytic performance. All these studies may be beneficial for the improvement of the process viability. As pointed out by Azadi et al. [64] most of the reviews on CSCWG indicate that only the catalytic activity has been well investigated, whereas only few studies dedicated on the improvement of the catalyst stability.

#### 1.8.1.1 Active Ru species during CSCWG

While many studies concentrated rather on the conversion of biomass and organic model compounds, only a few of them studied the mechanism involved during CSCWG over supported Ru catalysts [72–74]. Park et Tomiyasu [72] were the first to propose a reaction mechanism involving a redox cycle between  $\text{Ru}^{4+}$  and  $\text{Ru}^{2+}$  where the organic compounds are partially oxidized by  $\text{RuO}_2$  to produce CO and  $\text{H}_2\text{O}$ , while  $\text{Ru}^{4+}$  are reduced to  $\text{Ru}^{2+}$ . However, this mechanism has been recently disproved. Yamaguchi et al. [73] showed by *ex situ* extended X-ray absorption fine structure (EXAFS) spectroscopic analysis that metallic ruthenium was formed during CSCWG of lignin (450 °C, 37.1 MPa) over Ru/C catalysts. More recently, Rabe et al. [74] were the first to perform *in situ* X-ray Absorption Spectroscopy (XAS) analysis of a Ru/C catalyst during CSCWG of ethanol (390 °C, 25 MPa). The catalyst was rapidly reduced to metallic ruthenium around 150 °C by ethanol and remained under its metallic state up to 390 °C. This observation suggests that the active phase is metallic ruthenium rather than oxidized ruthenium. They proposed a mechanism for the  $\text{CH}_4$  formation, which is similar to the steam reforming of ethanol. They suggested that ethanol adsorbs on the catalyst and decomposes to acetaldehyde and  $\text{H}_2$ . CO remains strongly adsorbed and reacts quickly with  $\text{H}_2\text{O}$  to form  $\text{H}_2$  and  $\text{CO}_2$  via the WGS reaction. Then,  $\text{CO}_2$  is further hydrogenated to  $\text{CH}_4$  via the methanation reaction. Dreher [58] resolved the pathway of the methanation reaction by using *in situ* XAS during CSCWG of ethanol (400 °C, 26 MPa) in combination with chemical probing via isotope labeling and electronic structure calculations. Instead of the methanation pathway via CO and  $\text{H}_2$ , methanation proceeds via direct hydrogenation of  $\text{CH}_x$  adsorbates on the Ru surface.

### 1.8.2 Effect of sulfur during CSCWG

Many studies investigated the effect of sulfur species on the catalytic performance under hydrothermal conditions [40,58,63,65,75–78]. It was found that Ru was rapidly poisoned by sulfur compounds such as elemental sulfur, thiophene, 2-methyl-1-propanethiol, 4-hydroxythiolphenol, 4-methylthiophenol, dimethyl sulfoxide (DMSO), and sulfuric acid, under hydrothermal conditions leading to an irreversible loss of the catalytic activity. Osada et al. [76,77] studied in a batch reactor, the effect of various sulfur compounds during gasification of lignin (400 °C, 75.6 MPa). In presence of sulfur, the decrease of the gasification rate was caused by the diminution of the active sites of Ru. The C–C bond cleavage and the methanation reaction were both inhibited by sulfur, whereas the presence of a higher concentration of H<sub>2</sub> and CO<sub>2</sub> suggested that the WGS was still favored. *Ex situ* characterization of the spent catalyst by X-ray photoelectron spectroscopy (XPS) revealed that the poisoned active sites were ruthenium sulfide, ruthenium sulfite, and ruthenium sulfate. Waldner et al. [63,65] reported a deactivation of a Ru/C catalyst in presence of Na<sub>2</sub>SO<sub>4</sub> during continuous CSCWG of SLW (400 °C, 30 MPa). As a hypothesis, the formation of a stable ruthenium sulfate complex was suggested to be the reason for the deactivation of the catalyst, whereas the deactivation caused by a physical blockage by precipitation of Na<sub>2</sub>SO<sub>4</sub> was discarded. More recently Dreher et al. [78] investigated *in situ* by XAS the structural analysis of a working Ru/C catalyst during continuous CSCWG of ethanol (400 °C, 24.5 MPa). In presence of sulfur (DMSO), the results have shown that sulfur poisoning occurred at the surface of the Ru NPs where the sulfur surface coverage was ca. 40%. Hence, a partial sulfur coverage was enough for blocking the active sites of Ru. Regarding CSCWG of wet biomass, sulfur was reported to have detrimental effect on the catalytic performance of supported Ru catalysts [4,79,80]. Haiduc et al. [4] were the first to observe the effect of sulfur during CSCWG of microalgae *Phaeodactylum tricornutum* (*Phaeod. tric.*)(400 °C, 30 MPa) over a 2% Ru/C catalyst. They found out that a higher sulfur-to-catalyst ratio decreased significantly the carbon gasification efficiency (GE<sub>C</sub>) demonstrating the negative effect of sulfur on the catalytic performance. In a similar study performed by Guan et al. [79], the same trend was observed when gasifying *Nannochloropsis sp.* (410 °C) over a 5% Ru/C catalyst.

As sulfur was found to poison irreversibly the Ru catalysts during CSCWG, there is a necessity to develop sulfur-resistant Ru catalysts, efficient regeneration methods, and sulfur removal methods (e.g. sulfur adsorbent material) in order to achieve high periods on stream.

Up to now, only a few regeneration methods of sulfur poisoned Ru catalysts were investigated and proposed [36,58,65,75,81]. Osada et al. [81] reported a water regeneration method at subcritical conditions. They compared the catalytic performance during CSCWG of lignin (400 °C, 37.1 MPa) of a fresh Ru/TiO<sub>2</sub>, sulfur poisoned Ru/TiO<sub>2</sub>, and sulfur poisoned Ru/TiO<sub>2</sub> catalysts which were regenerated with water at different conditions ( $25 \leq T \leq 400$  °C,  $0.1 \leq P \leq 40$  MPa). GE<sub>C</sub> was 98% for the fresh catalyst, 21% for the sulfur poisoned catalyst and 21-57% for the regenerated catalysts. The best regeneration performance was achieved at a water density of 750-830 kg m<sup>-3</sup> (corresponding to 250-300 °C at 25 MPa). It is important to point out that the catalysts were not poisoned on stream during CSCWG but during the catalyst impregnation. In fact, the Ru/TiO<sub>2</sub> catalysts were soaked in sulfuric acid at room temperature and dried by evaporation. As reported by Elliott et al. [82] no poisoning effect of sulfate ions was observed at low temperature (100 °C). Waldner et al. [63,65] reported a similar result where no sulfur poisoning effect was observed when feeding with Na<sub>2</sub>SO<sub>4</sub> at a temperature of 200 °C. Therefore according to Elliott and Waldner's results, it remains questionable whether Osada's catalysts were really poisoned by sulfur. It is likely that the deposited sulfate ions were washed out during the subcritical pretreatment.

Waldner [65] proposed a more realistic regeneration method since a Ru/C catalyst was poisoned by Na<sub>2</sub>SO<sub>4</sub> on stream at SCW conditions. The regeneration was carried out with 1 wt % H<sub>2</sub>O<sub>2</sub> at 50 °C during 3 h and at 90 °C for additional 3.3 h. At the beginning, the catalytic activity was almost totally recovered with a gas composition close to the thermodynamic chemical equilibrium. However, within 24 h on stream, the catalytic activity steadily decreased up to 80%. Such a loss was explained by a too short regeneration period for ensuring a complete regeneration. More recently Dreher et al. [58,75] optimized the regeneration method proposed by Waldner and investigated *in situ* using XAS, the structural change of Ru under reaction conditions. After being sulfur poisoned by DMSO, the Ru/C catalyst was regenerated on stream using 3 wt % of H<sub>2</sub>O<sub>2</sub>. The catalyst regeneration was performed at different temperatures (75-125 °C) and regeneration time (20-240 min) in order to find the most suitable regeneration conditions. EXAFS measurements showed that S-Ru/C was entirely oxidized and converted to RuO<sub>2</sub>/C suggesting that the sulfur species were removed from the Ru surface. After the oxidative pre-treatment, the catalyst was reduced by ethanol (390 °C, 24.5 MPa) for its re-activation. The catalytic performance of the re-activated catalysts was assessed during CSCWG of ethanol (390 °C, 25 MPa). The regeneration method was efficient since the catalytic activity was similar to the fresh catalyst. It was found out that a second pre-treatment (2 × 20 min)

was required for the regeneration performed below 125 °C in order to achieve the same catalytic performance than the one at 125 °C (1 × 20 min). Moreover, a regeneration time of 4 h when carried out at 125 °C, affected the structure of the catalyst (formation of cracks), whereas when performed at 75 °C during the same period, no cracks were detected. Similarly to Waldner's experiment a decrease of the catalytic activity was observed after a few hours on stream. The change of the Ru NPs size and structure following the oxidative pre-treatment was proposed by the authors. However, *in situ* methods like XAS combined with *ex situ* electron microscopy are still needed for providing more information about the change of the Ru NPs size and structure before, during, and after the H<sub>2</sub>O<sub>2</sub> treatment.

### 1.8.3 Effect of salts

As mentioned in section 1.7, microalgae contained a large amount of minerals (*e.g.* chlorides, phosphorus, potassium) whose the amount and type differ considerably according to the microalgae species. These minerals can have positive and negative effects during CSCWG. Here, their advantages and drawbacks are discussed.

Positive effects:

- Act as homogeneous catalysts during liquefaction and CSCWG:

Alkali salts such as KOH, KHCO<sub>3</sub>, K<sub>2</sub>CO<sub>3</sub>, NaOH or Na<sub>2</sub>CO<sub>3</sub> were reported to have a catalytic effect since they may catalyze dehydrations, hydrolysis, aldol splitting, and Cannizzaro reactions [83–88]. Schmieder et al. [88] showed that the addition of KOH and K<sub>2</sub>CO<sub>3</sub> favored the WGS reaction during SCWG of carbohydrates, aromatic compounds, and glycine (550-600 °C, 25 MPa). KHCO<sub>3</sub> was reported to enhance not only the WGS reaction during SCWG of glucose (400-500 °C, 25 MPa) but also to reduce the amount of furfurals which are known to form undesired polymerized products [86]. The addition of NaOH was found to be beneficial for the enhancement of the decomposition of ketone and aldehyde into CO during partial oxidative gasification of n-hexadecane (400 °C, 40 MPa) [87]. The authors reported also the beneficial effect of NaOH during partial oxidative gasification of lignin (400 °C, 40 MPa) since in presence of NaOH, the enhancement of the decomposition of carbonyl compounds inhibited the char formation and promoted CO and H<sub>2</sub> formation. Fang et al. [85] studied the effect of Na<sub>2</sub>CO<sub>3</sub> during dissolution of willow (25-400 °C, up to 106 MPa) and showed that

$\text{Na}_2\text{CO}_3$  favored the dissolution, hydrolysis/liquefaction, inhibits solid residue formation, and protects the reactor from corrosion.

- Valuable co-products:

As discussed in section 1.3, the nutrient recycling is crucial for the economics of the process. Among the heteroatoms constituting the nutrients, phosphorus is of particular interest due to its slow natural cycle. As the consumption of phosphorus is foreseen to increase due to the augmentation of the world's population, the expected global peak in phosphorus production may be expected to occur around 2030 [89]. Currently, phosphorus is mainly produced from rock phosphate, which is a limited resource. Therefore the recycling of phosphorus from biomass will play a major role in a near future.

Negative effects:

- Precipitation at the inner surface of the equipment:

As discussed in section 1.5, under SCW conditions the solubility of salts is drastically reduced. As a consequence, salt precipitation may lead to reduce heat transfer and plugging of the process [16,90].

- Corrosion:

Corrosion was observed during SCWG but at a lower extent than during supercritical water oxidation [16]. Kruse et al. [91] reported severe corrosion when processing zoo biomass in a continuous stirred tank reactor (CSTR) (500 °C, 30 MPa). The presence of sulfur in the protein-containing biomass was likely the cause for the corrosion. At low and moderate temperatures ( $T < 500$  °C), corrosion is attenuated. However, there is still a necessity to perform more experiments over longer period of time ( $> 1000$  h) in order to evaluate the corrosion extent.

- Deactivation of the catalyst:

Some studies reported a decrease of the catalyst lifetime when processing organic compounds in presence of salts or real biomass [63,67,92]. A Ru/C catalyst was rapidly deactivated during SCWG of SLW with  $\text{Na}_2\text{SO}_4$  (400 °C, 30 MPa) [63]. The hypothesis for the loss

of activity was due to the formation of a stable Ru sulfate complex and not due to physical blockage by precipitation of  $\text{Na}_2\text{SO}_{4(s)}$ . Elliott et al. [67] found some inorganic compounds deposited on the catalyst when processing methanol with  $\text{NaNO}_3$  (360 °C, 21 MPa). However, no deactivation of the catalyst due to  $\text{NaNO}_3$  was claimed. Some mineral deposits (e.g. S, P, Mg, Ca) were observed on the catalyst surface during continuous CSCWG of microalgae (420 °C, 32 MPa) [92]. Due to the complexity of microalgae regarding its chemical composition, the deactivation of the catalyst could not be solely attributed to the salts deposits but also to coking and sulfur poisoning. In summary, up to now, no clear relation between salt precipitation and deactivation of the catalyst was demonstrated. Only alkali sulfate salts were shown to be problematic due to the irreversibly poisoning by sulfur.

Although the minerals contained in microalgae are beneficial for the viability of the process, separation techniques should be developed for an efficient removal of the salts. In this context, some research groups have developed separation techniques [42,93,94]. At Karlsruhe Institute of Technology (Germany), a high temperature hydrothermal process with a capacity of 100 kg h<sup>-1</sup> so called "VERENA" was built. The process aims at gasifying wet waste biomass (600-700 °C, up to 35 MPa) to a H<sub>2</sub>-rich gas in presence of a homogeneous catalyst (alkali salts) [93]. For preventing any plugging caused by the salt precipitation, the salt separation is performed at the bottom of the reactor with the help of the down-flow and gravity. The salts accumulated at the bottom are then removed from the process. For avoiding any salt precipitation, the heating up to the reaction temperature took place in the lower part of the reactor. With this configuration, they were able to work during 10 h without any plugging of the process. Elliott et al. [94] have developed a hydrothermal process for continuous catalytic hydrothermal gasification of microalgae (350 °C, 20 MPa) with a pumping capacity of 0.2-4 kg h<sup>-1</sup>. A preheater functioning as a CSTR was used for heating the feedstock to the reaction temperature. A vessel placed between the preheater and the reactor was installed. The latter aims at capturing and removing the solids. At Paul Scherrer Institut (PSI), a continuous CSCWG process (400-450 °C, 25-30 MPa) so called "KONTI-2" was developed with a pumping capacity of 1 kg h<sup>-1</sup> [40]. A salt separator located upstream of the reactor is used for continuous salt removal. After heating up of the feedstock with a preheater, the liquefied product enters the salt separator from the top. The salts precipitated to the bottom of the vessel and are removed from the process via a brine effluent, whereas the effluent rich in organic leaves the vessel at the top prior to entering the reactor.



### 1.8.4 Tar and coke formation

Tarry substances and carbon particles (coke) are undesired side-products during CSCWG since they reduce the  $GE_c$ , lead to plugging of the plant, and deactivate the catalyst. Tars are defined as non-volatile molecules of high molecular weight, which are soluble in polar solvents such as methanol or acetone. They are typically constituted by aromatic and polyaromatic compounds containing different functional groups. Müller [95] studied the degradation of glycerol under sub- and supercritical conditions and proposed a reaction pathway (see Figure 1.12). According to the degradation temperature, two similar pathways differing in the product composition were described, one at subcritical conditions (300-370 °C) and another at supercritical conditions (374-430 °C). The first degradation step is similar whether performed at sub- or supercritical conditions and leads to the formation of smaller, water-soluble products via mostly dehydration reactions. Then, a small fraction of these reactive intermediates reacts to form stable organic acids (acetic and propionic acid). At SCW conditions, most of the water-soluble intermediates are gasified directly to gaseous products composed of  $H_2$ ,  $CH_4$ , and higher hydrocarbon yields where the composition is temperature-dependent. At these conditions, only a small fraction of reactive intermediates reacts to tars (butane) and no or nearly no coke is produced. Under subcritical conditions, the product distribution differs considerably. In fact, most of the reactive intermediates form primary tars, which are further transformed to secondary tars (higher molar mass compared to primary tars), and finally react to coke. The latter is a stable product under subcritical conditions. The gas produced from reactive intermediates is low and composed mainly of  $CO$  and  $CO_2$ . Note that a negligible amount of gas ( $CO_2$ ,  $H_2$ , and  $CO$ ) is produced from the tars.

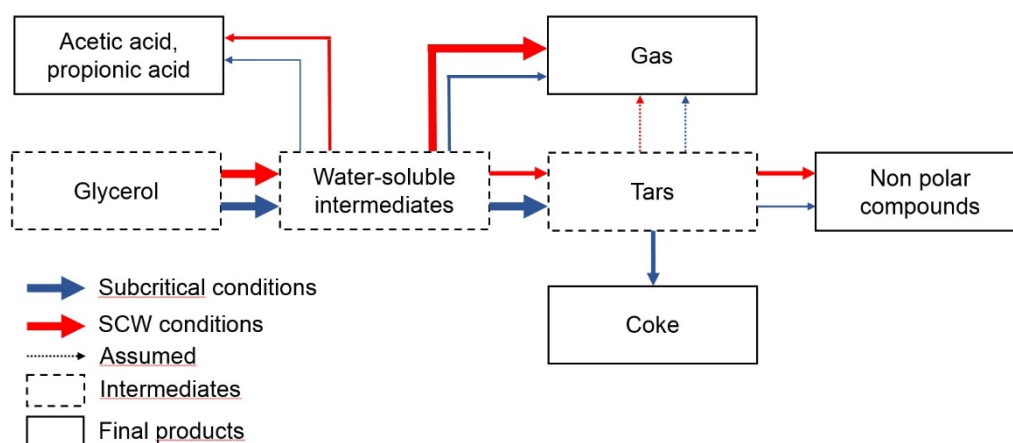


**Figure 1.12.** Reaction pathway for the degradation of glycerol under sub- and SCW conditions (adapted from [95]).

As an illustration of cokes, Figure 1.13 shows that the coke morphology differs whether degraded under sub- or supercritical conditions. At 300 °C, the cokes consist of filigree-interconnected spheres where the latter form a framework having a well-defined shape. At 400 °C, no spheres can be observed and the cokes look like a ceramic material. The coke particles are relatively large with an edge length of about 100 µm.

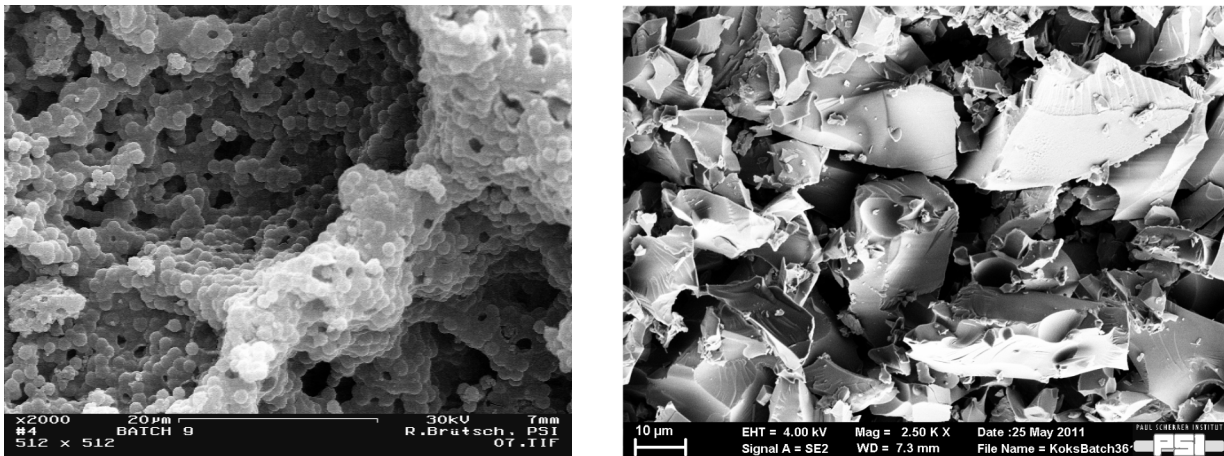


**Figure 1.13.** Scanning electron microscopy (SEM) pictures of cokes formed during the degradation of 20 wt % glycerol at 300 °C (left side) and 400 °C (right side) with a reaction time of 60 min (taken from [95]).

Karayildirim et al. [96] proposed two possible reaction pathways to form carbon particles depending on the biomass hardness (see Figure 1.14). In the case of cellulose, biomass degradation followed by polymerization of the intermediates to solid microspheres (cokes) predominates (pathway A). Whereas for “hard” biomass containing a high lignin content, biomass converts rather to char which has a similar structure to the original biomass (pathway B). Some parameters such as the heating rate of the feedstock and the density of SCW (influence the solubility) are relevant for reducing coke formation. In fact, Matsumura et al. [97] showed that a fast heating rate of the feedstock (glucose and cabbage slurry) led to higher  $GE_c$ . A high solubility of tar and coke is also needed for minimizing coke formation.

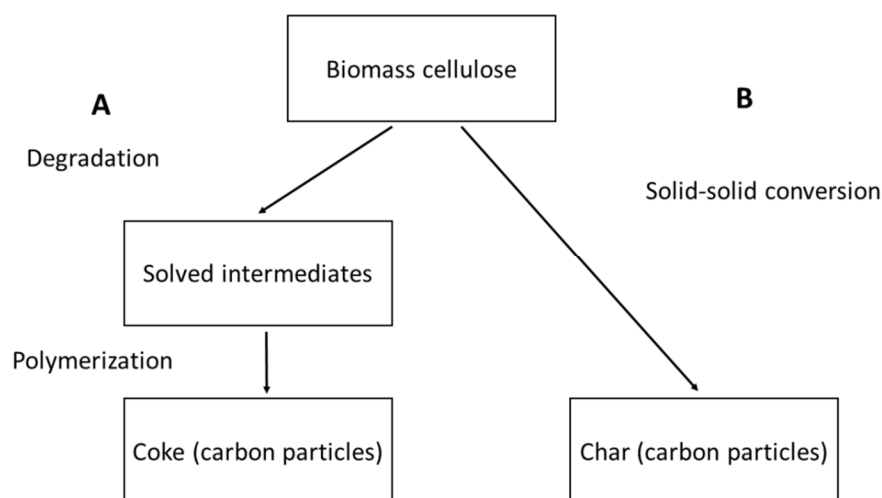


**Figure 1.14.** Possible reaction pathways for the formation of coke (adapted from [96]).

Tar and coke formation was already reported to be a serious issue when processing biomass feedstocks in a continuous test-rig. Zöhrer [36] observed a rapid plugging ( $< 2$  h) of KONTI-2 during continuous liquefaction ( $430\text{ }^{\circ}\text{C}$ ,  $28\text{ MPa}$ ) of fermentation residues. The main reason for the fast stop of the operation was a high amount of sticky tars accumulated in the process (half of the carbon contained in the feed) causing a high increase of the pressure ( $> 2\text{ MPa}$ ). Tars were suspected to be formed in the subcritical region of the preheater. Additionally to tar formation, cokes were also observed in the effluents leaving the salt separator suggesting that further condensation of the “tar-phase” to coke occurred. By increasing the temperature of the salt separator from  $430\text{ }^{\circ}\text{C}$  to  $470\text{ }^{\circ}\text{C}$ , tar and coke formation was even higher leading to a premature stop of the experiment.

Tar and coke formation is not only an issue for the stability of the process but may deposit on the catalyst bed as well. May et al. [98] observed a deposition of carbon on the bed when gasifying glycerol ( $510\text{ }^{\circ}\text{C}$  and  $550\text{ }^{\circ}\text{C}$ ,  $35\text{ MPa}$ ) over a  $\text{Ru}/\text{ZrO}_2$  catalyst. Interestingly, carbon deposits were found solely on the inert  $\text{ZrO}_2$  particles that were used to dilute the catalyst bed indicating that Ru is needed for reducing coking. Zöhrer et al. [69] studied the stability of some Ru catalysts supported on metal oxides ( $\text{TiO}_2$  and  $\text{ZrO}_2$ ) during CSCWG of glycerol ( $400\text{ }^{\circ}\text{C}$ ,  $28.5\text{ MPa}$ ) and observed coke deposits on the spent catalysts. Brandenberger [17] characterized a spent 2%  $\text{Ru}/\text{C}$  catalyst after CSCWG of (*Phaeod. tric.*) ( $420\text{ }^{\circ}\text{C}$ ,  $32\text{ MPa}$ ) and found coke deposits on the catalyst surface, too. De Vlieger et al. [99] observed that reforming of acetic acid ( $275\text{ }^{\circ}\text{C}$ ,  $25\text{ MPa}$ ) over  $\text{Pt}/\text{Al}_2\text{O}_3$  catalysts led to a fast deactivation of the catalyst within 3 h due to coke deposition on the catalyst surface while

no deactivation occurred when reforming other alcohols (methanol, ethanol). Dreher [58] also reported the decrease of the catalyst lifetime after 3 h on-stream when gasifying 21 wt % acetic acid (390 °C, 25 MPa) over a 2% Ru/C catalyst. It was suggested that the polymerization rate of acetic acid dominated the overall gasification rate at subcritical conditions leading to coke deposition on the catalyst. Recently, De Vlieger et al. [100] found out that a carbon nanotube (CNT) supported Ru catalyst was stable during reforming of acetic acid at 270 °C and 23 MPa and at 400 °C and 25 MPa as well, while in the subcritical region (340 °C, 23 MPa) a fast deactivation was observed. The high ionic product at subcritical conditions was the cause for the deactivation of the catalyst due to an over-oxidation of Ru. Since no carbon deposits were detected, it seems that CNF supported Ru catalysts are less prone to coking due to the absence of micropores. Recently, Kudo et al. [101] found out that an increase of the Ru loading (from 7 wt % to 21 wt %) can significantly minimized coking during catalytic hydrothermal gasification of lignin (350 °C, 20 MPa) over a Ru/C catalyst. In fact, only a small amount of coke was observed on the spent 21% Ru/C and its physical properties were well preserved in comparison to those of the spent 7% Ru/C.

## 1.9 The SunCHem process

In the frame of the SunCHem process, CSCWG was chosen as the conversion technology for converting microalgae to methane. Its main advantages over other technologies are shown in Table 1.3. Although the technical feasibility of the conventional gasification and the anaerobic digestion has been already demonstrated, CSCWG has the highest thermal efficiency since wet biomass can be processed without the need of a drying step. Unlike the anaerobic digestion, CSCWG can fully convert wet biomass to gaseous products without leaving behind unconverted organic material allowing to improve further its thermal efficiency. As mentioned in section 1.4.1.2, short residence times are needed for converting wet biomass reducing the size of the reactors compared to those designed for the anaerobic digestion. However, many technical challenges have still to be overcome in order to demonstrate the technical feasibility of a continuous process and are discussed later on. In the past, in our group, many gasification experiments of microalgae were performed in batch reactor by using supported Ru catalysts. It was reported that *Spirulina platensis* and *Phaeod. tric.* can be both efficiently converted to gaseous products [4,102]. Due to the high content of heteroatoms (e.g. sulfur), an excess of catalyst (mass ratio of catalyst to algae of 8) was needed to reach a high conversion and a gas composition similar to the thermodynamic chemical equilibrium. In fact,

a fraction of the active sites is sacrificed as adsorbent for these poisoning elements while the free active sites of Ru can convert and gasify the organic intermediates. These preliminary batch experiments showed the necessity for removing efficiently the heteroatoms present in microalgae in order to avoid the poisoning of the catalyst.

**Table 1.3.** Comparison of CSCWG with other typical technologies (adapted from [4]).

Characteristic	Conventional gasification & methanation	Anaerobic digestion	CSCWG
Feed type	Wood, grass ( $w_{H_2O} < 15\%$ )	Manure, household residues, sewage sludge, marine algae	Most wet types ( $w_{H_2O} > 60\%$ )
Thermal efficiency (biomass to $CH_4$ )	54-58% (absolutely dry wood)	25-50% (< 8% dry matter manure)	70-77 <sup>a</sup>
Residence time	< 10 min	20-33 days	< 30 min
Technological readiness	Good	Very good (commercially available)	R&D
Advantages	High efficiency for dry biomass, close to commercialization	Established commercialized, fertilizer by-product	Full conversion, high efficiency, fertilizer by-product
Drawbacks	Low efficiency for wet biomass	Residues, low efficiency, plant size, requirement of co-substrates	Technical barriers to be solved

[a] Gassner et al. [12]

In Figure 1.15 a simplified scheme of the SunChem process is shown. The latter aims at combining the generation of methane via continuous CSCWG with the production of chemicals from microalgae. The process can be divided in five steps. The first step is the production of microalgae using either photobioreactors (PBR) or open ponds. During the microalgae growth,  $CO_2$  is fixed and metabolized into biomass and  $O_2$  by photosynthesis. Atmospheric  $CO_2$  or even anthropogenic  $CO_2$  (coming from exhaust gases of fossil fuel power plants) can be used as the carbon source. Hence,  $CO_2$  sequestration is another asset of this process. The second step consists in removing mechanically the excess of water in order to concentrate the slurry up to 15-20 wt %. The water fraction rich in nutrients is recycled for the microalgae culture. Then, the microalgae slurry is liquefied at 350 °C under 28-30 MPa and the salts are separated and recycled back for the microalgae growth. In the fourth step, the organic fraction is catalytically gasified to methane (60 vol %) and  $CO_2$  (40 vol %). Finally,  $CO_2$  is separated and recycled to the microalgae cultivation system and a fraction of the

methane is used for heating the process. The novelty of this process is the recycling of all the liquid (rich in nutrients) and gaseous ( $\text{CO}_2$ ) effluents into the microalgae growth system.

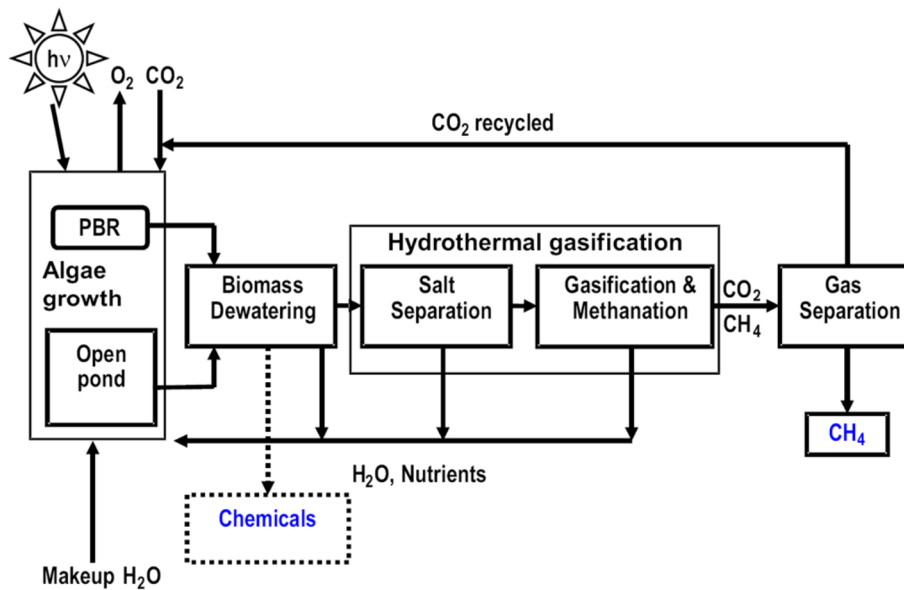


**Figure 1.15.** Simplified scheme of the SunChem process for the production of methane and chemicals using microalgae. (taken from [4]).

## 1.10 Continuous CSCWG of microalgae

While many studies investigated CSCWG of microalgae in unstirred batch reactor, according to our knowledge, only three research papers reported their work using a continuous-flow reactor [4,20,102–104]. Elliott et al. [94] were the first to report continuous catalytic hydrothermal gasification (350 °C, 20 MPa) of different microalgae species (e.g. *Spirulina*, *Nannochloropsis salina*). More recently, in our group at PSI, Brandenberger [17,92] performed continuous CSCWG of microalgae (*Phaeod. tric.*) (420 °C, 32 MPa) over a Ru/C catalyst. Elsayed et al. [105,106] conducted continuous SCWG of microalgae (*Scenedesmus obliquus*) (600 °C, 28 MPa) with a homogeneous catalyst ( $\text{K}_2\text{CO}_3$ ) at a feed rate of  $0.29 \text{ kg h}^{-1}$ . A high  $\text{GE}_c$  ( $> 90\%$ ) and a  $\text{H}_2$ -rich gas (46 vol %) was obtained over a period of 50 h. However, their process differs from those of Elliott and Brandenberger since its purpose is the  $\text{H}_2$  production with the use of a homogeneous catalyst at high temperatures.

As Elliott's work aims at developing a similar continuous gasification process that the one, which is currently under development in our group, a more detailed study of Elliott and Brandenberger's works is required. In Table 1.4, the process parameters used by Elliott and Brandenberger are com-

pared. Although both of them aim at producing methane from microalgae, many process parameters differ considerably. Elliott operates in the subcritical region where gasification of microalgae is carried out over a commercial 7.8% Ru/C catalyst, whereas Brandenberger works at SCW conditions with a commercial 2% Ru/C catalyst. Many microalgae species having different feed concentrations were gasified by Elliott, while only one specie by Brandenberger. According to that, it seems that Elliott acquired more experience and was able to assess more thoroughly the effect of the process parameters (*e.g.* feedstock, feed rate). In fact, in his research paper, eight different experiments were reported, whereas only one experiment was undertaken by Brandenberger.

**Table 1.4.** Process parameters used in Elliott and Brandenberger's experiments [17,94].

Process parameter	Elliott's work	Brandenberger's work
Feed	<i>Spirulina</i> , wild mix, <i>Chara</i> , defatted diatomaceous algae, <i>Nannochloropsis salina</i> , Nanno LEA	<i>Phaeod. tric.</i>
Feed concentration, wt %	8-25	7
Preheater temperature, °C	334-345	360
Salt separator temperature, °C	N.A.	470
Reactor temperature, °C	315-351	420
Pressure, MPa	20-21	32
Feed rate	1.0-1.5 L h <sup>-1</sup>	0.8 kg h <sup>-1</sup>
WHSV, g <sub>Org</sub> g <sub>cat</sub> <sup>-1</sup> h <sup>-1</sup>	~ 0.2-0.6	0.4
Time on stream, h	3.5-11.2	4.5
Catalyst	7.8% Ru/C	2% Ru/C
Amount of catalyst, g	500	118

Apart from the process parameters, their respective experimental setup should be compared and discussed. As shown in Figure 1.16 and 1.17, both setups are equipped with a fixed-bed plug flow reactor for the gasification and methanation of microalgae. However, the pumps, the preheater, and the separation units located upstream of the catalytic reactor are distinct.

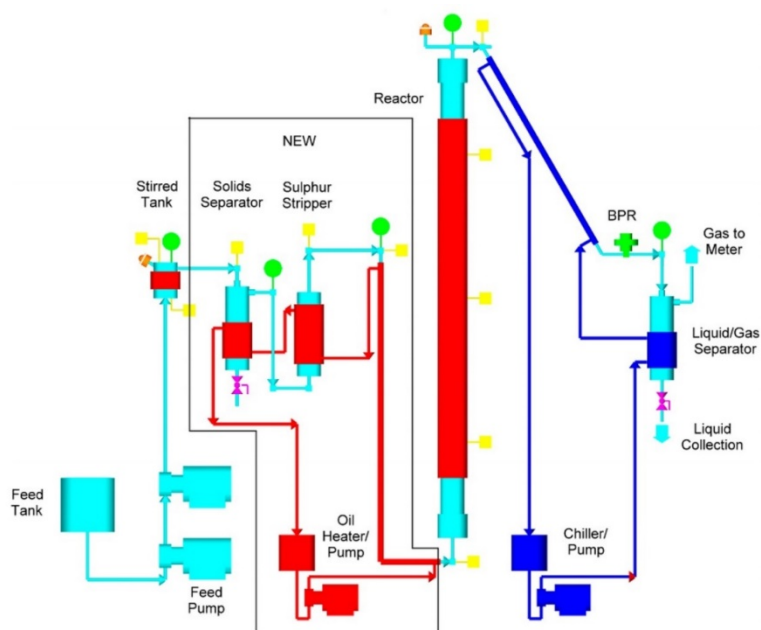


**Figure 1.16.** Simplified flow-scheme of Elliott's setup (adapted from [94]). BPR: back-pressure regulator.

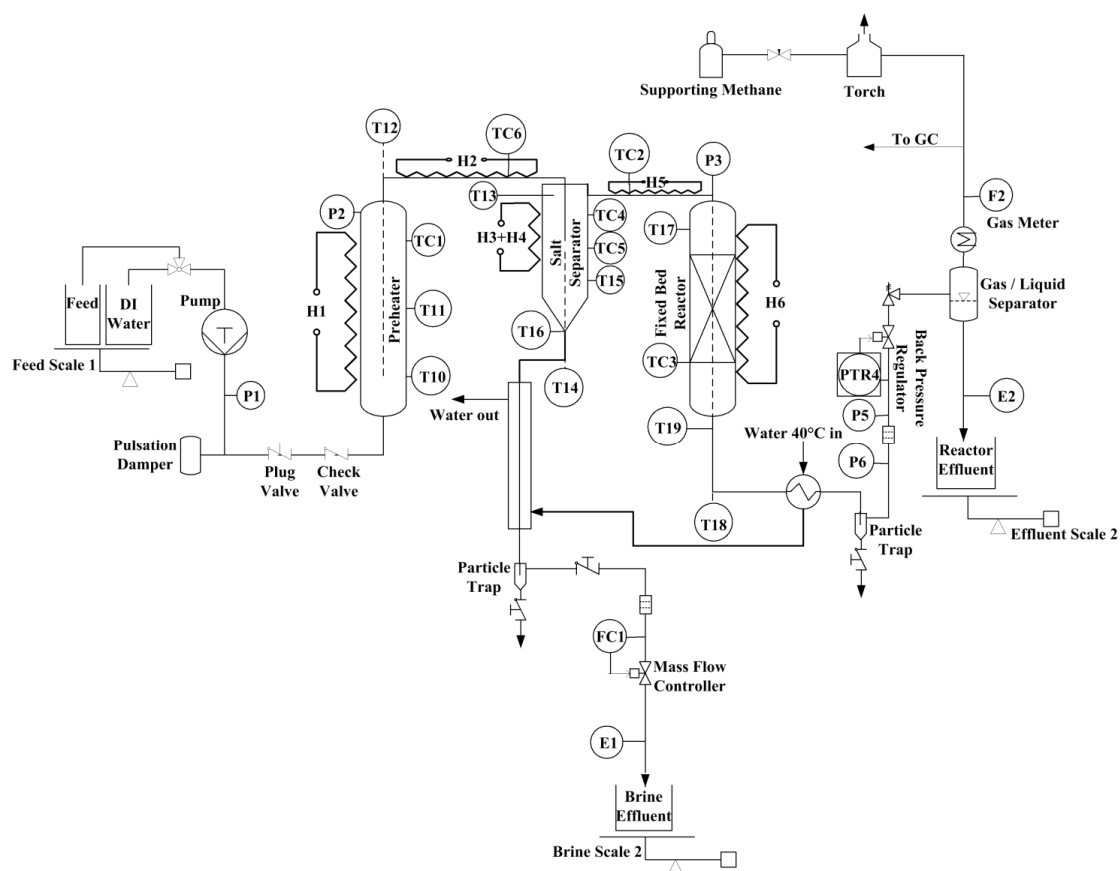


**Figure 1.17.** Simplified flow-scheme of Brandenberger's setup (KONTI-2). Note that the latter is described in detail in section 2.4.3.



In Table 1.5, the process units of both experimental setups are described. The pumping system designed by Elliott is a modified syringe pump while the one of KONTI-2 is a simple HPLC pump. Hence, a syringe pump is more appropriated for feeding with microalgae. The preheater in Elliott's setup, which aims at liquefying microalgae, consists of a vessel equipped with a Carberry-type rotating basket functioning as a CSTR. Then, the liquefied feed enters a mineral separator unit where the salts are removed from the process. Elliott described the design of the separator as a simple dip leg vessel wherein the solids (e.g. phosphate, calcium) fell to the bottom of the vessel while the liquids passes overhead through a filter to the reactor. The solid is removed batchwise from the bottom without any interruption of the process. A major difference with Brandenberger's setup should be pointed out. In fact, the salt separator of KONTI-2, which includes a simple vessel, uses the unique properties of SCW for removing the salts. Hence, instead of harvesting the salts batchwise, this configuration allows to collect them continuously. An additional unit located between the mineral separator and the reactor has been implemented by Elliott. The latter aims at removing sulfur with an adsorbent (Raney Ni) in order to protect the catalyst bed. At that point, no sulfur removal unit was added in KONTI-2, meaning that the damage caused by reduced sulfur species could not be avoided. Although both reactors are rather similar, the one used by Elliott has a higher volume allowing to add a higher catalyst charge.

**Table 1.5.** Description of the process units of Elliott and Brandenberger's setups.

Process unit	Elliott's setup	Brandenberger's setup
Pump	Syringe pump (modified Isco 500D pump)	HPLC pump (Varian, PrepStar, Solvent Delivery Module SD-1)
Preheater	Vessel equipped with a Carberry-type rotating basket (1 L, 316 SS)	Vessel (length 1.70 m, 12 mm ID, 18 mm OD, SS 1.4435)
Mineral separator	Dip tube vessel	Dip tube vessel (length 694 mm, 12 mm ID, 50 mm OD, titanium grade 5)
Sulfur removal	Sulfur stripper filled with Raney Ni	N.A.
Reactor	Vessel (length 1.83 m, 25.4 mm ID, 304 SS)	Vessel (length 1.40 m, 12 mm ID, 18 mm OD, SS 1.4435)

The most relevant observations from Elliott's paper are summarized below:

- A gas composition containing a CH<sub>4</sub>-rich gas (49-63 vol %) was obtained demonstrating the high catalytic activity of Ru/C for favoring the methanation.

- A high level of total organic carbon conversion (96.6-100.0%) of the reactor effluent was achieved during all the experiments showing the high activity of the catalyst for converting microalgae.
- A  $GE_c$  varying from 40% to 106% was reported. The low  $GE_c$  was attributed to the carbon deposition in the mineral separator that was feedstock-dependent.
- The separated mineral byproducts were composed mainly with carbon (35 wt %), nitrogen (4 wt %), and ash (41-46 wt %) when feeding with the concentrated feed (22 wt %). Note that the elements contained in the feedstock were clearly the source of the precipitated minerals. The latter was rich in elements such as Na, K, P, S, Mg, Ca, and Fe. The results revealed that the minerals could be harvested and reused as nutrients for the microalgae growth.
- When processing the low concentrated feed (8 wt %), the longest run was achieved (11.2 h) without any incident. Moreover, the separated mineral byproducts contained a lower amount carbon (9 wt %) and nitrogen (1 wt %) but a higher amount of ash (84 wt %).
- Analysis of the reactor effluent showed a high concentration of  $NH_4^+$ , dissolved  $CO_2$ , K, and Na. Ion chromatography analysis revealed that  $Cl^-$ ,  $NO_3^-$  passed through the reactor, while  $PO_4^{3-}$  and  $SO_4^{2-}$  rather precipitated in the mineral separator. It was proposed that the less soluble alkaline earth (Mg and Ca), which were found at a low level in the reactor effluent, precipitated as sulfates and phosphates.
- At the end of each experiment, signs of deactivation of the catalyst were observed (*e.g.* decrease of  $CH_4$  concentration and increase of  $H_2$  and  $C_2H_6$  concentrations). Sulfur poisoning was the most likely reason since sulfur was detected in the reactor effluent.
- Analysis of the spent Raney Ni and the catalyst showed the low effectiveness of Raney Ni for the sulfur removal since a sulfur concentration gradient (increasing from the reactor inlet) along the catalyst bed was detected. Moreover, some traces of Ni were found in the reactor effluent suggesting its solubilization from the adsorbent bed.

- Characterization of the spent Ru/C catalyst revealed a lower Ru content in comparison to the fresh catalyst. The dilution of Ru caused by carbon deposits or other elemental deposits was believed to be the reason since no Ru was detected in the reactor effluent.

The most relevant observations from Brandenberger's paper are summarized below:

- A gas composition containing a low CH<sub>4</sub> concentration (13 vol %) in comparison to the high H<sub>2</sub> concentration (26 vol %) was recorded. The poor catalytic activity for the methanation can be attributed to a fast deactivation of the catalyst. In fact, the gas composition was far from the calculated thermodynamic chemical equilibrium.
- The GE<sub>C</sub> was only 31% and the total organic carbon of the reactor effluent was several thousand ppm indicating a low catalytic activity for converting microalgae to gaseous products.
- No salt separation occurred since the electrical conductivity of the reactor effluent was three times higher than the one of the brine effluent. Hence, the salt separator did not work properly when fed with microalgae.
- Characterization of the spent Ru/C catalyst showed a strong decrease of the BET specific surface area and the Ru dispersion. It was concluded that sulfur poisoning, coking, and mineral deposits were responsible for the deactivation of the catalyst.

By comparing both studies, Elliott obtained the most promising results since a gas composition similar to the thermodynamic chemical equilibrium was achieved. The use of a higher amount of catalyst containing a higher Ru loading and the effective removal of minerals may be the reasons for such a better achievement in comparison to Brandenberger. However, as mentioned by Elliott, many efforts are still needed, especially in the improvement of the separation techniques, before taking this novel technology to a scale for industrial demonstration.

## 1.11 Problem statement

As discussed in the previous sections, continuous CSCWG of microalgae for methane production is a promising technology in comparison to conventional conversion technologies. In the past, many efforts were undertaken for demonstrating the successful conversion of algal biomass to biofuels in batch reactor. For instance, these batch studies were of importance for a better understanding of

the effect of the heteroatoms (*e.g.* sulfur) contained in microalgae on the deactivation of the catalyst. However, the transition from a batch process towards a continuous process is not straightforward and many technical challenges have still to be overcome. The current status on the development of a continuous process revealed that a better understanding and improvement of the process units (*e.g.* catalytic reactor, salt separator) are still required prior to demonstrating its technical feasibility. For this purpose, the following points are of interest:

- Although Ru/C catalyst showed good catalytic performance during continuous CSCWG of microalgae, a better comprehension of the role of the carbon support is needed. In fact, its stability and its influence over coking during CSCWG remain still unclear.
- A systematic study of the effect of the synthesis factors (*e.g.* Ru dispersion, salt precursor, surface functional groups) on the catalytic performance under SCW conditions. Up to now, few studies dedicated to the improvement of the catalyst design for CSCWG.
- There is still a necessity to find out the most suitable catalyst support for CSCWG among the reported stable supports (carbon, *rutile*-TiO<sub>2</sub>, *monoclinic*-ZrO<sub>2</sub>, and  $\alpha$ -Al<sub>2</sub>O<sub>3</sub>). Unlike previous works, this evaluation should be carried out in continuous reactor setup over mid-term periods (a few days) by working at a high WHSV. In fact, it is important to operate below 100% conversion for a proper comparison.
- An optimization of the current salt separator for continuous CSCWG of microalgae is a crucial step. An effective salt removal, especially inorganic sulfur, is determinant for avoiding catalyst poisoning. Furthermore, the economics of the process can be improved by an effective nutrient recovery.
- Concerning the removal of reduced sulfur (*e.g.* H<sub>2</sub>S), which cannot be mineralized in the salt separator, new options should be investigated. A continuous regeneration of sulfur poisoned Ru/C catalyst by oxidative treatment would not be sufficient for ensuring long-term continuous operations. As mentioned by Brandenberger [17], the addition of a new sulfur unit located upstream of the catalytic reactor is mandatory. As the performance of Raney Ni was not satisfactory, ZnO was proposed by Brandenberger as a potential candidate.

## 1.12 Scope of the thesis

The aim of this doctoral dissertation is to demonstrate the technical feasibility of continuous CSCWG of microalgae for the sustainable production of methane. In order to reach this objective, the work focuses first on the assessment and optimization of the catalytic reactor and the separation techniques (salt separator and sulfur removal). Then, a new process demonstration unit (PDU), so called KONTI-C is built based on the new acquired knowledge. The latter aims at gasifying microalgae continuously with a pumping capacity of  $1\text{--}2\text{ kg h}^{-1}$ . The general approach of the doctoral dissertation is described as follows:

### 1) Assessment and optimization of the catalytic performance of Ru/C catalysts (chapter 3):

As a first step, the stability of a selected activated carbon is tested under SCW conditions in order to determine its potential to be used as a catalyst support. Then, its catalytic performance is assessed during SCWG of isopropanol (IPA) in a new fixed-bed plug flow reactor (PFR). This first gasification experiment aims at evaluating the influence of the carbon support on the coke formation. The catalytic performance of Ru/C catalysts, which are prepared with the selected support, is studied during CSCWG of IPA. Some relevant synthesis factors (*e.g.* Ru dispersion, Ru loading, salt precursor, solvent used during the catalyst preparation, surface functional groups) are systematically investigated. The performance of a Ru/C is compared with other Ru catalysts supported on metal oxides and with our commercial standard catalyst (2% Ru/C<sub>BASF</sub>).

### 2) Improvement of the salt separator with model salt solutions (chapter 4):

The performance of the salt separator of our existing PDU (KONTI-2) is evaluated and optimized with model salt solutions containing inorganic sulfur ( $\text{SO}_4^{2-}$ ). The primary objective is to remove efficiently sulfur from the reactor effluent for preventing any damage to the catalyst located downstream.

### 3) Continuous sulfur removal under SCW conditions (chapter 5):

The stability and the sulfur adsorption performance of a commercial ZnO adsorbent are studied under SCW conditions in a fixed-bed PFR. The purpose is to show its potential for the removal of reduced sulfur in a continuous test rig.

### 4) Continuous liquefaction and CSCWG of microalgae (chapter 6):

The new acquired knowledge in the previous chapters are implemented in the development of a new PDU (KONTI-C). Prior to processing microalgae, several experiments are performed with model salt solutions for evaluating the performance of the new salt separator. Some continuous liquefaction experiments with microalgae are carried out. The aim is to assess the stability of the process regarding plugging. The sulfur adsorption performance and the catalytic activity of the commercial ZnO adsorbent are investigated during continuous liquefaction of microalgae. Then, continuous CSCWG of microalgae is performed over a selected Ru/C catalyst. The catalytic performance and the performance of the salt separator are evaluated.

#### 5) Gasification campaign in Wädenswil (CH) (chapter 7):

As a final step, a gasification campaign of 100 h is carried out on the microalgae production site of ZHAW in Wädenswil (CH). The goal of the campaign is to demonstrate the technical feasibility and to evaluate the future challenge for a further scale up ( $100 \text{ kg h}^{-1}$ ) of this novel technology.

### 1.13 Structure of dissertation

This doctoral dissertation is divided in 8 chapters, as described below:

#### *Chapter 1 – Introduction*

A presentation of the context, the scope of the work.

#### *Chapter 2 – Experimental Part*

A description of the catalyst preparation, the materials, the characterization/analytical methods, and the experimental setups used in this doctoral thesis.

#### *Chapter 3 – Assessment and Improvement of the Catalytic Performance of Ru/C Catalysts*

An evaluation and optimization of the catalytic performance of Ru/C catalysts with IPA as an organic model compound.

#### *Chapter 4 – Optimization of the Salt Separator*

An assessment and optimization of the salt separator with model salt solutions.

#### *Chapter 5 – Continuous Sulfur Removal in Supercritical Water Conditions*

A study of the stability and an evaluation of the sulfur adsorption performance of a commercial ZnO adsorbent under SCW conditions.

*Chapter 6 – Continuous Liquefaction and Catalytic Supercritical Water Gasification of Microalgae*

An investigation of continuous liquefaction and CSCWG of microalgae within KONTI-C.

*Chapter 7 – Gasification Campaign in Wädenswil (CH)*

A presentation of the gasification campaign performed on the microalgae production site of ZHAW in Wädenswil (CH).

*Chapter 8 – Conclusion*

A conclusion of the achieved results with recommendations for further work.

## Chapter 2 Experimental Part

In this section, the experimental methods such as the catalyst preparation methods, the materials, the characterization/analytic methods, and the experimental setups are presented.

### 2.1 Catalysts preparation

#### 2.1.1 Pre-treatment of the catalyst support

Prior to active phase impregnation, all the catalyst supports were crushed and/or sieved to a size fraction of  $0.3 < d_p < 0.8$  mm in order to respect the ratio  $d_{\text{reactor}}/d_p > 10$ . The carbon support used for the study of the surface functional groups (see section 3.5.5) was pre-treated with  $\text{HNO}_3$  (30 vol %) for 5 h at 90 °C under reflux. After filtration, the carbon support pre-treated with  $\text{HNO}_3$  ( $\text{C}_{\text{HNO}_3}$ ) was washed with deionized (DI) water until neutralization of the filtrate was reached and finally dried at 90 °C overnight in an oven.  $\text{C}_{\text{HNO}_3}$  was then treated under He at 450 °C for 4 h in order to remove the less thermally stable surface functional groups. The thermally pre-treated  $\text{C}_{\text{HNO}_3}$  support is denoted as  $\text{C}_{\text{HT}}$ .

#### 2.1.2 Impregnation with the Ru salt precursor

The supported Ru catalysts were prepared by wet impregnation with a Ru salt precursor ( $\text{RuCl}_3 \cdot x\text{H}_2\text{O}$  or  $\text{Ru}(\text{NO})(\text{NO}_3)_3$ ) in a water or in an acetone solution. The impregnation was performed in a rotary evaporator during a few hours under constant stirring. After the solvent evaporation, the catalysts were washed with pure water during filtration and dried in an oven at 90 °C overnight. Finally, the catalysts were either reduced or calcined. The Ru catalysts supported on carbon were reduced under flowing  $\text{H}_2/\text{Ar}$  (10:90, 20 mL min<sup>-1</sup>) at 450 °C during 4 h whereas the Ru catalysts supported on metal oxides were calcined with air (20 mL min<sup>-1</sup>) at 450 °C during 4 h.

The Ru loading was calculated with ICP-OES by measuring the dissolved Ru concentration in the solution before and after the impregnation by taking into account the Ru losses during the catalyst washing. The information of the prepared supported Ru catalyst are listed in Table 2.1.



**Table 2.1.** Description of the prepared supported Ru catalysts used in this work.

Catalyst	Support	Ru loading wt %	Ru salt precursor	Solvent	Time of impregnation h
0.5% Ru/C <sub>w</sub>	carbon <sup>a</sup>	0.6	RuCl <sub>3</sub> ·xH <sub>2</sub> O	water	24
2% Ru/C <sub>w</sub>	carbon <sup>a</sup>	2.3	RuCl <sub>3</sub> ·xH <sub>2</sub> O	water	24
2% Ru/C <sub>a</sub>	carbon <sup>a</sup>	2.1	RuCl <sub>3</sub> ·xH <sub>2</sub> O	acetone	24
4% Ru/C	carbon <sup>a</sup>	4.2	RuCl <sub>3</sub> ·xH <sub>2</sub> O	acetone	24
4% Ru/C <sub>HNO3</sub>	carbon <sup>a</sup>	4	RuCl <sub>3</sub> ·xH <sub>2</sub> O	acetone	24
4% Ru/C <sub>HT</sub>	carbon <sup>a</sup>	4.2	RuCl <sub>3</sub> ·xH <sub>2</sub> O	acetone	24
2% Ru/C <sub>nitro</sub>	carbon <sup>a</sup>	2	Ru(NO)(NO <sub>3</sub> ) <sub>3</sub>	water	6
2% Ru/TiO <sub>2</sub>	<i>rutile</i> -TiO <sub>2</sub>	1.8	Ru(NO)(NO <sub>3</sub> ) <sub>3</sub>	water	6
1% Ru/ZrO <sub>2</sub>	<i>monoclinic</i> -ZrO <sub>2</sub>	1.2	Ru(NO)(NO <sub>3</sub> ) <sub>3</sub>	water	6
1% Ru/Al <sub>2</sub> O <sub>3</sub>	$\alpha$ -Al <sub>2</sub> O <sub>3</sub>	1.2	Ru(NO)(NO <sub>3</sub> ) <sub>3</sub>	water	6

[a] Org10\_CO

## 2.2 Materials

In Table 2.2, the list of all the materials used in this work is depicted.

**Table 2.2.** Materials used in this work.

Susbtance	Purity	Supplier
DI water	$\leq 5 \mu\text{S cm}^{-1}$	In-house DI water grid
Acetone	$\geq 99.8\%$	Merck KGaA
Ethanol	$> 99.8\%$	Thommen-Furler AG
IPA	$> 99.8\%$	VWR BDH Prolabo
Sodium sulfate	$> 99.0\%$	Merck KGaA
Potassium sulfate	$> 99.0\%$	Sigma-Aldrich
Nitric acid	$> 99.9\%$	Merck KGaA
Hydrochloric acid	$> 99.9\%$	VWR BDH Prolabo
Sodium bicarbonate	$> 99.9\%$	Merck KGaA
Sodium carbonate	$> 99.9\%$	Merck KGaA
Sodium hydroxide	$> 99.9\%$	Merck KGaA
Sodium sulfide nonahydrate	$\geq 98.0\%$	Sigma-Aldrich
Sodium hydrosulfide hydrate	N.A.	Sigma-Aldrich
Sulfanilamide	$\geq 99.0\%$	Sigma-Aldrich
Boric acid	$\geq 99.5\%$	Merck KGaA
Katalco™ 32-5 (ZnO + cement)	N.A.	Johnson Matthey Catalysts
Activated carbon (Org10_CO)	N.A.	Desotec
Titania dioxide (rutile)	N.A.	Norpro Saint Gobain SA
Zirconia (monoclinic)	N.A.	Norpro Saint Gobain SA
Alumina (alpha)	$\geq 99.0\%$	Alfa Aesar
Activated carbon (C <sub>BASF</sub> )	N.A.	BASF
2% Ru/C <sub>BASF</sub>	N.A.	BASF
5% Ru/C <sub>BASF</sub>	N.A.	BASF
Ruthenium (III) chloride hydrate	$> 99.9\%$	Alfa Aesar
Ruthenium (III) nitrosyl nitrate	$> 99.9\%$	Sigma-Aldrich
<i>Phaeod. tric.</i>	N.A.	Subitec
<i>Chlorella vul.</i>	N.A.	ZHAW Wädenswil

## 2.3 Characterization and analytic methods

### 2.3.1 N<sub>2</sub>-physisorption

N<sub>2</sub>-physisorption measurements were performed with an Autosorb-1 (*Quantachrome Instruments*) for determining the porosity and the BET specific surface area (BET SSA). The total pore volume was measured at  $p/p_0 = 0.99$  and the mesopore volume with the t-plot method. In this method, a multi-layer formation is modeled to calculate a layer thickness ( $t$ ) as a function of the increasing relative pressure ( $p/p_0$ ). Prior to N<sub>2</sub>-physisorption degassing under He at 300 °C for 6 h was carried out for all the samples.

### 2.3.2 CO pulse chemisorption

CO pulse chemisorption were carried out in a fully automated instrument (*TPD/R/O 1100, Thermo Scientific*) connected to a thermal conductivity detector (TCD). Briefly, the injected gas reacts with the active sites (in this case Ru) until all the active sites have reacted. During the first few pulses, the injected gas may be fully consumed (no pulses are recorded at the outlet). As the sample reaches saturation, peaks representing concentrations of unreacted CO molecules appear. After the saturation, the area of the CO pulse remains unchanged. The quantity of adsorbed CO molecules is calculated by the difference between the total amount of gas injected and the sum of the injected gas that did not react with the active sites [107]. The sample was reduced under H<sub>2</sub>/Ar (10:90, 20 mL min<sup>-1</sup>) at 450 °C for 4 h in order to clean the ruthenium surface from any deposited carbon species. Then it was flushed with pure He at 450 °C for 1.5 h for removing H<sub>2</sub> from the catalyst and finally cooled down to room temperature (RT). The CO pulses were carried out with CO/He (20:80) at RT. The Ru dispersion, defined as the ratio of the surface Ru atoms of a catalyst to the total Ru atoms, was calculated by assuming 1 as the stoichiometric factor for CO:Ru. The following formula was used for determining the Ru dispersion:

$$D_{CO} = \frac{N_{ads} \cdot F_s \cdot M_{met} \cdot 10}{w_{met}} \quad (2.1)$$

Where  $N_{ads}$  is the amount of gas adsorbed during pulse chemisorption (mmol g<sup>-1</sup>);  $F_s$  corresponds to the stoichiometric factor (moles of metal/moles of gas);  $M_{met}$  is the metal atomic weight (g mol<sup>-1</sup>) and  $w_{met}$  is the metal loading on a mass basis (wt %). The average metal particle sizes were calculated as:

$$d_{p,CO} = \frac{d_{at} \cdot 5.01}{D_{CO}} \quad \text{for } D_{CO} < 0.2 \quad (2.2)$$

$$d_{p,CO} = \frac{d_{at} \cdot 3.32}{D_{CO}^{1.23}} \quad \text{for } 0.2 < D_{CO} < 0.92 \quad (2.3)$$

where  $d_{at}$  is the atomic diameter of Ru ( $d_{at} = 2.6 \text{ \AA}$ ) [108].

### 2.3.3 H<sub>2</sub> temperature-programmed reduction (H<sub>2</sub>-TPR)

H<sub>2</sub>-TPR measurements were performed in a fully automated instrument (*TPD/R/O 1100, Thermo Scientific*) connected to a TCD. The sample was heated ( $10 \text{ }^\circ\text{C min}^{-1}$ ) from RT to  $350 \text{ }^\circ\text{C}$  under flowing Ar ( $20 \text{ mL min}^{-1}$ ) and then kept at this temperature for 30 min to remove impurities and water. Then the sample was cooled to RT and passivated with O<sub>2</sub>/He (5:95,  $20 \text{ mL min}^{-1}$ ) at  $100 \text{ }^\circ\text{C}$  for 30 min. Finally, the sample was cooled to RT again and the gas was switched to H<sub>2</sub>/Ar (10:90,  $20 \text{ mL min}^{-1}$ ). TPR was performed from RT to  $450 \text{ }^\circ\text{C}$  with a temperature ramp of  $10 \text{ }^\circ\text{C min}^{-1}$ .

### 2.3.4 Temperature-programmed oxidation (TPO)

TPO measurements were conducted with a thermogravimetric analyzer (*TGA; NETZSCH STA 449 C*) coupled to a FTIR detector for detecting CO<sub>2</sub> and SO<sub>2</sub>. The sample was loaded and heated from RT to  $110 \text{ }^\circ\text{C}$  under Ar atmosphere for 30 min and then heated up to  $900 \text{ }^\circ\text{C}$  at  $10 \text{ }^\circ\text{C min}^{-1}$  under flowing O<sub>2</sub>/Ar (10:90,  $10 \text{ mL min}^{-1}$ ).

### 2.3.5 CO<sub>2</sub>/CO-temperature-programmed desorption (CO<sub>2</sub>/CO-TPD)

The CO<sub>2</sub>/CO-TPD measurements were carried out with a thermogravimetric analyzer (*TGA; NETZSCH STA 449 C*) coupled to a FTIR detector for detecting CO<sub>2</sub> and CO. Prior to the analysis, the sample was dried in a vacuum oven at  $60 \text{ }^\circ\text{C}$  overnight for removing water. Then, the sample was measured from RT to  $900 \text{ }^\circ\text{C}$  with a ramp of  $10 \text{ }^\circ\text{C min}^{-1}$  under flowing Ar ( $20 \text{ mL min}^{-1}$ ).

### 2.3.6 Carbon, nitrogen, and sulfur elemental analysis (CNS)

CNS analysis were measured with an elemental analyzer (*Vario EL cube, Elementar*). Liquid and solid samples were burned at  $1150 \text{ }^\circ\text{C}$  in a quartz glass reactor with the help of a WO<sub>3</sub> catalyst. In a second quartz glass reactor, NO<sub>x</sub> species were reduced to N<sub>2</sub> by a Cu catalyst. Carbon is detected as CO<sub>2</sub> and

nitrogen as  $\text{N}_2$  with a TCD while sulfur as  $\text{SO}_2$  with an IR detector. Sulfanilamide was used as standard sample to determine the daily factor (theoretical content/actual content).

### 2.3.7 Total carbon (TC), total organic carbon (TOC), and total inorganic carbon (TIC) analysis

The TC, TOC, and TIC of liquid samples were analyzed with a TOC analyzer (*Vario TOC cube, Elementar*). The samples were injected into a quartz glass reactor where they were burnt at 850 °C under a constant oxygen carrier gas flow (200 mL min<sup>-1</sup>).  $\text{CO}_2$  was detected with a non-dispersive infrared (NDIR) detector for determining the TC. For measuring the TIC, the samples were injected into a 10 wt % solution of  $\text{H}_3\text{PO}_4$  and the evolving  $\text{CO}_2$  was stripped with the oxygen carrier gas flow and transported to the detector. Then, the TOC was obtained by subtracting the TIC from the TC.

### 2.3.8 TC, TOC, and TIC analysis measured on-line

The TC, TOC, and TIC of the liquid samples harvested during the experiments performed in KONTI-C, were measured on-line by a TOC analyzer (*GE Analytical Instruments, Sievers InnovOx On-Line TOC Analyzer*)

### 2.3.9 Elemental composition of biomass samples

The elemental composition of the biomass samples (*e.g.* microalgae) were measured at ETHZ (Laboratory for Organic Chemistry). The following elements were analyzed: C, H, N, O, S, P, and Cl. The following analyzers were used: carbon, nitrogen, hydrogen (*LECO CHN-900*), oxygen (*LECO RO-478*), sulfur (*LECO CHNS-932*), phosphorus (photometer), chloride (ion chromatography).

### 2.3.10 $\text{NH}_4^+$ -determination

The  $\text{NH}_4^+$  concentration of the aqueous samples was measured with a Nanocolor® 300D photometer (*Macherey-Nagel*) in combination with Nanocolor® Ammonium 50 tube test kits.

### 2.3.11 Ash content of biomass samples

The ash content (wt %) was determined at 900 °C for 1 h in a furnace. For accurate measurements, the ash content was measured three times for each sample.

### 2.3.12 Dry matter of the feed (microalgae)

The dry matter of the feed for the experiments performed in chapter 6, was determined by heating a sample (ca. 10 g) in a vacuum oven at 60 °C and 0.03 MPa. The latter operation was repeated several times for the same feed in order to ensure a low standard deviation. The values obtained were then compared with those provided by the manufacturer (*Subitec*). During the gasification campaign (see chapter 7), the dry matter values were measured and provided by the ZHAW.

### 2.3.13 pH-determination

The pH measurements were performed either by color-fixed indicator sticks (*Macherey-Nagel Ref 92115*) or by a pH-meter (*SCHOTT®, Handylab pH/LF12*).

### 2.3.14 Sulfide test paper

Sulfide test paper (*Macherey-Nagel Ref 90761*), having a detection limit of 5 ppm, was used to detect  $S^{2-}$  in the liquid samples.

### 2.3.15 Off-line gas chromatograph (GC)

The gas was analyzed with a GC (*HP 6890*, columns: HP-Plot Q 30m x 0.53mm x 40 $\mu$ m and HP-Plot Molecular Sieve 5A, 30m x 0.53mm x 40 $\mu$ m) with helium as the carrier gas using a TCD to detect  $CO_2$ ,  $CH_4$ ,  $CO$ , and  $H_2$  and a Flame Ionization Detector (FID) for higher hydrocarbons ( $C_2H_6$  and  $C_3H_8$ ).

### 2.3.16 On-line micro gas chromatograph (microGC)

The gas composition during the experiments performed in KONTI-C, was measured on-line by a microGC (*INFICON, 3000 Micro GC*) with Ar as the carrier gas using a TCD. The gas samples were withdrawn automatically every 5 min and passed through two parallel columns (A, B).  $CH_4$ ,  $CO$ , and  $H_2$  were analyzed in column A, whereas  $CO_2$  and  $C_{2+}$  in column B.

### 2.3.17 Gas chromatography-mass spectroscopy (GC-MS)

GC-MS (*Agilent 5975C*) was used to analyze the liquid effluent obtained during SCWG with IPA (Blank experiment) (see chapter 3, section 3.3) and the solid residue obtained during the gasification campaign (see chapter 7, section 7.5). GC-MS measurement of the solid residue (after its extraction with toluene) was carried out by the following procedure: the solid residue (10 g) was added to a toluene

solution (50 mL) and heated under reflux at 120 °C during 12 h. After filtration, the toluene phase of the filtrate (3 mL) was diluted with toluene (6 mL) and analyzed by GC-MS.

### 2.3.18 Boehm titration

The surface functional groups quantification was performed by Boehm titration following the standardization procedure proposed by Goertzen et al. [109,110]. This method relies on the existence of oxygen surface groups having different acidities that can be neutralized by bases having diverse strength.  $\text{NaHCO}_3$ ,  $\text{Na}_2\text{CO}_3$  and  $\text{NaOH}$  were used in this work. As the weakest base,  $\text{NaHCO}_3$  neutralizes only the carboxylic groups,  $\text{Na}_2\text{CO}_3$  neutralizes the lactonic/carboxylic groups and  $\text{NaOH}$  neutralizes the phenolic/lactonic/carboxylic groups. The number of mole of each surface functional group was estimated by difference. A 1.5 g of the carbon support was added to 50 mL of one of the three bases: 0.05 M  $\text{NaHCO}_3$ ; 0.05 M  $\text{Na}_2\text{CO}_3$  and 0.05 M  $\text{NaOH}$ . Then, the samples were sealed and shaken for 24 h at RT by a linear shaker. After filtration, an aliquot of 10 mL from the sample solution was taken and neutralized by an excess of 0.05 M  $\text{HCl}$  and then back-titrated with 0.05 M  $\text{NaOH}$ . The endpoint was determined by phenolphthalein (colour indicator). Note that the titration was performed under inert atmosphere (Ar) to avoid dissolution of  $\text{CO}_2$  from the atmosphere. The determination of the moles of carbon surface functionalities ( $n_{\text{CSF}}$ ) on the carbon surface was calculated by the following equation according to the back-titration method:

$$n_{\text{CSF}} = \frac{n_{\text{HCl}}}{n_{\text{B}}} [B]V_{\text{B}} - ([\text{HCl}]V_{\text{HCl}} - [\text{NaOH}]V_{\text{NaOH}}) \frac{V_{\text{B}}}{V_{\text{A}}} \quad (2.4)$$

Where  $[B]$  and  $V_{\text{B}}$  correspond to the concentration and the volume, respectively, of the reaction base mixed with the carbon support.  $[\text{HCl}]$  and  $V_{\text{HCl}}$  are the concentration and the volume of the acid added to the aliquot ( $V_{\text{A}}$ ) previously taken from  $V_{\text{B}}$ .  $[\text{NaOH}]$  and  $V_{\text{NaOH}}$  are related to the concentration and to the volume used in the back-titration that neutralizes the remaining moles of acid. Finally,  $n_{\text{HCl}}/n_{\text{B}}$  is the molar ratio of acid to base allowing to distinguish between monoprotic vs. diprotic reaction bases.

### 2.3.19 Inductively coupled plasma optical emission spectroscopy (ICP-OES)

Elemental screening and quantitative elemental analysis of aqueous samples were performed by an ICP-OES device (*SPECTRO Ciros Vision SOP*). The samples were nebulized and sprayed into the Ar plasma flame (6000-8000 °C). The analyzer was calibrated with different dilutions of multi-element

standard solutions (purchased either from *Kraft* or from *Merck*). To gain concentrations within the calibrated range, the samples were diluted by a factor of 100 with DI water. Each sample was measured several times until a low standard deviation was obtained and the last three measurements were used.

### 2.3.20 Wavelength dispersive X-ray fluorescence (WDXRF)

Elemental analysis of the catalyst and the solid residue were carried out with wavelength dispersive X-ray fluorescence (WDXRF) analysis over a WDXRF spectrometer (*S4 Explorer, Bruker AXS*). Prior to the analysis, the samples were dried in a vacuum oven at 60 °C and 0.02 MPa during 2h. Then, the samples were mixed with boric acid in a mortar and pressed in order to obtain a solid pellet.

### 2.3.21 X-ray photoelectron spectroscopy (XPS)

XPS analysis were carried out with a *VG Escalab 220i XL* apparatus by using a monochromatic Al K  $\alpha$  ( $h\nu = 1486.6$  eV) radiation as the X-ray source.

### 2.3.22 X-ray diffraction analysis (XRD)

XRD measurements were performed on a D8 ADVANCE (*Bruker*) diffractometer using Cu K1 radiation ( $= 1.5406$  Å). The Ru NPs size was calculated by the Scherrer equation as follows:

$$d_{p,XRD} = \frac{K \cdot \lambda}{\beta \cdot \cos\theta} \quad (2.5)$$

Where K is a dimensionless shape factor having a typical value of 0.9,  $\lambda$  is the X-ray wavelength (Å),  $\beta$  is the line broadening at half the maximum intensity (FWHM) (radians), and  $\theta$  is the Bragg angle (°).

### 2.3.23 Scanning electron microscopy and energy dispersive X-ray spectroscopy (SEM-EDX)

SEM-EDX was used for the elemental mapping. The measurements were performed at PSI. The samples were measured at an accelerating voltage of 17 kV.

### 2.3.24 Scanning transmission electron microscopy (STEM)

The Ru NPs were characterized by STEM at ETHZ (ScopeM). The measurements were performed with a spherical aberration corrected dedicated STEM microscope (*Hitachi HD-2700 CS*) with a cold emission source, operated at an acceleration voltage of 200 kV and equipped with a high angle annular dark field (HAADF) detector. For each sample, different areas were carefully selected in order to have a reliable representation of the average Ru NPs size. The average Ru NPs size ( $d_{p,STEM}$ ) and the dispersion ( $D_{STEM}$ ) were calculated as:

$$d_{p,STEM} = \frac{\sum_i n_i \cdot d_i^3}{\sum_i n_i \cdot d_i^2} \quad (2.6)$$

$$D_{STEM} = \sqrt[1.23]{\frac{d_{at} \cdot 3.32}{d_{p,STEM}}} \quad \text{for } 0.2 < D_{STEM} < 0.92 \quad (2.7)$$

$$D_{STEM} = \frac{d_{at} \cdot 5.01}{d_{p,STEM}} \quad \text{for } D_{STEM} < 0.2 \quad (2.8)$$

Where  $n_i$  is the number of particles with diameter  $d_i$  [108].

## 2.4 Experimental setups

### 2.4.1 Stability test of the carbon support in mini-batch reactor

The physical structure stability of the carbon support in SCW was assessed with an unstirred stainless steel mini-batch reactor (*HIP, 316 SS*) having a volume of 5.11 mL (length 101.7 mm, 7.8 mm i.d.) (see Figure 2.1). The temperature inside the reactor was recorded with a shielded Type K thermocouple and recorded on-line using a *Labview®*-based control program. The setup was already available at the start of the thesis and was used during several theses [17,36,58,65,95].



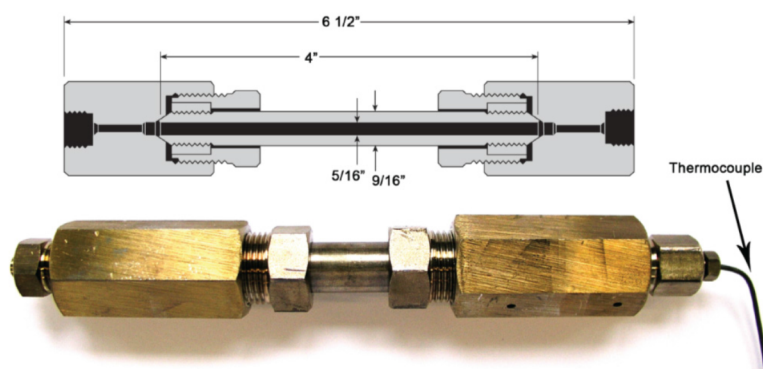


**Figure 2.1.** Picture of the mini-batch reactor (taken from [17]).

#### 2.4.2 Gasification and sulfur adsorption experiments in the continuous reactor setup (PFR)

CSCWG of IPA and sulfur adsorption experiments were carried out in a new fixed-bed PFR (see Figure 2.2 and 2.3). The reactor setup was developed and built during this doctoral thesis. The water (F-1) and the feed (F-2) were pumped by a HPLC pump (*Waters 515*) at a constant mass flow rate ( $\dot{m} = 3 \text{ g min}^{-1}$ ). For accurate mass flow rate measurements, the feed tank was put on an analytical balance (*Mettler Toledo PG6002-S*). A manual valve (V-1) allowed switching from the water to the feed effluent. A preheater was needed for assuring isothermal conditions along the catalyst bed. The PFR consisted of a stainless steel tube (*SITEC*, length 400 mm, 8 mm i.d.). The catalyst loading was around 0.07-0.78 g depending on the experiment. The first 350 mm of the reactor were filled with a carbon material ( $0.8 < d_p < 2 \text{ mm}$ ). A movable thermocouple (T1) was installed within the reactor for recording temperature during CSCWG. The PFR was placed in an electric oven for heating. The reactor effluent passed through a metal filter ( $2 \mu\text{m}$ ) to retain any solid particles. The fluid was cooled down by passing through a water tank. A safety valve (V-2) was installed for preventing any overpressure in the system. The pressure in the system was maintained by a backpressure regulator (V-3). Finally, the gas and the liquid were separated at ambient conditions in a phase separator made of glass. The temperature (T1) and the pressure (P1) were recorded continuously with a computer using a *Labview*<sup>®</sup>-based control program.

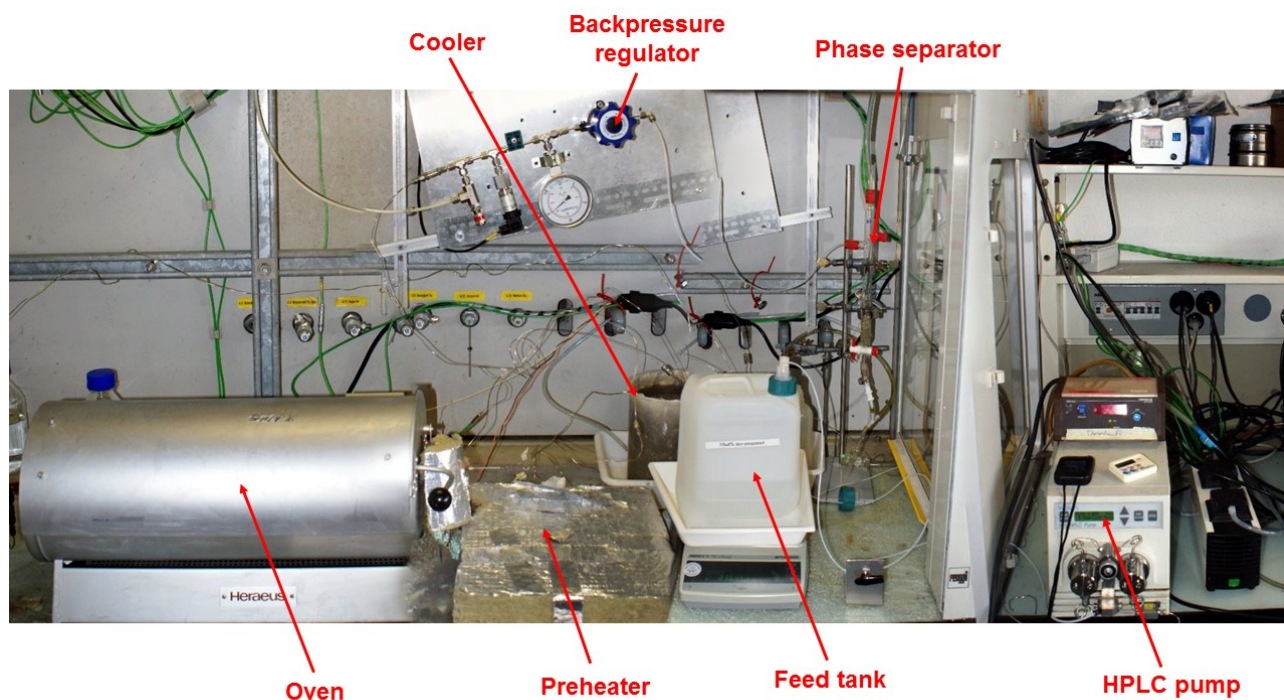


**Figure 2.2.** Photograph of the fixed-bed PFR setup.

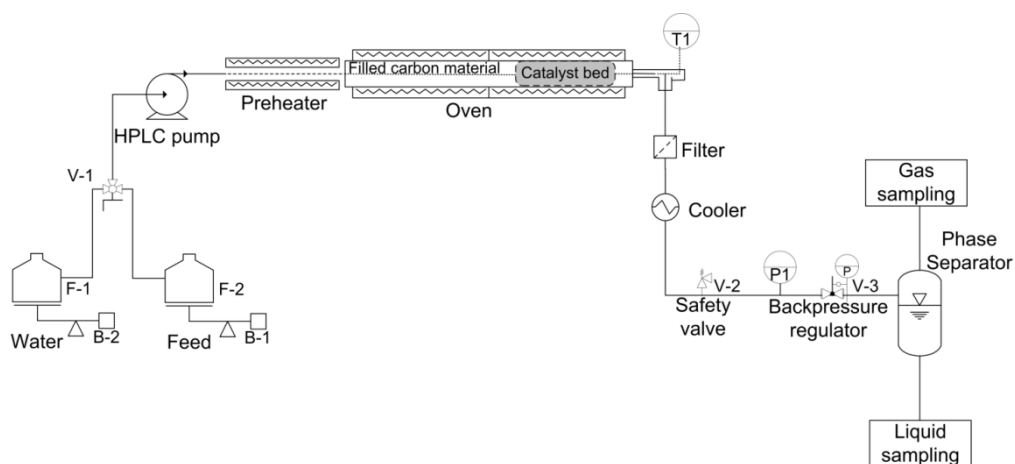


**Figure 2.3.** Schematic of the fixed-bed PFR setup. Legend: B-balance, F-feed, V-valve, T-thermocouple, P-pressure sensor.

#### 2.4.3 Salt separation experiments in the continuous reactor setup (KONTI-2)

For the salt separation experiments described in chapter 4, KONTI-2 was used to assess and to optimize the salt separator (see Figure 2.4 and 2.5). KONTI-2 was already available at the start of the thesis and was built during Waldner's thesis [65]. Briefly, the laboratory plant can be divided in 7 sections: Feeding section; pre-heating; salt separation; fixed-bed reactor; cooling; pressure control; and gas-liquid phase separation. The feed section consists of two tanks, one for the aqueous salt

mixture and the other for DI water used to flush the plant. Both tanks were placed on a balance in order to monitor the mass flow rate. A high-pressure pump (*Varian PrepStar SD-1 Solvent Delivery System*) was used for feeding with DI water and the model solutions. The pre-heater section was heated electrically (stainless steel 1.4435, length 1700 mm, 12 mm i.d., and 18 mm o.d.) but for the salt separation experiments, the preheater temperature was settled to 25 °C. At the entrance of the salt separator, the feed was super-heated (450-500 °C). A detailed description of the salt separator can be found in chapter 4. The brine effluent was withdrawn at the bottom of the salt separator. The mass flow rate of the brine effluent was controlled with a mass flow controller (*Bronkhorst Liquiflow*). The largest fraction of the feed left the salt separator by a transfer tube at the top of the salt separator and entered the fixed-bed reactor (stainless steel 1.4435, length 1400 mm, 12 mm i.d. and 18 mm o.d.) but the latter has been removed and replaced by a pipe for the salt separation experiments. After the salt separator, the stream was cooled by a coiled tube (stainless steel 1.4435, length 3800 mm, 2.4 mm i.d., 6.35 mm o.d., manufactured in our workshop). Depressurization to atmospheric pressure was performed in two steps using a high pressure control valve (*Kämmer*) and a pressure controller (*Flowserver*), followed by a spring-loaded relief valve (*Sitec, Switzerland*). The gas and the liquid phase were separated in a phase separator made of borosilicate glass. The electrical conductivities of the brine and phase separator effluent were both recorded on-line by a conductivity meter (*WTW Cond 340i*) using a flow-through cell fabricated in-house. All the effluents were collected and weighed by an analytical balance for recording the mass flow rate on-line. The laboratory plant was operated and controlled by a remote control using a *Labview*®-based control program.

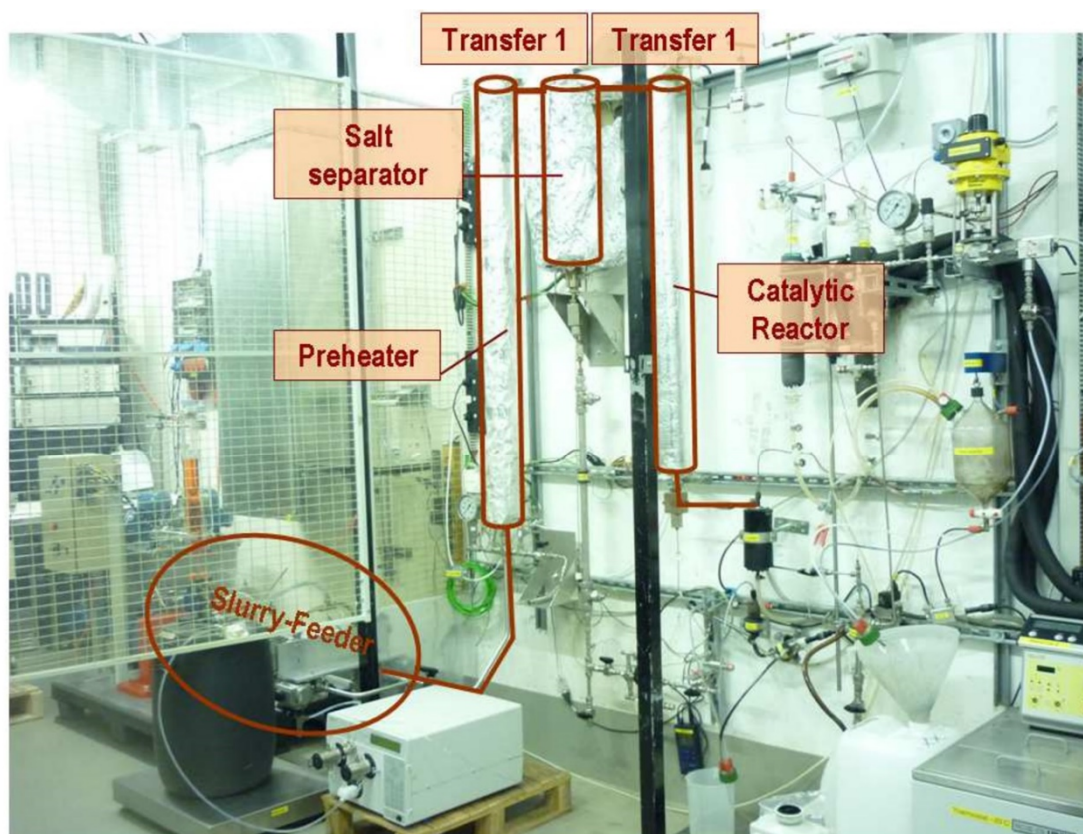


**Figure 2.4.** Photograph of KONTI-2 (taken from [36]).

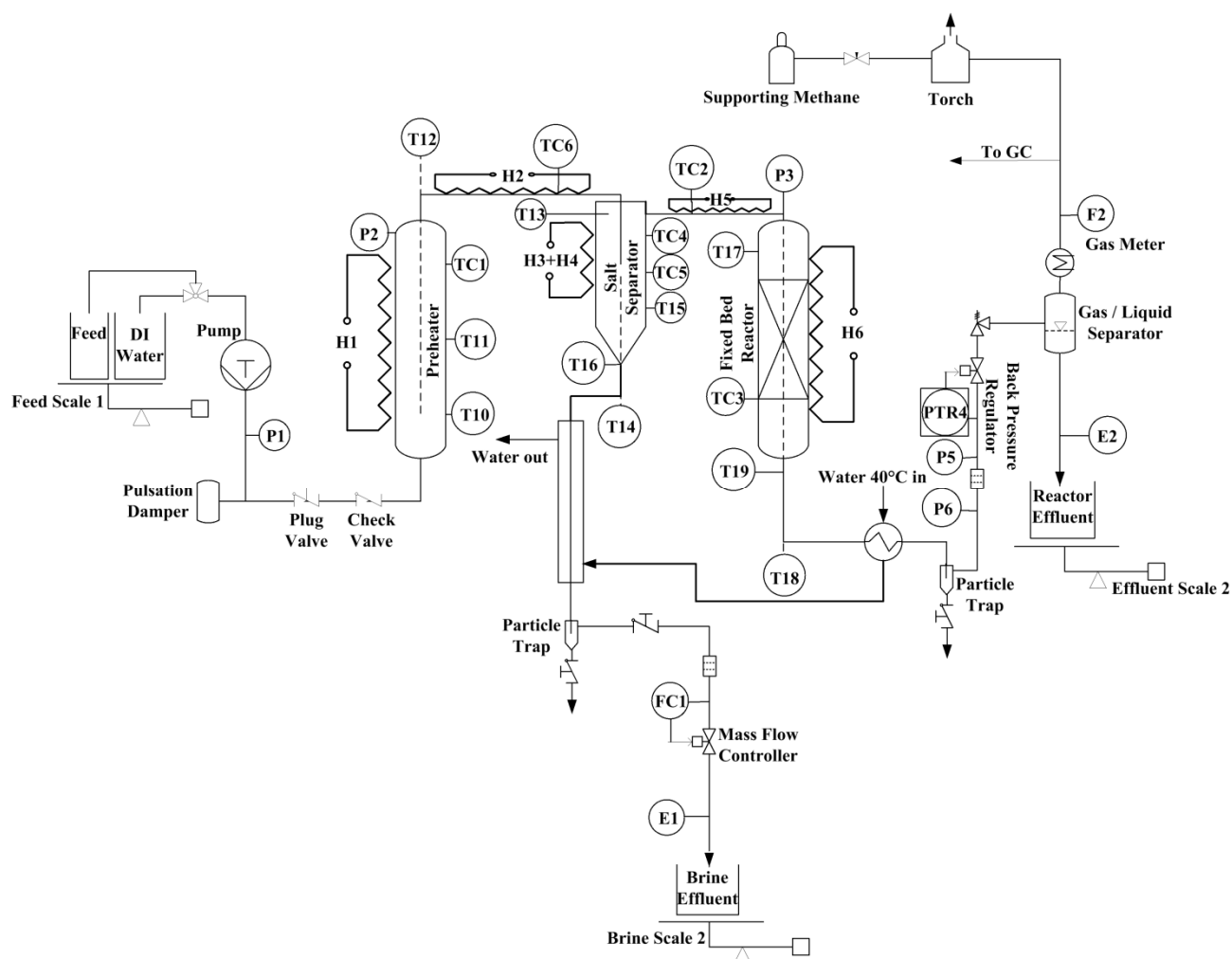


**Figure 2.5.** Simplified flow sheet of KONTI-2. Legend: E-electrical conductivity meter, F-gas flow meter, FC-flow controller, H-electrical heater, P-pressure sensor, PTR-back pressure regulator, T-thermocouple, TC-temperature controller. (taken from [40]).

#### 2.4.4 Liquefaction and gasification experiments in the continuous reactor setup (KONTI-C)

Continuous liquefaction and CSCWG experiments of microalgae were carried out in the new PDU (KONTI-C) having a feeding capacity of 1-2 kg h<sup>-1</sup>. KONTI-C was developed and built during this thesis based on the results obtained in this work. Note that the description of the plant was adapted from Breinl's master thesis [111]. A picture of KONTI-C and a simplified flow-scheme are shown in Figure 2.6 and 2.7 (a more detailed flow diagram can be found in Appendix A.2). The plant has been installed in a shipping container (6.64 x 2.44 x 2.90 m) and can be divided in six main sections: feeding section; salt separator; salt removal; reactor; pressure control; and phase separator. The feeding section consists of a tank for the DI water and the feed, two pumps, and an analytical balance. One pump is a HPLC pump (*Varian PrepStar SD-1 Solvent Delivery System*) for feeding with DI water and the model solutions, the other one is a piston pump (Slurry feeder) for feeding with microalgae. The

Slurry feeder is constituted by two cylinders (*SS316LM*) with a working volume of 2.6 L each and can be operated at a frequency of 0-50 Hz. It has been designed and constructed in-house; a detailed description can be found elsewhere [36]. The balances (*KERN & SOHN GmbH, IFS 60K0.5DL*) were used to record the feed rate when feeding with the HPLC pump. Unfortunately, when feeding with the Slurry feeder, the feed rate could not be measured since no mass flow meter was available. After being pressurized, the feed passed through a filter (pore size: 250  $\mu\text{m}$  or 25  $\mu\text{m}$ ) and then entered the salt separator (*SITEC*, steel grade: 1.4980, inner length: 300 mm, inner diameter: 40 mm) via a standpipe (steel grade: 1.4404) which is extended by 100 mm into the salt separator. The standpipe had an inner diameter of 3 mm and an orifice of 1 mm at the end. The salt separator was heated electrically by two heating blocks for generating a certain temperature profile inside. The temperature was measured at the inner wall at different heights by thermocouples and along the axis by a temperature lance (in-house constructed), which was dipped at the top of the salt separator. The salt separator had two outlets, one for delivering the liquefied feed to the reactor and one for extracting the concentrated brine.

After being cooled to 20-30  $^{\circ}\text{C}$  (*Huber, Unichiller MPC006*), the brine effluent passed through a particle trap, a filter (pore size: 25  $\mu\text{m}$ ), and a mass flow controller (*Bronkhorst®, Liquiflow*) which was located before the pressure relief valve. The flow controller (*Liquiflow*) could be varied between 0-100% and was calibrated for a mass flow rate of 0-3.2  $\text{g min}^{-1}$ . After pressure relief, the brine effluent entered a liquid/gas phase separator. The carbon content (TC, TOC, and TIC) in the liquid was measured on-line by a TOC analyzer (*GE Analytical Instruments, Sievers InnovOx On-Line TOC Analyzer*). The liquid phase was harvested in a tank which was placed on an analytical balance (*KERN & SOHN GmbH, IFS 30K0.2DL*) for monitoring the mass flow rate.

The liquefied feed leaving at the top of the salt separator was transferred via a heated tube (steel grade: 1.4404, approx. length: 1600 mm, inner diameter: 0.25 in) to the catalytic reactor (*SITEC*, steel grade: 1.4435, inner length: 1515 mm, inner diameter: 36 mm). The reactor was heated electrically by two heating blocks. The temperature was measured along the axis by a temperature lance (in-house constructed) which was dipped at the top of the reactor. The lower part of the reactor was filled with the ZnO adsorbent (*Katalco 32-5*) and the upper part filled with the catalyst (5% Ru/C<sub>BASF</sub>).

After being cooled (20-30 °C) the reactor effluent passed through a particle trap, a filter (pore size: 25 µm). A second filter was installed in parallel for switching from one to the other by a three-way-valve in case of plugging. The reactor effluent was depressurized to atmospheric pressure by a manually adjustable spring-loaded relief valve (*SITEC*). A control valve (*Kämmer*) combined with a pressure controller (*Flowserve*) located upstream of the relief valve regulated the pressure in a range of 5 MPa.

Then, the depressurized fluid entered a liquid/gas phase separator (borosilicate glass, 2000 mL) which was fixed at a digital spring balance (*HiTec Zang GmbH, GraviDos®*) used for recording the mass flow rate. The gas phase leaving the phase separator at the top was cooled to 8 °C (*JCT Analysetechnik GmbH, JCP-S*) and the gas flow rate was recorded by a gas meter (*Wohlgroth*). The gas composition was measured on-line by a microGC (*INFICON, 3000 Micro GC*). The carbon content (TC, TOC, and TIC) in the liquid phase was measured by the same TOC analyzer as the one used for the brine effluent. Finally, the liquid phase was harvested in a tank which was positioned on an analytical balance (*KERN & SOHN GmbH, IFS 60K0.5DL*) for monitoring the mass flow rate.

Additionally to the above mentioned equipment, the pressure was measured at several locations and the electrical conductivities of the brine and reactor effluent were measured on-line by conductivity meters (*SCHOTT®, Handylab pH/LF12*). Furthermore, up to nine liquid samples of each brine and reactor effluent used for off-line analysis could be withdrawn automatically by an auto-sampler (in-house constructed, included *VICI valve C25-6180 EMH*). All temperatures, pressures, balance signals, electrical conductivities of the effluents, carbon content in brine and reactor effluent, gas composition and the gas flow rate were monitored on-line. The laboratory plant was operated by a remote control using a *Labview®*-based control program, which has been developed by Erich De Boni (see Appendix A.1).







## 2.4.5 General procedure for the experiments

### 2.4.5.1 *Stability test of the carbon support*

A 0.5 g of the carbon support was added with 1.5 g of DI water into the reactor. Then, it was tightly closed with the help of a torque wrench and placed into a fluidized sand bath (Techne SBL-2D) to be heated up to 420 °C under 35 MPa for 5 h. After cooling, the carbon support was recovered by filtration and dried at 110 °C overnight. A second run of 5 h following the same procedure was undertaken in order to reach 10 h of SCW treatment.

### 2.4.5.2 *CSCWG of IPA (PFR)*

The PFR was heated with DI water. Once the steady state was reached, the feed was switched to IPA. Prior to each sampling, the feed rate was determined by using a stopwatch. The time interval was 10 min. The liquid samples were taken in 40 mL flasks and analyzed off-line with a TOC analyzer. The gas was collected in a sample bag (3L SKC) at different time intervals and analyzed by GC (off-line). At the end of the experiment, the reactor was cooled down with DI water overnight.

### 2.4.5.3 *Salt separation experiments (KONTI-2)*

Prior to feeding the salt solution, the plant was heated with DI water until the steady state was reached. Then, the feed was switched to the salt solution. The performance of the salt separation was determined by measuring the conductivity in the brine and the reactor effluents. Liquid samples were also taken for sulfur elemental analysis. At the end of the experiment, KONTI-2 was cooled down with DI water and rinsed at RT overnight.

### 2.4.5.4 *Sulfur adsorption experiments (PFR)*

The reactor was heated with DI water to the reaction temperature. When the steady state was reached, water was switched to the model solution. For accurate measurements of the feed rate, the latter was determined by using a stopwatch and by reading the weight loss on the analytical balance. The time interval was 5 min. The liquid samples were taken in 40 mL flasks and 1 mL of KOH (0.5 N) was added in each sample for avoiding any sulfur loss caused by H<sub>2</sub>S formation. In fact, the pH should be above 9 to form only sulfur ions (S<sup>2-</sup>). Sulfide test papers were used during the experiment for measuring qualitatively S<sup>2-</sup>. The quantitative analysis of sulfur were performed with ICP-OES. At the end of the experiment, the reactor was cooled down with DI water overnight.

#### 2.4.5.5 Continuous liquefaction and CSCWG of microalgae (KONTI-C)

The plant was already started the previous day of the experiment in order to check all the instruments (e.g. pressure sensors, thermocouples, conductivity on-line). Then, KONTI-C was pressurized and heated up with DI water at the desired setpoint for ensuring the absence of any leaks in the process. In parallel, some standard samples were measured by the microGC and the TOC analyzer. When all the instruments were ready, KONTI-C was cooled down with DI and rinsed at RT overnight for obtaining very low values of the conductivity.

The day of the experiment, KONTI-C was pressurized and heated up with DI water to the desired setpoint. Approximately, 2-3 h were needed for the temperature to reach the steady state. Prior to switching the feed to microalgae, one cylinder of the Slurry feeder was filled and emptied several times with microalgae in order to get a representative value of the feed concentration (*i.e.* dilution effect caused by some dead zones located inside the cylinder coming from previous experiments). For a proper feed analysis, prior to switching to microalgae, a feed sample was directly harvested from the cylinder. During the heating phase, the microGC and the TOC analyzer were switched on and some standard samples were measured. Once the steady state was reached, the plant was fed with the cylinder containing microalgae. The liquid samples in the brine and the reactor effluents were harvested at a regular time interval depending on the experiment for off-line analysis (e.g. CNS, ICP-OES). At the end of the experiment, KONTI-C was cooled down with DI water and rinsed at RT overnight.

## 2.5 Terms and definitions

### 2.5.1 Weight hourly space velocity (WHSV)

For comparing the catalytic performance based on the Ru amount, the weight hourly space velocity normalized to one gram of Ru ( $WHSV_{gRu}$ ) was used for CSCWG with IPA:

$$WHSV_{gRu} = \frac{\dot{m}_{org}}{m_{cat} \cdot w_{Ru}} \quad (2.9)$$

For CSCWG of microalgae, WHSV normalized to one gram of catalyst was used:

$$WHSV = \frac{\dot{m}_{org}}{m_{cat}} \quad (2.10)$$

### 2.5.2 Total organic carbon conversion ( $X_C$ )

The observed activity is defined as the total organic carbon conversion ( $X_C$ ) from the feed to the reactor effluent:

$$X_C (\%) = 1 - \frac{\dot{m}_{TOC,Reactor}}{\dot{m}_{TOC,Feed}} \cdot 100\% \quad (2.11)$$

Where  $\dot{m}_{TOC,Reactor}$  and  $\dot{m}_{TOC,Feed}$  are the mass flow rates of carbon (TOC) in the reactor effluent and the feed, respectively.

### 2.5.3 Carbon gasification efficiency ( $GE_C$ )

$GE_C$  is the relation between the total amount of carbon in the gas phase and the total amount of carbon in the feed, defined as:

$$GE_C (\%) = \frac{\dot{m}_{C,Gas}}{\dot{m}_{C,Feed}} \cdot 100\% \quad (2.12)$$

Where  $\dot{m}_{C,Feed}$  is the mass flow rate of carbon in the feed and  $\dot{m}_{C,Gas}$  corresponds to the mass flow rate of carbon in the gas.

For the experiments performed in KONTI-C (see chapter 7),  $GE_C$  was calculated by subtracting the loss of the brine effluent:

$$GE_C (\%) = \frac{\dot{m}_{C,Gas}}{\dot{m}_{C,Feed} - \dot{m}_{C,Brine}} \cdot 100\% \quad (2.13)$$

Where  $\dot{m}_{C,Brine}$  is the mass flow rate of carbon in the brine effluent.

#### 2.5.3.1 Error estimation

The propagation of uncertainty for  $GE_C$  is expressed by:

$$\Delta GE_C (\%) = \left( \left| \frac{\Delta \dot{m}_{C,Gas}}{\dot{m}_{C,Feed} - \dot{m}_{C,Brine}} \right| + \left| -\frac{\dot{m}_{C,Gas}}{(\dot{m}_{C,Feed} - \dot{m}_{C,Brine})^2} \cdot (\Delta \dot{m}_{C,Feed} + \Delta \dot{m}_{C,Brine}) \right| \right) \cdot 100\% \quad (2.14)$$

### 2.5.4 Rate of coke deposition ( $R_{\text{Coke dep.}}$ )

$R_{\text{Coke dep.}}$  is the rate of coke deposition estimated during CSCWG of IPA. It is calculated from a carbon mass balance as follows:

$$R_{\text{Coke dep.}} (\text{mmol C min}^{-1}) = \dot{n}_{\text{C,Feed}} - \dot{n}_{\text{C,Reactor}} - \dot{n}_{\text{C,Gas}} \quad (2.15)$$

$\dot{n}_{\text{C,Feed}}$ ,  $\dot{n}_{\text{C,Reactor}}$ , and  $\dot{n}_{\text{C,Gas}}$  correspond to the molar flow rate of carbon in the feed, the reactor effluent, and the gas.

### 2.5.5 Turnover frequency (TOF)

TOF was calculated as the total mole of IPA consumed per active Ru site (measured by STEM) per second:

$$\text{TOF} (\text{s}^{-1}) = \frac{-\Delta \dot{n}_{\text{IPA}}}{\text{mol}_{\text{Ru}} \cdot D_{\text{STEM}}} \quad (2.16)$$

### 2.5.6 Carbon, nitrogen, and sulfur recoveries

The carbon, nitrogen, and sulfur recoveries calculated during the experiments performed in KONTI-C are expressed as:

$$\text{Recovery}_{\text{C}} (\%) = \frac{\dot{m}_{\text{C,Brine}} + \dot{m}_{\text{C,Reactor}} + \dot{m}_{\text{C,Gas}}}{\dot{m}_{\text{C,Feed}}} \cdot 100\% \quad (2.17)$$

$$\text{Recovery}_{\text{N}} (\%) = \frac{\dot{m}_{\text{N,Brine}} + \dot{m}_{\text{N,Reactor}}}{\dot{m}_{\text{N,Feed}}} \cdot 100\% \quad (2.18)$$

$$\text{Recovery}_{\text{S}} (\%) = \frac{\dot{m}_{\text{S,Brine}} + \dot{m}_{\text{S,Reactor}}}{\dot{m}_{\text{S,Feed}}} \cdot 100\% \quad (2.19)$$

And the sulfur accumulation in the process and the sulfur recovery of the brine effluent are:

$$\dot{m}_{\text{S,Accumulation}} (\text{mg min}^{-1}) = \dot{m}_{\text{S,Feed}} - \dot{m}_{\text{S,Brine}} - \dot{m}_{\text{S,Reactor}} \quad (2.20)$$

$$\text{Recovery}_{\text{S,Brine}} (\%) = \frac{\dot{m}_{\text{S,Brine}}}{\dot{m}_{\text{S,Feed}}} \cdot 100\% \quad (2.21)$$

### 2.5.6.1 Error estimation

The propagation of uncertainty for carbon, nitrogen, and sulfur recoveries are expressed:

$$\Delta Recovery, i (\%) = \left( \frac{\sum_y |\Delta \dot{m}_{i,y}|}{\dot{m}_{i,Feed}} + \left| -\frac{\sum_y \dot{m}_{i,y}}{(\dot{m}_{i,Feed})^2} \cdot \Delta \dot{m}_{i,Feed} \right| \right) \cdot 100\% \quad (2.22)$$

Where  $\Delta \dot{m}_{i,y}$  corresponds to the mass flow rate of  $i$  in the effluent  $y$ , *i.e.* brine, reactor, or gas.

And the propagation of uncertainty for the sulfur accumulation is:

$$\Delta \dot{m}_{S,Accumulation} (mg \min^{-1}) = \sqrt{\Delta \dot{m}_{S,Feed}^2 + \Delta \dot{m}_{S,Brine}^2 + \Delta \dot{m}_{S,Reactor}^2} \quad (2.23)$$

### 2.5.7 Chemical equilibrium gas composition

The thermodynamic chemical equilibrium calculation was performed using the Aspen 2006 Plus® simulation package by using the Peng-Robinson equation of state. The values for the gas composition at the thermodynamic chemical equilibrium (450 °C, 30 MPa and 10 wt % IPA) are: CO<sub>2</sub> = 24.7 vol %; CH<sub>4</sub> = 65.6 vol %; H<sub>2</sub> = 8.7 vol %; CO = 0.7 vol %.

## Chapter 3 Assessment and Improvement of the Catalytic Performance of Ru/C Catalysts

This chapter aims at assessing and improving the catalytic performance of Ru/C catalysts during CSCWG of IPA. Firstly, the stability of the physical structure of the carbon support is tested at SCW conditions. Secondly, a blank experiment with an empty reactor and then with the carbon support itself is carried out. Then, the performance of Ru/C catalysts are assessed at a low  $WHSV_{gRu}$  in order to show how the catalyst works under industrial conditions ( $X_c = 100\%$ ) and at a high  $WHSV_{gRu}$  ( $X_c < 100\%$ ) for the assessment of the catalyst stability. The effect of various synthesis factors such as the Ru dispersion, the Ru loading, the solvent used during the catalyst preparation, the salt precursor, and the surface functional groups of carbon are systematically investigated. Finally, the performance of a prepared Ru/C is compared with our commercial Ru/C catalyst and other Ru catalysts supported on metal oxides.

Most of the results presented in this chapter have been summarized and published in:

- *Catalysis Science & Technology* (see Peng G., Steib M., Gramm F., Ludwig C., Vogel F., "Synthesis factors affecting the catalytic performance and stability of Ru/C catalysts for supercritical water gasification", *Catalysis Science & Technology*, 2014, **4**, 3329 – 3339)
- *Catalysis Science & Technology* (see Peng G., Gramm F., Ludwig C., Vogel F., "Effect of carbon surface functional groups on the synthesis of Ru/C catalysts for supercritical water gasification", *Catalysis Science & Technology*, 2015, **5**, 3658 – 3666.

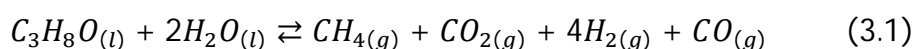
Some of the results presented here were obtained in the frame of an internship (Matthias Steib) performed in our group under my supervision during my doctoral studies. His contribution can be found in section 3.3, 3.4, 3.5.1, and 3.5.2.

### 3.1 CSCWG of IPA

Most of the continuous CSCWG studies performed have been carried out with water soluble model compounds such as glycerol, sorbitol, ethylene glycol, cresol, phenol, and glucose

[60,63,71,90,98,112–125]. Among these water-soluble compounds organic acids and alcohols have a greater relevance due to their presence as intermediate products during SCWG of real biomass and their relatively good stability in SCW [126]. As discussed in section (1.8.4), carboxylic acid compounds are potentially more problematic to gasify than alcohols because they may form coke precursors decreasing the catalyst lifetime. Consequently, for minimizing any fast deactivation of the catalyst caused by coke deposits, IPA as a model compound is used in this work.

The overall stoichiometry for SCWG of IPA is:



At 450 °C and 30 MPa, the gas composition at the thermodynamic chemical equilibrium for 10 wt % IPA is: CO<sub>2</sub> = 24.7 vol %; CH<sub>4</sub> = 65.4 vol %; H<sub>2</sub> = 8.7 vol %; CO = 0.7 vol %<sup>1</sup>.

### 3.2 Stability of the physical structure of the carbon support in SCW

Prior to active phase impregnation, it is necessary to ensure the good stability of the physical structure of the carbon support in order to prevent any activity loss due to a structure collapsing. To this aim its physical structure stability was tested at SCW conditions in a mini-batch reactor at 420 °C and 35 MPa for 5 and 10 h. As shown in Table 3.1, the physical structure of the carbon support after 5 and 10 h in SCW conditions was relatively well preserved.

**Table 3.1.** Physical structure evolution of the carbon support at SCW conditions (420 °C, 35 MPa).

Exp.	Sample	BET SSA m <sup>2</sup> g <sup>-1</sup>	V <sub>mesop.</sub> cm <sup>3</sup> g <sup>-1</sup>	V <sub>microp.</sub> cm <sup>3</sup> g <sup>-1</sup>
	Fresh C	802	0.69	0.14
BT1	After 5 h in SCW	779	0.56	0.18
BT2	After 10 h in SCW	717	0.45	0.17

Some slight modifications of the meso/micropore volume can be observed suggesting that the SCW caused more micropores and less mesopores. The increase of the micropore volume in SCW was likely due to the removal of some impurities trapped in the micropores. We can also appreciate the high specific surface area (> 700 m<sup>2</sup> g<sup>-1</sup>) of this material. In comparison with refractory metal oxides

<sup>1</sup> Calculated by using Aspen 2006 Plus®

like  $\alpha$ -Al<sub>2</sub>O<sub>3</sub>, *rutile*-TiO<sub>2</sub> or ZrO<sub>2</sub>, which were reported [64,68,69,127] to be stable in SCW conditions, their specific surface area is much lower and does not exceed 150 m<sup>2</sup> g<sup>-1</sup>. Thus, the potential for achieving highly dispersed Ru NPs on the carbon support appears to be much higher.

### 3.3 Blank SCWG experiment

The first SCWG experiment aims at assessing the stability of IPA under SCW conditions in the absence of a catalyst as well as at checking the catalytic activity of the reactor wall. A blank experiment with an empty reactor (exp. CS0) was carried out at 450 °C and 30 MPa and a residence time of 59 s (density of water at reaction conditions is 148 g L<sup>-1</sup>). The total organic carbon conversion ( $X_c$ ) was close to zero, and no gas production was measured indicating the inertness of the reactor wall as well as the stability of IPA at these conditions. GC-MS analysis confirmed that IPA was stable since no decomposition products were found. For the next experiment, the reactor was filled only with the support carbon material in order to check its activity during SCWG. According to Figure 3.1,  $X_c$  decreased steadily from 82% to 12% during the first 6 h of gasification. Such a high initial activity of the carbon support was not expected. In Table 3.2, the results of the SCWG after 24 h are summarized.

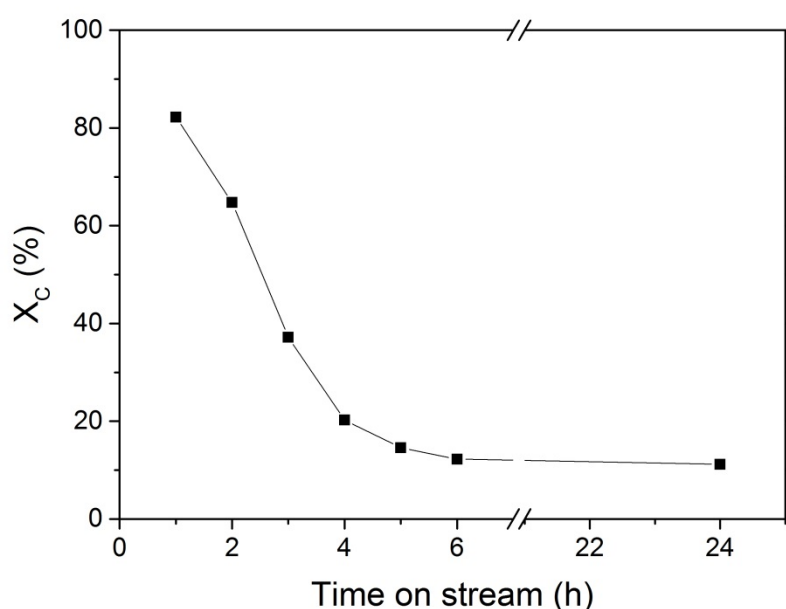


**Figure 3.1.** SCWG of 10 wt % IPA over the carbon support material at 450 °C and 30 MPa during 24 h on-stream with  $\dot{m} = 3$  g min<sup>-1</sup> (exp. CS1).



**Table 3.2.** Results of the SCWG of 10 wt % IPA over the neat carbon support material performed at 450 °C and 30 MPa during 24 h with  $\dot{m} = 3 \text{ g min}^{-1}$ .

Exp.	Sample	Time h	$X_c$ %	$GE_c$ %	$R_{\text{Coke dep.}}$ $\text{mmol C min}^{-1}$	Gas composition, vol %					
						CH <sub>4</sub>	CO <sub>2</sub>	H <sub>2</sub>	CO	C <sub>2</sub> H <sub>6</sub>	C <sub>3</sub> H <sub>x</sub>
CS1	Fresh C	24	11	4	1.2	3.3	0.5	96.1	0.2	< 0.1	5.0

The absence of high concentrations of CO (and CO<sub>2</sub>) indicates that the C-O bond in IPA is efficiently broken. The low methane concentration shows that the methanation reaction is not favored in the absence of the catalyst, and the presence of C<sub>3</sub>H<sub>x</sub> indicates that IPA lost its hydroxyl group by reacting with the carbon surface. Interestingly,  $GE_c$  was much lower than  $X_c$ , meaning that the carbon contained in the feed was only partially converted to the gas phase. Based on the  $GE_c$  and  $X_c$  values after 24 h on-stream, a carbon accumulation of ca.  $1.2 \text{ mmol C min}^{-1}$  has been calculated. Thus a plausible explanation of the observed trend in activity is that the IPA decomposed to H<sub>2</sub>, water, and solid carbon (coke) on the surface of the carbon support, whose pores were progressively filled up by the coke, thereby reducing the activity of the support. Unlike carboxylic acid compounds which tend to polymerize before reaching the active phase leading to deactivation of the catalyst [58], it seems that IPA underwent decomposition on the catalyst support itself. The liquid effluent was analyzed by GC-MS and the result showed that IPA was the main product in the liquid phase. However, the presence of a small amount of benzene was recorded. Chakinala et al. [126] studied the conversion of 1-propanol at SCW conditions (600 °C, 25 MPa) in a batch reactor for 15 min and also observed the formation of a small quantity of benzene, confirming the occurrence of aromatization reactions. In summary, the carbon surface was active enough for decomposing IPA to coke and H<sub>2</sub>, likely due to impurities and/or surface functional groups.

In Table 3.3, it can be seen that the absence of Ru led to a complete loss of the microporosity as well as a considerable loss of the mesoporosity after 24 h.

**Table 3.3.** Physical structure evolution of the carbon support after 24 h of SCWG with 10 wt % IPA (450 °C, 30 MPa).

Sample	BET SSA $\text{m}^2 \text{g}^{-1}$	$V_{\text{mesop.}}$ $\text{cm}^3 \text{g}^{-1}$	$V_{\text{microp.}}$ $\text{cm}^3 \text{g}^{-1}$
Fresh C	802	0.69	0.14
C after SCWG	84	0.21	0.0

These results are relevant because they show that if IPA cannot be entirely converted to gaseous products, it reacts with the carbon surface to form coke resulting in a drastic loss of the porosity. The fact that also the mesopores are affected by coke formation means that the coke is likely to deposit also on the Ru NPs, which would lead to the deactivation of the catalyst.

A TPO analysis was carried out in order to confirm the presence of coke deposits after SCWG with IPA. As shown in Figure 3.2, the carbon support after SCWG of IPA started to oxidize at a lower temperature (400 °C) than the fresh carbon support (500 °C). These results, although not very conclusive, support the presence of less thermally stable carbon species (i.e. coke deposits) on the used carbon support after SCWG of IPA. The carbon support appears to be more thermally resistant after the SCWG treatment since the maximum consumption peak was shifted from 620 °C to 645 °C. The removal of  $-CH_2$  and  $-CH$  groups during the SCWG treatment might be the reason for the enhancement of the thermal resistance of the support [128]. A diminution of the amount of ash was also observed in the TPO. At 900 °C, the weight loss of the fresh carbon support remained constant at 9 mg meaning that 1 mg of ash remained, whereas for the used carbon the remaining ash was only 0.2 mg.

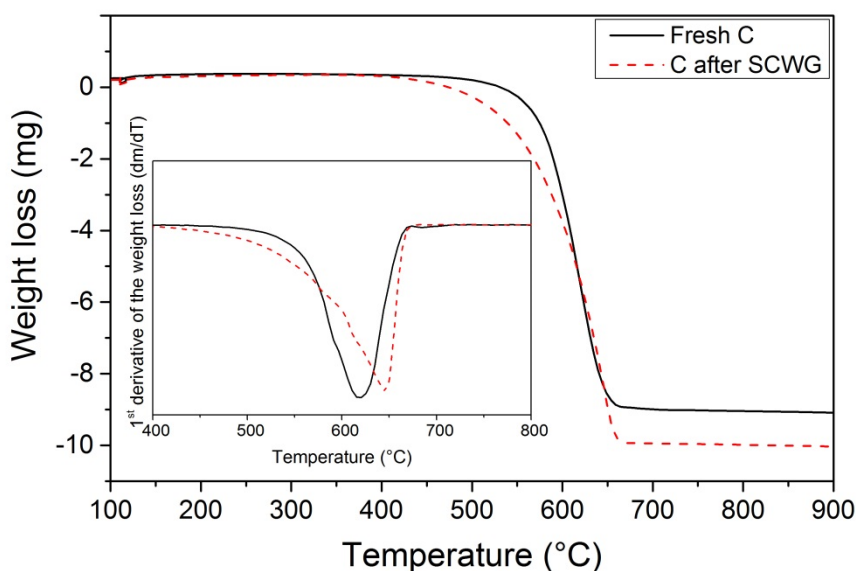


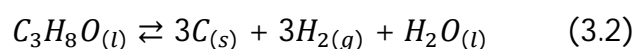
**Figure 3.2.** TPO analysis of the fresh carbon support and of the carbon support after SCWG with 10 wt % IPA (450 °C, 30 MPa). Initial sample mass was 10 mg for both samples.

Finally, as shown in Table 3.4, CHONS elemental analysis of the carbon support confirmed the presence of additional carbon after SCWG. The decrease of oxygen, nitrogen, and sulfur can be likely attributed to the decomposition of some functional groups and the washing out of some dust from the pores. Whereas the slight increase of hydrogen may come from a decomposition of IPA over the carbon surface. The explanation why the total elemental content sums up to 92% for the fresh C comes from the elements in the ash that were not quantified.

**Table 3.4.** CHONS elemental analysis of the fresh carbon support and of the carbon support after SCWG with 10 wt % IPA (450 °C, 30 MPa).

Sample	C wt %	H wt %	O wt %	N wt %	S wt %
Fresh C	85.12 ± 0.05	0.75 ± 0.03	5.00 ± 0.00	0.68 ± 0.04	0.26 ± 0.02
C after SCWG	95.70 ± 0.29	1.12 ± 0.03	1.46 ± 0.01	0.22 ± 0.02	0.11 ± 0.01

To explain these results we propose a decomposition of IPA on the surface of the support to form elemental carbon ("coke"), H<sub>2</sub>, and water according to:



Thus, the average carbon content of the support after SCWG of IPA would increase, as shown in Table 3.4. The measured gas composition, *i.e.* 96 vol % H<sub>2</sub>, further supports this hypothesis (see Table 3.2).

### 3.4 Catalytic performance of Ru/C catalysts

The first experiment aims at assessing the catalytic performance of a Ru/C catalyst under industrial conditions ( $X_C = 100\%$ ) over a few days experiment. In Figure 3.3, a CSCWG experiment of 10 wt % IPA over a 2% Ru/C<sub>a</sub> catalyst is presented. During the first hours on-stream the liquid effluent was collected in order to detect any leaching of Ru. The analysis of the effluent by ICP-OES did not reveal any Ru showing the strong interaction between the carbon support and Ru. At a relatively low weight hourly space velocity (1228 g<sub>org</sub> g<sub>Ru</sub><sup>-1</sup> h<sup>-1</sup>), the observed total carbon conversion was 99% during the first 28 h and began slowly to decrease to 90% after 96 h of CSCWG. However, as illustrated in Table 3.5, even at  $X_C = 90\%$  the gas composition was close to the thermodynamic chemical equilibrium. GE<sub>C</sub> was similar to  $X_C$  proving that all the carbon contained in the feed was fully con-

verted to the gas phase with no noticeable coke deposition within the reactor ( $R_{\text{Coke dep.}} \approx 0$ ). Nevertheless, it is worth noting that  $GE_c$  values are less accurate than  $X_c$  values obtained by TOC analysis. The main reasons are that gas flow rate measurements are not always accurate due to some gas accumulation inside the setup, and fluctuations of the mass flow rate. Therefore the observed activity is calculated solely from  $X_c$  in this work.

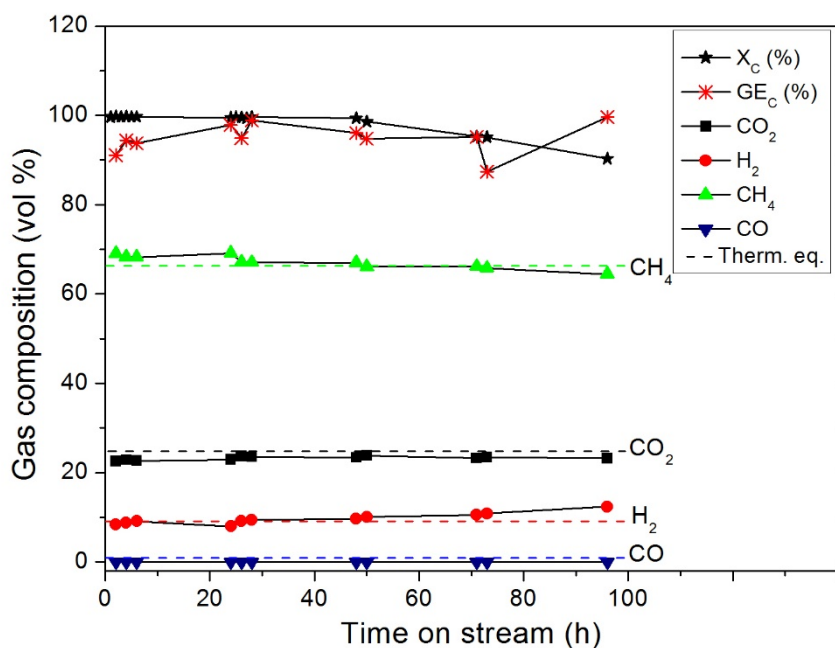


**Figure 3.3.** CSCWG of 10 wt % IPA over the 2% Ru/C<sub>a</sub> catalyst at 450 °C and 30 MPa for 96 h on-stream with  $WHSV_{gRu} = 1228 \text{ g}_{Org} \text{ g}_{Ru}^{-1} \text{ h}^{-1}$ . The dashed lines denote the calculated thermodynamic equilibrium concentrations (exp. CS2).

**Table 3.5.** Results summary after 96 h of CSCWG with 10 wt % IPA over the 2% Ru/C<sub>a</sub> catalyst at 450 °C and 30 MPa with  $WHSV_{gRu} = 1228 \text{ g}_{Org} \text{ g}_{Ru}^{-1} \text{ h}^{-1}$ .

Exp.	Catalyst	Time h	$X_c$ %	$GE_c$ %	$R_{\text{Coke dep.}}$ $\text{mmol C min}^{-1}$	Gas composition, vol %					
						$CH_4$	$CO_2$	$H_2$	$CO$	$C_2H_6$	$C_3H_x$
CS2	2% Ru/C <sub>a</sub>	96	90	100	$\approx 0$	64.4	23.2	12.4	< 0.1	< 0.1	< 0.1

As depicted in Table 3.6, the physical structure of the catalyst was well preserved after 96 h of gasification revealing the robustness of the carbon support at these conditions.

**Table 3.6.** Physical structure of the fresh and spent 2% Ru/C<sub>a</sub> catalysts.

Catalyst	Time h	$WHSV_{gRu}$ $\text{g}_{Org} \text{ g}_{Ru}^{-1} \text{ h}^{-1}$	BET SSA $\text{m}^2 \text{ g}^{-1}$	$V_{\text{total}}$ $\text{cm}^3 \text{ g}^{-1}$	$V_{\text{mesop.}}$ $\text{cm}^3 \text{ g}^{-1}$	$V_{\text{microp.}}$ $\text{cm}^3 \text{ g}^{-1}$
2% Ru/C <sub>a</sub>	0	N.A.	619	0.65	0.54	0.11
	96	1228	896	0.65	0.41	0.24

Another interesting phenomenon should be point out. While the total pore volume remains nearly constant, the volume of the mesopores decreases while at the same time the one of the micropores increases to twice the value of the fresh support. Up to now there is no good explanation for such a large increase but it is likely that the washing out of some dust from the pores may form some additional micropores.

This first gasification experiment demonstrated the good catalytic performance of Ru/C catalysts during CSCWG of IPA under industrial conditions as well as its high robustness. Nevertheless, the performance of Ru/C catalysts should be studied also at a higher  $WHSV_{gRu}$  ( $X_c < 100\%$ ) in order to evaluate its stability. For this purpose, a 0.5% Ru/C<sub>w</sub> was tested at a high  $WHSV_{gRu}$  of  $5202 \text{ g}_{org} \text{ g}_{Ru}^{-1} \text{ h}^{-1}$  over a period of 24 h. As shown in Figure 3.4 and in Table 3.7, a deactivation of the catalyst can be observed. After 24 h, the catalyst was completely deactivated with an observed activity close to the one obtained during SCWG performed over the neat carbon support material (compare Table 3.2).

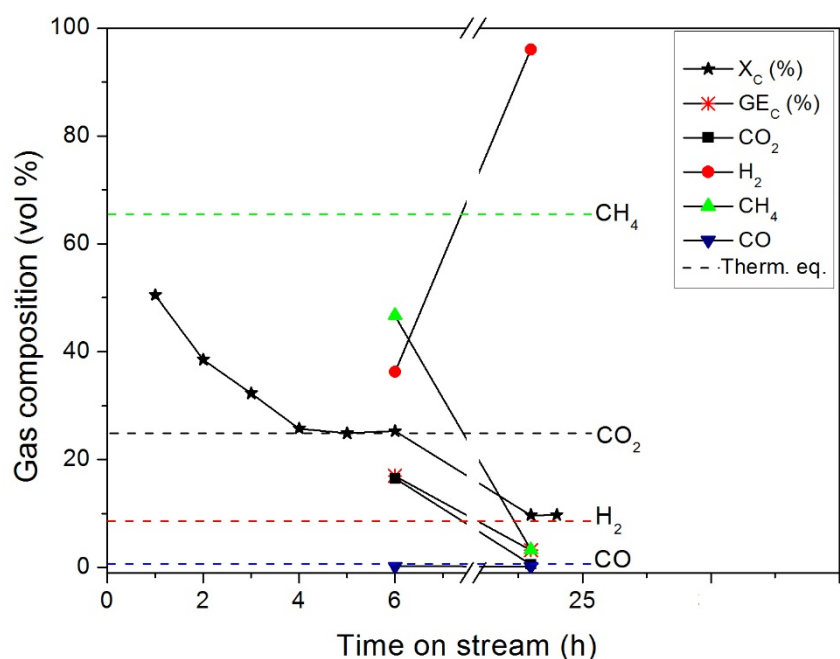


**Figure 3.4.** CSCWG of 10 wt % IPA over the 0.5% Ru/C<sub>w</sub> catalyst at 450 °C and 30 MPa for 24 h on-stream with  $WHSV_{gRu} = 5202 \text{ g}_{org} \text{ g}_{Ru}^{-1} \text{ h}^{-1}$ . The dashed lines denote the calculated thermodynamic equilibrium concentrations (exp. CS3).

**Table 3.7.** Results summary after 24 h of CSCWG with 10 wt % IPA over the 0.5% Ru/C<sub>w</sub> catalyst at 450 °C and 30 MPa with  $WHSV_{gRu} = 5202 \text{ g}_{Org} \text{ g}_{Ru}^{-1} \text{ h}^{-1}$ .

Exp.	Catalyst	Time h	X <sub>c</sub> %	GE <sub>c</sub> %	R <sub>Coke dep.</sub> mmol C min <sup>-1</sup>	Gas composition, vol %					
						CH <sub>4</sub>	CO <sub>2</sub>	H <sub>2</sub>	CO	C <sub>2</sub> H <sub>6</sub>	C <sub>3</sub> H <sub>x</sub>
CS3	0.5% Ru/C <sub>w</sub>	24	10	3	1	3.2	0.6	96.3	0.2	< 0.1	3.7

It is also interesting to note the very low GE<sub>c</sub> showing that the carbon contained in the feed could not be converted to the gas phase and most likely remained inside the reactor (as coke). GE<sub>c</sub> was inferior to X<sub>c</sub>, confirming that coke formation occurred. This supports two parallel reactions: i) coke formation on the support, and ii) catalytic decomposition on the Ru. Some of the coke, likely at the interface of the Ru NPs and the support, may react with H<sub>2</sub> to form some CH<sub>4</sub>. The high H<sub>2</sub> concentration and the low CH<sub>4</sub> concentration can both be easily explained by the inhibition of the methanation reaction due to a complete deactivation of the catalyst. In addition, the presence of C<sub>3</sub>H<sub>x</sub> indicates that the catalyst is not able to cleave all C-C bonds. As illustrated in Table 3.8, a considerable loss of the porosity was measured after 24 h.

**Table 3.8.** Physical structure of the fresh and spent 0.5% Ru/C<sub>w</sub> catalysts.

Catalyst	Time h	$WHSV_{gRu}$ $\text{g}_{Org} \text{ g}_{Ru}^{-1} \text{ h}^{-1}$	BET SSA $\text{m}^2 \text{ g}^{-1}$	V <sub>total</sub> $\text{cm}^3 \text{ g}^{-1}$	V <sub>mesop.</sub> $\text{cm}^3 \text{ g}^{-1}$	V <sub>microp.</sub> $\text{cm}^3 \text{ g}^{-1}$
0.5% Ru/C <sub>w</sub>	0	N.A.	765	0.88	0.75	0.13
	24	5202	455	0.62	0.60	0.02

N<sub>2</sub>-physisorption results have shown that CSCWG of IPA led to a loss of the porosity strengthening the decrease of the catalyst lifetime caused by coke deposits. It was reported by Wambach et al. [129] that the deactivation of the catalyst of a commercial 2% Ru/C during CSCWG of aqueous organics was due to a coverage of the Ru NPs by a thin carbonaceous layer. Brandenberger [17] characterized a 2% Ru/C catalyst after CSCWG of microalgae (420 °C, 32 MPa) and observed with TEM-EDX, coke deposits covering the Ru NPs. According to them, these coke deposits were a cause for the relatively fast deactivation of the catalyst. In Figure 3.5, the Ru NPs coverage by coke seems to be confirmed by the H<sub>2</sub>-TPR results of the fresh and spent 0.5% Ru/C<sub>w</sub> catalysts. In fact, the H<sub>2</sub> uptake for the reduction of RuO<sub>2</sub> was about four times smaller for the aged catalyst indicating that a con-

siderable fraction of Ru was not available. Concerning the other reduction peaks at higher temperature, almost all disappeared after CSCWG showing that the weakly bonded carbon species and/or the surface functional groups were removed during CSCWG.

As shown in Figure 3.6, after 24 h of CSCWG the Ru NPs size of the 0.5% Ru/C<sub>w</sub> has slightly increased from  $4.6 \pm 0.1$  nm to a value of  $4.9 \pm 0.1$  nm. By comparing the histogram of the particle size distribution for the fresh and spent 0.5% Ru/C<sub>w</sub> (compare Figure 3.6 and Figure 3.7 (a)), it seems that the distribution slightly shifted to larger particle sizes indicating that small Ru NPs sintered during CSCWG. Such a small Ru NPs growth was already reported by Waldner et al. [63] and Dreher et al. [78] under similar conditions.

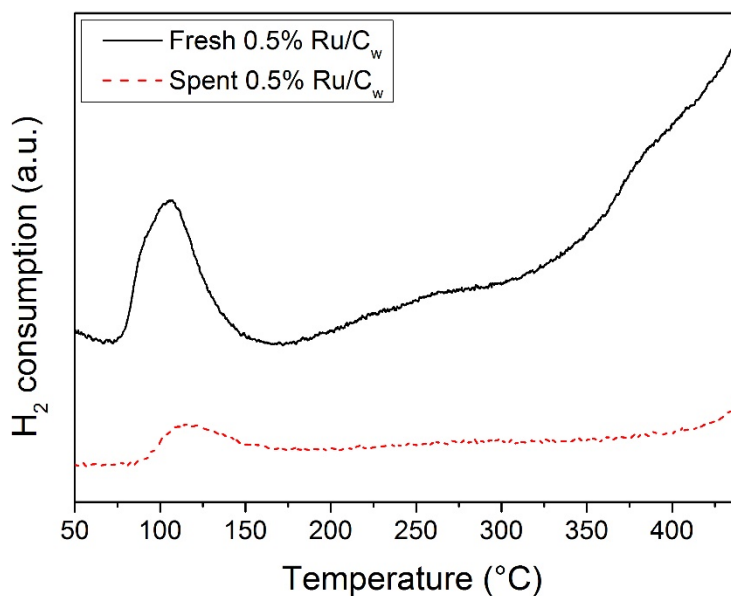


**Figure 3.5.** H<sub>2</sub>-TPR profiles of the fresh and spent 0.5% Ru/C<sub>w</sub> catalysts.

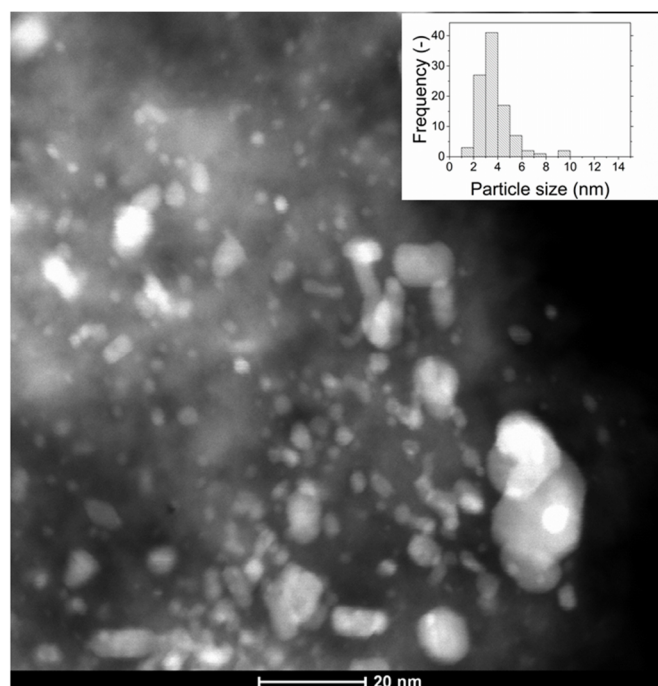


**Figure 3.6.** HAADF-STEM image of the spent 0.5% Ru/C<sub>w</sub> catalyst.

### 3.5 Effect of the synthesis factors

In this section, some relevant synthesis factors (*e.g.* the Ru dispersion, the solvent use during the wet impregnation, the Ru loading, the salt precursor, and carbon surface functional groups) are assessed. The motivation is to improve further the catalytic performance of Ru/C catalysts during CSCWG.

#### 3.5.1 Effect of the Ru dispersion

It is well known that most of the catalytic reactions occur at the surface of the active phase, often meaning that higher metal dispersion results in better activity. In this section, the Ru dispersion effect on the catalytic performance during CSCWG is assessed. In Table 3.9, the characteristics of Ru/C catalysts are listed. The specific surface area was affected by the impregnation with Ru and was found to decrease with the Ru loading for the Ru/C<sub>w</sub> catalysts. A higher Ru loading led to a larger Ru NP size, which reduced the pore volume and the specific surface area. The Ru NPs cannot be located inside the micropores because the micropores are too small (< 2 nm) for the Ru NPs.

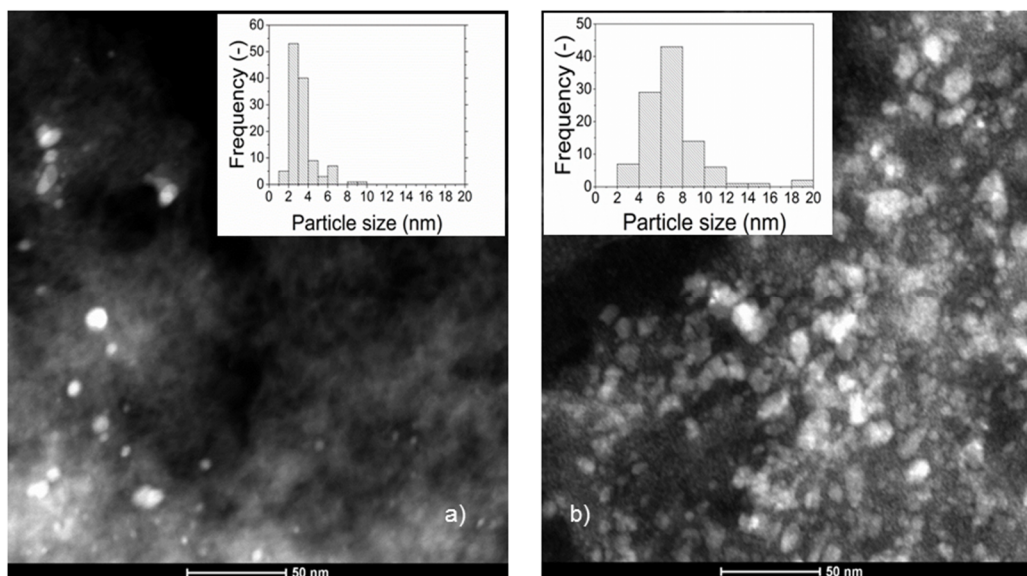


**Table 3.9.** Characteristics of the fresh Ru/C catalysts.

Catalyst	BET SSA $\text{m}^2 \text{g}^{-1}$	$V_{\text{mesop.}}$ $\text{cm}^3 \text{g}^{-1}$	$V_{\text{microp.}}$ $\text{cm}^3 \text{g}^{-1}$	$\text{H}_2$ consumption $\mu\text{mol g}^{-1}\text{a}$	$D_{\text{CO}}$ _b	$D_{\text{STEM}}$ _c	$d_{\text{p,CO}}$ $\text{nm}^b$	$d_{\text{p,STEM}}$ $\text{nm}^c$
Fresh C	802	0.69	0.14	0.0	N.A.	N.A.	N.A.	N.A.
0.5% Ru/C <sub>w</sub>	765	0.75	0.13	3.5	0.12	0.26	11	$4.6 \pm 0.1$
2% Ru/C <sub>w</sub>	737	0.73	0.11	32.0	0.08	0.14	16	$9.7 \pm 0.3$

[a] Determined from  $\text{H}_2$ -TPR [b] determined by CO pulse chemisorption [c] determined by STEM.

The fact that the micropore volume decreases slightly after impregnation could be due to the blockage of the entrance of some of the micropores. The conservation of the mesopore volume of both catalysts indicates that the Ru NPs are rather in the macropores. The lower  $\text{H}_2$  consumption for the 0.5% Ru/C<sub>w</sub> in comparison to the 2% Ru/C<sub>w</sub> is caused by the lower Ru loading deposited on the catalyst. In Figure 3.7, the Ru NPs for the 0.5% Ru/C<sub>w</sub> and 2% Ru/C<sub>w</sub> catalysts are shown, the white dots correspond to the Ru NPs. As expected, a higher Ru loading lead to a larger Ru NPs size as well as a wider distribution. This observation was also confirmed by CO pulse chemisorption. Interestingly, the Ru NPs size values obtained by CO pulse chemisorption have been overestimated (ca. 6 nm) for both catalysts. The cause for this overestimation of the Ru NPs is investigated in the next section (section 3.5.2).

**Figure 3.7.** HAADF-STEM images of the (a) 0.5% Ru/C<sub>w</sub> and (b) 2% Ru/C<sub>w</sub> catalysts.

As illustrated in Figure 3.8 and in Table 3.10, a relevant effect of the Ru dispersion was observed where the 0.5% Ru/C<sub>w</sub> exhibited a higher activity, *i.e.* a higher carbon conversion  $X_c$ , than the 2% Ru/C<sub>w</sub> after 6 h of CSCWG when basing the WSHV on the amount of Ru, not on total catalyst mass.

Interestingly, their respective TOF were almost equal. In a recent study, Masini et al. [130] reported that larger Ru NPs (7-10 nm) were a bit more active than smaller NPs (4 nm) for the methanation reaction carried out in gas-phase confirming the structure sensitivity of the methanation. The presence of a higher concentration of under-coordinated sites (*e.g.* kinks or steps) on the larger Ru NPs was responsible for the catalytic activity enhancement. In fact, Vendelbo et al. [131] demonstrated that the CO bond dissociation only occurs on the steps of Ru. The high capability for the CO bond dissociation is crucial since the latter is reported to be the rate-determining step for the methanation reaction [131,132]. Due to the broad particle size distribution of the Ru/C<sub>w</sub> catalysts it is impossible to assess the Ru NPs effect and thus to conclude the structure sensitivity of the methanation reaction from our data.

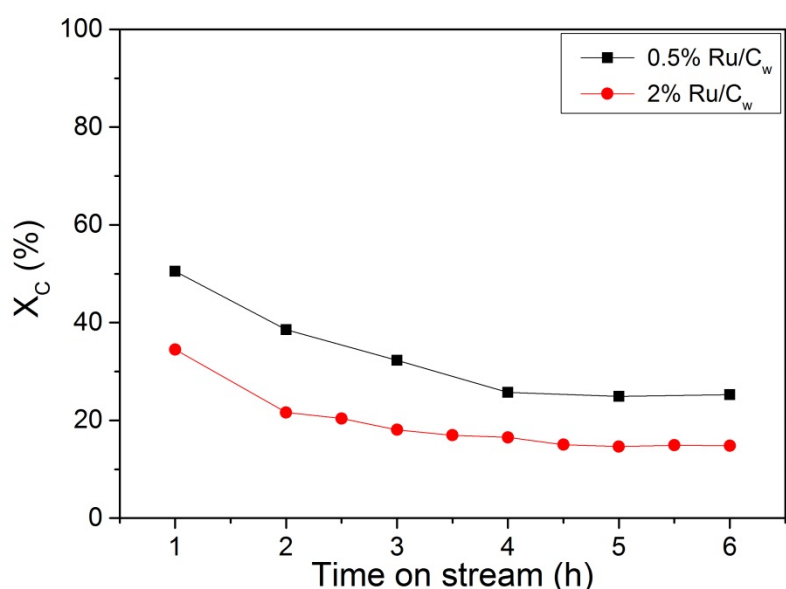


**Figure 3.8.** Assessment of the Ru dispersion effect during CSCWG of 10 wt % IPA at 450 °C and 30 MPa with  $WHSV_{gRu} = 5202 \text{ g}_{Org} \text{ g}_{Ru}^{-1} \text{ h}^{-1}$  (exp. CS3 and CS4).

**Table 3.10.** Results of the CSCWG of 10 wt % IPA for Ru/C catalysts performed at 450 °C, 30 MPa with  $WHSV_{gRu} = 5202 \text{ g}_{Org} \text{ g}_{Ru}^{-1} \text{ h}^{-1}$ .

Exp.	Catalyst	Time h	X <sub>C</sub> %	TOF s <sup>-1</sup>	GE <sub>C</sub> %	R <sub>Coke dep.</sub> mmol C min <sup>-1</sup>	Gas composition, vol %					
							CH <sub>4</sub>	CO <sub>2</sub>	H <sub>2</sub>	CO	C <sub>2</sub> H <sub>6</sub>	C <sub>3</sub> H <sub>x</sub>
CS3	0.5% Ru/C <sub>w</sub>	6	25	2.4	17	1.2	46.7	16.5	36.2	0.2	< 0.1	< 0.1
CS4	2% Ru/C <sub>w</sub>	6	15	2.6	5	1.4	22.1	9.5	68.1	0.2	< 0.1	2.9

As observed in the section 3.3, a similar carbon deposition rate was measured for both catalysts revealing a progressive coke deposition inside the reactor.

### 3.5.2 Effect of the solvent (water vs. acetone)

Here, the effect of two common solvents, water and acetone, used during the catalyst preparation is investigated. The properties of the catalysts are listed in Table 3.11. The conservation of the meso/micropore volume for the 2% Ru/C<sub>w</sub> indicates that the Ru NPs are rather located in the macropores. Whereas the decrease of the mesopore volume for the 2% Ru/C<sub>a</sub> indicates that some Ru NPs are in the mesopores. This would suggest that the Ru NPs of the 2% Ru/C<sub>a</sub> are smaller than the 2% Ru/C<sub>w</sub>. According to the CO pulse chemisorption and the STEM measurements, the use of acetone is more favorable for achieving a better Ru dispersion.

**Table 3.11.** Characteristics of the fresh Ru/C catalysts.

Catalyst	BET SSA m <sup>2</sup> g <sup>-1</sup>	V <sub>mesop.</sub> cm <sup>3</sup> g <sup>-1</sup>	V <sub>microp.</sub> cm <sup>3</sup> g <sup>-1</sup>	H <sub>2</sub> consumption μmol g <sup>-1a</sup>	D <sub>CO</sub> - <sup>b</sup>	D <sub>STEM</sub> - <sup>c</sup>	d <sub>p,CO</sub> nm <sup>b</sup>	d <sub>p,STEM</sub> nm <sup>c</sup>
Fresh C	802	0.69	0.14	0	N.A.	N.A.	N.A.	N.A.
2% Ru/C <sub>w</sub>	737	0.73	0.11	32	0.08	0.14	16	9.7 ± 0.3
2% Ru/C <sub>a</sub>	619	0.54	0.11	47	0.11	0.35	12	3.1 ± 0.1

[a] Determined from H<sub>2</sub>-TPR [b] determined by CO pulse chemisorption [c] determined by STEM.

By looking at the histograms of the particle sizes (see Figure 3.9), the Ru/C catalysts prepared with water exhibit a much broader Ru NPs size distribution proving thus the advantage of using acetone during the catalyst preparation in order to obtain a narrow distribution. As mentioned elsewhere [133] acetone is able to favor a higher interaction between RuCl<sub>3</sub> and the hydrophobic surface of carbon during the impregnation leading to a higher Ru dispersion. Here also, the Ru NPs size values obtained by CO pulse chemisorption have been overestimated (by 6-9 nm) for all the catalysts. As an explanation, the presence of residual chloride coming from the salt precursor (RuCl<sub>3</sub>) may be the cause. It is also known [134,135] that residual chloride reduces the CO adsorption capacity of the catalyst by poisoning the surface of the Ru NPs. As illustrated in Figure 3.10, some residual chloride species were detected on the 2% Ru/C<sub>w</sub> (0.28 at%) by XPS, while no chloride species were found on the 2% Ru/C<sub>a</sub>. Yin et al. [133] also observed that the Ru/C catalysts prepared with acetone resulted in a lower concentration of residual chloride in comparison to the catalysts prepared by water. According to them, water enhances the anchoring of residual chloride on the carbon support during the catalyst preparation.

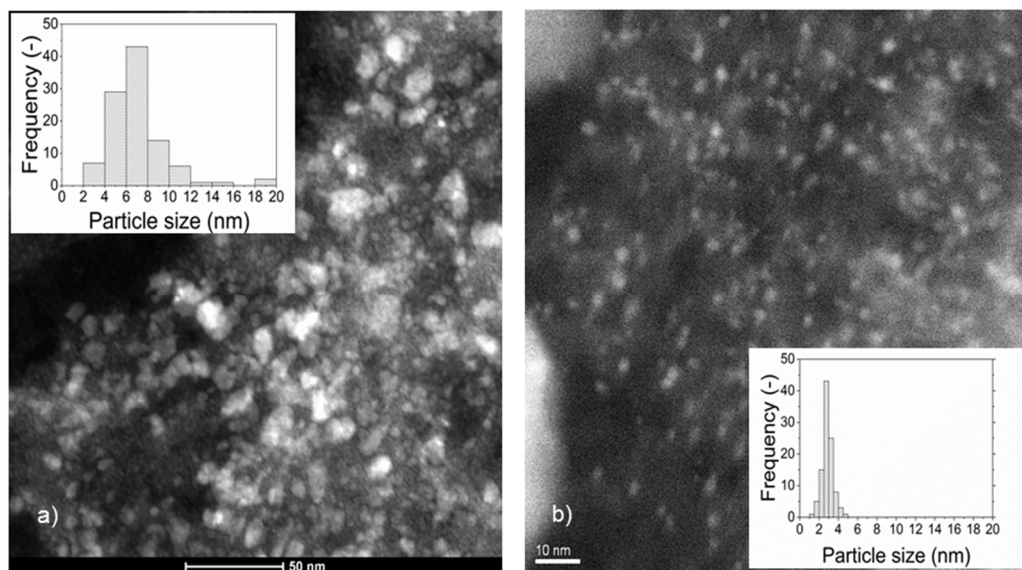


**Figure 3.9.** HAADF-STEM images of the (a) 2% Ru/C<sub>w</sub> and (b) 2% Ru/C<sub>a</sub> catalysts.

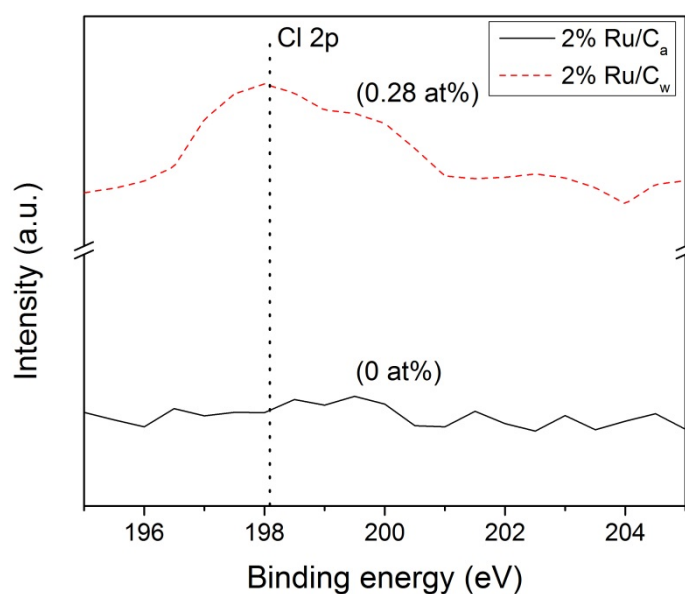


**Figure 3.10.** Cl 2p (198.1 eV) XPS patterns of 2% Ru/C<sub>w</sub> and 2% Ru/C<sub>a</sub> catalysts.

In Figure 3.11, the H<sub>2</sub>-TPR results show a first reduction peak at ca. 100-110 °C corresponding to the reduction of RuO<sub>2</sub> to Ru<sup>0</sup> as reported by Rossetti et al. [136]. The reduction peak for the catalyst prepared with water is slightly lower (104 °C) than for the one prepared with acetone (111 °C). Yin et al. [133] also observed this shift to higher temperature when using acetone. According to them, the use of acetone renders the reduction of the precursor more difficult. Their explanation is a higher interaction between RuO<sub>2</sub> and the carbon support. The lower H<sub>2</sub> consumption for the 2%

Ru/C<sub>w</sub> in comparison to the 2% Ru/C<sub>a</sub> was likely due to the higher Ru dispersion for the catalyst prepared with acetone. On the other hand, the presence of residual chloride on the 2% Ru/C<sub>w</sub> can also explain the lower H<sub>2</sub> consumption as mentioned by Guerrero-Ruiz and al. [137]. About the other peaks around 240 °C, 260 °C, 330 °C, and 440 °C, MS analysis has identified CH<sub>4</sub> formation suggesting hydrogenation of carbon oxide (surface functional groups) to CH<sub>4</sub> or of other carbon species weakly bonded [137]. The absence of these additional reduction peaks for the fresh carbon support is due to the absence of Ru and lower Ru loading. In fact, the reduction of these carbon oxides/species in the vicinity of the Ru NPs is catalyzed by Ru.

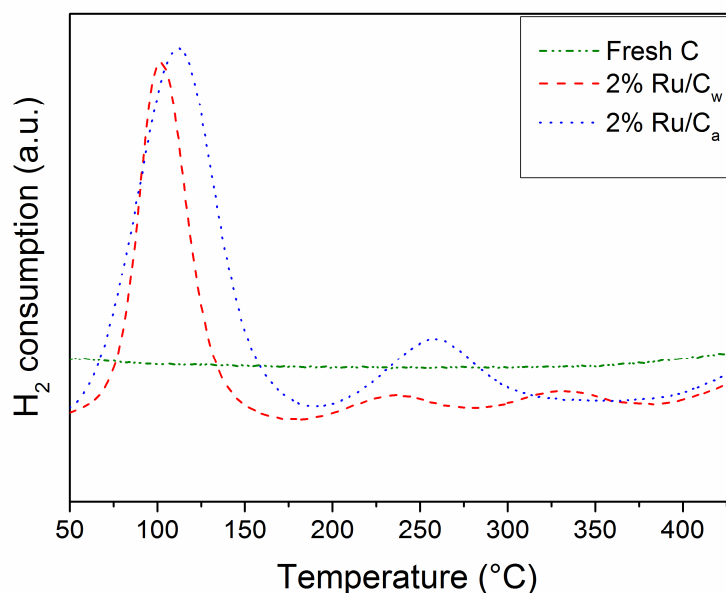


**Figure 3.11.** H<sub>2</sub>-TPR profiles of the fresh C, 2% Ru/C<sub>w</sub>, and 2% Ru/C<sub>a</sub> catalysts.

As shown in Figure 3.12, a relevant effect of the solvent used during catalyst preparation was found where the activity for the 2% Ru/C<sub>a</sub> was higher than the 2% Ru/C<sub>w</sub>. As it can be seen in Table 3.12, the TOF was found to be twice smaller for the 2% Ru/C<sub>w</sub>. Such a high difference cannot only be explained by the higher Ru dispersion but mainly by the lower concentration of residual chloride. Indeed, Yin et al. [133] also found a beneficial effect of acetone vs. water during NH<sub>3</sub> decomposition over Ru/CNT catalysts. They concluded that water enhances the anchoring of residual chloride on the carbon support during the catalyst preparation. In fact, residual chloride coming from the Ru precursor (RuCl<sub>3</sub>) is well known to act as a strong inhibitor of Ru/C catalysts affecting negatively the

catalytic performance. As previously observed, the presence of residual chloride inhibited the adsorption of CO on the Ru surface. Since the CO bond dissociation is the rate-determining step for the methanation reaction, such poor activity in presence of residual chloride was expected [131].

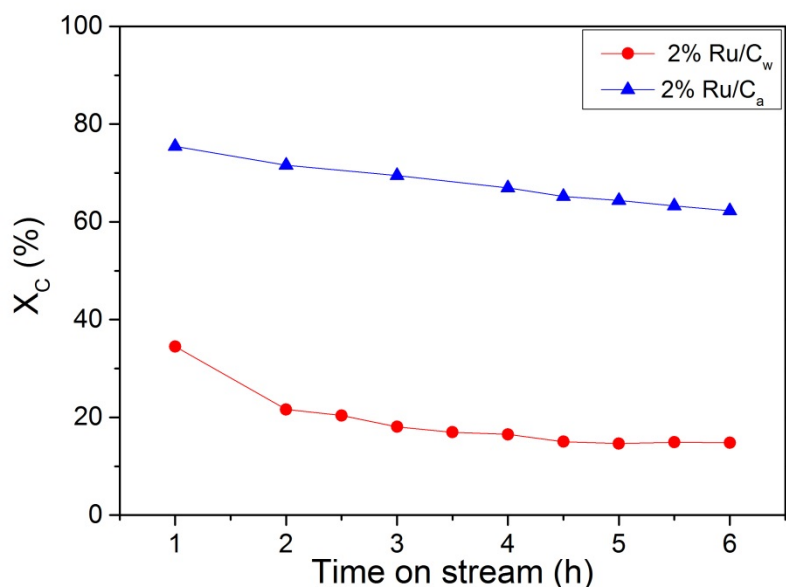


**Figure 3.12.** Assessment of the solvent effect during CSCWG of 10 wt % IPA at 450 °C and 30 MPa with  $WHSV_{gRu} = 5202 \text{ g}_{Org} \text{ g}_{Ru}^{-1} \text{ h}^{-1}$  (exp. CS4 and CS5).

**Table 3.12.** Results of the CSCWG of 10 wt % IPA for Ru/C catalysts performed at 450 °C, 30 MPa with  $WHSV_{gRu} = 5202 \text{ g}_{Org} \text{ g}_{Ru}^{-1} \text{ h}^{-1}$ .

Exp.	Catalyst	Time h	X <sub>c</sub> %	TOF s <sup>-1</sup>	GE <sub>c</sub> %	R <sub>Coke dep.</sub> mmol C min <sup>-1</sup>	Gas composition, vol %					
							CH <sub>4</sub>	CO <sub>2</sub>	H <sub>2</sub>	CO	C <sub>2</sub> H <sub>6</sub>	C <sub>3</sub> H <sub>x</sub>
CS4	2% Ru/C <sub>w</sub>	6	15	2.6	5	1.4	22.1	9.5	68.1	0.2	< 0.1	2.9
CS5	2% Ru/C <sub>a</sub>	6	62	4.3	49	2.0	56.0	22.1	21.6	0.3	< 0.1	< 0.1

As expected, a progressive deactivation of the catalyst caused by coke deposits was also observed for the Ru/C prepared with acetone. Therefore the effect of acetone has not improved the coking resistance of the catalyst.

### 3.5.3 Effect of the salt precursor

In the last section (3.5.2), it was found that the presence of residual chloride coming from the Ru salt precursor ( $\text{RuCl}_3 \cdot x\text{H}_2\text{O}$ ) has significantly decreased the catalytic activity by poisoning the active sites of Ru. Thereby, there is a necessity to assess the catalytic performance of a catalyst prepared

with a chloride free salt precursor. To that aim, the performance of a catalyst prepared with a chloride free salt precursor ( $\text{Ru}(\text{NO})(\text{NO}_3)_3$ ), denoted here as 2% Ru/C<sub>nitro</sub>, is compared with a catalyst prepared with  $\text{RuCl}_3 \cdot x\text{H}_2\text{O}$ . The properties of the fresh Ru/C catalysts are listed in Table 3.13.

**Table 3.13.** Characteristics of the fresh Ru/C catalysts.

Catalyst	BET SSA $\text{m}^2 \text{g}^{-1}$	$V_{\text{mesop.}}$ $\text{cm}^3 \text{g}^{-1}$	$V_{\text{microp.}}$ $\text{cm}^3 \text{g}^{-1}$	$D_{\text{CO}}$ - <sup>a</sup>	$d_{\text{p,CO}}$ $\text{nm}^a$
Fresh C	802	0.69	0.14	N.A.	N.A.
2% Ru/C <sub>nitro</sub>	653	0.58	0.12	0.61	1.6
2% Ru/C <sub>a</sub>	619	0.54	0.11	0.11	12.0

[a] Determined by CO pulse chemisorption.

According to the  $\text{N}_2$ -physisorptions results, the similarity of the meso/micropore volume suggests that Ru NPs size is in the same range for both catalysts. The CO pulse chemisorption measurements reveal a significant difference since the Ru dispersion is almost 6 times higher for the 2% Ru/C<sub>nitro</sub>. Such a result shows that in absence of residual chloride, the CO adsorption is greatly facilitated on the Ru surface. Gallegos-Suarez et al. [138] reported a higher CO adsorption for the Ru/C catalyst prepared with  $\text{Ru}(\text{NO})(\text{NO}_3)_3$  in comparison to the catalyst prepared with  $\text{RuCl}_3$ . In Figure 3.13 and in Table 3.14, it is shown that the catalytic performance for the 2% Ru/C<sub>nitro</sub> is greatly improved in comparison to the 2% Ru/C<sub>a</sub>. In fact, by working at a high  $\text{WHSV}_{\text{gRu}}$  ( $5202 \text{ g}_{\text{Org}} \text{ g}_{\text{Ru}}^{-1} \text{ h}^{-1}$ ), the 2% Ru/C<sub>nitro</sub> was able to efficiently convert IPA to gaseous products ( $X_c = 100\%$ ) with a gas composition similar to the thermodynamic chemical equilibrium. Whereas the conversion of IPA was not fully achieved ( $X_c < 100\%$ ) for the 2% Ru/C<sub>a</sub>. Moreover, a progressive deactivation of the catalyst due to coke deposition was observed for the 2% Ru/C<sub>a</sub>. In absence of residual chloride, the catalytic performance was improved due to a non-diminished CO adsorption on the Ru surface. As previously discussed, a high CO adsorption is required for achieving a good methanation. A similar beneficial effect of  $\text{Ru}(\text{NO})(\text{NO}_3)_3$  compared to  $\text{RuCl}_3$  was reported during SCWG of lignin ( $400^\circ\text{C}$ ,  $37.1 \text{ MPa}$ ) over Ru/C catalysts carried out in a batch reactor [73,139]. The authors found that the catalyst prepared with  $\text{Ru}(\text{NO})(\text{NO}_3)_3$  had a smaller Ru NPs than the one prepared with  $\text{RuCl}_3$ . Hence, well-dispersed Ru NPs were more active for CSCWG of lignin.

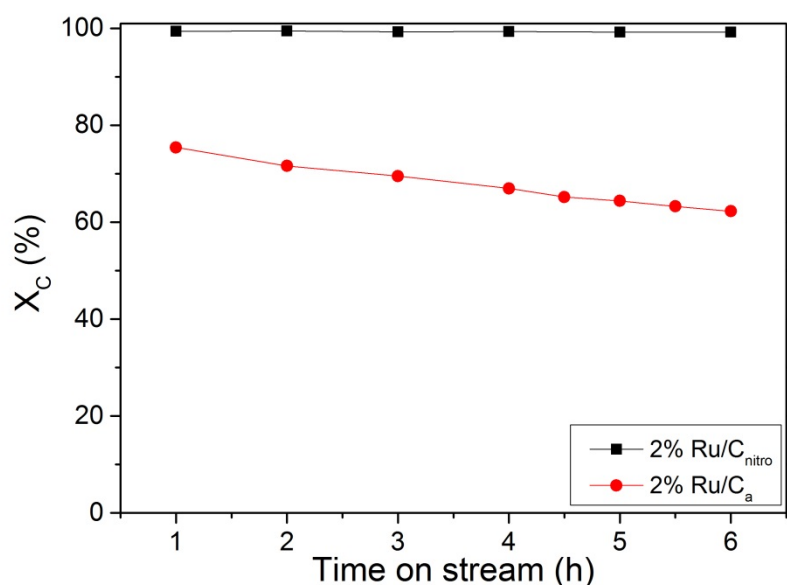


**Figure 3.13.** Assessment of the effect of salt precursor during CSCWG of 10 wt % IPA at 450 °C and 30 MPa with  $\text{WHSV}_{\text{gRu}} = 5202 \text{ g}_{\text{Org}} \text{ g}_{\text{Ru}}^{-1} \text{ h}^{-1}$  (exp. CS5 and CS6).

**Table 3.14.** Results of the CSCWG of 10 wt % IPA for Ru/C catalysts performed at 450 °C, 30 MPa with  $\text{WHSV}_{\text{gRu}} = 5202 \text{ g}_{\text{Org}} \text{ g}_{\text{Ru}}^{-1} \text{ h}^{-1}$ .

Exp.	Catalyst	Time h	X <sub>c</sub> %	GE <sub>c</sub> %	R <sub>Coke dep.</sub> mmol C min <sup>-1</sup>	Gas composition, vol %					
						CH <sub>4</sub>	CO <sub>2</sub>	H <sub>2</sub>	CO	C <sub>2</sub> H <sub>6</sub>	C <sub>3</sub> H <sub>x</sub>
CS6	2% Ru/C <sub>nitro</sub>	6	99	101	≈ 0	66.9	24.5	8.7	0.0	< 0.1	< 0.1
CS5	2% Ru/C <sub>a</sub>	6	62	49	2	56.0	22.1	21.6	0.3	< 0.1	< 0.1

### 3.5.4 Effect of the Ru loading

In section 3.4, it was found that the catalyst lifetime was affected by coke deposition on the catalyst. The decomposition of IPA to solid carbon (coke) and H<sub>2</sub> over the carbon surface was responsible for the loss of the catalytic activity. Hence, coking is a major concern in CSCWG. For minimizing the coke deposits, the carbon surface should be decorated with an appropriated Ru concentration. In fact, a too low Ru concentration might lead to a higher coke deposition rate, since there is a higher probability that the molecules of IPA decompose on the carbon surface instead of being gasified on the Ru surface. As discussed in section 1.8.4, the increase of the Ru loading was reported to improve the coking resistance of a Ru/C catalyst during hydrothermal gasification of lignin (350 °C, 20 MPa) [101]. For this purpose, in the present section, we compare the stability of two commercial Ru/C<sub>BASF</sub>



catalysts containing 2 wt % and 5 wt % of Ru, respectively. The catalyst properties are listed in Table 3.15.

**Table 3.15.** Characteristics of the fresh Ru/C catalysts.

Catalyst	BET SSA $\text{m}^2 \text{g}^{-1}$	$V_{\text{mesop.}}$ $\text{cm}^3 \text{g}^{-1}$	$V_{\text{microp.}}$ $\text{cm}^3 \text{g}^{-1}$	$D_{\text{CO}}$ - <sup>a</sup>	$d_{\text{p,CO}}$ $\text{nm}^a$
Fresh $\text{C}_{\text{BASF}}$	1265	0.20	0.42	0.00	N.A.
2% Ru/ $\text{C}_{\text{BASF}}$	1271	0.18	0.44	0.41	3
5% Ru/ $\text{C}_{\text{BASF}}$	1254	0.21	0.42	0.23	5

[a] Determined by CO pulse chemisorption.

The preservation of the meso-/micropore volume after the Ru impregnation for both catalysts suggests that the Ru NPs are located rather in the macropores. Therefore according to the  $\text{N}_2$ -physisorption results, it seems that both catalysts exhibit an egg-shell profile. As expected a higher Ru loading leads to a smaller Ru dispersion as well as a larger Ru NPs size. As shown in Figure 3.14 and 3.15, by operating at the same  $\text{WHSV}_{\text{gRu}}$ , a remarkable effect of the Ru loading was observed where the 5% Ru/ $\text{C}_{\text{BASF}}$  exhibited a better stability than the 2% Ru/ $\text{C}_{\text{BASF}}$  over a period of 50 h. The decrease of the catalytic activity for the 2% Ru/ $\text{C}_{\text{BASF}}$  was considerable, from 73% down to 16%. By contrast, the 5% Ru/ $\text{C}_{\text{BASF}}$  lost only 10% of its initial activity. By looking at their respective  $\text{GE}_c$  values, they were below  $X_c$  for both catalysts indicating a carbon accumulation in the reactor setup. Interestingly, the difference between  $\text{GE}_c$  and  $X_c$  is more pronounced for the 2% Ru/ $\text{C}_{\text{BASF}}$  suggesting a higher carbon deposition rate. This is a relevant information proving that coking can be significantly reduced by appropriately decorating the carbon surface with Ru. In Table 3.16, their corresponding rate of coke deposition were calculated based on a carbon mass balance and the latter was found to be more than twice higher for the 2% Ru/ $\text{C}_{\text{BASF}}$  in comparison to the 5% Ru/ $\text{C}_{\text{BASF}}$ . The higher initial activity of the 2% Ru/ $\text{C}_{\text{BASF}}$  was caused by its higher Ru dispersion. The gas composition well reflects the activity loss for the 2% Ru/ $\text{C}_{\text{BASF}}$  over the period of 50 h. At the beginning, the  $\text{CH}_4$  concentration is high and relatively close to the thermodynamic chemical equilibrium due to the high catalytic activity. At the end of the experiment, in line with the deactivation of the catalyst observed, the  $\text{CH}_4$  concentration drastically dropped, whereas the  $\text{H}_2$  concentration increased. Such an inhibition of the methanation reflects the incapability of Ru for C-O bond cleavage due to coke deposits which have progressively covered the Ru NPs. Inversely, the stable gas composition for the 5% Ru/ $\text{C}_{\text{BASF}}$  demonstrates its higher stability. Indeed, due to its lower coke content, the Ru NPs are still uncovered by coke and were still able to cleave efficiently the C-O bonds. The absence of CO for both Ru/ $\text{C}_{\text{BASF}}$  catalysts

show that the WGS reaction was favored, although the catalytic activity of the 2% Ru/C<sub>BASF</sub> has been affected by coke deposits.

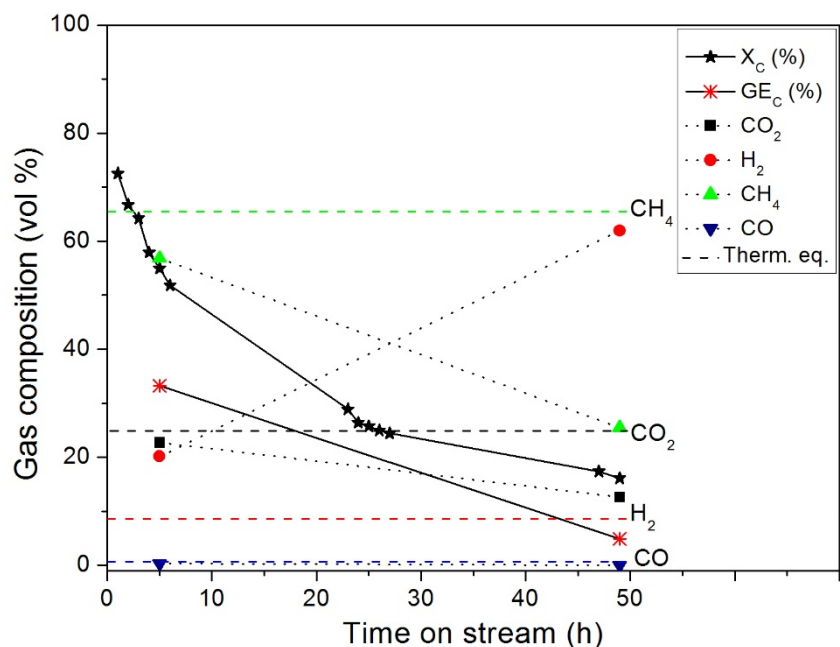


**Figure 3.14.** CSCWG (450 ° C, 30 MPa) of 10 wt % IPA over the 2% Ru/C<sub>BASF</sub> catalyst during 50 h with  $WHSV_{gRu} = 5202 \text{ g}_{Org} \text{ g}_{Ru}^{-1} \text{ h}^{-1}$ . The dashed lines denote the calculated thermodynamic equilibrium concentrations (exp. CS8).

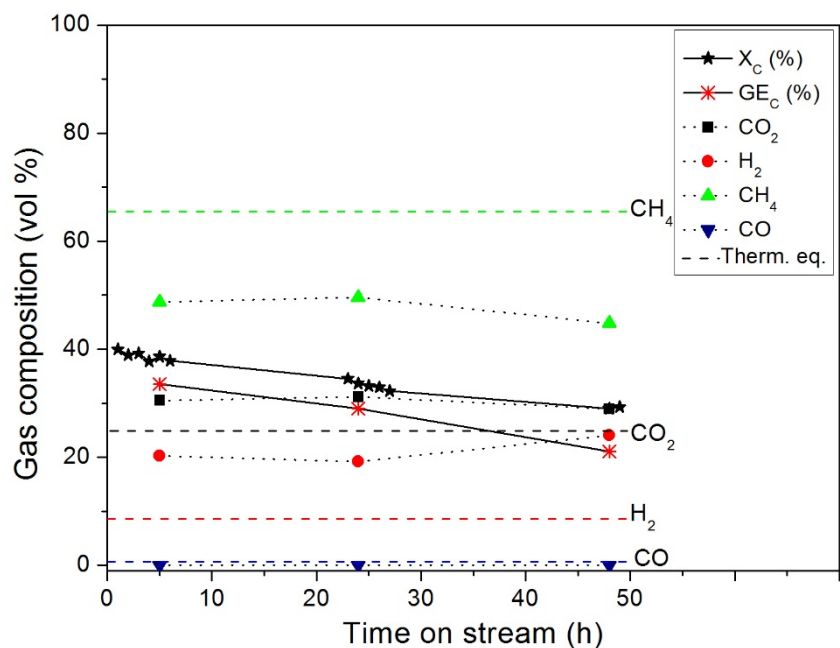


**Figure 3.15.** CSCWG (450 ° C, 30 MPa) of 10 wt % IPA over the 5% Ru/C<sub>BASF</sub> catalyst during 50 h with  $WHSV_{gRu} = 5202 \text{ g}_{Org} \text{ g}_{Ru}^{-1} \text{ h}^{-1}$ . The dashed lines denote the calculated thermodynamic equilibrium concentrations (exp. CS9).

**Table 3.16.** Results of the CSCWG of 10 wt % IPA for Ru/C<sub>BASF</sub> catalysts performed at 450 °C, 30 MPa with  $WHSV_{gRu} = 5202 \text{ g}_{Org} \text{ g}_{Ru}^{-1} \text{ h}^{-1}$ .

Exp.	Catalyst	Time h	$X_c$ %	$GE_c$ %	$R_{Coke \text{ dep.}}$ $\text{mmol C min}^{-1}$	Gas composition, vol %			
						CH <sub>4</sub>	CO <sub>2</sub>	H <sub>2</sub>	CO
CS8	2% Ru/C <sub>BASF</sub>	50	16	5	2.6	25.4	12.6	62.0	0.0
CS9	5% Ru/C <sub>BASF</sub>	50	29	21	1.2	44.8	28.9	24.1	0.0

In Table 3.17, it can be seen that the porosity of the 2% Ru/C<sub>BASF</sub> was drastically affected, while the latter was well preserved for the 5% Ru/C<sub>BASF</sub>. This loss can be related to coke deposits that have progressively filled the pores of the catalyst. Apparently, the coke deposits blocked a considerable fraction of the micropore volume since the latter lost ca. 9 times of its initial volume. Unlike the 2% Ru/C<sub>BASF</sub>, the microporosity of the 5% Ru/C<sub>BASF</sub> increased. The washing out of some dust from the pores during CSCWG may be an explanation for such an increase.

**Table 3.17.** Physical structure of the fresh and spent Ru/C<sub>BASF</sub> catalysts.

Catalyst	Time h	BET SSA $\text{m}^2 \text{ g}^{-1}$	$V_{mesop.}$ $\text{cm}^3 \text{ g}^{-1}$	$V_{microp.}$ $\text{cm}^3 \text{ g}^{-1}$
2% Ru/C <sub>BASF</sub>	0	1271	0.18	0.44
	50	225	0.10	0.05
5% Ru/C <sub>BASF</sub>	0	1254	0.21	0.42
	50	1345	0.24	0.45

In Figure 3.16, an additional experiment with the 5% Ru/C<sub>BASF</sub> was carried out at a lower  $WHSV_{gRu}$  ( $2586 \text{ g}_{Org} \text{ g}_{Ru}^{-1} \text{ h}^{-1}$ ) by doubling the charge of the catalyst. As expected, the initial activity was higher than during the experiment CS9 due to the higher Ru content. As previously observed, the stability was remarkably well preserved over a period of 50 h since only a loss of 15% of its initial activity was measured. The higher CH<sub>4</sub> concentration in comparison to the experiment CS9 was due to the higher catalytic activity. The similarity between  $X_c$  and  $GE_c$  suggests that coke deposition occurred at a smaller extent.

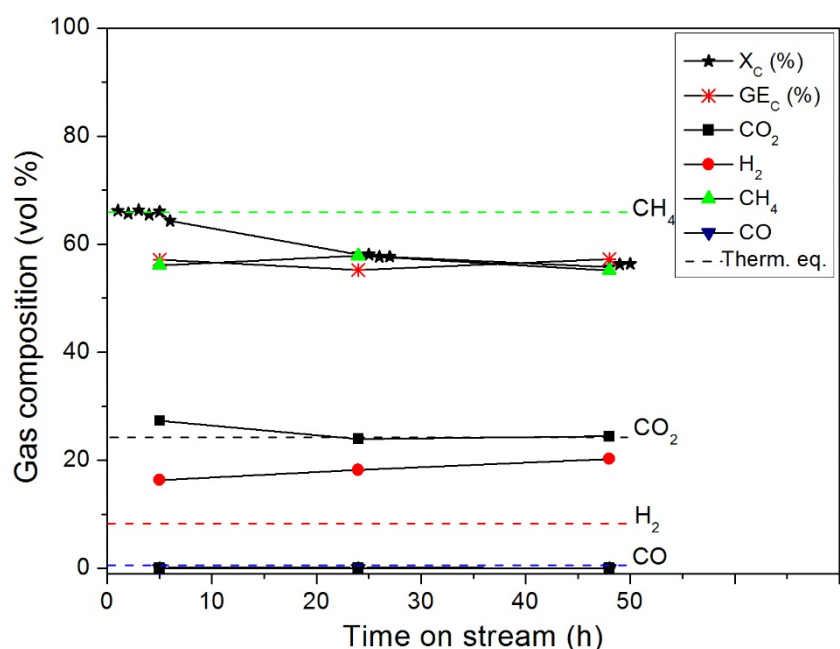


**Figure 3.16.** CSCWG (450 °C, 30 MPa) of 10 wt % IPA over the 5% Ru/C<sub>BASF</sub> catalyst during 50 h with  $WHSV_{gRu} = 2586$  g<sub>org</sub> g<sub>Ru</sub><sup>-1</sup> h<sup>-1</sup>. The dashed lines denote the calculated thermodynamic equilibrium concentrations (exp. CS10).

### 3.5.5 Effect of the surface functional groups of carbon

In this section, we study the effect of the surface acidity of carbon on the synthesis of Ru/C catalysts by adding different surface functional groups (*e.g.* -COOH, -OH groups) with HNO<sub>3</sub> prior to active phase impregnation, and test them during CSCWG with 10 wt % IPA in water. It is well known that introducing surface functional groups by acid treatment is beneficial for the metal dispersion of many carbon supported noble metal catalysts [140]. The surface functional groups are known to act as “anchoring sites” during the catalyst preparation favoring a better metal dispersion. It was reported that the pre-treatment of the carbon support with HNO<sub>3</sub> was able to improve the Pt dispersion from 13% up to 92% compared to the fresh Pt/C catalyst [141]. Wang et al. [142] reported also the benefit of the HNO<sub>3</sub> pre-treatment on the Pt dispersion for multi-walled carbon nanotubes (MWCNT) supported Pt catalysts. Numerous studies [135,143] reported on the benefit of the HNO<sub>3</sub> pre-treatment for Ru/C catalysts. For instance, Li et al. [135] found that the HNO<sub>3</sub> pre-treatment was able to enhance the Ru dispersion from 17% up to 38% in comparison to the fresh catalyst. Zhu et al. [143] reported an increase of the Ru dispersion from 24% to 60% after the HNO<sub>3</sub> pre-treatment. Gallegos-Suarez et al. [138] studied recently the effect of the surface functional groups during hydrogenolysis of glycerol over Ru/C catalysts and they observed that the HNO<sub>3</sub> pre-treatment of the carbon support led to a smaller Ru dispersion. For the fresh 4% Ru/C catalyst they found a Ru

dispersion of 19%, whereas the dispersion was 15% for the catalyst prepared with  $\text{HNO}_3$ . According to them, the surface functional groups were responsible for the Ru NPs sintering during the thermal treatment. These contradictory observations might be explained by the nature of carbon which is a versatile material containing a variety of impurities as well as exhibiting different surface and physical structure properties. In relation to gaseous fuel production, Wang et al. [142,144] studied the effect of the surface functional groups during aqueous phase reforming of ethylene glycol over single-walled carbon nanotubes (SWCNT) and MWCNT supported Pt catalysts. They observed that the surface functional groups negatively affected the catalytic activity. Although the Pt dispersion was improved for the catalyst prepared with  $\text{HNO}_3$ , according to them, the lower catalytic activity was related to the polarity change of the support which caused more adsorption competition on the Pt surface between water and ethylene glycol.

Some structural properties of the carbon support are listed in Table 3.18.

**Table 3.18.** Structural properties of the carbon support.

Sample	BET SSA $\text{m}^2 \text{g}^{-1}$	$V_{\text{total}}$ $\text{cm}^3 \text{g}^{-1}$	$V_{\text{mesop.}}$ $\text{cm}^3 \text{g}^{-1}$	$V_{\text{microp.}}$ $\text{cm}^3 \text{g}^{-1}$	Ash content wt %
Fresh C	802	0.83	0.69	0.14	11.0
$\text{C}_{\text{HNO}_3}$	781	0.63	0.45	0.18	4.9
$\text{C}_{\text{HT}}$	999	0.66	0.37	0.29	4.6

The physical structure of the carbon support was affected by the  $\text{HNO}_3$  pre-treatment since a loss of the BET SSA and the total pore volume occurred. This decrease of the porosity was caused either by a collapse of the physical structure or by a physical blockage of the pores by the formation of humic substances during the  $\text{HNO}_3$  pre-treatment [145–147]. After the thermal pre-treatment, the micropore volume increased by almost 30% while the mesopore volume decreased by 35%. Possibly ashes and humic acids trapped in the micropores were removed and led to the increased microporosity. The ash content was reduced by 55% after the  $\text{HNO}_3$  pre-treatment, showing its efficiency for cleaning the pores as reported by others [143,148].

In Table 3.19, CHONS elemental analysis results show a decrease of the carbon content after the  $\text{HNO}_3$  pre-treatment due to the increase of the oxygen content, whereas the nitrogen and the hy-

drogen concentration increased after the oxidation pre-treatment.  $\text{HNO}_3$  is able to provide a nitronium ion ( $\text{NO}_2^+$ ) to an aromatic ring (nitration reaction) [147,149]. After the thermal pre-treatment, a fraction of the nitrogen was released probably by desorption of  $\text{NO}_2$  that is reported to decompose around  $280^\circ\text{C}$  [149]. The new increase of the carbon concentration after the thermal pre-treatment reflects the loss of oxygen. Indeed, a considerable fraction of the acidic oxygen-containing functional groups (*e.g.* carboxylic groups) are removed during the thermal treatment [147]. The sulfur concentration was found to decrease slightly after the  $\text{HNO}_3$  pre-treatment.

**Table 3.19.** CHONS elemental analysis of the carbon support.

Sample	C wt %	H wt %	O wt %	N wt %	S wt %
Fresh C	$85.12 \pm 0.05$	$0.75 \pm 0.03$	$5.00 \pm 0.00$	$0.68 \pm 0.04$	$0.26 \pm 0.02$
$\text{C}_{\text{HNO}_3}$	$78.58 \pm 0.10$	$0.91 \pm 0.01$	$13.00 \pm 0.00$	$1.26 \pm 0.04$	$0.17 \pm 0.01$
$\text{C}_{\text{HT}}$	$81.88 \pm 0.05$	$0.70 \pm 0.02$	$10.00 \pm 0.00$	$1.08 \pm 0.06$	$0.19 \pm 0.01$

In Figure 3.17, the first peak at  $217^\circ\text{C}$  can be assigned to the decomposition of the carboxylic groups [150].

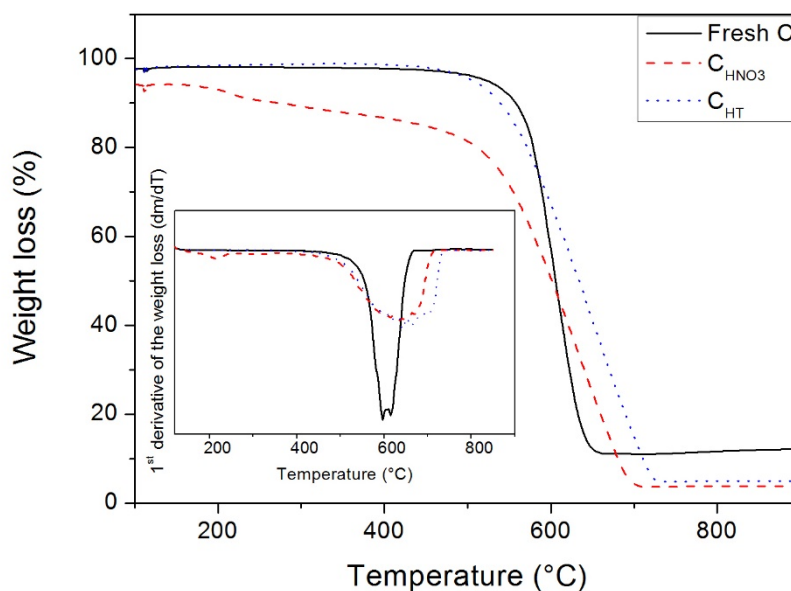


**Figure 3.17.** TPO analysis of the fresh C,  $\text{C}_{\text{HNO}_3}$ , and  $\text{C}_{\text{HT}}$ .

The  $C_{HNO_3}$  started to oxidize at a lower temperature (ca. 430 °C) than the fresh C and the  $C_{HT}$ . The fresh C appears to be fully oxidized at 600 °C, whereas the temperature was shifted to 630 °C and 670 °C for the  $C_{HNO_3}$  and  $C_{HT}$ , respectively. According to this observation, it seems that the  $HNO_3$  pre-treatment enhanced the thermal resistance of the carbon support. Moreover, the thermal pre-treatment further increased its thermal stability. Chiang et al. [128] reported that the thermal stability of the MWCNT was improved after the  $H_2SO_4/HNO_3$  pre-treatment. According to them, some existing reactive groups on the support such as  $-CH_2$  and  $-CH$  are decomposed during the acidic pre-treatment, rendering the material more thermally resistant. During the TPD experiments the surface functional groups decompose within a specific temperature range (according to the type of surface functional groups) to produce  $CO_2$ ,  $CO$ , and  $H_2O$ . In Figure 3.18, the TPD results for the fresh C support show only a small  $CO_2$  desorption peak at 700 °C likely corresponding to carboxylic anhydride while the  $CO$  signal above 900 °C can be related to carbonyl and/or quinone [151]. After the  $HNO_3$  pre-treatment the  $CO_2$  desorption peaks at ca. 300 °C and 500 °C can be assigned to carboxylic and lactone, respectively. The  $CO_2$  and  $CO$  desorption peaks above 700 °C are attributed to more thermally stable groups such as carboxylic anhydride, quinone, and carbonyl. The effect of the thermal pre-treatment under He carried up to 500 °C removed a large quantity of carboxylic groups, whereas the more thermally stable groups were preserved.

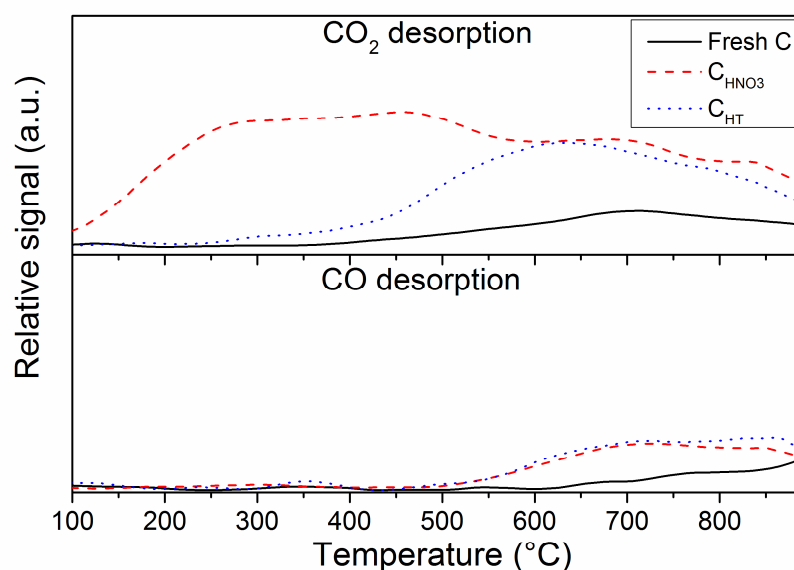


**Figure 3.18.**  $CO_2$  and  $CO$ -TPD analysis of the fresh C,  $C_{HNO_3}$ , and  $C_{HT}$ .

In Figure 3.19, the Boehm titration results reveal a good correlation with the TPD results since no carboxylic groups and only a small amount of lactonic groups were detected on the fresh C. After the  $\text{HNO}_3$  pre-treatment, a considerable increase of the carboxylic and lactonic groups was observed, and the total number of acidic sites was ca. 11 times higher. Hence, the pre-treatment with  $\text{HNO}_3$  was able to change the carbon surface properties from a hydrophobic surface to a more hydrophilic surface. As expected, the thermal pre-treatment mainly removed the less thermally stable groups, *i.e.* the carboxylic groups. The quantification of the thermally more stable surface functional groups (carbonyl, quinone) has a much higher uncertainty, probably due to their low concentration, as also reported by Li et al. [135].

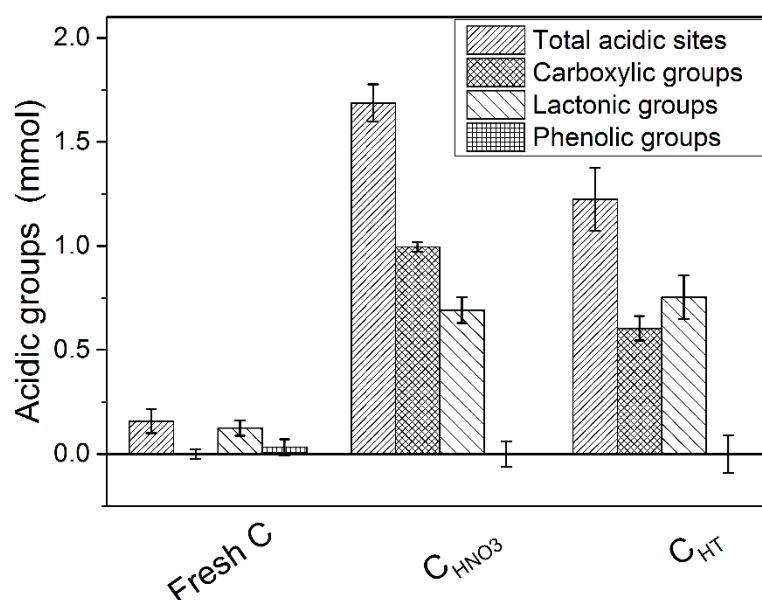


**Figure 3.19.** Boehm titration results of the fresh C,  $\text{C}_{\text{HNO}_3}$ , and  $\text{C}_{\text{HT}}$ .

The characteristics of Ru/C catalysts are listed in Table 3.20.

**Table 3.20.** Characteristics of the Ru/C catalysts.

Catalyst	BET SSA $\text{m}^2 \text{g}^{-1}$	$V_{\text{total}}$ $\text{cm}^3 \text{g}^{-1}$	$V_{\text{microp.}}$ $\text{cm}^3 \text{g}^{-1}$	$\text{H}_2$ consumption $\mu\text{mol g}^{-1\text{a}}$	$D_{\text{CO}}$ _b	$D_{\text{STEM}}$ _c	$d_{\text{p,CO}}$ $\text{nm}^b$	$d_{\text{p,STEM}}$ $\text{nm}^c$
4% Ru/C	551	0.67	0.08	790	0.09	0.26	15.3	$4.5 \pm 0.2$
4% Ru/ $\text{C}_{\text{HNO}_3}$	728	0.70	0.14	964	0.13	0.39	9.9	$2.7 \pm 0.1$
4% Ru/ $\text{C}_{\text{HT}}$	646	0.61	0.12	867	0.10	0.31	12.5	$3.6 \pm 0.1$

[a] Determined from  $\text{H}_2$ -TPR [b] determined by CO pulse chemisorption [c] Determined by STEM.



The impregnation with Ru affected the specific surface area significantly (compare with Table 3.18). Although the three Ru/C catalysts have the same Ru loading, their respective specific surface area differs considerably. According to the Ru NPs measurements, it seems that larger Ru NPs led to a reduction of the specific surface area and of the micropore volume. The blockage of the entrance of some of the micropores by larger Ru NPs may be the reason.

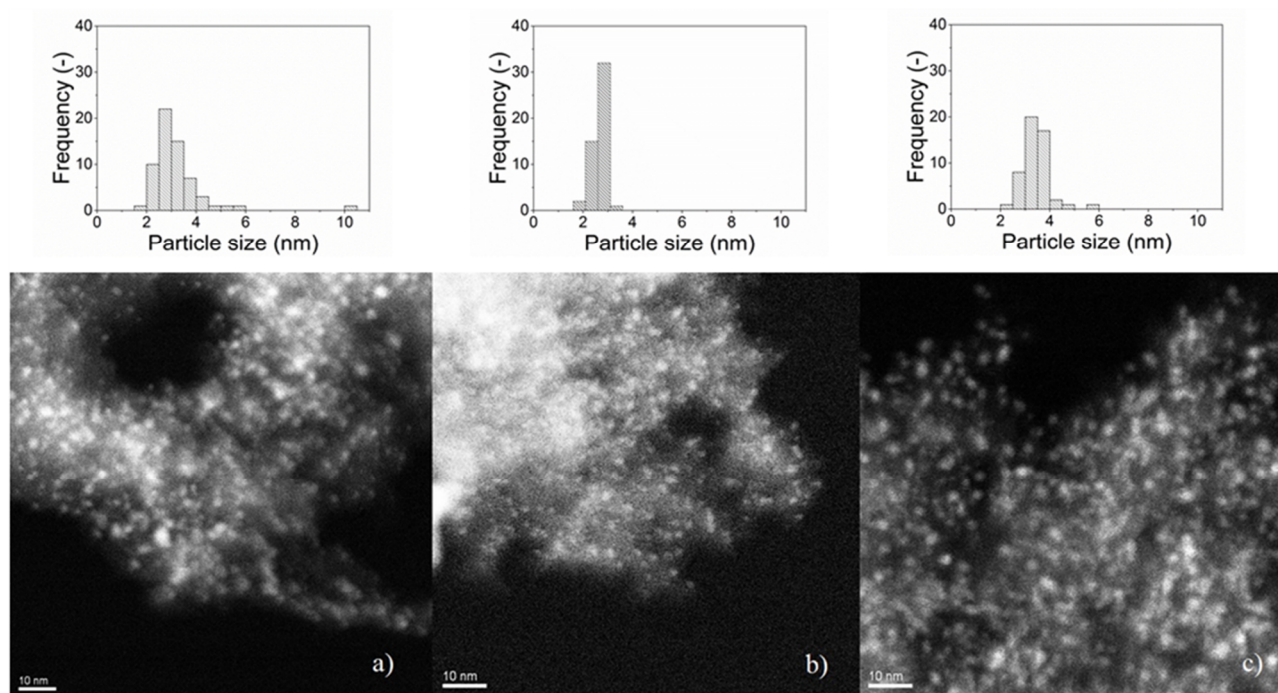


**Figure 3.20.** STEM images of the (a) 4% Ru/C, (b) 4% Ru/C<sub>HNO<sub>3</sub></sub>, and (c) 4% Ru/C<sub>HT</sub> catalysts.

Figure 3.20 shows the STEM images of the three Ru/C catalysts where the bright dots represent the Ru NPs. According to the histograms of the particle size distribution, the Ru NPs size distribution of the 4% Ru/C appears to be larger in comparison to the 4% Ru/C<sub>HNO<sub>3</sub></sub> and 4% Ru/C<sub>HT</sub> since Ru NPs from 2-10 nm can be seen. The main reason is the lack of anchoring sites which help to obtain smaller Ru NPs during the catalyst preparation [135,140]. The larger Ru NPs of the 4% Ru/C<sub>HT</sub> in comparison to the 4% Ru/C<sub>HNO<sub>3</sub></sub> reveals that carboxylic groups play an important role for the Ru dispersion improvement. The CO chemisorption results confirmed that the surface functional groups are needed for the Ru dispersion improvement. However, the Ru NPs size based on the CO chemisorption has been overestimated (7-11 nm) for the three Ru/C catalysts. The presence of residual chloride coming from the Ru salt precursor (RuCl<sub>3</sub>) is responsible for the inhibition of the CO adsorption on the Ru surface [134,135,152]. Therefore in presence of residual chloride, the STEM measurements are much more reliable for the determination of the Ru NPs size. In Figure 3.21, the

H<sub>2</sub>-TPR results of the three Ru/C catalysts are depicted. After integration of the reduction peaks (see Table 3.20), the 4% Ru/C<sub>HNO<sub>3</sub></sub> exhibits the highest H<sub>2</sub> consumption, likely due to the reduction of some surface functional groups in the vicinity of the Ru NPs and/or its higher Ru dispersion in comparison to the two other catalysts.

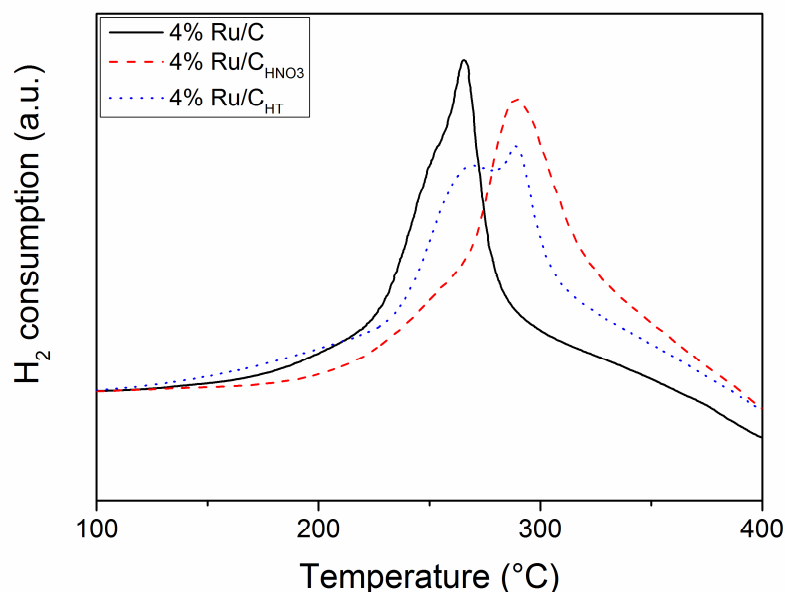


**Figure 3.21.** H<sub>2</sub>-TPR profiles of the 4% Ru/C, 4% Ru/C<sub>HNO<sub>3</sub></sub>, and 4% Ru/C<sub>HT</sub> catalysts.

Two distinct reduction peaks can be seen for the Ru/C catalysts. The reduction peaks at 265 °C and 290 °C can be both attributed to the reduction of RuCl<sub>3</sub> to Ru<sup>0</sup> [133,137]. Interestingly, it seems that the presence of the surface functional groups favored the reduction of Ru at higher temperature suggesting a better interaction between Ru and the carbon support. Gallegos-Suarez et al. [138] observed a similar shift from 197 °C to 247 °C when the Ru/C catalyst was pre-treated with HNO<sub>3</sub>. For the 4% Ru/C<sub>HT</sub>, the two distinct reduction peaks strengthen the fact that the carboxylic groups contribute to the enhancement of the metal-support interaction.

The catalysts were tested with 10 wt % IPA at 450 °C and 30 MPa. As shown in Figure 3.22 and in Table 3.21, by working at a WHSV<sub>Ru</sub> of 1972 g<sub>Org</sub> g<sub>Ru</sub><sup>-1</sup> h<sup>-1</sup>, all the three catalysts were able to gasify properly IPA to a CH<sub>4</sub> –rich gas during 50 h.

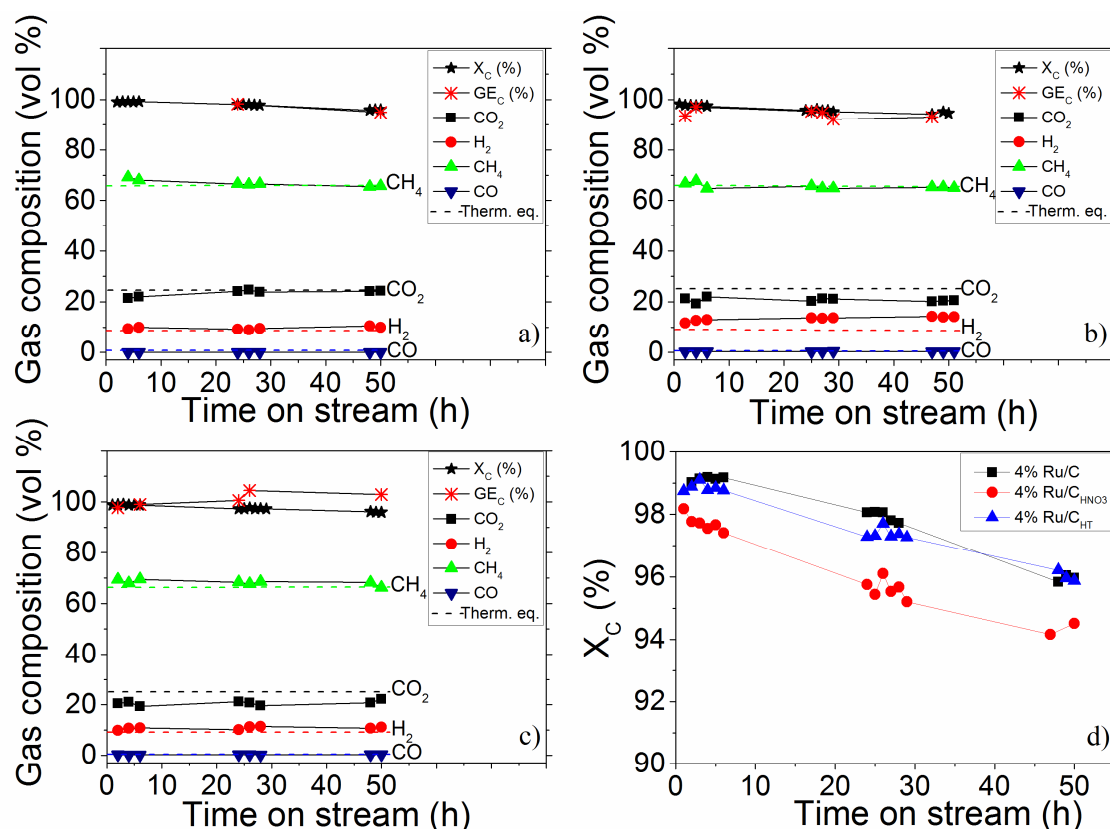


**Figure 3.22.** CSCWG (450 °C, 30 MPa) of 10 wt % IPA over the (a) 4% Ru/C (exp. CS11), (b) 4% Ru/C<sub>HNO3</sub> (exp. CS12), (c) and 4% Ru/C<sub>HT</sub> (exp. CS13) catalysts during 50 h with  $\text{WHSV}_{\text{gRu}} = 1972 \text{ g}_{\text{Org}} \text{ g}_{\text{Ru}}^{-1} \text{ h}^{-1}$ . (d) Represents the evolution of the total organic carbon conversion ( $X_c$ ) of the three Ru/C catalysts. The dashed lines denote the calculated thermodynamic equilibrium concentrations.

**Table 3.21.** Results summary after 50 h of CSCWG (450 °C, 30 MPa) of 10 wt % IPA for the Ru/C catalysts performed at  $\text{WHSV}_{\text{gRu}} = 1972 \text{ g}_{\text{Org}} \text{ g}_{\text{Ru}}^{-1} \text{ h}^{-1}$ .

Exp.	Catalyst	Time h	$X_c$ %	$GE_c$ %	Gas composition, vol %					
					CH <sub>4</sub>	CO <sub>2</sub>	H <sub>2</sub>	CO	C <sub>2</sub> H <sub>6</sub>	C <sub>3</sub> H <sub>x</sub>
CS11	4% Ru/C	50	96	102	65.8	24.3	9.9	< 0.1	< 0.1	< 0.1
CS12	4% Ru/C <sub>HNO3</sub>	50	95	101	65.0	20.6	14.1	0.3	< 0.1	< 0.1
CS13	4% Ru/C <sub>HT</sub>	50	96	102	66.2	22.3	11.2	0.4	< 0.1	< 0.1

The gas composition was close to the thermodynamic chemical equilibrium indicating the good performance of Ru/C catalysts for enhancing the methanation reaction. Furthermore, the absence of higher hydrocarbons ( $\geq \text{C}_2$ ) in the gaseous product is also a reliable indication confirming the high activity of Ru/C catalysts for C-C bond cleavage. After 50 h, the catalytic activity of all catalysts dropped from 99% to ca. 95%. This slight decrease was due to a progressive coke deposition on the Ru/C catalyst as discussed in section 3.4. Although the Ru dispersion of the 4% Ru/C<sub>HNO3</sub> was higher than the two other catalysts, its catalytic activity was found to be slightly lower (see Figure 3.22 (d)).

Moreover, the lower  $\text{CH}_4$  and higher  $\text{H}_2$  and  $\text{CO}$  concentration for the 4% Ru/ $\text{C}_{\text{HNO}_3}$  seems to indicate that the methanation reaction was not fully achieved in comparison to the 4% Ru/C. Wang et al. [142] observed the same negative effect of the carboxylic groups during aqueous phase reforming (225 °C, 2.7 MPa) of ethylene glycol over Pt/MWCNT catalysts where the catalytic activity of the catalyst prepared with  $\text{HNO}_3$  was ca. 30% lower than the fresh Pt/MWCNT catalyst. They had also thermally pre-treated (1000 °C under He) the carbon support after the  $\text{HNO}_3$  pre-treatment and reported an activity ca. 15% lower in comparison to the fresh Pt/MWCNT catalyst. They claimed that the main reason for the lower catalytic activity was a change of the carbon surface polarity that inhibited the adsorption of the reactants caused by the carboxylic groups surrounding the Pt NPs. The Ru NPs size effect might also be responsible for the different activity observed. Masini et al. [130] observed that the turnover frequency was higher for 10 nm Ru NPs than for 4 nm NPs confirming the structure-sensitivity of the methanation reaction. According to them, larger Ru NPs exhibit a higher concentration of under-coordinated sites (*e.g.* kinks or steps) which are reported to be needed for the improvement of the CO bond dissociation since the latter only takes place on these specific sites [131]. The high capability for the CO bond cleavage is determinant since the latter is known to be the rate-determining step of the methanation reaction [131,132].

The Ru/C catalysts were characterized by  $\text{N}_2$ -physisorption after CSCWG (see Table 3.22). Although some slight changes of the porosity were noted after 50 h, the physical structure of the catalysts was well preserved. These results are relevant because they confirm the high stability as well as the robustness of the physical structure of the carbon support during CSCWG. The micropore volume of the spent 4% Ru/C increased to twice the value of the fresh catalyst. A similar result was reported in section 3.4. Up to now there is no good explanation for such a large increase but it is likely that the washing out of some dust from the pores may open some additional micropores, since the carbon support of the 4% Ru/C was not pre-treated.

**Table 3.22.** Physical structure of the fresh and spent Ru/C catalysts.

Catalyst	Time h	BET SSA $\text{m}^2 \text{g}^{-1}$	$V_{\text{total}}$ $\text{cm}^3 \text{g}^{-1}$	$V_{\text{mesop.}}$ $\text{cm}^3 \text{g}^{-1}$	$V_{\text{microp.}}$ $\text{cm}^3 \text{g}^{-1}$
4% Ru/C	0	551	0.67	0.59	0.08
	50	712	0.72	0.57	0.15
4% Ru/ $\text{C}_{\text{HNO}_3}$	0	728	0.70	0.56	0.14
	50	693	0.72	0.60	0.12
4% Ru/ $\text{C}_{\text{HT}}$	0	646	0.61	0.49	0.12
	50	680	0.64	0.51	0.13

In Figure 3.23, three distinct CO<sub>2</sub> desorption peaks were observed for the three spent catalysts. Although these peaks look relatively similar, some differences in their intensity and desorption temperature appear. For instance, the intensity of the first desorption peak (270-290 °C) increases in the following order: 4% Ru/C<sub>HNO3</sub> > 4% Ru/C<sub>HT</sub> > 4% Ru/C, while the opposite is observed for the desorption peak at 460 °C. Interestingly, the CO<sub>2</sub> desorption peak at high temperature is shifted to higher temperature for the 4% Ru/C<sub>HT</sub> (580 °C) in comparison to the two other catalysts (530 °C). In Figure 3.24, a similar trend was observed for the 4% Ru/C<sub>HT</sub> since the CO desorption started at 580 °C while for the other catalysts the latter began at 530 °C. At the moment it is not clear what this desorption peak corresponds to. It may be either some CO<sub>2</sub>/CO species bonded on the Ru surface or even some functional groups in the vicinity of Ru. These peaks might be related to the CO<sub>2</sub>/CO desorption from different Ru active sites. In fact, each catalyst exhibits specific active sites according to its Ru NPs size distribution.

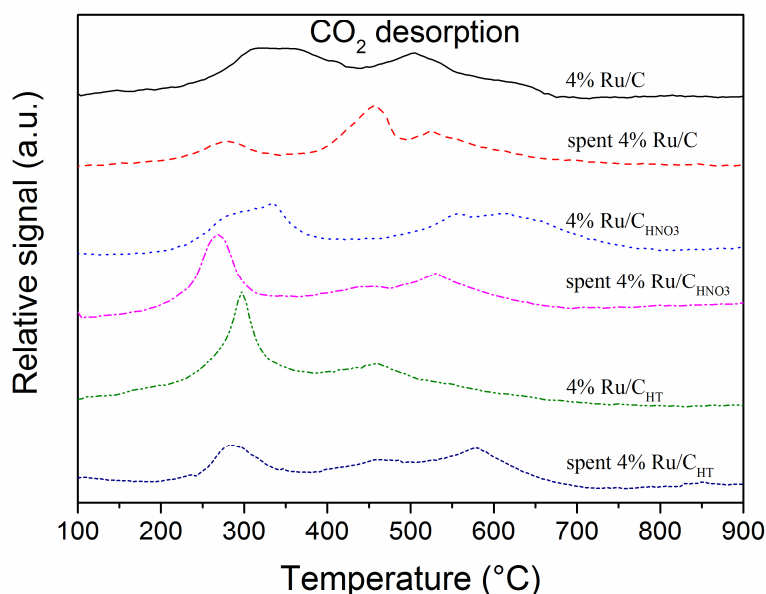


**Figure 3.23.** CO<sub>2</sub>-TPD analysis of the fresh and spent catalysts.

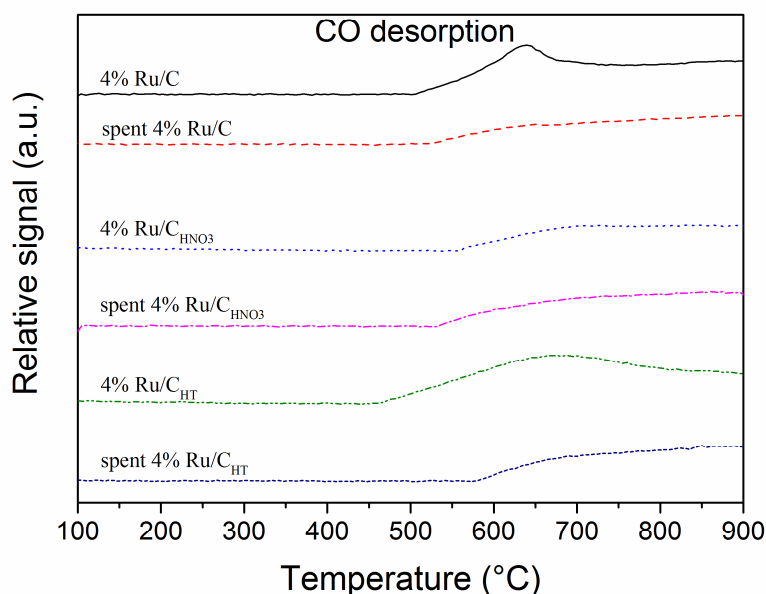


**Figure 3.24.** CO-TPD analysis of the fresh and spent catalysts.

It is also interesting to discuss the TPD spectra of the fresh Ru/C catalysts. It seems that the Ru incorporation on the carbon support followed by the reduction treatment have both considerably changed the carbon surface functionality (compare with Figure 3.18). For instance, for the 4% Ru/C, three CO<sub>2</sub> desorption peaks at 310 °C, 370 °C, and 510 °C are observed, whereas for the fresh C only one desorption peak at 700 °C are detected. The same observation can be done for the CO desorption peak at 640 °C since the CO desorption occurred above 830 °C for the fresh C. It seems likely that the presence of Ru and the reduction treatment are both responsible for this shift to lower temperatures. The desorption of the surface functional groups in the vicinity of the Ru NPs are certainly influenced and facilitated by the interaction with Ru. The similarity of the CO<sub>2</sub> desorption peaks for the 4% Ru/C<sub>HNO3</sub> with the 4% Ru/C indicates that the carboxylic groups were removed during the reduction treatment. This is a relevant observation confirming that prior to CSCWG the carboxylic groups were fully decomposed. Consequently, it seems unlikely that the lower catalytic activity for the 4% Ru/C<sub>HNO3</sub> was due to a change of the carbon surface acidity but rather due to the formation of smaller Ru NPs exhibiting less under-coordinated sites with the HNO<sub>3</sub> pre-treatment.

### 3.6 Comparison of the performance of Ru catalysts supported on carbon and different metal oxides

In this section, the catalytic performance of Ru catalysts supported on carbon and metal oxides are compared. Only the metal oxide supports reported to be stable at SCW conditions such as *rutile*-TiO<sub>2</sub>, *monoclinic*-ZrO<sub>2</sub> and  $\alpha$ -Al<sub>2</sub>O<sub>3</sub> were used for the study [13,64,69]. All the catalysts tested were prepared with the same salt precursor (Ru(NO)(NO<sub>3</sub>)<sub>3</sub>). In addition to the Ru catalysts supported on metal oxides, the catalytic performance of our standard commercial catalyst (2% Ru/C<sub>BASF</sub>) is compared as well.

In Table 3.23, the characteristics of the supported Ru catalysts are listed. The BET SSA of the metal oxide catalysts was smaller than the one of the Ru catalysts supported on carbon. It seems that a higher BET specific surface area favors a higher Ru dispersion. Although the BET SSA of the Ru/ZrO<sub>2</sub> was significantly smaller than the one of Ru/C catalysts, its Ru dispersion was still high. This result demonstrates that a relatively small BET SSA of  $\sim 20 \text{ m}^2 \text{ g}^{-1}$  was already large enough for achieving highly dispersed Ru nanoparticles by a wet impregnation method. As no information was provided by the manufacturer concerning the preparation method of the 2% Ru/C<sub>BASF</sub>, no reason explaining its lower Ru dispersion compared to the 2% Ru/C<sub>nitro</sub> can be provided.

**Table 3.23.** Characteristics of the fresh supported Ru catalysts.

Catalyst	BET SSA $\text{m}^2 \text{ g}^{-1}$	D <sub>CO</sub> - <sup>a</sup>	d <sub>p,CO</sub> $\text{nm}^a$
2% Ru/TiO <sub>2</sub>	4	0.08	16.3
1% Ru/ZrO <sub>2</sub>	23	0.52	1.9
1% Ru/Al <sub>2</sub> O <sub>3</sub>	5	0.06	23.3
2% Ru/C <sub>nitro</sub>	653	0.61	1.6
2% Ru/C <sub>BASF</sub>	1271	0.41	3.0

[a] Determined by CO pulse chemisorption.

Figure 3.25 shows the catalytic performance of the supported Ru catalysts during CSCWG of 10 wt % IPA (450 °C, 30 MPa) over a period of 50 h. In order to operate at carbon conversions below 100%, a high WHSV<sub>gRu</sub> was used. For the Ru/C<sub>nitro</sub> catalyst, this space velocity was still too low to reach incomplete conversion but it was at the limit of our setup. The stability of the catalysts decreased in the following order: Ru/C<sub>nitro</sub> > Ru/ZrO<sub>2</sub> > Ru/Al<sub>2</sub>O<sub>3</sub>  $\approx$  Ru/TiO<sub>2</sub> > Ru/C<sub>BASF</sub>. Although the initial activity of all the Ru catalysts supported on metal oxides was similar, depending on the type of metal oxide, the difference of the activity loss was considerable. For instance, the Ru/TiO<sub>2</sub> and the

Ru/Al<sub>2</sub>O<sub>3</sub> lost ca. 25% and 14% of their initial activity, respectively, during the first 5 h, whereas the Ru/ZrO<sub>2</sub> lost only ca. 7%. The better stability of the Ru/ZrO<sub>2</sub> might be due to a higher gasification rate compared to the coke formation rate. In contrast, after 50 h the stability of the Ru/C<sub>nitro</sub> remained almost unaffected. Such a good stability can be explained by the high capacity of the small Ru NPs for fully converting IPA to gaseous products at such a high WHSV<sub>gRu</sub>. In fact, it is known that a high Ru dispersion is needed for achieving a high activity during CSCWG of IPA. Our standard commercial catalyst exhibited the poorest stability showing that a systematic study of the synthesis factors considerably improved the performance of Ru/C catalysts.

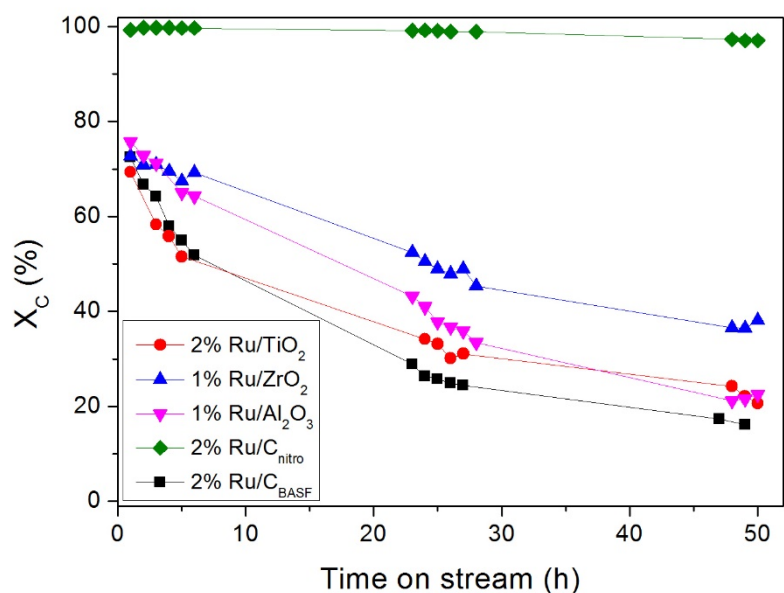


**Figure 3.25.** CSCWG of 10 wt % over Ru catalysts supported on carbon and metal oxides at 450 °C and 30 MPa for 50 h with WHSV<sub>gRu</sub> = 5202 g<sub>Org</sub> g<sub>Ru</sub><sup>-1</sup> h<sup>-1</sup> (exp. CS7, CS8, CS14, CS15, and CS16).

In Table 3.24, the gas composition confirms the good catalytic performance of Ru/C<sub>nitro</sub> since the CH<sub>4</sub> concentration was close to the thermodynamic chemical equilibrium. The lower CH<sub>4</sub> and higher H<sub>2</sub> concentrations for the others Ru catalysts reveal that the methanation reaction was less favored, due to a decreased rate for C-O bond cleavage. Since no CO was detected, it seems that the WGS reaction was still favored at a low X<sub>c</sub>. Interestingly, the GE<sub>c</sub> values were smaller than X<sub>c</sub> values indicating a carbon accumulation. Hence, coke deposition from the decomposition of IPA on the catalyst support surface seems to take place for the tested Ru catalysts. According to the GE<sub>c</sub> and X<sub>c</sub> values for the Ru/Al<sub>2</sub>O<sub>3</sub>, no coking occurred. As GE<sub>c</sub> was calculated based on the gas flow rate, some inaccuracies caused by gas accumulation inside the setup might occur, explaining the difficulty for the



coke quantification of the Ru/Al<sub>2</sub>O<sub>3</sub>. Moreover, due its low BET SSA, a lower coke extent can be expected since less surface is available to decompose IPA to coke. Therefore rendering more difficult to quantify the coke accumulation.

**Table 3.24.** Results of the CSCWG of 10 wt % IPA for Ru supported catalysts performed at 450 °C, 30 MPa with  $WHSV_{gRu} = 5202 \text{ g}_{org} \text{ g}_{Ru}^{-1} \text{ h}^{-1}$ .

Exp.	Catalyst	Time h	X <sub>c</sub> %	GE <sub>c</sub> %	R <sub>Coke dep.</sub> mmol C min <sup>-1</sup>	Gas composition, vol %					
						CH <sub>4</sub>	CO <sub>2</sub>	H <sub>2</sub>	CO	C <sub>2</sub> H <sub>6</sub>	C <sub>3</sub> H <sub>x</sub>
CS14	2% Ru/TiO <sub>2</sub>	50	21	14	1.3	46.1	18.5	35.4	< 0.1	< 0.1	0.3
CS15	1% Ru/ZrO <sub>2</sub>	50	38	27	1.4	48.2	21.0	30.7	< 0.1	< 0.1	0.4
CS16	1% Ru/Al <sub>2</sub> O <sub>3</sub>	50	22	22	≈ 0.0	43.5	18.0	38.5	< 0.1	< 0.1	< 0.1
CS7	2% Ru/C <sub>nitro</sub>	50	97	87	1.6	64.9	20.8	14.3	< 0.1	< 0.1	< 0.1
CS8	2% Ru/C <sub>BASF</sub>	50	16	5	2.6	25.4	12.6	62.0	< 0.1	< 0.1	< 0.1

In Figure 3.26, the CO<sub>2</sub>-TPO results of the fresh and spent Ru catalysts supported on metal oxides confirm that coke formation occurred during CSCWG of IPA since CO<sub>2</sub> desorption peaks were observed on the spent catalysts. The higher peak intensity for the Ru/TiO<sub>2</sub> and Ru/Al<sub>2</sub>O<sub>3</sub> in comparison to the Ru/ZrO<sub>2</sub> confirms the better coking resistance of the latter. The different CO<sub>2</sub> desorption peaks are likely related to the desorption of carbonaceous species located on the Ru surface and the catalyst support.

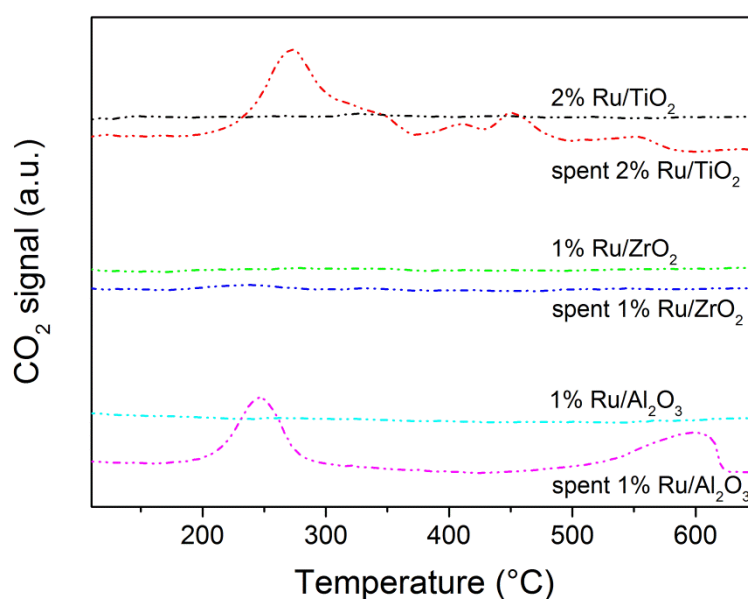


**Figure 3.26.** CO<sub>2</sub>-TPO of the fresh and spent metal oxides supported Ru catalysts.

As the coke deposits cannot be characterized by CO<sub>2</sub>-TPO for the Ru/C catalysts due to the combustion of the carbon support itself, the latter were characterized by N<sub>2</sub>-physisorption. In Table 3.25, it can be seen that the physical structure of the Ru/C<sub>nitro</sub> was well preserved after 50 h on-stream. Although a small fraction of the mesopore volume was lost, likely caused by coke deposits, the total pore volume remained high. This observation suggests that the amount of coke inside the pores is low. By contrast, the considerable loss of the porosity for the 2% Ru/C<sub>BASF</sub> reveals a high amount of coke deposits.

**Table 3.25.** Physical structure of the fresh and spent Ru/C catalysts.

Catalyst	Time h	BET SSA m <sup>2</sup> g <sup>-1</sup>	V <sub>mesop.</sub> cm <sup>3</sup> g <sup>-1</sup>	V <sub>microp.</sub> cm <sup>3</sup> g <sup>-1</sup>
2% Ru/C <sub>nitro</sub>	0	653	0.58	0.12
	50	670	0.53	0.13
2% Ru/C <sub>BASF</sub>	0	1271	0.18	0.44
	50	225	0.10	0.05

In Figure 3.27, the X-ray diffractograms of the fresh and spent Ru catalysts supported on metal oxides reveal the good stability of their crystal structure since the diffractograms of the spent catalysts were similar to the fresh catalysts. Thereby, the deactivation of the catalyst could not be due to a collapsing of their crystal structure. These results also demonstrate the robustness of such metal oxides material in SCW environment. Note that the small diffraction peaks at 28.1 ° and 35.1 ° for the Ru/TiO<sub>2</sub> and Ru/Al<sub>2</sub>O<sub>3</sub> can be attributed to RuO<sub>2</sub> [153,154]. These peaks indicate that the Ru NPs size was above 5 nm since XRD is not able to detect small Ru NPs (< 5 nm) [155]. By using the Scherrer equation, a Ru NPs size of 15 nm and 28 nm for the Ru/Al<sub>2</sub>O<sub>3</sub> and spent Ru/Al<sub>2</sub>O<sub>3</sub> was calculated. Hence, it seems that Ru sintering took place for the Ru/Al<sub>2</sub>O<sub>3</sub>. However, due to the low intensity of the diffraction peak (28.1 °), some inaccuracies may occur explaining the difference with the Ru NPs size determined with CO chemisorption. Unfortunately, the Ru NPs size of Ru/TiO<sub>2</sub> could not be calculated due to an overlapping of the diffraction peaks.

In Figure 3.28, the absence of diffraction peaks for the fresh and spent Ru/C<sub>nitro</sub> catalysts at Bragg angles of 28.1 °, 35.1 °, 38.4 °, 42.1 °, 44.0 °, 54.3 °, 58.3 °, 69.4 ° and 78.3 ° reveals that RuO<sub>2</sub> and reduced Ru NPs were very small [153]. The observed diffraction peaks can be attributed to the activated carbon support itself. Note that the diffraction peak at 26.6 ° is reported to be caused by the partly graphitized structure of carbon support [156,157]. The other diffraction peaks were likely due

to the presence of impurities (*e.g.* ash) having a certain crystallinity. Interestingly, most of the diffraction peaks disappeared after CSCWG suggesting that the harsh conditions of SCW modified the graphitization degree of the carbon support and washed out some impurities.

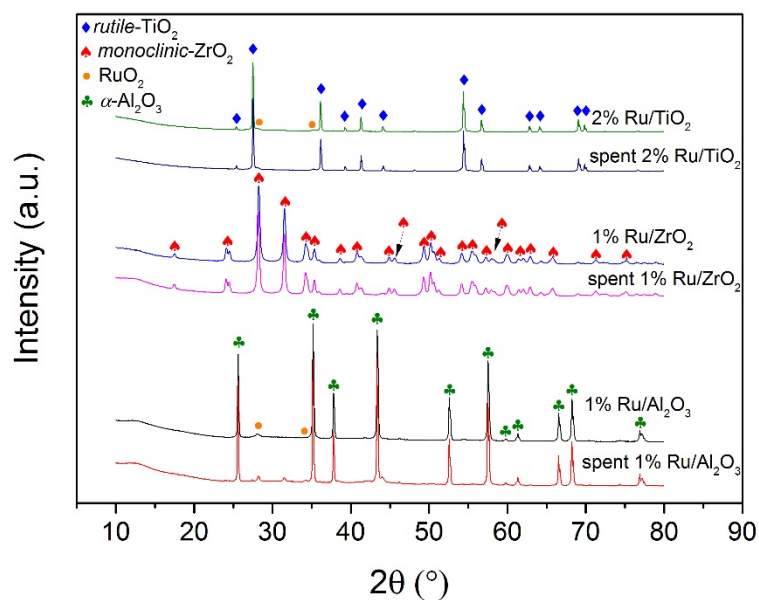


**Figure 3.27.** X-ray diffractograms of the fresh and spent Ru catalysts supported on metal oxides.

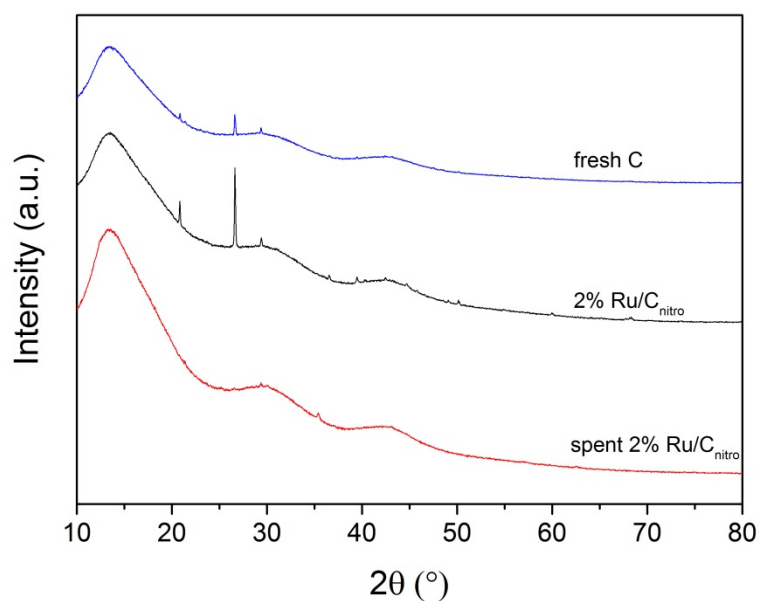


**Figure 3.28.** X-ray diffractograms of the carbon support, fresh and spent Ru/C catalysts.

### 3.7 Summary

In this chapter, the catalytic performance of Ru/C catalysts was assessed with 10 wt % IPA at 450 °C and 30 MPa in a fixed-bed PFR. The results have shown:

- A high stability of the physical structure of the carbon support in SCW conditions (420 °C, 35 MPa) demonstrating its good potential to be used as a catalyst support for CSCWG.
- In absence of Ru, IPA decomposes to solid carbon (coke) and H<sub>2</sub> over the carbon support leading to a complete loss of the microporosity.
- The good catalytic performance of a Ru/C catalyst during CSCWG of IPA under industrial conditions ( $X_c = 100\%$ ) over a period of 96 h at a relatively low  $WHSV_{gRu}$  (1228 g<sub>Org</sub> g<sub>Ru</sub><sup>-1</sup> h<sup>-1</sup>). The gas composition was close to the thermodynamic chemical equilibrium with no noticeable coke deposition. The physical structure of the catalyst was well preserved after this long period on stream proving its robustness.
- At a high  $WHSV_{gRu}$  (5202 g<sub>Org</sub> g<sub>Ru</sub><sup>-1</sup> h<sup>-1</sup>) a progressive deactivation of the catalyst was observed. The cause was the decomposition of IPA to coke over the carbon surface that progressively filled up the pores of the activated carbon resulting in a covering of the Ru NPs. Coking has been confirmed by N<sub>2</sub>-physisorption and by H<sub>2</sub>-TPR analysis of the spent catalyst. HAADF-STEM analysis showed only a slight increase of the Ru NPs size, excluding any deactivation due to sintering.
- The Ru dispersion was found to be a relevant factor for the improvement of the catalytic activity since the 0.5% Ru/C<sub>w</sub> ( $D = 0.26$ ) was more active than the 2% Ru/C<sub>w</sub> ( $D = 0.14$ ).
- When the catalyst was prepared with acetone (2% Ru/C<sub>a</sub>) instead of water (2% Ru/C<sub>w</sub>), the Ru dispersion was significantly improved. HAADF-STEM measurements revealed a smaller Ru NPs size and a narrower size distribution for the 2% Ru/C<sub>a</sub>. XPS analysis showed that the concentration of the residual chloride coming from the Ru salt precursor (RuCl<sub>3</sub>) was much lower on the 2% Ru/C<sub>a</sub>. Consequently, the catalytic activity of the 2% Ru/C<sub>a</sub> was higher than the 2% Ru/C<sub>w</sub>.
- The catalytic performance of a catalyst prepared with a chloride free salt precursor Ru(NO)(NO<sub>3</sub>)<sub>3</sub> (2% Ru/C<sub>nitro</sub>) was much higher than the catalyst prepared with RuCl<sub>3</sub>·xH<sub>2</sub>O

(2% Ru/C<sub>a</sub>). The Ru dispersion measured by CO pulse chemisorption was ca. 6 times higher for the 2% Ru/C<sub>nitro</sub>. The absence of residual chloride greatly facilitated the CO adsorption on the Ru surface resulting in a better performance of the methanation reaction.

- The effect of the Ru loading was found to be a critical parameter for the improvement of the catalyst stability. In fact, a high Ru loading is needed for minimizing the carbon deposition caused by the decomposition of IPA over the carbon surface. As a result, the stability of a 5% Ru/C<sub>BASF</sub> was much higher than the one of a 2% Ru/C<sub>BASF</sub>.
- The surface functional groups added by pre-treating the carbon support with HNO<sub>3</sub> were needed during the catalyst preparation for the improvement of the Ru dispersion. In fact, the carboxylic groups play a relevant role as anchoring groups for the Ru salt precursor. However, during CSCWG of IPA, the latter did not improve the catalytic performance.
- The catalytic performance of a Ru/C<sub>nitro</sub> catalyst was compared with other Ru catalysts supported on metal oxides (Ru/TiO<sub>2</sub>, Ru/ZrO<sub>2</sub>, and Ru/Al<sub>2</sub>O<sub>3</sub>) over a period of 50 h. The stability of the catalysts decreased in the following order: Ru/C<sub>nitro</sub> > Ru/ZrO<sub>2</sub> > Ru/Al<sub>2</sub>O<sub>3</sub> ≈ Ru/TiO<sub>2</sub>. The better performance of the Ru/C<sub>nitro</sub> was due to the high capacity of the small Ru NPs for fully converting IPA to gaseous products. The CO<sub>2</sub>-TPD measurements confirmed the presence of carbon deposits on the spent metal oxides supported Ru catalysts proving that coking was responsible for the deactivation of the catalyst.
- The 2% Ru/C<sub>nitro</sub> exhibited a much higher catalytic activity and stability over a period of 50 h than our standard commercial catalyst (2% Ru/C<sub>BASF</sub>).

## Chapter 4 Optimization of the Salt Separator

The removal of the minerals contained in microalgae is crucial for maintaining the stability of the process. As discussed in chapter 1 (section 1.8.3), the salts were identified to be problematic for the equipment (*e.g.* corrosion, plugging) and for the catalyst (*e.g.* physical blockage of the pores, irreversible poisoning by inorganic sulfur). In this chapter, the performance of the salt separator of KONTI-2 is first evaluated by performing some experiments with model salt solutions ( $\text{Na}_2\text{SO}_4/\text{K}_2\text{SO}_4$  in  $\text{H}_2\text{O}$ ,  $\text{Na}_2\text{SO}_4/\text{K}_2\text{SO}_4$  in 10 wt % IPA). Secondly, these experiments are repeated with a new configuration of the salt separator.

### 4.1 Performance of the salt separator

In Figure 4.1, a sketch of the salt separator of KONTI-2 is depicted. The feed enters from the top of the salt separator where it is super-heated at 450 °C. At these conditions, due to their low solubility, the salts precipitate. The main fraction of the feed leaves the salt separator at the top prior entering the catalytic reactor. At the bottom of the salt separator, the salts are continuously withdrawn via the brine effluent.

The process parameters of the salt separation experiments of a type 2-type 2 ternary mixture ( $\text{Na}_2\text{SO}_4/\text{K}_2\text{SO}_4$ ) are listed in Table 4.1.

**Table 4.1.** Process parameters of the salt separation experiments of a ternary mixture ( $\text{Na}_2\text{SO}_4\text{-K}_2\text{SO}_4$ ) performed in the salt separator of KONTI-2.

Exp.	Salt 1	Salt 2	$C_{\text{Salt 1}}$ $\text{mol kg}^{-1}$	$C_{\text{Salt 2}}$ $\text{mol kg}^{-1}$	Solvent	Feed rate $\text{g min}^{-1}$	Liquiflow <sub>Brine</sub> %	$T_{\text{salt top}}$ °C	$T_{\text{salt bottom}}$ °C	P MPa
SP1	$\text{Na}_2\text{SO}_4$	$\text{K}_2\text{SO}_4$	0.1	0.05	$\text{H}_2\text{O}$	$12.9 \pm 0.1$	100	450	450	28
SP2	$\text{Na}_2\text{SO}_4$	$\text{K}_2\text{SO}_4$	0.1	0.05	10 wt % IPA	18 <sup>a</sup>	100	450	450	28

[a] Corresponds to the set value, note that the actual value of the feed rate was not available.

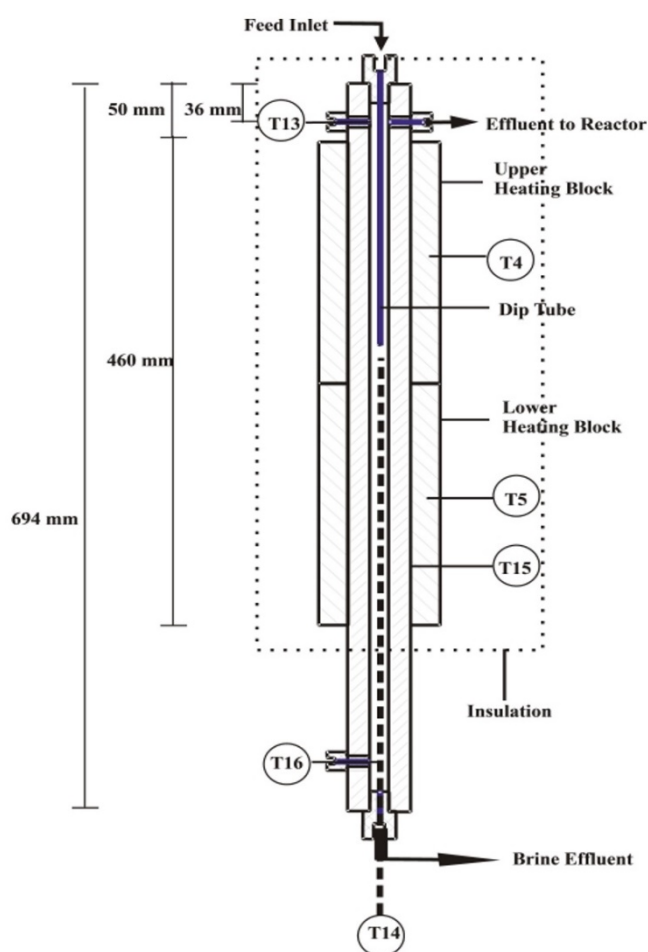


**Figure 4.1.** Sketch of the salt separator of KONTI-2 (taken from [40]).

In Figure 4.2 (a), the results reveal a poor salt separation since the conductivity of the reactor effluent remained relatively high (ca.  $3000\text{--}4500\ \mu\text{S cm}^{-1}$ ). This reflects the difficulty of separating a type 2-type 2 mixture due to its low solubility at SCW conditions. In fact, at these conditions the recovery of type 2 salts is problematic due to their precipitation at the inner surface of the salt separator. Interestingly, it was reported by Schubert [40] that the separation performance of an equal molar  $\text{Na}_2\text{SO}_4/\text{K}_2\text{SO}_4$  was astonishingly satisfactory and very similar to a type 1 mixture. As an explanation, the formation of mixed salts  $\text{Na}_x\text{K}_y\text{SO}_4$  was proposed for such a good salt recovery in the brine effluent. In our case, the higher  $\text{Na}_2\text{SO}_4$  to  $\text{K}_2\text{SO}_4$  molar ratio might be the reason for the low salt recovery. However, Reimer et al. [158] reported a similar type 1 behaviour for the same molar ratio of a  $\text{Na}_2\text{SO}_4/\text{K}_2\text{SO}_4$  mixture by studying the phase behaviour of aqueous salts solution with isochoric high pressure differential scanning calorimetry. As shown in Figure 4.2 (b), relatively high pressure fluctuations were recorded suggesting that salt precipitation took place. As both pressure sensors

exhibited the same fluctuations, the salt precipitation affected the plant up to the backpressure regulator. It is not excluded that these fluctuations were due to a problem of the backpressure regulator itself caused either by the salt deposits or by a malfunction.

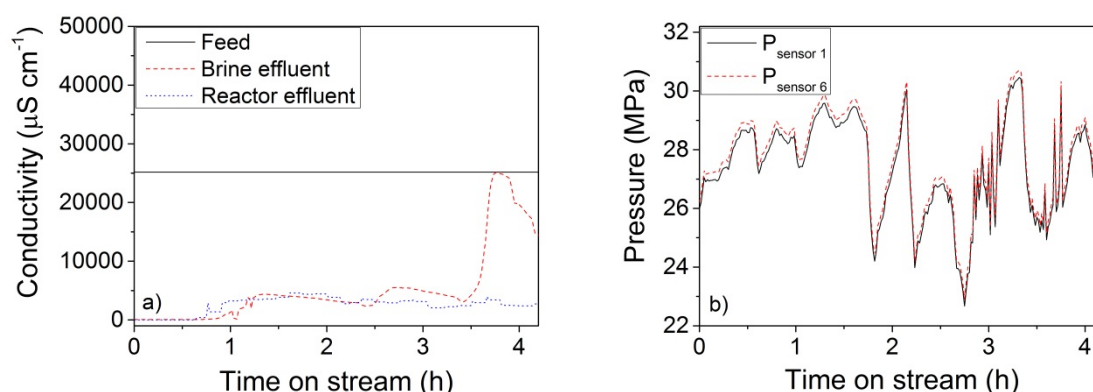


**Figure 4.2.** (a) Evolution of the conductivity of the feed, the brine, and the reactor effluents during the experiment SP1. (b) Pressure profile recorded during the experiment SP1.  $P_{\text{sensor 1}}$  is the pressure sensor located before the salt separator and  $P_{\text{sensor 6}}$  is located after the salt separator.

For the next experiment, the feed has been modified by adding 10 wt % of IPA in order to assess the effect of an organic compound on the separation performance. As illustrated in Figure 4.3 (a), in presence of IPA, the salt separation was found to be even poorer since the conductivity in the reactor effluent increased after 2.5 h up to 16000  $\mu\text{S cm}^{-1}$ . As depicted in Figure 4.3 (b), the pressure was quite stable in comparison to the experiment SP1 suggesting that the salt precipitation was minimized in presence of IPA.

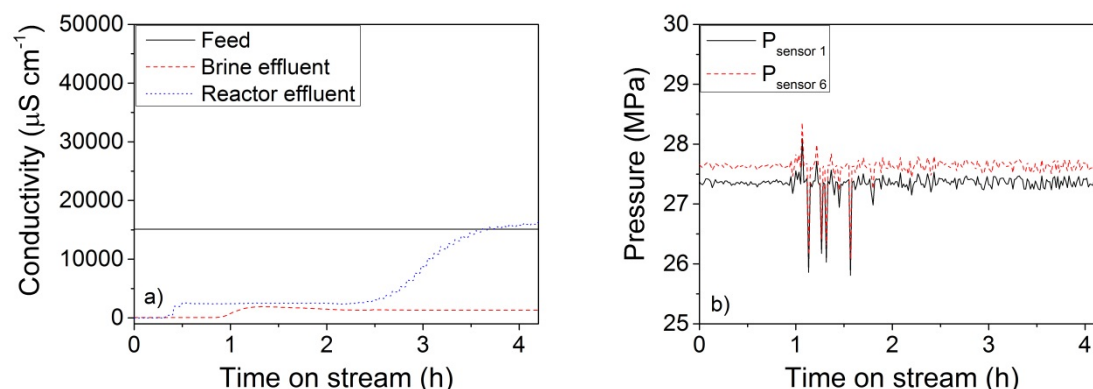


**Figure 4.3.** (a) Evolution of the conductivity of the feed, the brine, and the reactor effluents during the experiment SP2. (b) Pressure profile recorded during the experiment SP2.  $P_{\text{sensor 1}}$  is the pressure sensor located before the salt separator and  $P_{\text{sensor 6}}$  is located after the salt separator.



In Table 4.2, the sulfur concentration of the brine and the reactor effluents was measured off-line by elemental analysis. A good correlation with the conductivity values was observed. The presence of sulfur likely as sulfate, in the reactor effluent shows that the performance of the salt separator is not optimal yet. The higher sulfur concentration in the reactor effluent during the experiment SP2 suggests that IPA negatively affected the separation. Unfortunately, due to a problem encountered with the analytical balances, the feed rate and the mass of flow rate of the brine were not recorded. Consequently, no sulfur mass balance was performed for this experiment. The sulfur recovery of the brine effluent was rather low due the high amount of deposited salts in the process. In fact, salt precipitation at the inner surface of the salt separator was the most likely reason for such a poor sulfur recovery. During the cooling of the process with DI water, a high increase of the conductivity in the brine effluent up  $76500 \mu\text{S cm}^{-1}$  (not presented in Figure 4.2) was recorded confirming that a high concentration of salt was accumulated in the salt separator.

**Table 4.2.** Sulfur mass balance performed during experiment SP1 and SP2 (calculated at time on stream = 4 h).

Exp.	$\dot{m}_{\text{S,Feed}}$ $\text{mg min}^{-1}$	$\dot{m}_{\text{S,Brine}}$ $\text{mg min}^{-1}$	$\dot{m}_{\text{S,Reactor}}$ $\text{mg min}^{-1}$	$\dot{m}_{\text{S,Accumulation}}$ $\text{mg min}^{-1}$	Recovery <sub>S,Brine</sub> %
SP1	$65.8 \pm 2.4$	$10.8 \pm 0.8$	$3.3 \pm 0.1$	$51.8 \pm 2.5$	$16.4 \pm 2.2$
SP2	N.A.	N.A.	$61.6 \pm 4.9$	N.A.	N.A.

## 4.2 New design of the salt separator

As the current configuration of the salt separator was not satisfactory for ensuring a proper salt separation, a new design of the salt separator was proposed by changing the feed entrance from the top to the bottom (see Figure 4.4.) The idea is to operate with a temperature gradient along the salt separator. At the top, the temperature is maximal for ensuring SCW conditions ( $T > 374 \text{ }^{\circ}\text{C}$ ) where the salt solubility is low while the solubility of the non-polar organic compounds is high. Therefore the salts can be precipitated to the bottom by gravity while the organic fraction can be withdrawn at the top. At the bottom, the temperature is settled such a way that a subcritical region ( $T < 374 \text{ }^{\circ}\text{C}$ ) is formed in which the salt solubility is higher. Thereby, the salts can dissolve in the aqueous phase and recover in the brine effluent.

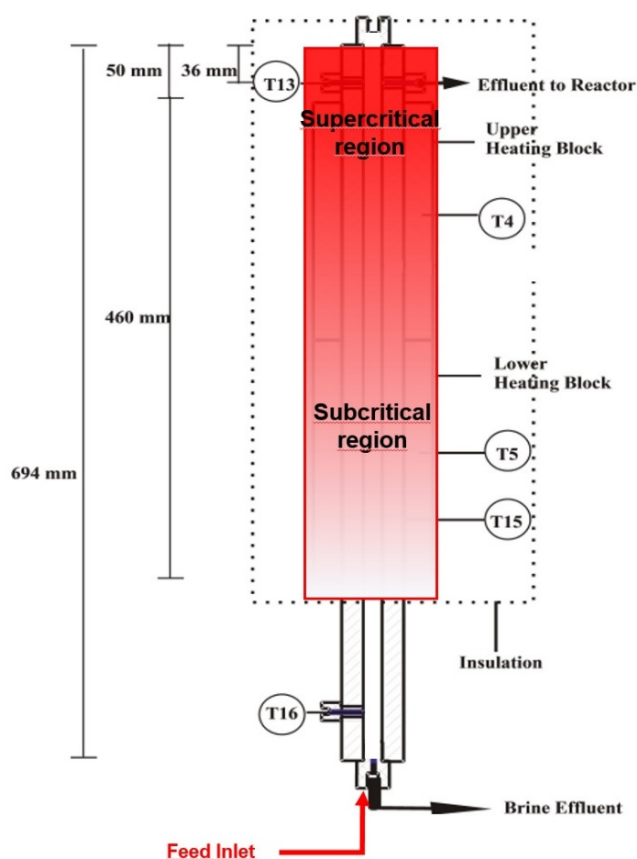


**Figure 4.4.** Sketch of the new configuration of the salt separator of KONTI-2 (adapted from [40]).

The process parameters of the salt separation experiments of a type 2-type 2 ternary mixture ( $\text{Na}_2\text{SO}_4/\text{K}_2\text{SO}_4$ ) are listed in Table 4.3.

**Table 4.3.** Process parameters of the salt separation experiments of a ternary mixture ( $\text{Na}_2\text{SO}_4\text{-K}_2\text{SO}_4$ ) performed with the new design of the salt separator.

Exp.	Salt 1	Salt 2	$C_{\text{Salt 1}}$ $\text{mol kg}^{-1}$	$C_{\text{Salt 2}}$ $\text{mol kg}^{-1}$	Solvent	Feed rate $\text{g min}^{-1}$	Liquiflow <sub>Brine</sub> %	$T_{\text{salt top}}$ $^{\circ}\text{C}$	$T_{\text{salt bottom}}$ $^{\circ}\text{C}$	P MPa
SP3	$\text{Na}_2\text{SO}_4$	$\text{K}_2\text{SO}_4$	0.1	0.05	10 wt % IPA	$14.8 \pm 0.5$	100	450	450	28
SP4	$\text{Na}_2\text{SO}_4$	$\text{K}_2\text{SO}_4$	0.1	0.05	10 wt % IPA	$9.0 \pm 0.2$	100	450	450	28
SP5	$\text{Na}_2\text{SO}_4$	$\text{K}_2\text{SO}_4$	0.05	0.05	10 wt % IPA	$8.9 \pm 0.1$	100/50	450	450	28

As shown in Figure 4.5 (a), the new design was beneficial since the conductivity was maximal in the brine effluent whereas the latter was close to zero in the reactor effluent. Astonishingly, under the same conditions that during the experiments SP1 and SP2, all the salts were properly removed from

the reactor effluent. Although the salt separation was satisfactory, some plugging issues occurred in the salt separator after only 30 min. In fact, the pressure dangerously increased up to 36.6 MPa (see Figure 4.5 (b)). Consequently, the experiment was stopped after 1 h for avoiding any damages to the equipment.

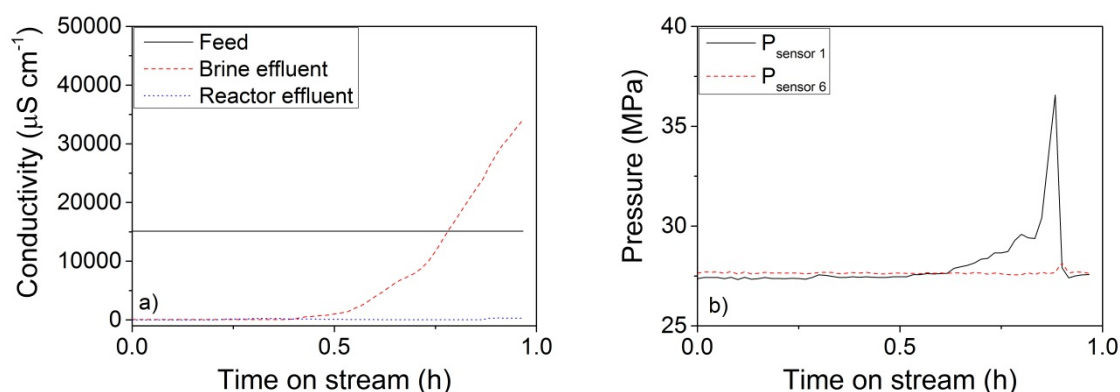


**Figure 4.5.** (a) Evolution of the conductivity of the feed, the brine, and the reactor effluents during the experiment SP3. (b) Pressure profile recorded during the experiment SP3.  $P_{\text{sensor 1}}$  is the pressure sensor located before the salt separator and  $P_{\text{sensor 6}}$  is located after the salt separator.

In order to improve stability of the process, the feed rate was reduced to  $9 \text{ g min}^{-1}$  for decreasing the feed velocity inside the salt separator. A lower feed rate may minimize the salt precipitation at the inner surface of the salt separator in the supercritical region since more salts may remain in the subcritical region. As observed in Figure 4.6 (a) and (b), the reduction of the feed rate has notably improved the stability of the process since no pressure increase was recorded. Moreover, no salts were detected in the reactor effluent during all the experiment.

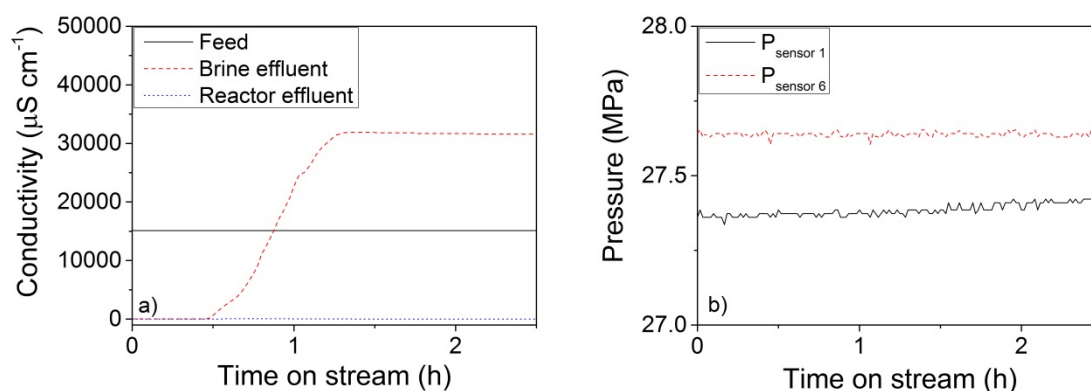


**Figure 4.6.** (a) Evolution of the conductivity of the feed, the brine, and the reactor effluents during the experiment SP4. (b) Pressure profile recorded during the experiment SP4.  $P_{\text{sensor 1}}$  is the pressure sensor located before the salt separator and  $P_{\text{sensor 6}}$  is located after the salt separator.

For the last experiment, the salt solution has been modified in order to have an equal molar mixture of  $\text{Na}_2\text{SO}_4/\text{K}_2\text{SO}_4$ . Such a salt mixture was used and reported by Schubert [40] to behave like a type 1 salt and its recovery in the brine effluent was found to be satisfactory. In Figure 4.7 (a), the high conductivity in the brine effluent demonstrates the high efficiency of the new design. These results reveals that a type 1 salt can be successfully removed from the reactor effluent. By reducing the Liquiflow from 100% to 50% after 5 h, the conductivity almost doubled in the brine effluent. Therefore it seems that the salts can be further concentrated by reducing the Liquiflow. Although some small pressure fluctuations occurred when the Liquiflow was reduced (see Figure 4.7 (b)), the stability of the process was satisfactory during all the experiment.

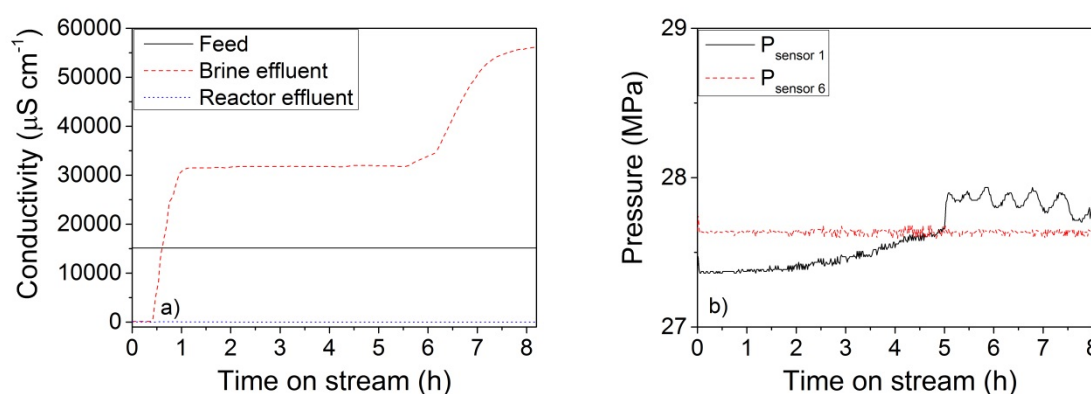


**Figure 4.7.** (a) Evolution of the conductivity of the feed, the brine, and the reactor effluents during the experiment SP5. (b) Pressure profile recorded during the experiment SP5.  $P_{\text{sensor 1}}$  is the pressure sensor located before the salt separator and  $P_{\text{sensor 6}}$  is located after the salt separator.

In Table 4.4, the good performance for the new design of the salt separator are confirmed since almost no sulfur was detected in the reactor effluent (in the detection limits of the CNS elemental analyzer).

**Table 4.4.** Sulfur mass balance performed during the experiments SP3, SP4, and SP5 (calculated at the end of the experiment).

Exp.	$\dot{m}_{\text{S,Feed}}$ $\text{mg min}^{-1}$	$\dot{m}_{\text{S,Brine}}$ $\text{mg min}^{-1}$	$\dot{m}_{\text{S,Reactor}}$ $\text{mg min}^{-1}$	$\dot{m}_{\text{S,Accumulation}}$ $\text{mg min}^{-1}$	Recovery <sub>S,Brine</sub> %
SP3	$75.5 \pm 4.7$	$42.1 \pm 2.6$	$1.0 \pm 0.1$	$32.5 \pm 5.4$	$55.7 \pm 7.1$
SP4	$45.9 \pm 2.3$	$35.1 \pm 1.5$	$0.2 \pm 0.0$	$10.7 \pm 2.8$	$76.4 \pm 7.1$
SP5	$28.3 \pm 0.5$	$34.9 \pm 1.5$	$0.2 \pm 0.0$	$-6.8 \pm 1.6$	$123.3 \pm 7.6$

These results are relevant because they show that the inorganic sulfur can be efficiently removed from the reactor effluent. Consequently, the damages to the catalyst located downstream can be minimized. Although the sulfur recovery of the brine effluent was much higher than the one obtained during the experiment SP1, it seems that salt precipitation also took place but at a lower extent with this new configuration. Interestingly, for the experiment SP5, when the Liquiflow was reduced, a negative salt accumulation was calculated. Such a result was caused by a high amount of salts in the brine effluent. It is likely that the salts were not recovered in the brine at a constant rate, *i.e.* the steady state was not reached.

### 4.3 Summary

In this chapter, continuous salt removal of model salt solutions ( $\text{Na}_2\text{SO}_4/\text{K}_2\text{SO}_4$  in  $\text{H}_2\text{O}$ ,  $\text{Na}_2\text{SO}_4/\text{K}_2\text{SO}_4$  in 10 wt % IPA) was investigated in the salt separator of KONTI-2. The objective was to assess and to optimize the performance of the salt separator. The results are summarized below:

- The performance of the salt separator of KONTI-2 was not satisfactory since the salts were not efficiently removed from the reactor effluent. In presence of IPA, based on the conductivity, the salt concentration in the reactor effluent was higher suggesting that IPA rendered more difficult the salt separation.
- The sulfur recovery of the brine effluent was only 16% for the experiment performed with  $\text{Na}_2\text{SO}_4/\text{K}_2\text{SO}_4$  in  $\text{H}_2\text{O}$ . The reason for such a poor sulfur recovery was caused by the salt precipitation at the inner surface of the salt separator.
- The modification of the design of the salt separator by modifying the configuration of the feed entrance (feeding from the bottom of the salt separator) was crucial for the improvement of the salt separation. In fact, all the salts and the inorganic sulfur were efficiently removed from the reactor effluent and concentrated in the brine effluent.
- The reduction of the feed rate was needed for reducing the pressure fluctuations occurring in the process.
- The Liquiflow is a key parameter for improving the salt recovery in the brine effluent. The reduction of the Liquiflow from 100% to 50% almost doubled the salt concentration in the

brine effluent. However, some pressure fluctuations were observed when reducing the Liquiflow. Hence, the Liquiflow is a sensitive parameter regarding the stability of the process.

- Although some significant improvements were achieved with the new design, the sulfur recovery of the brine effluent was not 100%.



## Chapter 5 Continuous Sulfur Removal in Supercritical Water Conditions

As discussed in chapter 1 (section 1.8.2), sulfur has a detrimental effect on the catalytic performance of supported Ru catalysts. In order to demonstrate the technical feasibility of the process, there is a necessity for removing efficiently sulfur prior to CSCWG. For this purpose, in this section, the stability and the sulfur adsorption performance of a commercial ZnO adsorbent (*Katalco 32-5*) under SCW conditions are evaluated.

Some of the results were obtained in the frame of a master thesis (Markus Roth) [159] performed in our group under my supervision during my doctoral studies. His contribution can be found in section 5.1, 5.2, 5.3, and 5.4.

### 5.1 Characteristics of the ZnO adsorbent (*Katalco 32-5*)

The information provided by the manufacturer regarding the physical properties and the chemical composition of the adsorbent are listed in Table 5.1. The three components are ZnO with a small amount of aluminum oxide and calcium oxide. According to the manufacturer, these two metal oxides are used as cement to bind the ZnO particles.

**Table 5.1.** Physical properties and chemical composition of the ZnO adsorbent.

Density kg m <sup>-3</sup>	d <sub>p</sub> mm	Composition, wt %		
		ZnO	Aluminium oxide	Calcium oxide
1350	2.8-4.8	60-100	3-7	3-7

Note that the adsorbent was designed mainly for the purification of syngas (H<sub>2</sub>S removal) at low temperatures.



## 5.2 Stability in SCW

As the ZnO adsorbent was exclusively designed for gas cleaning, there is a need to evaluate its stability in the harsh environment of SCW prior to assessing its sulfur adsorption performance. The stability was assessed in a fixed-bed PFR at 400 °C and 28 MPa over a period of 3 h and 18 h with a feed rate of 3 g min<sup>-1</sup>. After the experiment, the adsorbent was harvested and characterized with N<sub>2</sub>-physisorption and XRD for evaluating the stability of its physical and crystal structure. As it can be seen in Figure 5.1, hardly any change of its visual aspect was observed after 18 h in SCW and its mechanical stability (hardness) was well preserved, too.

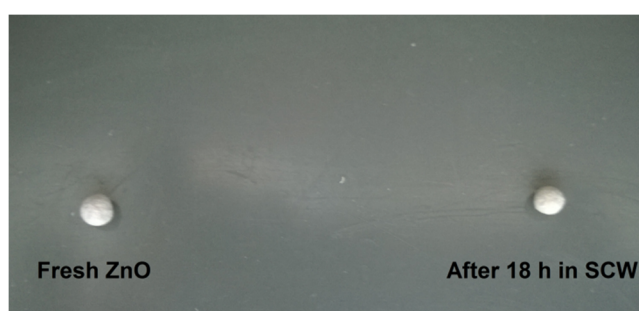


**Figure 5.1.** Visual aspect of the fresh and spent (after 18 h in SCW) adsorbents.

However, as shown in Table 5.2, the physical structure underwent significant change in SCW since the BET SSA and the total pore volume decreased. The collapsing of some pores may explain this loss of porosity. As a result, larger pores were formed. The fact that the pore size was larger after 3 h than after 18 h was not expected and no clear explanation can be provided. Based on the N<sub>2</sub>-physisorption analysis, it is not clear if only the cement-matrix was affected or the ZnO particles as well.

**Table 5.2.** Evolution of the physical structure of the ZnO adsorbent at SCW conditions (400 °C, 28 MPa).

Exp.	Sample	BET SSA m <sup>2</sup> g <sup>-1</sup>	V <sub>total</sub> cm <sup>3</sup> g <sup>-1</sup>	Pore size Å
	Fresh ZnO	23	0.17	151
SA1	After 3 h in SCW	5	0.06	451
SA2	After 18 h in SCW	4	0.05	219

In Figure 5.2, the XRD diffractograms of the fresh and spent adsorbents are depicted. The diffractograms of the fresh adsorbent shows a high crystal structure where ZnO, zinc aluminium carbonate

hydroxide hydrate (ZACHH), aragonite ( $\text{CaCO}_3$ ), and calcite ( $\text{CaCO}_3$ ) were detected. In accord with the manufacturer's description, ZACHH, aragonite, and calcite constitute the cement-matrix whereas ZnO corresponds to the adsorbent itself. Interestingly, following the SCW treatment, only ZnO and calcite were observed. The absence of diffraction peaks for ZACHH and aragonite confirms that these components were transformed to another phase and/or washed out. Parker et al. [160] reported that aragonite was transformed to calcite at 400 °C. Although this study was not performed under SCW conditions, it is likely that aragonite was converted to calcite.

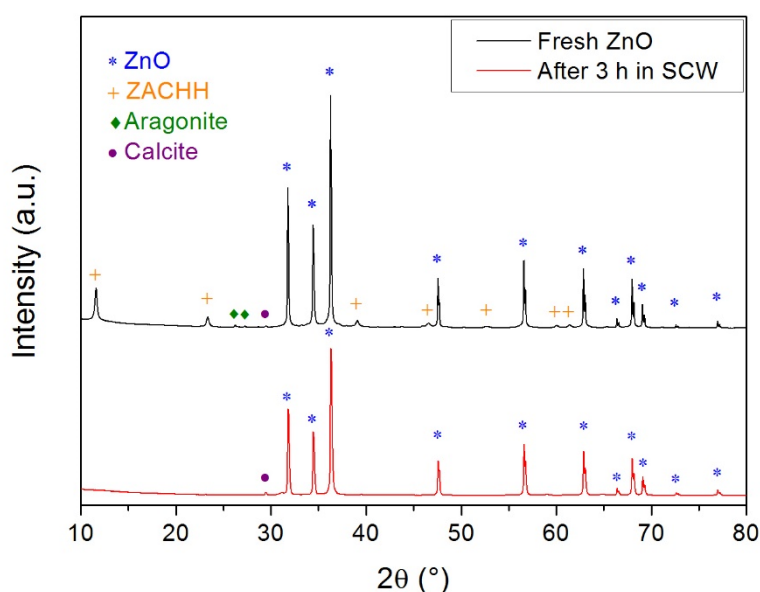
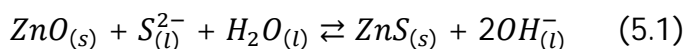


**Figure 5.2.** X-ray diffractograms of the fresh and spent (after 3 h in SCW) adsorbents.

According to the  $\text{N}_2$ -physisorption and the XRD measurements, the crystal structure of ZnO remained stable in SCW while the loss of the porosity was likely due to a collapse of the cement matrix since the crystal structures of ZACHH and aragonite were affected.

### 5.3 Performance of the ZnO adsorbent

Sulfur adsorption experiments were carried out under SCW conditions (400 °C, 30 MPa) with sodium sulfide ( $\text{Na}_2\text{S} \cdot 9\text{H}_2\text{O}$ ) as a model compound. The objective is to assess the performance of ZnO for continuous removal of reduced sulfur. The following sulfidation reaction takes place ( $\text{pH} > 10$ ):



The capability of ZnO for removing sulfur under SCW conditions (400 °C, 30 MPa) was already reported during conversion of bitumen [161]. Recently, Ates et al. [162] investigated the performance of ZnO during desulfurization of hexyl sulfide in hexadecane (400 °C, 25 MPa). They found that 62% of the surface was converted to ZnS demonstrating the good potential of ZnO as a sulfur adsorbent.

In Table 5.3, the process parameters of the sulfur adsorption experiments are listed.

**Table 5.3.** Process parameters of the sulfur adsorption experiments performed in PFR.

Exp.	Feed	pH	$C_{\text{Sulfur, feed}}$ $\text{mg L}^{-1\text{a}}$	$m_{\text{ZnO}}$ g	Feed rate $\text{g min}^{-1}$	T °C	P MPa
SA3	4 mM $\text{Na}_2\text{S}\cdot 9\text{H}_2\text{O}$	10.5	127	-	3	400	30
SA4	4 mM $\text{Na}_2\text{S}\cdot 9\text{H}_2\text{O}$	10.5	133	2	3	400	30
SA5	4 mM $\text{Na}_2\text{S}\cdot 9\text{H}_2\text{O}$	10.5	120	1	3	400	30
SA6	4 mM $\text{Na}_2\text{S}\cdot 9\text{H}_2\text{O}$ + 10 wt % IPA	10.5	121	1	3	400	30

[a] Determined with ICP-OES.

As shown in Figure 5.3, in absence of ZnO, sulfur reached the feed concentration in 1 h. This first blank experiment confirmed that sulfur was hardly adsorbed in the reactor setup. However, in presence of ZnO, sulfur was adsorbed by the adsorbent proving its good potential for removing sulfur. Even by adding 10 wt % of IPA, the sulfur adsorption capacity of ZnO was not affected in presence of an organic compound. The fact that sulfur was not fully adsorbed and that its concentration increased progressively, was likely due to the low ratio between the reactor diameter ( $d_{\text{reactor}} = 8.0$  mm) and the particle diameter ( $d_p = 2.8\text{-}4.8$  mm). The calculated ratio was relatively low with a value of 1.7-2.9. Channeling at the reactor wall is reported to be significant for ratio below 30 and mass transfer rates are also reported to be lower in presence of large particles [163].

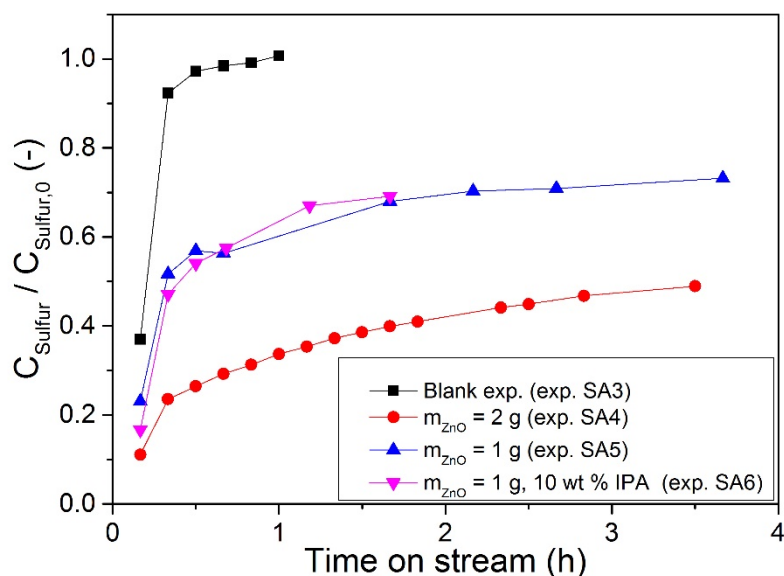


**Figure 5.3.** Sulfur adsorption performance of the ZnO adsorbent with 4 mM  $\text{Na}_2\text{S} \cdot 9\text{H}_2\text{O}$  at 400 °C and 30 MPa.

As the adsorbent was used as received for CSCWG of microalgae performed in KONTI-C (see chapter 6 and 7), it was decided to assess its performance without any modification of the latter (*e.g.* crushing).

After the experiment, the adsorbent was harvested and analyzed by sulfur elemental analysis,  $\text{N}_2$ -physisorption, and XRD. In Figure 5.4, it can be seen that some change of its visual aspect occurred since the surface of the particle was covered by a thin grey layer. Thus, it seems that some chemical modifications on the surface took place.

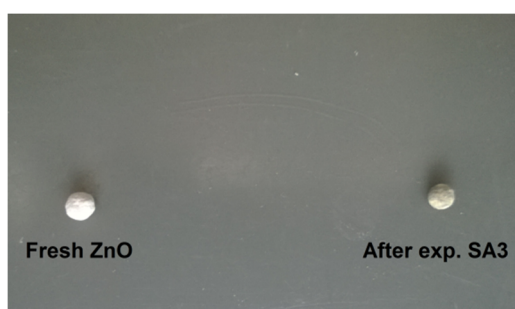


**Figure 5.4.** Visual aspect of the fresh and spent adsorbents (after exp. SA3).

As shown in Table 5.4, the BET SSA and the total pore volume were reduced to similar values than those obtained after the treatment in SCW (compare with Table 5.2). Hence, the physical structure

was not affected by the sulfidation reaction itself. According to the sulfur elemental analysis, a considerable amount of sulfur was found on the spent ZnO suggesting that sulfur was adsorbed.

**Table 5.4.** Physical structure and sulfur elemental analysis of the fresh and spent adsorbents (after exp. SA3).

Sample	Time on stream h	BET SSA $\text{m}^2 \text{g}^{-1}$	$V_{\text{total}}$ $\text{cm}^3 \text{g}^{-1}$	Pore size $\text{\AA}$	S wt %
Fresh ZnO	0	23	0.17	151	$0.04 \pm 0.01$
Spent ZnO	3.6	4	0.04	194	$2.84 \pm 0.07$

In Figure 5.5, as confirmed by the XRD measurements, a ZnS phase was formed. This result proves that  $\text{S}^{2-}$  was adsorbed by ZnO to form ZnS. As observed after the SCW treatment, the crystal structures of ZnO and calcite remained unaffected whereas those of ZACHH and aragonite were transformed and/or washed out.

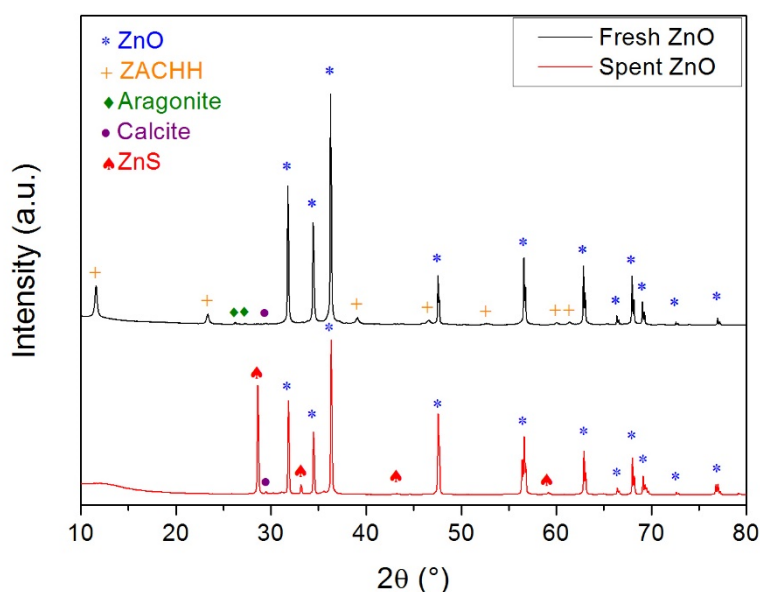


**Figure 5.5.** X-ray diffractogram of the fresh and spent adsorbents (after exp. SA3).

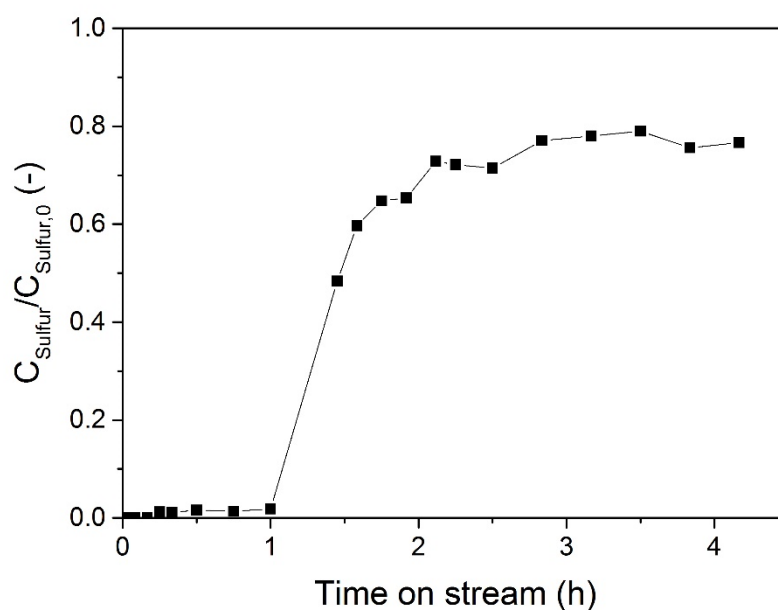
## 5.4 Corrosion

In the frame of M. Roth's master thesis, the corrosion of the reactor was investigated when feeding with  $\text{Na}_2\text{S} \cdot 9\text{H}_2\text{O}$ . Unlike the previous sulfur adsorption experiments, the particle size of the adsorbent was reduced ( $d_p = 0.6 \text{ mm}$ ) in order to minimize the channeling at the reactor wall. As shown in Table 5.5, a higher feed concentration was used resulting in a higher pH value.

**Table 5.5.** Process parameters of the sulfur adsorption experiments performed in PFR.

Exp.	Feed	pH	$C_{\text{Sulfur, feed}}$ $\text{mg L}^{-1\text{a}}$	$m_{\text{ZnO}}$ g	Feed rate $\text{g min}^{-1}$	T $^{\circ}\text{C}$	P MPa
SA7	23 mM $\text{Na}_2\text{S}\cdot 9\text{H}_2\text{O}$	11.5	750	2	3	400	28
SA8	23 mM $\text{Na}_2\text{S}\cdot 9\text{H}_2\text{O}$	11.5	750	2	3	400	28

As depicted in Figure 5.6, unlike previous sulfur experiments, sulfur was fully adsorbed during 1 h. Hence, channeling at the reactor wall was significantly reduced. However, the concentration of the feed was never reached suggesting that sulfur remained in the reactor. By repeating the same experiment (exp. SA8), the breakthrough curve was shifted from 1.5 h to 3.8 h (determined with sulfide papers). The results reveal a low reproducibility of the breakthrough curves when working at a high pH.

**Figure 5.6.** Sulfur adsorption performance of ZnO with 23 mM  $\text{Na}_2\text{S}\cdot 9\text{H}_2\text{O}$  at 400  $^{\circ}\text{C}$  and 28 MPa (exp. SA7).

By opening the reactor after the experiment SA8, the frit was fully decomposed, while the adsorbent formed a hard lump (see Figure 5.7). Consequently, at a high pH,  $\text{Na}_2\text{S}\cdot 9\text{H}_2\text{O}$  was found to be highly corrosive under SCW conditions.



**Figure 5.7.** Left: Frit after experiment SA7. Right: ZnO adsorbent after experiment SA8.

The corrosion of two types of reactor (Inconel 625 and AISI 316L) was also studied. For these experiments, the pH value was reduced and  $\text{Na}_2\text{S}\cdot 9\text{H}_2\text{O}$  has been replaced by  $\text{NaHS}\cdot x\text{H}_2\text{O}$  (lower  $\text{pK}_\text{A}$  value). These experiments were carried out with a PFR having a vertical orientation (KONTI-1) described elsewhere [36,159]. The process parameters are listed in Table 5.6. Note that both experiments were performed solely with an empty reactor.

**Table 5.6.** Process parameters of the sulfur adsorption experiments performed in KONTI-1.

Exp.	Feed	pH	$C_{\text{Sulfur, feed}}$ $\text{mg L}^{-1\text{a}}$	$m_{\text{ZnO}}$ g	Feed rate $\text{g min}^{-1}$	T $^\circ\text{C}$	P MPa
SA9	3 mM $\text{NaHS}\cdot x\text{H}_2\text{O}$	9.0	100	N.A.	5	400	28
SA10	3 mM $\text{NaHS}\cdot x\text{H}_2\text{O}$	9.0	100	N.A.	10	400	28

As it can be seen in Figure 5.8, no sulfur was detected during the whole experiment whereas the electrical conductivity increased above the one of the feed. The conductivity peak observed after 20 min may be caused by the washing out of some elements from the reactor. The production of  $\text{H}_2$  was observed. According to these results, it seems that oxidation of sulfur ( $\text{S}^{2-}$ ) to elemental sulfur was catalyzed by the high Ni content of Inconel 625 (58 wt %). The values of the conductivity above those of the feed suggest that corrosion occurred. By opening the reactor after the experiment, a high amount of black mud was found which could be attributed to corrosion products.

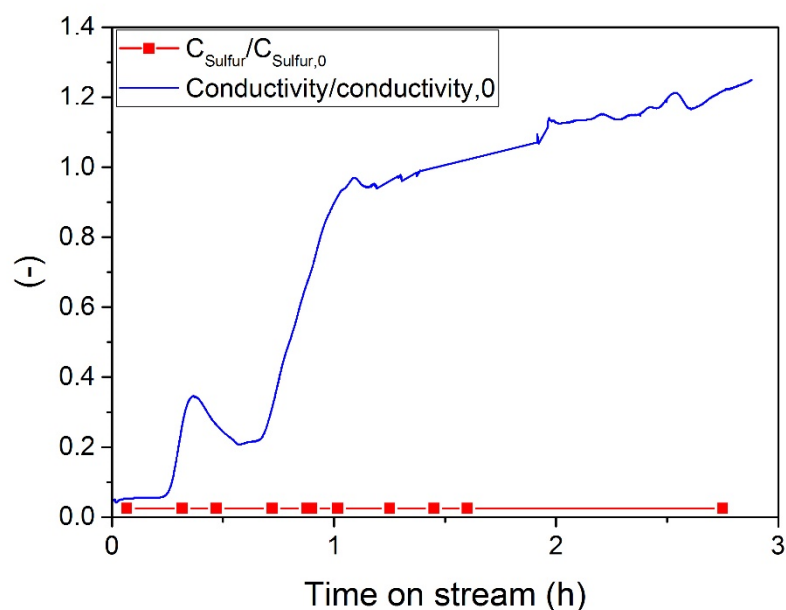


**Figure 5.8.** Evolution of the conductivity and the sulfur concentration when feeding with 3 mM  $\text{NaHS} \cdot x\text{H}_2\text{O}$  (400 °C, 28 MPa) in the Inconel 625 reactor (exp. SA9).

As shown in Figure 5.9, a considerable effect of the type of reactor was observed where both the conductivity and the sulfur concentration followed the same trend and reached similar values to those of the feed. By repeating three runs, where the reactor setup was flushed with DI water between each run, similar breakthrough curves were observed. Hence, AISI 316L which contains a lower Ni content (10-15 wt %) was found to be more appropriated than Inconel 625 for performing sulfur adsorption experiments under SCW conditions. Similarly to the experiment SA9, an inflexion point (at 9.5 min) was recorded during the first run. Its disappearance during the second and the third runs was likely due to aging of the reactor.



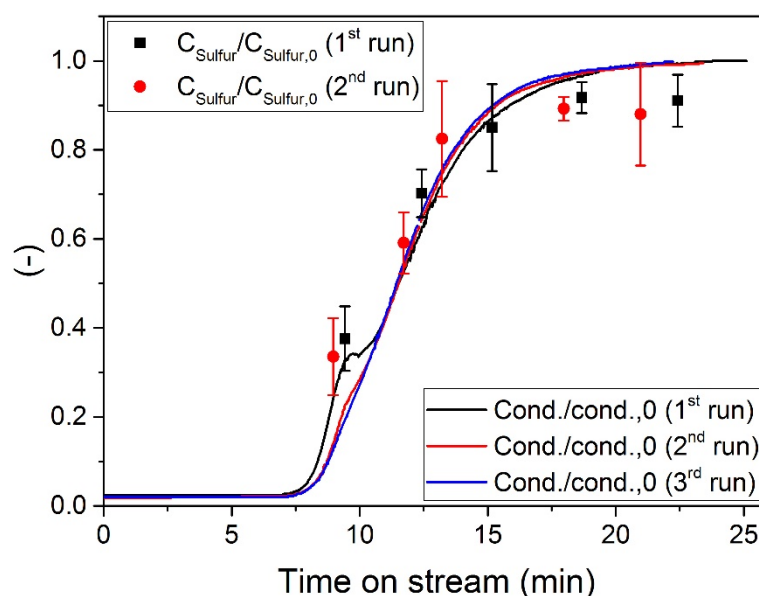


**Figure 5.9.** Evolution of the conductivity and the sulfur concentration when feeding with 3 mM NaHS · xH<sub>2</sub>O (400 °C, 28 MPa) in the AISI 316L reactor (exp. SA10).

## 5.5 Summary

In this chapter, the stability and the sulfur adsorption performance under SCW conditions (400 °C, 30 MPa) of a commercial ZnO adsorbent (*Katalco 32-5*) were studied. The results are summarized below:

- High stability of its mechanical properties (hardness) in SCW.
- The crystal structure of ZnO was stable in SCW while the loss of the porosity was likely due to a collapse of the cement matrix.
- Sulfur adsorption experiments were carried out with Na<sub>2</sub>S·9H<sub>2</sub>O as a model compound. It was found that ZnO was able to remove reduced sulfur (S<sup>2-</sup>) under SCW conditions.
- In presence of 10 wt % IPA, the sulfur adsorption performance of ZnO was not affected showing its capability for removing sulfur even in presence of an organic compound.
- Characterization of the spent ZnO adsorbent with XRD confirmed that ZnS was formed.
- By working at a high pH value (11.5) with Na<sub>2</sub>S·9H<sub>2</sub>O, no reproducibility of the breakthrough curves was observed due to a high corrosion of the adsorbent and the frit.

- The corrosion of two types of reactor (Inconel 625 and AISI 316L) was investigated with  $\text{NaHS} \cdot x\text{H}_2\text{O}$  at a pH of 9. Sulfur ( $\text{S}^{2-}$ ) was found to react with Inconel 625, likely due to its high Ni content. Whereas no reaction of sulfur with AISI 316L occurred suggesting its better suitability for performing sulfur adsorption experiments under SCW conditions.



## Chapter 6 Continuous Liquefaction and Catalytic Supercritical Water Gasification of Microalgae

This chapter presents the results of the continuous liquefaction and CSCWG of microalgae carried out in the new PDU (KONTI-C). The main objective is to get familiar with KONTI-C and to optimize it for the gasification campaign (see chapter 7). The process was developed based on the most promising results obtained in the previous chapters, *i.e.* the use of a catalyst having a higher Ru loading (5% Ru/C<sub>BASF</sub>), a new design of the salt separator, and the use of ZnO (*Katalco 32-5*) as a sulfur adsorbent. Due to the high amount of catalyst needed for the experiments performed with KONTI-C, it was required to use a commercial catalyst instead of the most effective prepared catalyst (2% Ru/C<sub>nitro</sub>). Moreover, in order to reduce pressure drop issues, the ZnO was used as received without crushing it. Prior to processing microalgae, some preliminary experiments with model salt solutions (Na<sub>2</sub>SO<sub>4</sub>/K<sub>2</sub>SO<sub>4</sub>) are carried out for assessing the performance of the new salt separator. Secondly, the stability of the process is evaluated when feeding with microalgae. Then, the catalytic reactor is filled with the ZnO adsorbent in order to determine its stability, sulfur adsorption performance, and catalytic activity. Finally, the catalytic performance of a commercial 5% Ru/C<sub>BASF</sub> catalyst during CSCWG is studied.

Most of the results were obtained in the frame of a master thesis (Jakob Breinl) [111] performed in our group under my supervision during my doctoral studies. His contribution can be found in section 6.1 and 6.2.

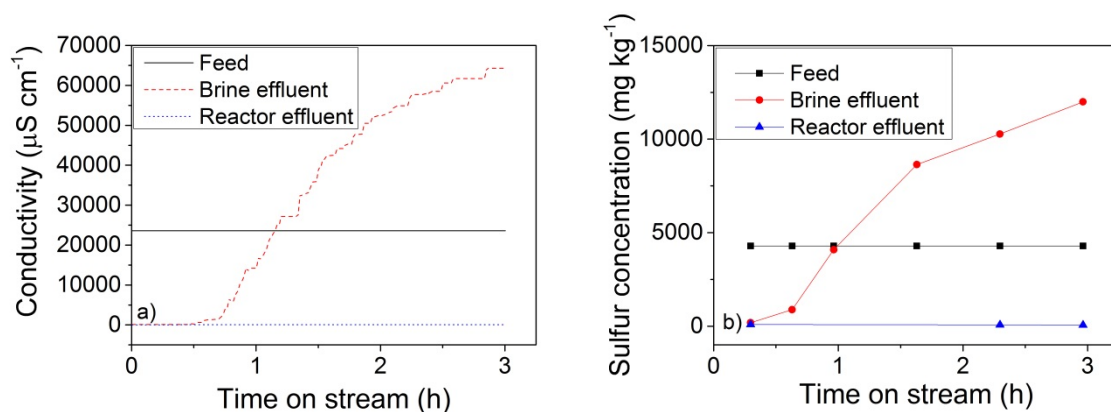
### 6.1 Assessment of the new salt separator with model salt solutions

Like in chapter 4, a similar Na<sub>2</sub>SO<sub>4</sub>/K<sub>2</sub>SO<sub>4</sub> salt solution was used for the preliminary experiments performed in KONTI-C. The process parameters of the salt separation experiments of a type 2-type 2 ternary mixture (Na<sub>2</sub>SO<sub>4</sub>/K<sub>2</sub>SO<sub>4</sub>) are listed in Table 6.1.

**Table 6.1.** Process parameters of the salt separation experiments of a ternary mixture ( $\text{Na}_2\text{SO}_4\text{-K}_2\text{SO}_4$ ) performed with KONTI-C.

Exp.	Salt 1	Salt 2	$C_{\text{Salt 1}}$ $\text{mol kg}^{-1}$	$C_{\text{Salt 2}}$ $\text{mol kg}^{-1}$	Solvent	Feed rate $\text{g min}^{-1}$	Liquiflow <sub>Brine</sub> %	$T_{\text{Salt top}}$ $^{\circ}\text{C}$	$T_{\text{Salt bottom}}$ $^{\circ}\text{C}$	P MPa
KT1	$\text{Na}_2\text{SO}_4$	$\text{K}_2\text{SO}_4$	0.1	0.05	water	$18 \pm 0.2$	100	430	240	28
KT2	$\text{Na}_2\text{SO}_4$	$\text{K}_2\text{SO}_4$	0.1	0.05	10 wt % IPA	$18.9 \pm 0.6$	100	430	240	28
KT3	$\text{Na}_2\text{SO}_4$	$\text{K}_2\text{SO}_4$	0.1	0.05	10 wt % IPA	$17.9 \pm 0.3$	50	430	240	28

As depicted in Figure 6.1 (a), the salt separation of a  $\text{Na}_2\text{SO}_4\text{-K}_2\text{SO}_4\text{-H}_2\text{O}$  salt solution was successful in the new salt separator since the conductivity of the brine effluent was very high ( $65000 \mu\text{S cm}^{-1}$ ) whereas the one of the reactor effluent was below  $70 \mu\text{S cm}^{-1}$ . A similar trend was observed for the sulfur concentration (Figure 6.1 (b)). After 3 h, the sulfur concentration in the brine was 2.8 higher than the one of the feed showing the good performance of the salt separator for concentrating sulfur in the brine effluent. In Figure 6.1 (c), the pressure fluctuations recorded by the pressure sensors located upstream of the salt separator ( $P_{\text{sensor 2-2}}$ ) and the one located in the middle of the salt separator ( $P_{\text{sensor 2-3}}$ ) suggest a salt precipitation. In fact, it is likely that a salt fraction have precipitated reflecting the pressure increase, and then were subsequently washed out when the pressure became too high.



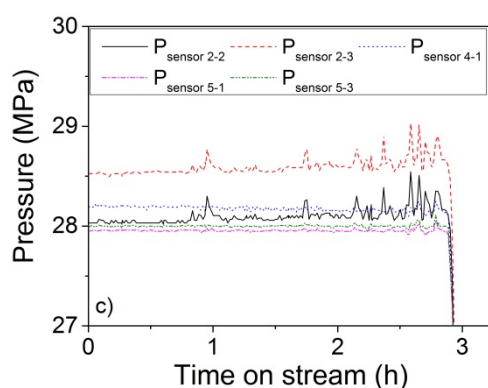


**Figure 6.1.** Evolution of the (a) conductivity and (b) sulfur concentration of the feed, the brine, and the reactor effluents during the experiment KT1. (c) Pressure profile recorded during the experiment KT1.  $P_{\text{sensor 2-2}}$  is located before the salt separator,  $P_{\text{sensor 2-3}}$  is located in the middle of the salt separator,  $P_{\text{sensor 4-1}}$  is located at the top of the reactor,  $P_{\text{sensor 5-1}}$  is located upstream of the reactor effluent filter, and  $P_{\text{sensor 5-3}}$  is located downstream of the reactor effluent filter.

In Table 6.2, according to the sulfur mass balance, the sulfur recovery of the brine effluent was only 44%. The reason for such a low recovery was due to a salt accumulation in the process as already discussed in chapter 4.

**Table 6.2.** Sulfur mass balance performed during experiment KT1 (calculated at time on stream = 3 h).

Exp.	$\dot{m}_{S,\text{Feed}}$ mg min <sup>-1</sup>	$\dot{m}_{S,\text{Brine}}$ mg min <sup>-1</sup>	$\dot{m}_{S,\text{Reactor}}$ mg min <sup>-1</sup>	$\dot{m}_{S,\text{Accumulation}}$ mg min <sup>-1</sup>	Recovery <sub>S,Brine</sub> %
KT1	77.1 ± 1.1	33.6 ± 1.5	0.8 ± 0.1	42.7 ± 1.8	43.6 ± 2.7

Despite the difficulty for closing the sulfur mass balance, this first experiment confirmed that the salts and the inorganic sulfur can be efficiently removed from the reactor effluent. For the next experiment, 10 wt % of IPA was added into a Na<sub>2</sub>SO<sub>4</sub>-K<sub>2</sub>SO<sub>4</sub>-H<sub>2</sub>O salt solution in order to assess the effect of an organic compound. In Figure 6.2 (a) and (b), no significant effect of IPA was observed since the performance of the salt separation was similar to the experiment KT1. As shown in Figure 6.2 (c), some relatively high pressure fluctuations for  $P_{\text{sensor 2-2}}$  and  $P_{\text{sensor 2-3}}$  were recorded whereas the pressure sensors located downstream of the salt separator maintained a stable pressure. As previously mentioned, these fluctuations may be related to a salt accumulation into the salt separator following by their subsequent breakdown.

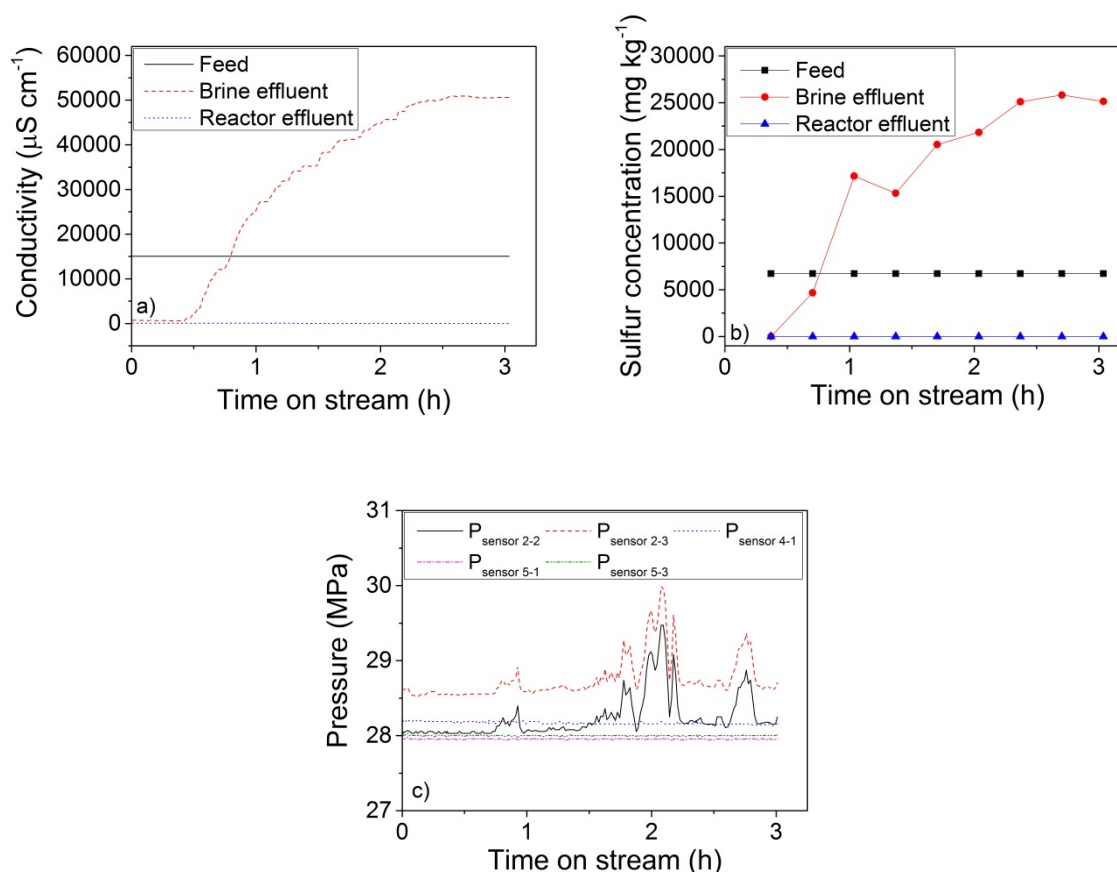


**Figure 6.2.** Evolution of the (a) conductivity and (b) sulfur concentration of the feed, the brine, and the reactor effluents during the experiment KT2. (c) Pressure profile recorded during the experiment KT2.  $P_{\text{sensor 2-2}}$  is located before the salt separator,  $P_{\text{sensor 2-3}}$  is located in the middle of the salt separator,  $P_{\text{sensor 4-1}}$  is located at the top of the reactor,  $P_{\text{sensor 5-1}}$  is located upstream of the reactor effluent filter, and  $P_{\text{sensor 5-3}}$  is located downstream of the reactor effluent filter.

In Table 6.3, the sulfur mass balance shows that only 8% of the sulfur contained in the feed could not be recovered in the brine effluent. Thereby, it seems that in presence of IPA, the sulfur recovery in the brine effluent was improved. Although the calculated uncertainty was high, the sulfur accumulation in the process was low.

**Table 6.3.** Sulfur mass balance performed during experiment KT2 (calculated at time on stream = 3 h).

Exp.	$\dot{m}_{\text{S,Feed}}$ $\text{mg min}^{-1}$	$\dot{m}_{\text{S,Brine}}$ $\text{mg min}^{-1}$	$\dot{m}_{\text{S,Reactor}}$ $\text{mg min}^{-1}$	$\dot{m}_{\text{S,Accumulation}}$ $\text{mg min}^{-1}$	Recovery <sub>S,Brine</sub> %
KT2	$123.4 \pm 5.4$	$113.8 \pm 5.4$	$1.5 \pm 0.1$	$8.1 \pm 7.7$	$92.2 \pm 8.6$

For the last experiment carried out with a model salt solution, the experiment KT2 was repeated by reducing the Liquiflow from 100% to 50%. The objective was to improve further the salt recovery in the brine effluent as previously performed in chapter 4 (see experiment SP5). For this experiment,

the catalytic reactor filled with activated carbon has been replaced by a bypass (pipe). According to Figure 6.3 (a) and (b), no significant effect of the Liquiflow was observed since the conductivity and the sulfur concentration were quite similar to the experiment KT2. The fact that the recorded mass flow rate of the brine effluent ( $4.2 \pm 0.3 \text{ g min}^{-1}$ ) was close to the one recorded during the experiment KT2 ( $4.4 \pm 0.2 \text{ g min}^{-1}$ ), may explain such a similarity. Due to some high pressure fluctuations of the pressure sensors ( $P_{\text{sensor 2-2}}$  and  $P_{\text{sensor 2-3}}$ ), which have started earlier and with a higher intensity than during the experiments KT1 and KT2, the Liquiflow was settled to 100% (at time on stream = 1.4 h) (see Figure 6.3 (c)). Therefore the effect of the Liquiflow could not be properly assessed but the latter was found to be a sensitive parameter for the stability of the process. Note that the drop of pressure between 2 h and 2.15 h was caused by some air pumped in the process.

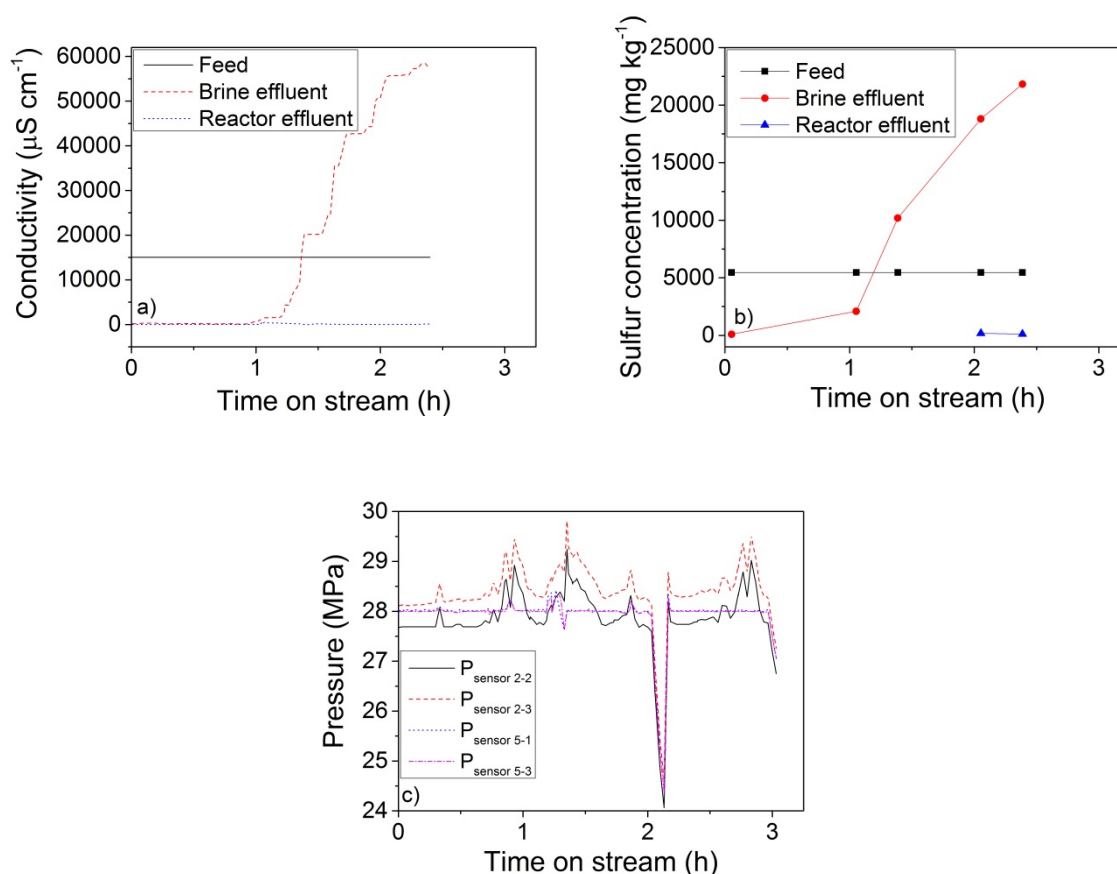


**Figure 6.3.** Evolution of the (a) conductivity and (b) sulfur concentration of the feed, the brine, and the reactor effluents during the experiment KT3. (c) Pressure profile recorded during the experiment KT3.  $P_{\text{sensor 2-2}}$  is located before the salt separator,  $P_{\text{sensor 2-3}}$  is located in the middle of the salt separator,  $P_{\text{sensor 5-1}}$  is located upstream of the reactor effluent filter, and  $P_{\text{sensor 5-3}}$  is located downstream of the reactor effluent filter.

Like for the experiment KT2, the sulfur recovery of the brine effluent was high and almost no sulfur accumulation was measured (see Table 6.4).



**Table 6.4.** Sulfur mass balance performed during experiment KT3 (calculated at time on stream = 2.4 h).

Exp.	$\dot{m}_{S,Feed}$ mg min <sup>-1</sup>	$\dot{m}_{S,Brine}$ mg min <sup>-1</sup>	$\dot{m}_{S,Reactor}$ mg min <sup>-1</sup>	$\dot{m}_{S,Accumulation}$ mg min <sup>-1</sup>	Recovery <sub>S,Brine</sub> %
KT3	102.1 ± 4.7	91.7 ± 10.7	1.7 ± 0.2	8.7 ± 11.7	89.8 ± 14.9

## 6.2 Continuous liquefaction and CSCWG of microalgae

After having assessed the performance of the new salt separator with model salt solutions and getting familiar with KONTI-C, in this section, continuous liquefaction and CSCWG experiments are carried out with algal biomass. *Phaeod. tric.* obtained as a slurry from *Subitec (Germany)* was selected for these preliminary experiments. In Table 6.5, the elemental composition of *Phaeod. tric.* is listed.

**Table 6.5.** Elemental composition of *Phaeod. tric.* calculated on a dry matter basis (taken from [26]).

Ash wt %	C wt %	H wt %	N wt %	S wt %	O wt %	P wt %	Cl wt %	Na wt %	Mg wt %	K wt %	Ca wt %
16.8	37.5	6.5	7.3	0.8	27.3	3.3	3	1.8	0.5	1.9	0.8

Note that the elemental composition of the slurry does not solely represent the chemical composition of the microalgae but also the composition of the cultivation medium, which contained mainly Na, Mg, P, CaCl<sub>2</sub>, and MgSO<sub>4</sub>. The explanation why the total elemental content sums up to 91% may come from the difficulty for measuring all the elements in the ash. The loss of a small fraction of C, H, N, S, and O as volatile compounds during the evaporation was also likely. For instance, NH<sub>4</sub>HCO<sub>3</sub> is known to decompose below 50 °C to NH<sub>3</sub>, H<sub>2</sub>O, and CO<sub>2</sub> [26].

### 6.2.1 Continuous liquefaction of microalgae

As the first experiments carried out with algal biomass in KONTI-C, two continuous liquefaction experiments were carried out. Their main objective were to evaluate the stability of the process. For the two last experiments, the reactor was filled with the ZnO adsorbent in order to investigate its sulfur adsorption performance and its catalytic effects. In Table 6.6, the process parameters of the four continuous liquefaction experiments are listed. Note that the feed rate could not be determined due to the lack of a mass flow meter. It was estimated by Zöhrer [36] that a Slurry feeder frequency of ca. 21 Hz corresponded to ca. 1 kg h<sup>-1</sup>. As the pumping capacity depends strongly on

the feedstock properties (e.g. viscosity), it is not reasonable to provide any number concerning the feed rate. Consequently, the determination of the mass balances,  $GE_C$ , and WHSV could not be performed.

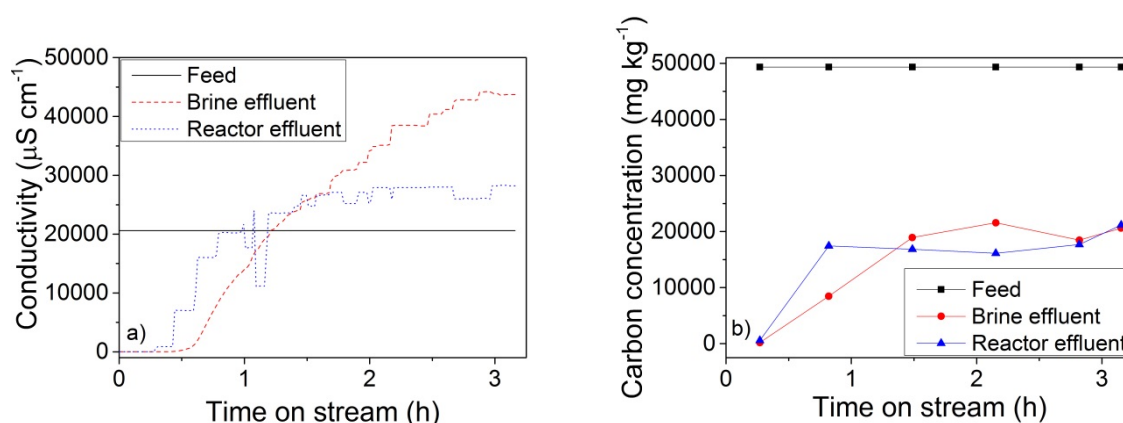
**Table 6.6.** Process parameters of the liquefaction experiments of microalgae performed with KONTI-C.

Exp.	Feed	Dry matter wt % <sup>a</sup>	$m_{ZnO}$ g	Slurry feeder freq. Hz	Liquiflow <sub>Brine</sub> %	$T_{Salt\ top}$ °C	$T_{Salt\ bottom}$ °C	$T_{Reactor}$ °C	P MPa
KT4	<i>Phaeod. tric.</i>	13	-	23	100	430	230	-	28
KT5	<i>Phaeod. tric.</i>	8	-	25	100	400	200	-	28
KT6	<i>Phaeod. tric.</i>	9	1944	24	90	410	230	400	28
KT7	<i>Phaeod. tric.</i>	6	1944	23	80	410	250	400	28

[a] Based on the C-feed compared to the C-content obtained by the elemental analysis (from Table 6.5).

### 6.2.1.1 Continuous liquefaction of microalgae (exp. KT4)

In Figure 6.4 (a), the higher conductivity of the brine effluent in comparison to the one of the reactor effluent indicates that a salt fraction has been separated. Unlike previous experiments performed with model salt solutions, the conductivity of the reactor effluent was relatively high. Hence, according to the conductivity measurements, it seems that the salt separation was not fully achieved. Apart from the salts, the presence of other compounds contained in the reactor effluent such as  $NH_4^+$ ,  $HS^-$  may have an effect on the measured conductivity. When working with microalgae, due to its complex chemical composition, it is not suitable to evaluate the performance of the salt separator based solely on the conductivity.



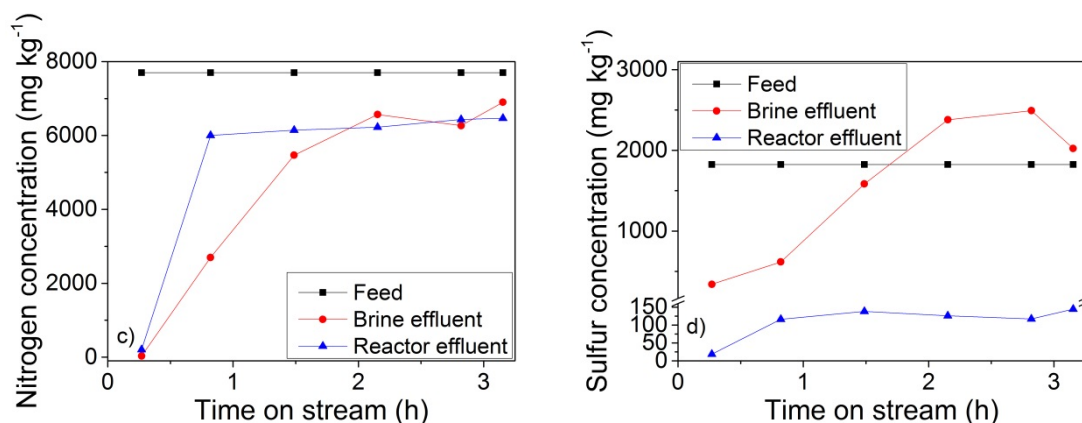
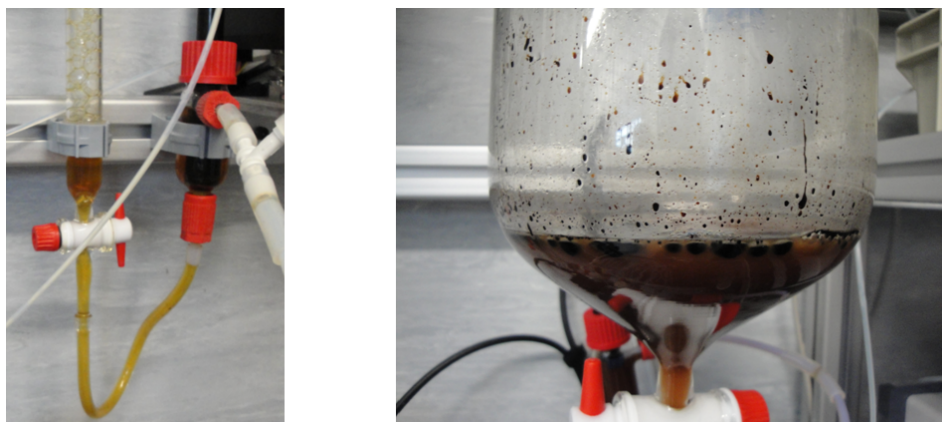


**Figure 6.4.** Evolution of the (a) conductivity, (b) carbon, (c) nitrogen, and (d) sulfur concentration of the feed, the brine, and the reactor effluents during the experiment KT4.

Astonishingly, more than half of the carbon concentration of the feed was recovered neither in the brine nor in the reactor effluents (see Figure 6.4 (b)). Although during this first liquefaction experiment, no gas sample was taken, such a high carbon accumulation inside the process was likely caused by tar and coke formation in the subcritical region of the salt separator during heating up of the feed. In fact, it is known that tar and coke formation occurs at subcritical temperatures (350–370 °C) and long residence times [95,164]. However, Christensen et al. [26] observed recently that more cokes were formed at SCW conditions (400–420 °C) than at subcritical conditions (275–350 °C) during hydrothermal liquefaction of *Phaeod. tric.*. Although this study was carried out in batch reactor with a heating up of 6–8 min, these results showed that coke formation is even higher at SCW conditions. According to Figure 6.4 (c), the nitrogen concentration of the brine and the reactor effluents was only slightly below the one of the feed indicating a better nitrogen recovery in comparison to the carbon recovery. Such a good nitrogen recovery may be explained by the formation of mainly ammonia via the deamination of amino acids. This result is in agreement with the high nitrogen recovery reported in the aqueous phase during hydrothermal liquefaction of *Phaeod. tric.* [26]. By looking at the sulfur concentration, it seems that most of the sulfur was recovered in the brine effluent likely as sulfate while only a low concentration (< 150 ppm) was measured in the reactor effluent suggesting a good performance of the salt separator.

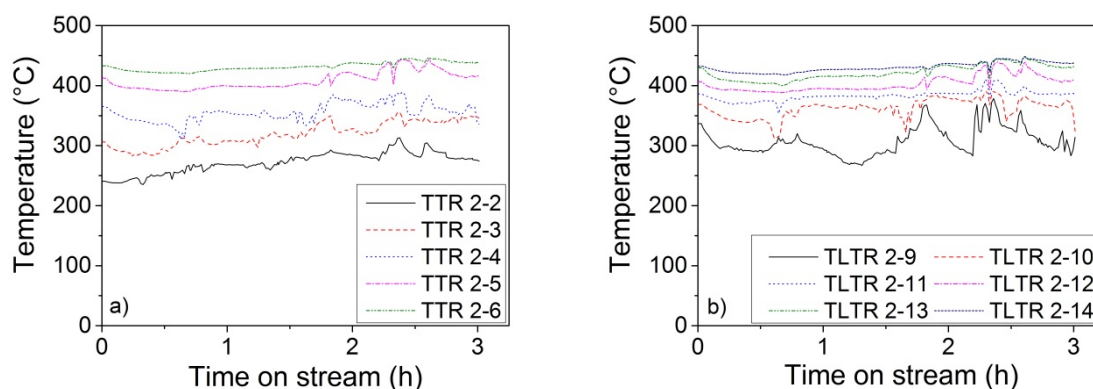
In Figure 6.5, a significant difference of the visual aspect between both effluents can be observed. The brine effluent had a homogenous orange-brown color free of tars and cokes, whereas the reactor effluent contained an aqueous and a tarry phase. Therefore the poor carbon recovery was due to tar and coke formation. The absence of tar and coke in the brine effluent shows that these non-

polar organic compounds were not able to leave the salt separator via the brine effluent, since the subcritical region acted as a barrier (low solubility for the tars).



**Figure 6.5.** Left: Phase separator of the brine effluent (taken at time on stream = 2.2 h) after experiment KT4. Right: Phase separator of the reactor effluent (taken at time on stream = 2.75 h) after experiment KT4.

The relatively high fluctuations of the temperature recorded by the thermocouples at the inner wall and the lance of the salt separator reveal a constant change of the fluid dynamics and/or the heat transfer (see Figure 6.6 (a) and (b)). The heat transfer from the bulk to the surface of the thermocouples was likely affected by tar and coke formation and/or salt deposits. It seems that these fluctuations are more important at the bottom of the salt separator (standpipe). In Figure 6.6 (c), the fluctuations of the pressure sensors located upstream ( $P_{\text{sensor 1-3}}$ ,  $P_{\text{sensor 1-4}}$ ,  $P_{\text{sensor 1-5}}$ , and  $P_{\text{sensor 2-2}}$ ) and in the middle of the salt separator ( $P_{\text{sensor 2-3}}$ ) coincided with the fluctuations of the thermocouple located close to the standpipe outlet (TLTR 2-9). It seems that some kind of plugging occurred inside the standpipe and/or at the bottom of the salt separator due to either coke formation, salt precipitation, and/or other particles.



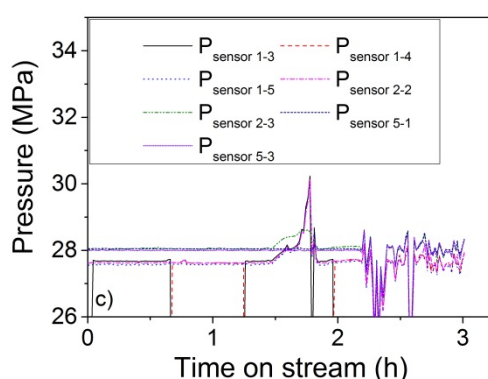


**Figure 6.6.** Temperature and pressure profile recorded during the experiment KT4. (a) The thermocouples located at the inner wall of the salt separator, starting from the bottom (TTR 2-2) to the top (TTR 2-6) and (b) the thermocouples located on the lance of the salt separator starting from the bottom (TLTR 2-9) to the top (TLTR 2-14). (c) Pressure sensors where  $P_{\text{sensor 1-3}}$ ,  $P_{\text{sensor 1-4}}$ , and  $P_{\text{sensor 1-5}}$  are located at the slurry feeder,  $P_{\text{sensor 2-2}}$  is located before the salt separator,  $P_{\text{sensor 2-3}}$  is located in the middle of the salt separator,  $P_{\text{sensor 5-1}}$  is located upstream of the reactor effluent filter, and  $P_{\text{sensor 5-3}}$  is located downstream of the reactor effluent filter.

After the liquefaction experiment, the process was cooled and rinsed with DI water overnight. The following day, the filters were removed, inspected, and cleaned. In Figure 6.7, it can be seen that the filters of the brine and reactor effluents were covered by tars. In line with which was observed in Figure 6.5, some tars on the filter of the reactor effluent were expected but the presence of tars on the filter of the brine effluent was hardly expected. It is likely that these tars were formed from organic compounds, which were not soluble in SCW. The inner of the salt separator was also inspected after the experiment. During the removal of the insulation, a leakage at the  $P_{\text{sensor 2-3}}$  was observed (Figure 6.8 (left)). The insulation was partially burnt and covered with a small amount of tars. Since no relevant pressure drops were recorded during the experiment, it seems that the leak was relatively small. By opening the salt separator, some salt deposits were detected at the bottom while the top was free of salts (Figure 6.8 (right)). The opposite might have been expected, since the salt solubility is low at SCW conditions. In fact, the salts might deposit rather at the top in the supercritical region. It is not excluded that the salts have precipitated at the top during the experiment, and then during cooling with DI water, the salts were partially dissolved and precipitated at the bottom of the salt separator. It is worth to mention that the salt separator was opened and inspected for the first time. Thereby, some salt deposits from previous experiments might remain at the bottom.

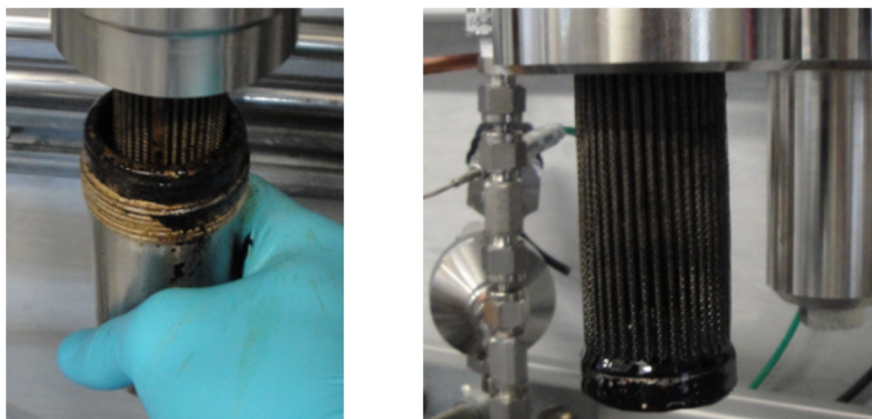


**Figure 6.7.** Left: Filter of the brine effluent after experiment KT4. Right: Filter of the reactor effluent after experiment KT4.

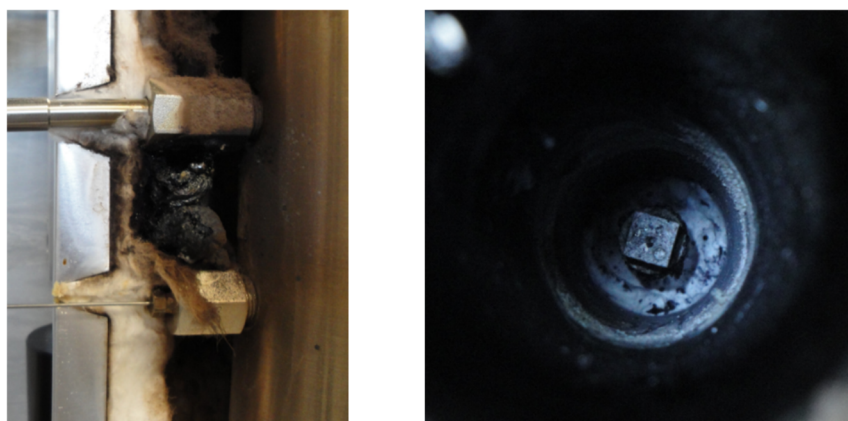


**Figure 6.8.** Left: Leakage at PTR 2-3. Right: Inside of the salt separator after experiment KT4.

#### 6.2.1.2 Continuous liquefaction of microalgae (exp. KT5)

As some plugging issues were observed during the previous liquefaction. The second experiment aimed at resolving these problems by increasing the feed rate for minimizing the plugging in the standpipe, and by reducing the temperature in the lower part of the salt separator for attenuating tar and coke formation. In Figure 6.9 (a), unlike the first liquefaction, the conductivity of the brine effluent remained below the one of the feed while the one of the reactor effluent reached the same value as the one of the feed. It seems that the conditions were too mild for a complete liquefaction. In Figure 6.9 (b), (c), and (d), the progressive increase of the carbon, the nitrogen, and the sulfur concentrations in the brine effluent up to values that were quite similar to those of the feed, was likely caused by the too mild conditions in the salt separator. Consequently, the liquefaction was not fully achieved. A different behaviour of the composition of the reactor effluent than the one of the brine effluent was observed. In fact, like in the previous liquefaction experiment (KT4), the carbon, the nitrogen, and the sulfur concentrations of the reactor effluent reached a steady state only



after 45 min and remained relatively constant during the experiment (with the exception of the sulfur concentration, which decreased after 1.4 h). More than half of the carbon contained in the feed was not recovered in the reactor effluent suggesting that tar and coke formation occurred. As the composition of the reactor effluent significantly differed from the one of the feed, it seems that the conditions in the upper part of the salt separator were harsh enough for liquefying the feed.

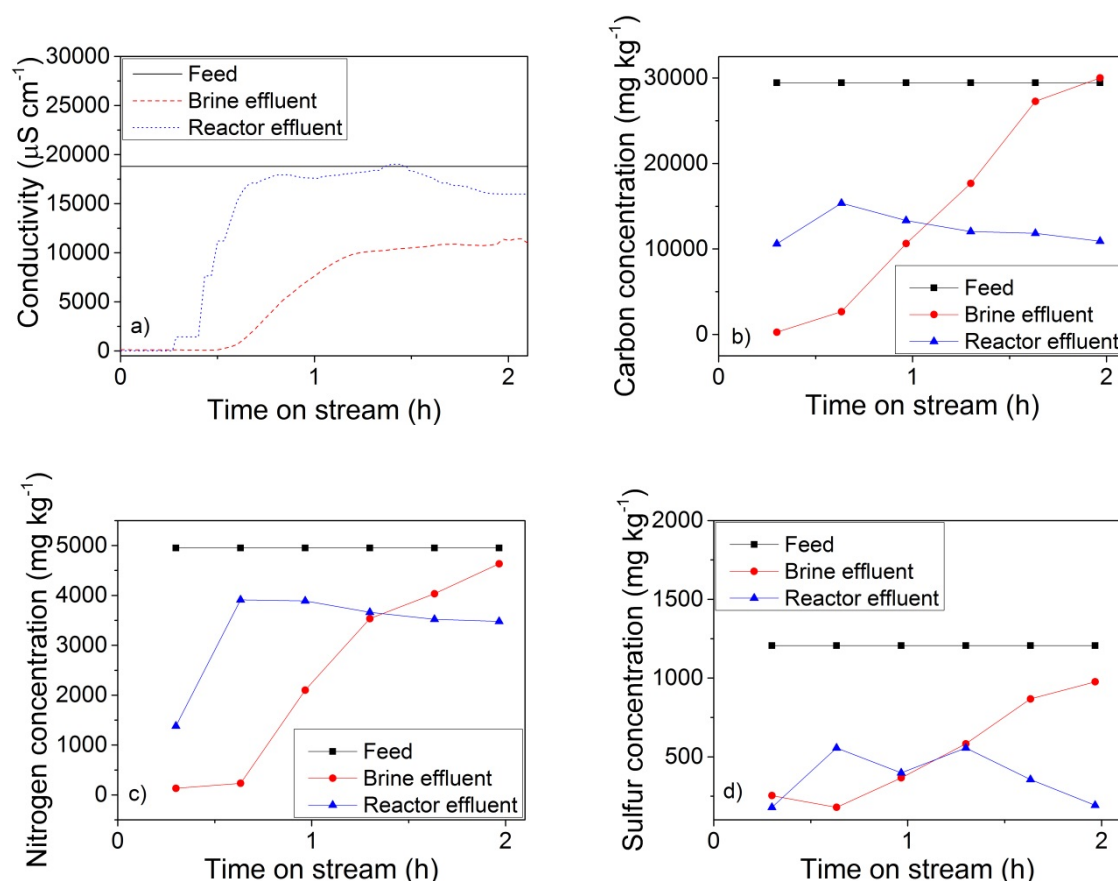


**Figure 6.9.** Evolution of the (a) conductivity, (b) carbon, (c) nitrogen, and (d) sulfur concentration of the feed, the brine, and the reactor effluents during the experiment KT5.

For this second liquefaction, gas samples in the phase separator of the brine and the reactor effluents were taken and analyzed off-line by GC. Since no gas accumulated in the gas bag at the brine effluent, the gas production was assumed to be negligible. The gas composition of the reactor effluent is depicted in Table 6.7.

**Table 6.7.** Gas composition of the reactor effluent during the experiment KT5 (sampling at time on stream = 1 h).

Sample	CO <sub>2</sub> vol %	H <sub>2</sub> vol %	CH <sub>4</sub> vol %	CO vol %
Reactor effl.	92	-	5	3

Although the conditions were relatively mild, the gas production reveals that the conditions at the top of the salt separator were harsh enough for liquefying microalgae. Mainly  $\text{CO}_2$  was produced indicating that some organic compounds were decomposed. Chakinala et al. [104] studied the effect of the temperature during non-catalytic gasification of 7.3 wt % *Chlorella vul.* in a quartz capillaries reactor. At 400 °C and 24 MPa, the  $\text{GE}_c$  was 14% and the gas composition was 98 mol % of  $\text{CO}_2$  and the rest was alkanes ( $\text{CH}_4$ ,  $\text{C}_2\text{-C}_3$ ). At this temperature, decarboxylation reactions are more dominant than free radical reactions which prevail at higher temperatures, explaining  $\text{CO}_2$  as the main gas product [54,96]. A similar gas composition was also observed when liquefying the same microalgae in batch reactor [26].

In Figure 6.10, the visual aspect of the brine effluent confirms that microalgae were hardly liquefied, since the color was similar to the one of the feed. Besides, the brine effluent had a similar smell that the one of the feed. Hence, a shorter residence time and a lower temperature at the bottom of the salt separator were not suitable for achieving a proper liquefaction.

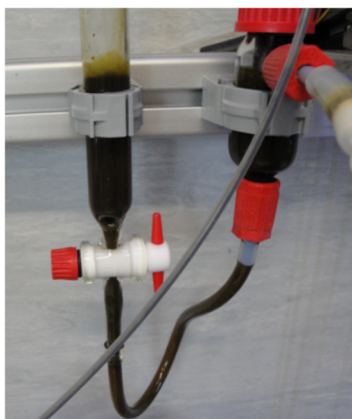


**Figure 6.10.** Phase separator of the brine effluent (taken at time on stream = 1.3 h) after experiment KT5.

Like for the first liquefaction experiment, severe fluctuations of the temperature were recorded at the inner wall and the lance of the salt separator indicating constant changes of the fluid dynamics and/or heat transfer (see Figure 6.11 (a) and (b)). After 1.5 h, the temperature at the bottom of the salt separator was increased in order to improve the liquefaction efficiency. Unfortunately, due to a malfunction of the Liquiflow, it was not possible to reach the steady state with the new temperature setpoint, and thus to assess properly its effect on the liquefaction performance. After 2 h, the mass flow rate of the brine effluent was not controlled by the Liquiflow anymore leading to a very high mass flow rate. Consequently, the pressure regulator was not able to maintain the pressure explaining the abrupt loss of pressure after 2.2 h in Figure 6.11 (c). It is worth noting that the high



pressure drop observed during the first experiment (exp. KT4) occurred after 1.8 h, whereas here it was measured after 2 h and at a lower extent. However, due to a malfunction of the Liquiflow, it is not possible to conclude any improvement of the process stability, since the experiment was stopped after 2.4 h.

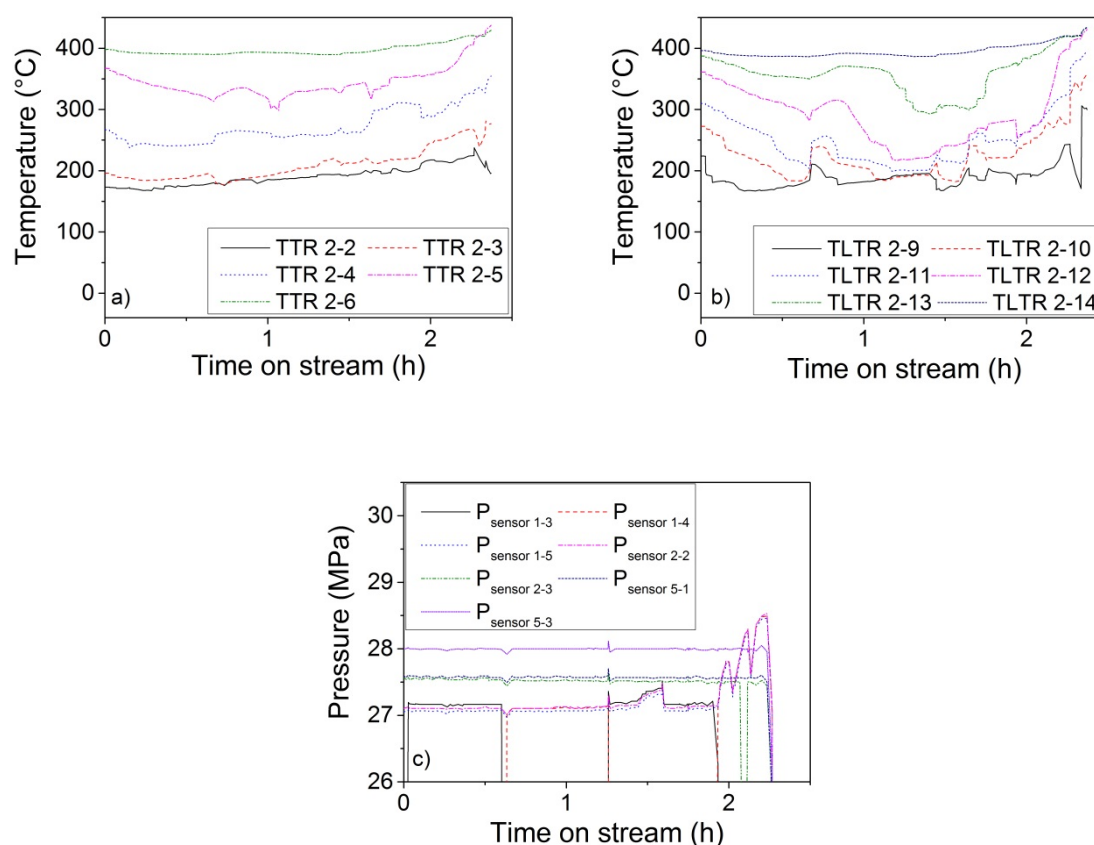


**Figure 6.11.** Temperature and pressure profile recorded during the experiment KT5. (a) The thermocouples located at the inner wall of the salt separator, starting from the bottom (TTR 2-2) to the top (TTR 2-6) and (b) the thermocouples located on the lance of the salt separator starting from the bottom (TLTR 2-9) to the top (TLTR 2-14). (c) Pressure sensors where  $P_{\text{sensor 1-3}}$ ,  $P_{\text{sensor 1-4}}$ , and  $P_{\text{sensor 1-5}}$  are located at the slurry feeder,  $P_{\text{sensor 2-2}}$  is located before the salt separator,  $P_{\text{sensor 2-3}}$  is located in the middle of the salt separator,  $P_{\text{sensor 5-1}}$  is located upstream of the reactor effluent filter, and  $P_{\text{sensor 5-3}}$  is located downstream of the reactor effluent filter.

### 6.2.1.3 Continuous liquefaction of microalgae over ZnO (exp. KT6)

Although the conditions in the salt separator were not yet optimized, the bypass installed downstream of the salt separator has been replaced by the catalytic reactor, which was entirely filled with ZnO. As the conditions during the previous experiment were too mild, the temperature setpoint at the bottom of the salt separator was increased and the feed rate reduced. In parallel, the defect Liquiflow has been exchanged and its operating setpoint was 90% instead of 100%. The idea was to operate the Liquiflow below its boundary value.

In Figure 6.12, the conductivity measurements of the brine and the reactor effluents were very similar to those of the previous liquefaction experiment (KT5) indicating an incomplete liquefaction. In Figure 6.13, the visual aspect of the filter of the brine effluent after the experiment confirms that the filter was covered with non-liquefied feed.

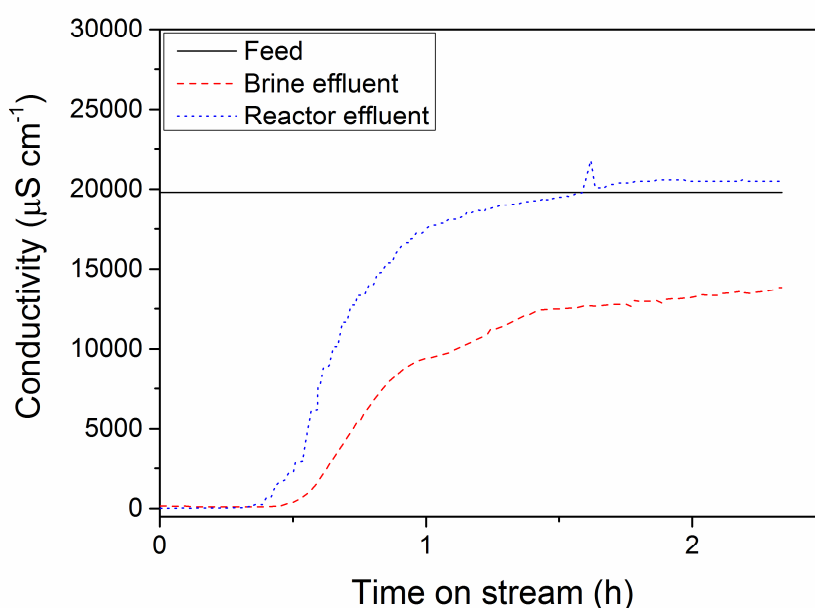


**Figure 6.12.** Evolution of the conductivity of the feed, the brine, and the reactor effluents during the experiment KT6.

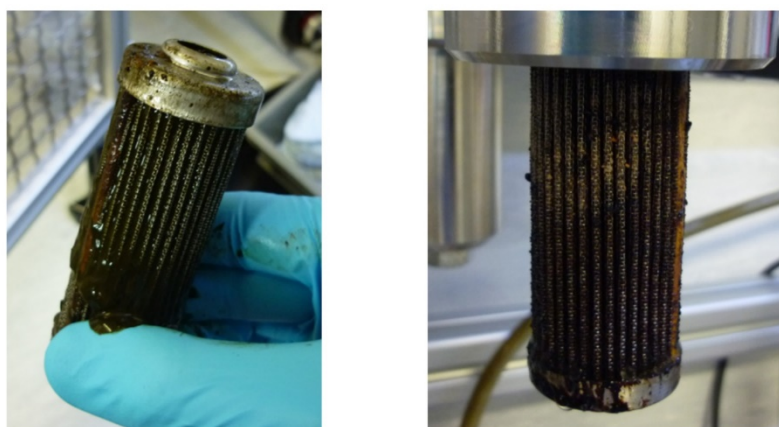


**Figure 6.13.** Left: Filter of the brine effluent after experiment KT6. Right: Filter of the reactor effluent after experiment KT6.

In Figure 6.14 (b), by looking at the temperature profile at the lance, it can be seen that the thermocouple located at the outlet of the standpipe (TLTR 2-9) indicates a temperature around 180 °C only, which was even below than during the experiment KT5 (190 °C < TLTR 2-9 < 200 °C). Unlike the

experiments KT5 and KT6, TLTR 2-9 was much higher ( $270\text{ }^{\circ}\text{C} < \text{TLTR 2-9} < 360\text{ }^{\circ}\text{C}$ ) for the first liquefaction (experiment KT4) which exhibited a successful liquefaction. Consequently, it seems that TLTR 2-9 can provide some relevant indications regarding the liquefaction efficiency.

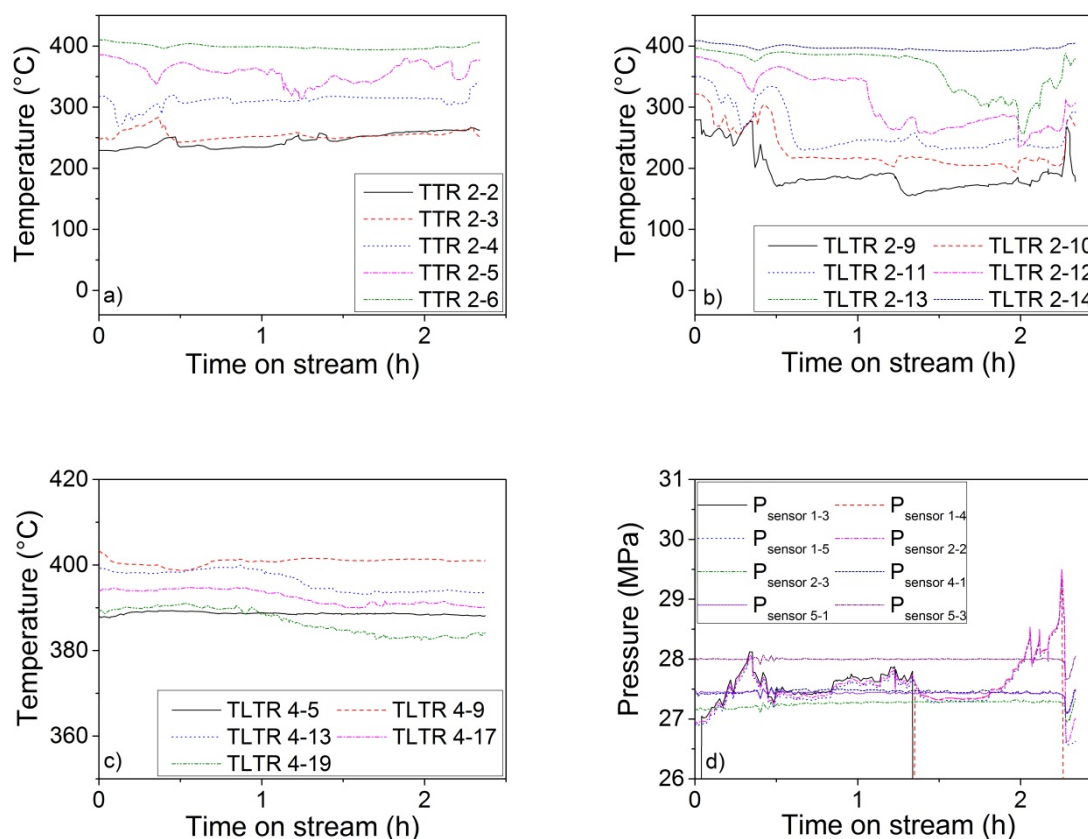


**Figure 6.14.** Temperature and pressure profile recorded during the experiment KT6. (a) The thermocouples located at the inner wall of the salt separator, starting from the bottom (TTR 2-2) to the top (TTR 2-6), (b) the thermocouples located on the lance of the salt separator starting from the bottom (TLTR 2-9) to the top (TLTR 2-14), and (c) the thermocouples located on the lance of the reactor starting from the bottom (TLTR 4-5) to the top (TLTR 4-19). (d) Pressure sensors where  $P_{\text{sensor 1-3}}$ ,  $P_{\text{sensor 1-4}}$ , and  $P_{\text{sensor 1-5}}$  are located at the slurry feeder,  $P_{\text{sensor 2-2}}$  is located before the salt separator,  $P_{\text{sensor 2-3}}$  is located in the middle of the salt separator,  $P_{\text{sensor 4-1}}$  is located in the reactor,  $P_{\text{sensor 5-1}}$  is located upstream of the reactor effluent filter, and  $P_{\text{sensor 5-3}}$  is located downstream of the reactor effluent filter.

Although the feed rate was reduced and the temperature at the bottom of the salt separator was increased in comparison to the experiment KT5, the lower temperature of TLTR 2-9 was likely caused by the change of the feed rate (from 23.7 Hz to 24.7 Hz) after 0.5 h. In fact, due to some unexpected pressure fluctuations in the standpipe occurring at the beginning of the experiment (see Figure 6.14 (d)), it was thought that some small particles coming from the feed were blocked in the standpipe. Thus, it was decided to increase the feed rate in order to resolve this issue. Like in the previous

experiments, the pressure in the standpipe severely increased at 2 h leading to the end of the experiment. For this experiment, it was decided not to perform any thorough off-line analysis (e.g. CNS, GC) but to repeat it.

#### 6.2.1.4 Continuous liquefaction of microalgae over ZnO (exp. KT7)

For the last continuous liquefaction experiment, the following modifications were performed: a new filter of the feed was installed (25  $\mu\text{m}$ ), the feed rate was slightly reduced (from 23.7 Hz to 23 Hz) as well as the Liquiflow (from 90% to 80%), and the temperature at the bottom of the salt separator was increased (from 230 °C to 250 °C). The main objective was to improve the liquefaction efficiency and the stability of the process regarding plugging in the standpipe. Although the Slurry feeder was set to 23 Hz, the actual feed rate calculated during the experiment was surprisingly high. The reason for such a high feed rate could not be explained but the difficulty of the Liquiflow for settling a constant flow seemed to be the cause. Therefore the liquefaction efficiency was significantly affected since the conductivity of the brine and the reactor effluents was below the one of the feed (see Figure 6.15 (a)). Moreover, the filter of the brine effluent was covered with non-liquefied microalgae after the experiment. Like during the first liquefaction experiment (exp. KT4) more than half of the carbon contained in the feed was recovered neither in the brine nor in the reactor effluents (see Figure 6.15 (b)). It seems that the carbon accumulation was not influenced by the presence of ZnO, and likely took place in the subcritical region of the salt separator. In Figure 6.15 (c), similarly to the experiment KT4, a better nitrogen recovery in comparison to the carbon recovery was observed. Interestingly, after 3 h, the nitrogen concentration in the reactor effluent dropped significantly whereas the one of the brine effluent increased. It is not excluded that the temperature recorded at the lance of the salt separator became too mild (TLTR 2-9 < 200 °C) for ensuring a proper deamination of amino acids (see Figure 16 (b)). In fact, a temperature above 300 °C and a residence time of few minutes are needed to decompose the amino acids to amines, amides, ammonia, thiols, organic acids, aldehydes, CO<sub>2</sub>, and H<sub>2</sub>S [17]. Due to the low liquefaction efficiency, the sulfur concentration in the brine effluent was below the one of the feed. As shown in Figure 6.15 (d), the sulfur concentration in the reactor effluent remained very low (in the detection limits of the S elemental analyzer) suggesting the good sulfur adsorption performance of ZnO.

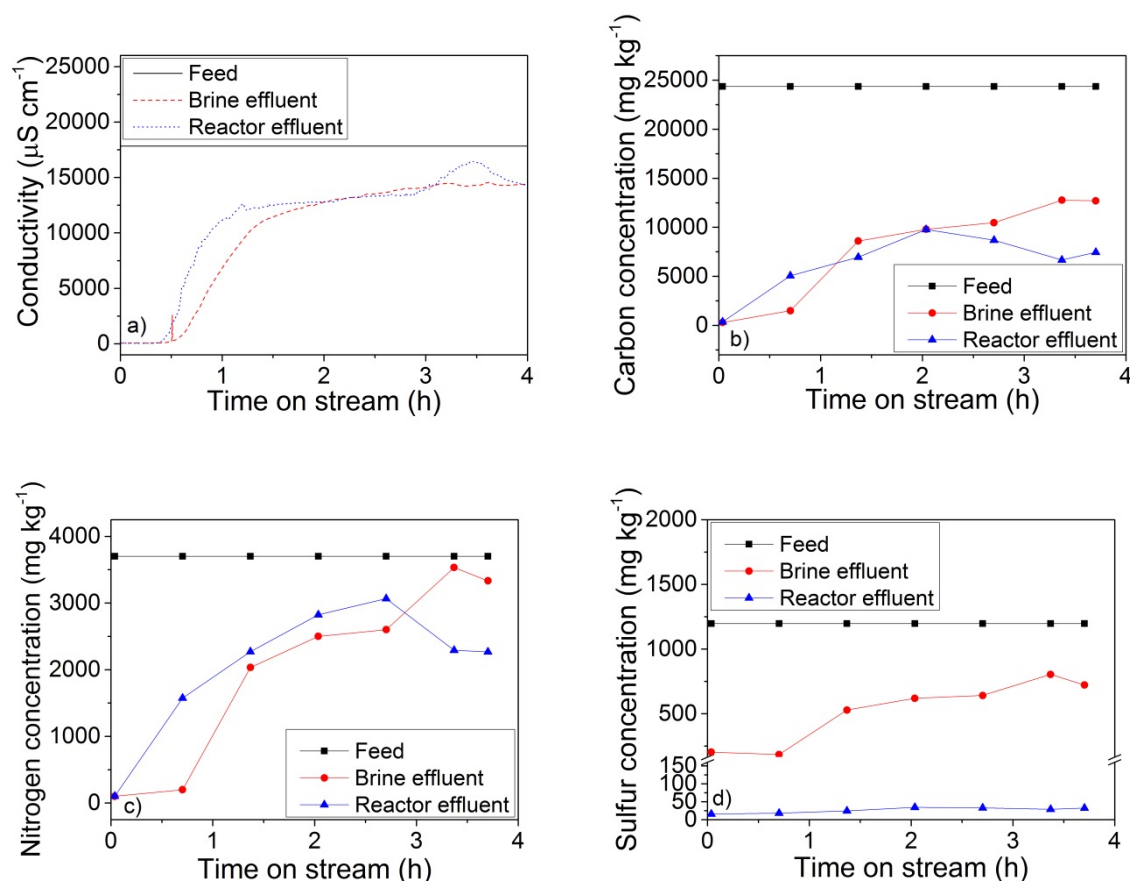


**Figure 6.15.** Evolution of the (a) conductivity, (b) carbon, (c) nitrogen, and (d) sulfur concentration of the feed, the brine, and the reactor effluents during the experiment KT7.

In Table 6.8, the gas composition was different from the liquefaction performed in absence of ZnO (experiment KT5). The presence of ZnO seems to favor the steam reforming and the WGS reactions, since 50 vol % of  $\text{H}_2$  and no CO were detected. Sinağ et al. [165] studied in an autoclave reactor the catalytic activity of ZnO during hydrothermal conversion of 10 wt % cellulose at different temperatures (300–600 °C) and pressures (8–34 MPa) with a reaction time of 1 h. The WGS reaction was enhanced in presence of ZnO, especially at 300 °C where the gas composition was mainly  $\text{CO}_2$  and  $\text{H}_2$ . Similarly to our results, in absence of ZnO, they obtained a gas composed of  $\text{CO}_2$  (90 vol %) and CO (10 vol %).

**Table 6.8.** Gas composition in the reactor effluent during the KT7 experiment (sampling at time on stream = 2 h).

Sample	$\text{CO}_2$ vol %	$\text{H}_2$ vol %	$\text{CH}_4$ vol %	CO vol %
Reactor effl.	50	49	1	-

As it can be seen in Figure 6.16 (b), at the beginning, the temperature at the lance of the salt separator (TLTR 2-9) was around 290 °C and dropped constantly during the experiment up to 125 °C.

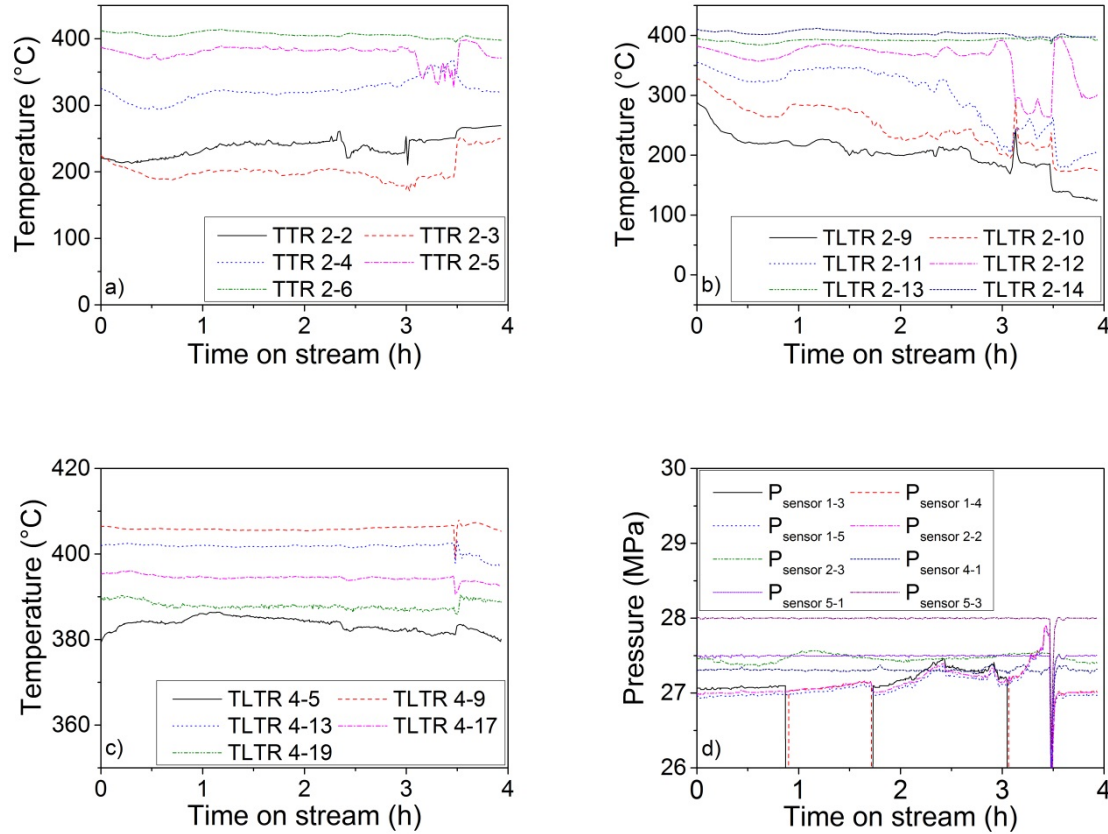


**Figure 6.16.** Temperature and pressure profile recorded during the experiment KT7. (a) The thermocouples located at the inner wall of the salt separator, starting from the bottom (TTR 2-2) to the top (TTR 2-6), (b) the thermocouples located on the lance of the salt separator starting from the bottom (TLTR 2-9) to the top (TLTR 2-14), and (c) the thermocouples located on the lance of the reactor starting from the bottom (TLTR 4-5) to the top (TLTR 4-19). (d) Pressure sensors where  $P_{\text{sensor 1-3}}$ ,  $P_{\text{sensor 1-4}}$ , and  $P_{\text{sensor 1-5}}$  are located at the slurry feeder,  $P_{\text{sensor 2-2}}$  is located before the salt separator,  $P_{\text{sensor 2-3}}$  is located in the middle of the salt separator,  $P_{\text{sensor 4-1}}$  is located in the reactor,  $P_{\text{sensor 5-1}}$  is located upstream of the reactor effluent filter, and  $P_{\text{sensor 5-3}}$  is located downstream of the reactor effluent filter.

Such a high drop may be related to the incapability of the Liquiflow for maintaining a constant mass flow rate. The other thermocouples located at the inner wall of the salt separator, at the top of the lance of the salt separator (TLTR 2-13, TLTR 2-14), and at the lance of the reactor exhibited a much constant temperature over the whole experiment (see Figure 6.16 (a), (b), and (c)). In Figure 6.16 (d), the pressure was more stable in comparison to the previous experiments where only a small increase up to 28 MPa was recorded in the standpipe. Therefore it seems that the installation of the new filter has improved the process stability. Note that the sudden drop of pressure recorded after 3.5 h was caused by an involuntary opening of a valve.

## 6.2.2 Continuous CSCWG of microalgae

After having improved the process stability regarding plugging of the standpipe and showed that sulfur can be efficiently removed by the ZnO adsorbent, two continuous CSCWG experiments were carried out with a reactor filled with ZnO and a 5% Ru/C<sub>BASF</sub> catalyst which was loaded downstream of the ZnO adsorbent. The main objective was to achieve a stable gasification of microalgae with a gas composition close to the thermodynamic chemical equilibrium over a period of few hours (5-7 h). In Table 6.9, the process parameters of the continuous CSCWG experiments are listed.

**Table 6.9.** Process parameters of the continuous CSCWG experiments of microalgae performed with KONTI-C.

Exp.	Feed	Dry matter wt % <sup>a</sup>	m <sub>ZnO</sub> g	m <sub>Cat.</sub> g	Slurry feeder freq. Hz	Liquiflow <sub>Brine</sub> %	T <sub>Salt top</sub> °C	T <sub>Salt bottom</sub> °C	T <sub>Reactor</sub> °C	P MPa
KT8	<i>Phaeod. tric.</i>	11	529	444	23	90	430	300	400	28
KT9	<i>Phaeod. tric.</i>	9	529	444	23	60	430	300	400	28

[a] Based on the C-feed compared to the C-content obtained by the elemental analysis (from Table 6.5).

### 6.2.2.1 Continuous CSCWG of microalgae (exp. KT8)

As the conditions were too mild during the previous liquefaction experiments for ensuring a complete liquefaction, the temperature at the bottom of the salt separator was increased from 250 °C to 300 °C. In parallel, the defect Liquiflow has been exchanged by another one in order to fix the issue encountered with the setpoint frequency of the Slurry feeder. In Figure 6.17, the higher conductivity of the brine and the reactor effluents in comparison to the feed suggests a good liquefaction. Moreover, the filter of the brine effluent was inspected after the experiment and no trace of non-liquefied microalgae was found. Unfortunately, the experiment was stopped only after 2 h due to a high pressure increase inside the process.



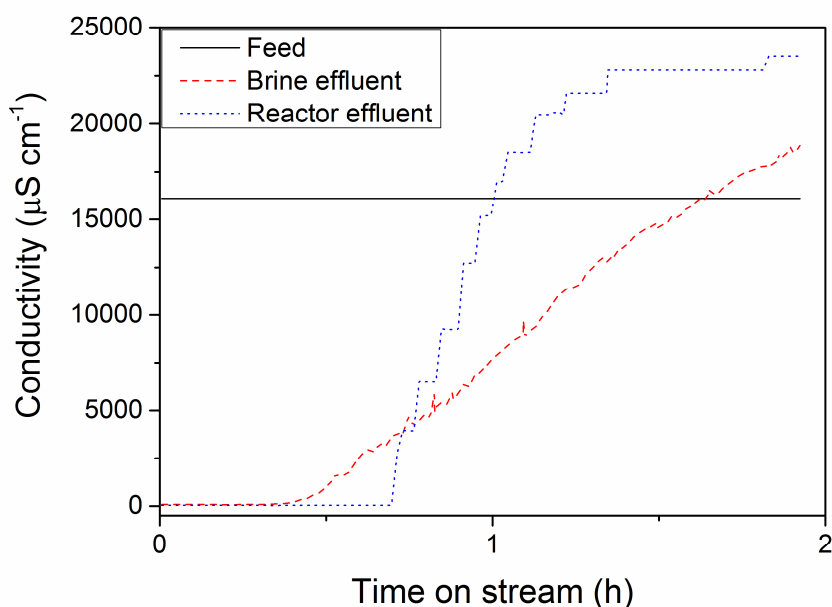


**Figure 6.17.** Evolution of the conductivity of the feed, the brine, and the reactor effluents during the experiment KT8.

In Figure 6.18, unlike the previous liquefaction experiments where the pressure increase took place solely in the standpipe, this time all the pressure sensors indicated a high pressure suggesting a problem with the pressure controller (Flowserve) and/or the pressure relief valve. Although the Slurry feeder was stopped immediately in order to reduce the pressure, as soon as it was restarted, the pressure increased again. As this problem was not solved, it was decided to stop the experiment. The reason for such a high pressure increase may be due to particles blocked in the Flowserve and/or the pressure relief valve. It is likely that the formation of methane hydrates took place and blocked the Flowserve and/or the pressure relief valve. In fact, it is reported that the formation of methane hydrates may occur at 28 MPa and 25 °C [166]. As the experiment was prematurely stopped and consequently the steady state was not reached, it was decided not to perform any off-line analysis of the liquid effluents. Additionally, due to some other problems encountered with the microGC, the gas composition could not be analyzed on-line.



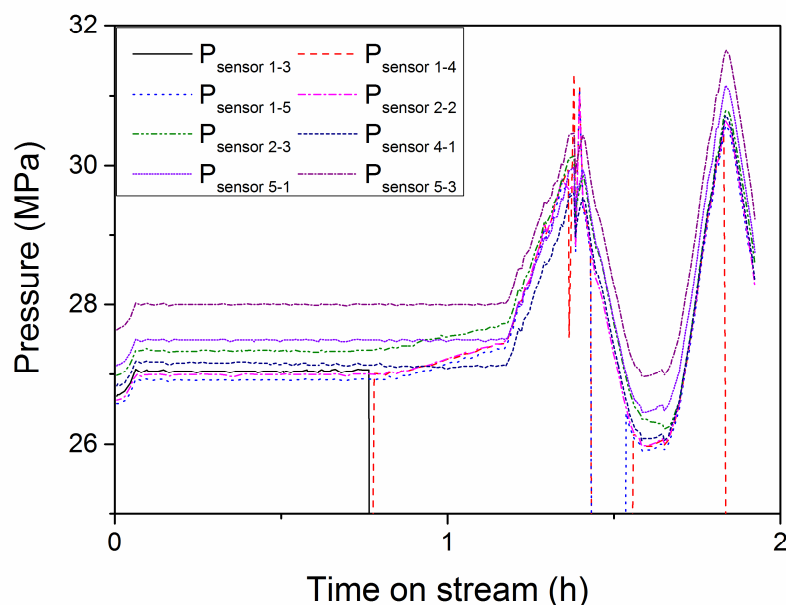
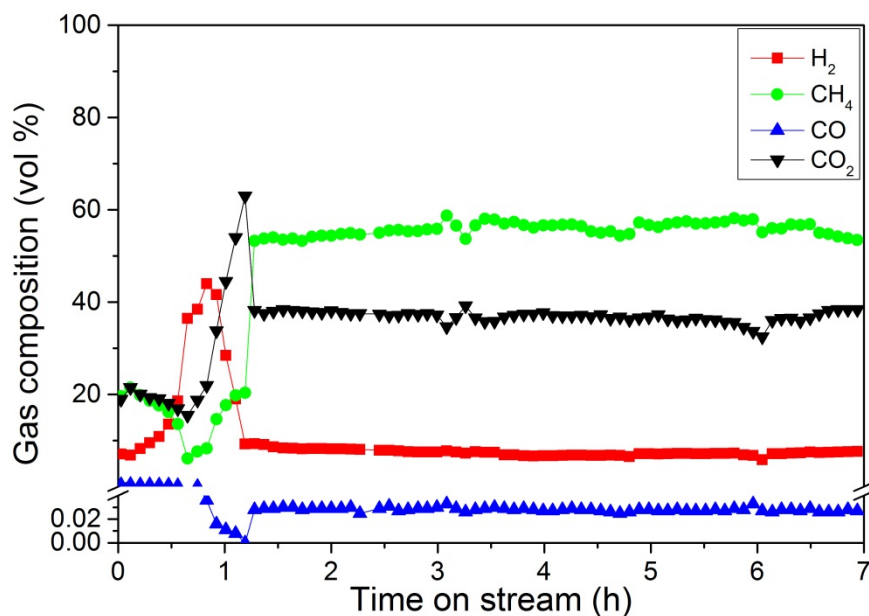


**Figure 6.18.** Pressure readings of the pressure sensors during the experiment KT8.  $P_{\text{sensor 1-3}}$ ,  $P_{\text{sensor 1-4}}$ , and  $P_{\text{sensor 1-5}}$  are located at the slurry feeder,  $P_{\text{sensor 2-2}}$  is located before the salt separator,  $P_{\text{sensor 2-3}}$  is located in the middle of the salt separator,  $P_{\text{sensor 4-1}}$  is located in the reactor,  $P_{\text{sensor 5-1}}$  is located upstream of the reactor effluent filter, and  $P_{\text{sensor 5-3}}$  is located downstream of the reactor effluent filter.

#### 6.2.2.2 Continuous CSCWG of microalgae (exp. KT9)

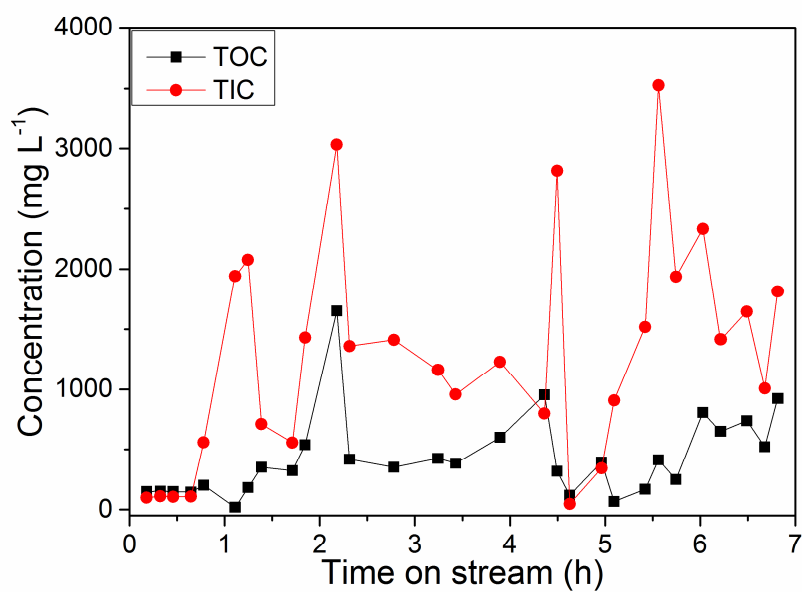
For the second continuous CSCWG experiment, a second relief valve was installed in parallel to the original one in case of any problem encountered with the original relief valve. As the liquefaction conditions for the previous experiment were satisfying, hardly any parameters were changed. Only the Liquiflow was reduced from 90% to 60% in order to improve the salt recovery. In Figure 6.19, a stable gas composition corresponding to the thermodynamic chemical equilibrium was obtained over a period of 7 h. The high  $\text{CH}_4$  concentration (ca. 57 vol %) demonstrates the good catalytic performance of the 5 %Ru/ $\text{C}_{\text{BASF}}$  catalyst for favoring the methanation reaction. The stability of the  $\text{CH}_4$  concentration confirmed that the catalyst preserved its catalytic activity. In fact, the decrease of the  $\text{CH}_4$  concentration with the simultaneous increase of the  $\text{H}_2$  concentration would indicate a loss of the catalytic activity. For instance, Brandenberger et al. [17] gasified 5 wt % glycerol and 6.5 wt % microalgae (*Phaeod. tric.*) continuously in KONTI-2. When glycerol was fed the gas composition was close to the thermodynamic chemical equilibrium and the reactor effluent was clear with a TOC value of 7 ppm indicating a full organic carbon conversion. Switching the feed from glycerol to microalgae, the gas composition changed drastically. The  $\text{CH}_4$  concentration dropped from 50 vol % to

13 vol % and the  $H_2$  concentration increased from 6 vol % to 28 vol % reflecting the deactivation of the catalyst.

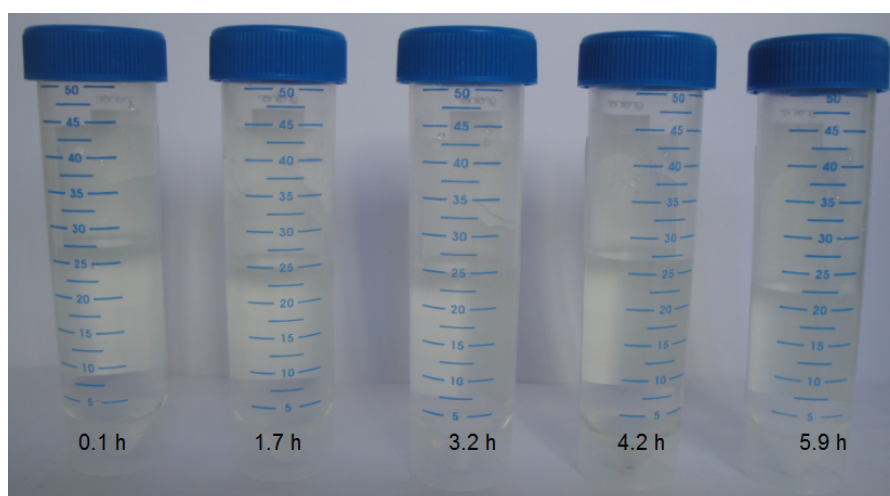


**Figure 6.19.** Evolution of the gas composition during the experiment KT9.

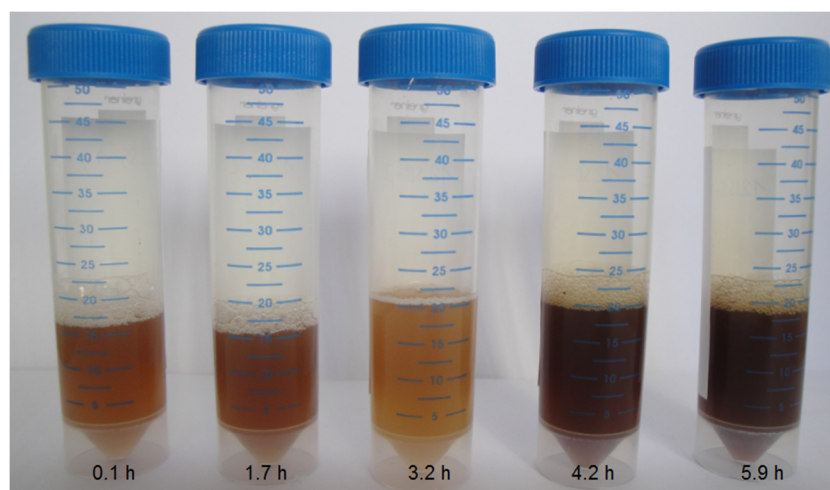
In Figure 6.20, the low TOC value of the reactor effluent (< 1700 ppm) demonstrates the high catalytic activity of the catalyst for converting the organic carbon to gaseous products. The catalyst was able to reduce up to 95.1-99.9% the TOC contained in the feed. The TIC values can be attributed to the dissolved  $CO_2$ . As it can be seen in Figure 6.21, a clear and transparent aqueous phase was observed during all the experiment suggesting a good gasification. The pH of the samples of the reactor effluent was slightly basic (ca. 8.5). The presence of ammonium in the effluent may explain the character basic of the effluent as reported by other researchers [17,94]. The homogenous orange-brown color of the brine effluent containing no tars and coke, suggested a good liquefaction (see Figure 6.22).



**Figure 6.20.** Evolution of the TOC and TIC recorded on-line during the experiment KT9.

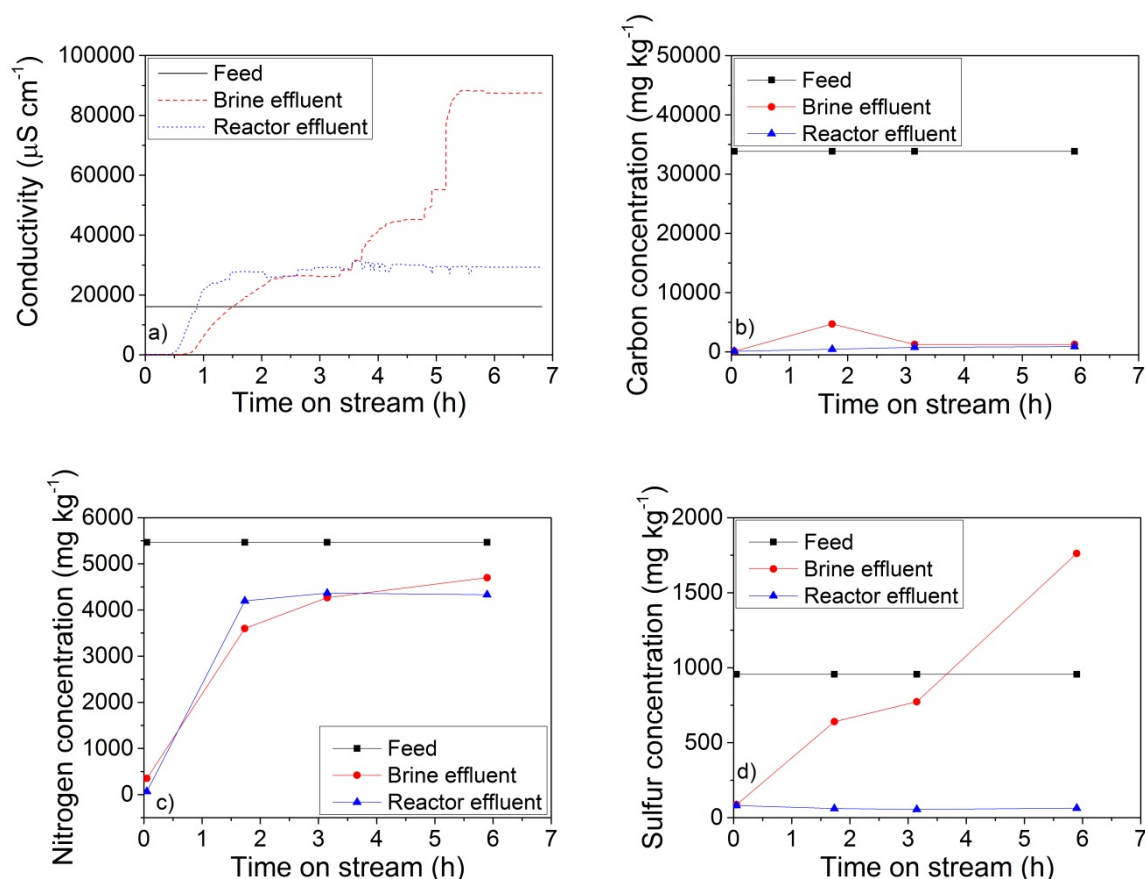


**Figure 6.21.** Picture of the reactor effluent samples taken during the experiment KT9.



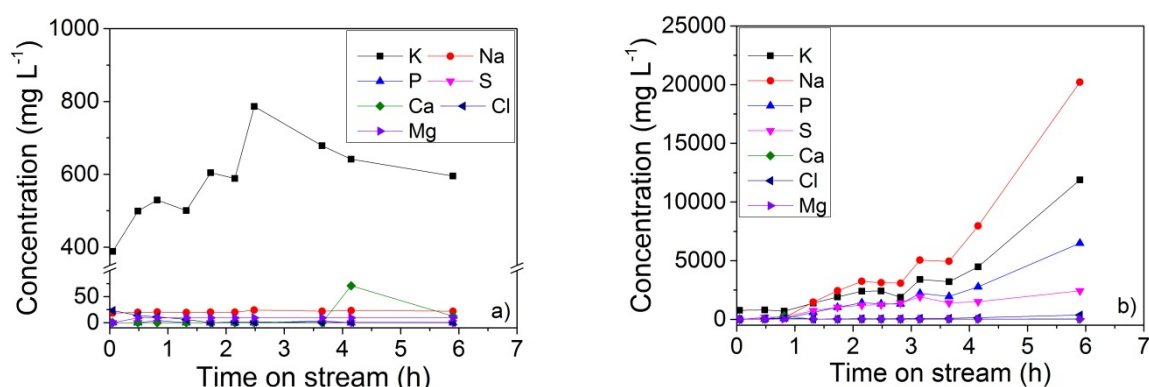
**Figure 6.22.** Picture of the brine effluent samples taken during the experiment KT9.

In Figure 6.23 (a), the higher conductivity of the reactor and the brine effluents compared to the one of the feed suggests a good liquefaction. After 3.5 h, the conductivity of the brine suddenly increased from 28000 to 88000  $\mu\text{S cm}^{-1}$  in line with the higher concentration of elements detected by ICP-OES (see Figure 6.24 (b)). Since no parameters were changed (*e.g.* Liquiflow) during the experiment, the sudden wash out of some minerals accumulated in the salt separator may be the reason. As shown in Figure 6.23 (b), the carbon concentration of both effluents is low, especially the one of the reactor effluent due to the high catalytic activity of the catalyst. Unfortunately, due to the absence of a mass flow meter, no information concerning the carbon recovery could be provided. Moreover, due to some problems encountered with the gas meter, the gas flow rate was not measured during the experiment. As observed in the previous liquefaction experiments, the nitrogen concentration of the brine and the reactor effluents was similar to the one of the feed (see Figure 6.23 (c)). CNS and ICP-OES measurements confirmed the absence of sulfur in the reactor effluent suggesting that sulfur was efficiently removed by the adsorbent (see Figure 6.23 (d) and 6.24 (a)). Unfortunately, it was decided not to open the reactor for harvesting the adsorbent and the catalyst because some additional experiments were carried out with the same charge prior to the gasification campaign (see chapter 7). Hence, at this stage, no analysis of the spent ZnO adsorbent and catalyst were performed.



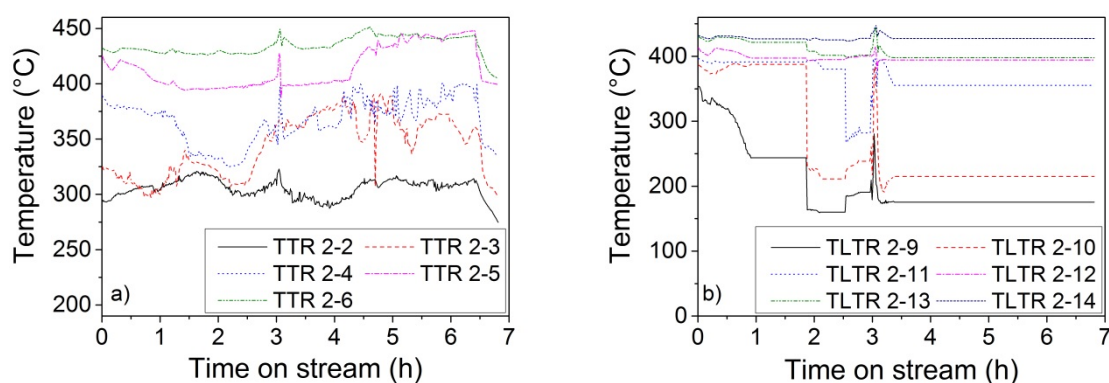
**Figure 6.23.** Evolution of the (a) conductivity, (b) carbon, (c) nitrogen, and (d) sulfur concentration of the feed, the brine, and the reactor effluents during the experiment KT9.

In Figure 6.24 (a), K was found to be the main element in the reactor effluent, whereas the content of Na, P, Ca, Cl, and Mg were below 50 ppm. Elliott et al. [94] reported that K was the major component in the reactor effluent during continuous hydrothermal gasification of microalgae at 350 °C and 20 MPa. According to them, the absence of other elements (e.g. Mg, Ca, P) was due to their lower solubility, which have likely precipitated as sulfates or phosphates. Interestingly, they detected these elements at a high concentration on the solid filter used to separate the minerals. In Figure 6.24 (b), a brine effluent containing a high concentration of minerals was achieved in which Na, K, P, and S were found to be the major components. These results reveal the good performance of the salt separator for recovering the minerals during continuous CSCWG of microalgae. Interestingly, during hydrothermal liquefaction of the same microalgae carried out in batch reactor, it was observed that Na, K, P, and S were almost exclusively recovered in the aqueous fraction, whereas Ca and Mg were only recovered in the solid residue [26]. Hence, the absence of Ca and Mg can be explained by their precipitation under SCW conditions.



**Figure 6.24.** ICP-OES analysis of the (a) reactor and (b) brine effluents during the experiment KT9.

As observed during the previous runs, the temperature profile at the inner wall of the salt separator exhibited some slight fluctuations and the temperature of TLTR 2-9 dropped from 350 °C up to 160 °C during the experiment (see Figure 6.25 (b)). Unfortunately, the thermocouples located at the lance of the salt separator were frozen during almost all the experiment rendering difficult the interpretation of the temperature profile. After 3 h, the temperature peak recorded at the lance of the salt separator and the reactor coincided with the pressure increase recorded in the salt separator (see Figure 6.25 (b) and (c)). As previously discussed, plugging of the standpipe caused by coke, salt precipitations, or/and other particles may be the reason of the pressure increase in the salt separator. As shown in Figure 6.25 (d), after only 1 h, all the pressure sensors indicate a sudden pressure increase. The same behavior was observed during the first continuous CSCWG experiment and the formation of methane hydrates was thought to be the cause. In order to minimize the formation of methane hydrates, it was decided to increase the temperature of the chiller from 25 °C to 30 °C. After this slight modification, only pressure increase in the salt separator was measured while the pressure in the reactor and at the Flowserve remained stable.





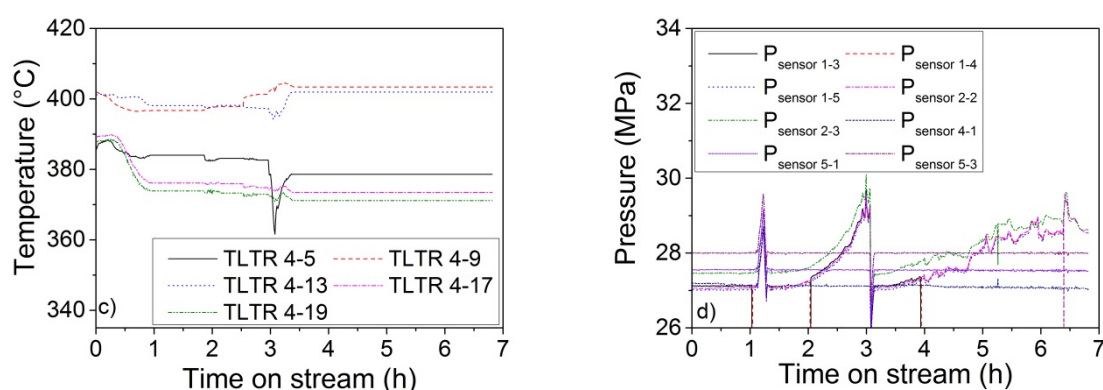


**Figure 6.25.** Temperature and pressure profile recorded during the experiment KT9. (a) The thermocouples located at the inner wall of the salt separator, starting from the bottom (TTR 2-2) to the top (TTR 2-6), (b) the thermocouples located on the lance of the salt separator starting from the bottom (TLTR 2-9) to the top (TLTR 2-14), and (c) the thermocouples located on the lance of the reactor starting from the bottom (TLTR 4-5) to the top (TLTR 4-19). (d) Pressure sensors where  $P_{\text{sensor 1-3}}$ ,  $P_{\text{sensor 1-4}}$ , and  $P_{\text{sensor 1-5}}$  are located at the slurry feeder,  $P_{\text{sensor 2-2}}$  is located before the salt separator,  $P_{\text{sensor 2-3}}$  is located in the middle of the salt separator,  $P_{\text{sensor 4-1}}$  is located in the reactor,  $P_{\text{sensor 5-1}}$  is located upstream of the reactor effluent filter, and  $P_{\text{sensor 5-3}}$  is located downstream of the reactor effluent filter.

### 6.3 Summary

In this chapter, continuous liquefaction and CSCWG of microalgae (*Phaeod. tric.*) were carried out within KONTI-C. The aim was to get familiar with KONTI-C and to assess/optimize: i) the stability of the process regarding plugging (e.g. tar and coke formation, salt precipitation), ii) the salt recovery in the brine effluent, iii) the sulfur adsorption performance of the ZnO adsorbent, and iv) the catalytic performance of a 5% Ru/C<sub>BASF</sub> catalyst. The most relevant results are summarized below:

- The preliminary experiments performed with model salt solutions (ternary mixture of Na<sub>2</sub>SO<sub>4</sub>-K<sub>2</sub>SO<sub>4</sub> in H<sub>2</sub>O; Na<sub>2</sub>SO<sub>4</sub>-K<sub>2</sub>SO<sub>4</sub> in 10 wt % IPA) showed that all the salts and the inorganic sulfur can be efficiently removed from the reactor effluent.
- In presence of IPA, the sulfur recovery of the brine effluent was close to 90% whereas in absence of IPA, the latter was only 44%.
- When microalgae were liquefied, the stability of the process was significantly affected by plugging occurring in the standpipe and/or at the bottom of the salt separator. Coke formation, salt precipitation, and/or other particles coming from the feed were thought to be the cause. Some process parameters such as the temperature and the feed rate were changed in order to improve the stability of the process. Unfortunately, no positive effect was observed. The replacement of a filter (250  $\mu\text{m}$ ) located upstream of the salt separator

by a smaller one (25  $\mu\text{m}$ ) has considerably improved the stability of the process. Hence, it seems that some particles coming from the feed were blocked in the standpipe.

- The conductivity recorded on-line was a reliable indicator for the liquefaction efficiency. In fact, when the conditions were too mild in the salt separator for a proper liquefaction, the conductivity of both effluents were similar and/or below the one of the feed. When the conditions were harsh enough for liquefying the biomass, both effluents exhibited a higher conductivity than the one of the feed.
- CNS elemental analysis showed that more than half of the carbon contained in the feed was recovered neither in the brine nor in the reactor effluents. Tar and coke formation inside the process were responsible. The nitrogen recovery was much higher than the one of carbon and slightly inferior to the one of the feed. Concerning the sulfur concentration, when the liquefaction efficiency was satisfactory, the sulfur concentration of the brine effluent was superior to the one of the feed.
- During the liquefaction experiments performed in absence of ZnO, a small amount of gas composed of mainly CO<sub>2</sub> (92 vol %), was produced in the reactor effluent. In presence of ZnO, the gas composition was composed of CO<sub>2</sub> (50 vol %) and H<sub>2</sub> (49 vol %) suggesting that ZnO favors the steam reforming and the WGS reactions.
- The absence of sulfur in the reactor effluent during the liquefaction and the CSCWG experiments revealed that ZnO was an effective sulfur adsorbent under SCW conditions.
- A stable gas composition similar to the thermodynamic chemical equilibrium was obtained over a period of 7 h during continuous CSCWG of microalgae over a 5% Ru/C<sub>BASF</sub> catalyst. The high CH<sub>4</sub> concentration (57 vol %) confirmed the good catalytic performance of the catalyst for favoring the methanation reaction.
- The catalyst was able to reduce up to 95.1-99.9 % the TOC contained in the feed demonstrating its high catalytic activity for converting the organic carbon to gaseous products.
- ICP-OES analysis of the brine effluent showed a high concentration of minerals such as Na, K, P, and S, whereas only a small concentration of K was measured in the reactor effluent.



These promising results revealed the good performance of the salt separator during continuous CSCWG of microalgae.

- Many technical problems (*e.g.* malfunction of the Liquiflow, pressure controller, pressure relief valve) occurred when working under SCW conditions with microalgae with such a complex PDU. Although the period was relatively short prior to the gasification campaign (only three months), these preliminary experiments with KONTI-C were crucial for acquiring more experience.

## Chapter 7 Gasification Campaign in Wädenswil (CH)

In this chapter, the results from the gasification campaign performed on the microalgae production site of ZHAW in Wädenswil (CH) is presented. This campaign was used to demonstrate the technical feasibility of methane production from microalgae (*Chlorella vul.*) via continuous CSCWG. The campaign was carried out non-stop over a period of 100 h with KONTI-C. In total, 13 persons of the SunChem project team participated in the gasification campaign.

### 7.1 Feedstock composition

In Table 7.1, the chemical composition of *Chlorella vul.* is listed. Note that the composition of the feedstock does not solely represent the chemical composition of the microalgae but also the one of the cultivation medium.

**Table 7.1.** Elemental composition of *Chlorella vul.* calculated on a dry matter basis.

C wt %	H wt %	N wt %	O wt %	S wt %	P wt %	Cl wt %	Ash content wt %
50.0 ± 0.1	7.1 ± 0.0	5.8 ± 0.0	33.8 ± 0.2	0.5 ± 0.0	0.6 ± 0.0	0.07	3.4 ± 0.0

### 7.2 Process parameters

The different process parameters of the gasification campaign are listed in Table 7.2. The first day (0-19 h), the microalgae were directly taken from the pond without any further treatment. Then, until the end of the campaign (25-99 h), the feed was taken from microalgae, which had been harvested from the same pond, dewatered, and frozen. Depending on the desired feed concentration, the microalgae were thawed and diluted with pure water. In order to improve the stability of the microalgae suspension, a small amount (< 0.05 wt % of the total feed slurry) of xanthan gum was added to the feed. Due to some overpressure issues encountered at certain times (after 13 h, 19 h, 56 h, and 84 h), the plant was flushed with pure water. Note that between 59-83 h, the temperature

at the top of the salt separator was in the subcritical region and lower than the one at the bottom of the reactor. Hence, the overpressure issues observed in that period may be explained by the salt precipitation at the reactor entrance. The mass of the commercial ZnO adsorbent (Katalco 32-5) (not based on a dry basis) and the 5% Ru/C<sub>BASF</sub> catalyst (based on a dry basis) was 713 g and 493 g, respectively.

**Table 7.2.** List of the process parameters during the gasification campaign (exp. KT10).

Dry matter wt %	Time on stream h	Slurry feeder freq. Hz	T <sub>Salt sep. bottom</sub> °C	T <sub>Salt sep. top</sub> °C	T <sub>Reactor bottom</sub> °C	T <sub>Reactor top</sub> °C	P MPa
2.8 <sup>a</sup>	0-13 <sup>*</sup>	20-21	274	414	407	390	28-29
2.8 <sup>a</sup>	18-19 <sup>*</sup>	21	267	418	404	385	28-29
6.5 <sup>b</sup>	25-50	20	299	412	420	379	28-29
14.8 <sup>b</sup>	50-56 <sup>*</sup>	20	287	396	415	372	28-29
6.0 <sup>b</sup>	59-83	17-19	264	368	394	363	25-26
3.0 <sup>b</sup>	83-84 <sup>*</sup>	N.A.	325	414	411	385	25-28
3.0 <sup>b</sup>	89-95	18-19	306	414	407	388	27-29
6.0 <sup>b</sup>	95-99	16-19	318	440	413	385	26-30

<sup>\*</sup> starting to rinse the plant with water [a] feed coming directly from the pond [b] feed coming from the freezer.

The mass flow rate was estimated by recording the amount of microalgae filled in the cylinder and by dividing that value by the time of feeding. For that, a short time of feeding (15-20 min) was settled for each cylinder of the Slurry feeder during the campaign. In Table 7.3, the estimated feed rates are listed and compared with those calculated by summing the rate of the effluents.

**Table 7.3.** Estimation of the feed rate during the gasification campaign.

Time on stream h	$\dot{m}_{\text{Feed}}$ g min <sup>-1</sup>	$\dot{m}_{\text{Brine}} + \dot{m}_{\text{Reactor}}$ g min <sup>-1</sup>
7	25.6 ± 1.7	22.0 ± 1.0
10	21.9 ± 3.7	21.9 ± 0.8
40	25.1 ± 0.8	24.4 ± 2.0
50	25.2 ± 0.4	25.0 ± 1.8
70	17.1 ± 1.8	20.9 ± 2.5
96	23.8 ± 0.7	21.0 ± 4.1

According to the standard error of the mean, the estimated feed rates are similar to the sum of the effluent rates. Consequently, the estimated feed rates were used for the calculation of the GE<sub>C</sub> and

the carbon, the nitrogen, and the sulfur recoveries. Moreover, the estimated WHSV was 0.08-0.42  $\text{g}_{\text{algae}} \text{g}_{\text{cat}}^{-1} \text{h}^{-1}$  by assuming an average feed rate of  $23 \text{ g min}^{-1}$  during the campaign. Note that the feed rate could not be estimated for each collected sample due to some issues encountered with the analytical balance used for recording the amount of microalgae filled in the cylinder.

### 7.3 Gas analysis

In Figure 7.1, the gas composition recorded on-line is depicted. During the first 10 h of the experiment, a gas containing mainly  $\text{H}_2$  (37 vol %),  $\text{CO}_2$  (33 vol %), and  $\text{CH}_4$  (30 vol %) was obtained. The relatively high  $\text{H}_2$  concentration in comparison to the  $\text{CH}_4$  concentration can be explained by the low concentration of the feed (ca. 3 wt %) [16]. For thermodynamic reasons, a lower concentration of biomass, or a higher concentration of water, favors the formation of  $\text{H}_2$ . When a higher feed concentration (ca. 6 wt %) was processed, the gas composition changed towards more methane and reached the concentrations which are expected from the thermodynamic chemical equilibrium [17]. A stable gas composition, containing a  $\text{CH}_4$ -rich gas (55-60 vol %) was recorded from 27 h to 55 h. The high  $\text{CH}_4$  concentration demonstrates the good catalytic performance of the 5% Ru/ $\text{C}_{\text{BASF}}$  catalyst for enhancing the methanation reaction. Note that due to a problem encountered with the microGC, the  $\text{CO}_2$  and  $\text{C}_{2+}$  concentrations were not measured. The  $\text{CO}_2$  concentration was estimated by subtracting the  $\text{H}_2$  and  $\text{CH}_4$  concentrations from 100 vol %. After 55 h, when a higher feed concentration was processed (15 wt %), the progressive decrease of the  $\text{CH}_4$  concentration with the simultaneous increase of the  $\text{H}_2$  concentration indicates a deactivation of the catalyst. After 70 h, the  $\text{CH}_4$  concentration stabilized and remained in the range of 7-18 vol % until the end of the gasification campaign. A similar change of the gas composition was observed in earlier experiments and could be attributed to sulfur poisoning and coking of the Ru/C catalyst [17]. Unlike in the present experiment, this change occurred very quickly when the feed was switched to 6.5 wt % *Phaeod. tric.*. It is likely that the absence of a sulfur removal step and the lower ruthenium loading of the catalyst were the reasons for such a fast deactivation of the catalyst in the earlier experiment. In fact, in the earlier work, the liquefied feed coming from the salt separator entered directly the catalytic reactor without any further pre-treatments [17].

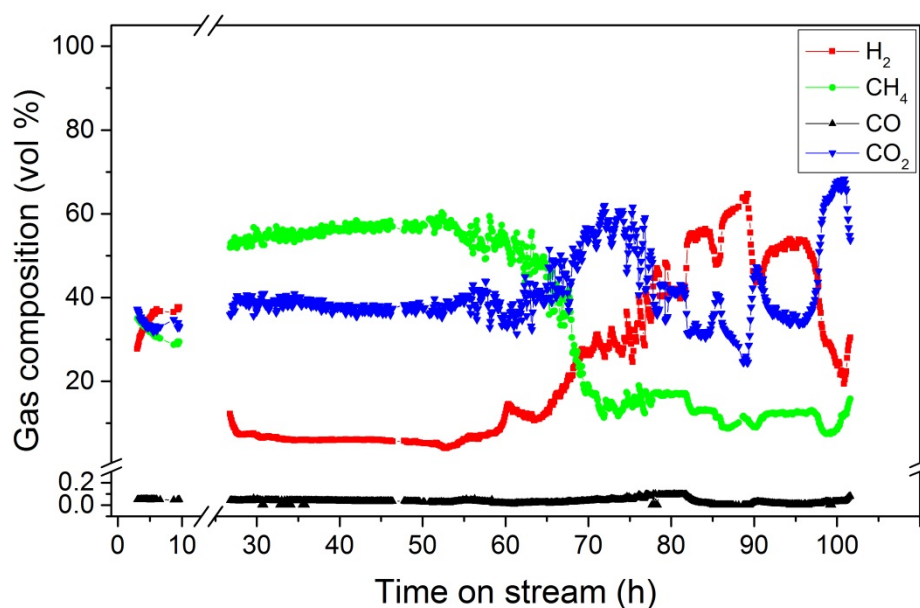


**Figure 7.1.** Gas composition measured on-line.

In Figure 7.2, the gas production measured on-line and the  $GE_c$  are shown. The gas production reflects the catalytic activity well, and its significant decrease after 55 h can be related to the deactivation of the catalyst. Large variations in the gas production were recorded between 50 h and 55 h when processing the concentrated feed (15 wt %) showing the difficulty of the process to reach a steady state. During the first 10 h of the experiment, the  $GE_c$  was surprisingly low and the precipitation of the microalgae suspension inside the Slurry feeder was the most likely reason. In fact, after 13 h, a high increase of the pressure was observed upstream of the salt separator leading to a flushing of the plant with DI water. Then, it was decided to add a small amount of xanthan gum in order to stabilize the slurry. When the gas composition was close to the thermodynamic chemical equilibrium between 40-50 h, the  $GE_c$  was only 45-50%. Note that after 45 h, a considerable amount of tarry products leaving the salt separator through the brine effluent was observed. The fact that these tars were not quantified and not taken into account in the  $GE_c$  calculation would explain the low  $GE_c$ . In fact, according to equation 2.13, if this carbon loss in the brine effluent would have been taken into account, the  $GE_c$  values would have been higher. Elliott et al. [94] reported  $GE_c$  values fluctuating between 40-106% according to the microalgae species. They explained these low  $GE_c$  values by the loss of carbon in the mineral separator. After 70 h, in line with the decrease of the gas production, the  $GE_c$  dropped below 17%.

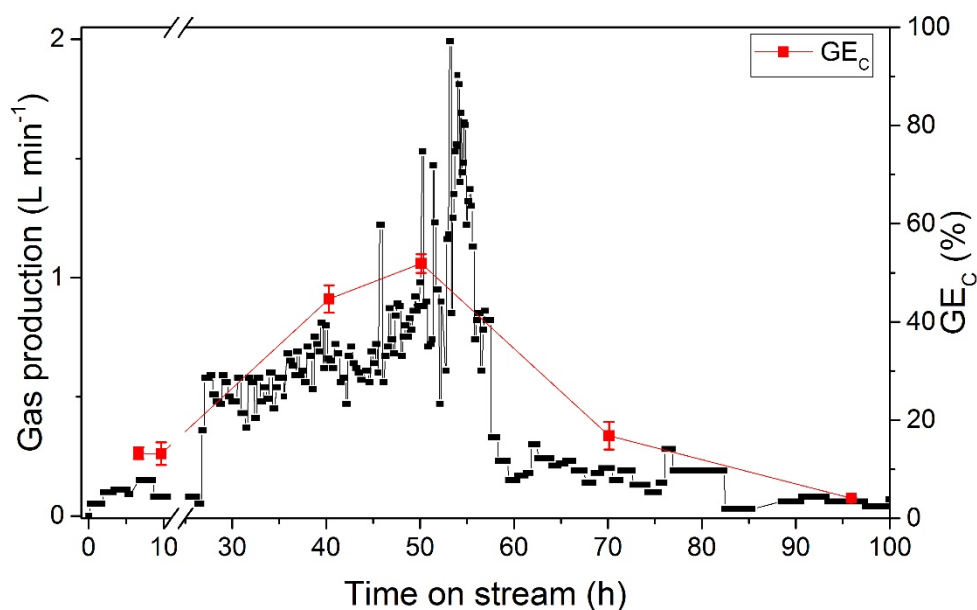


**Figure 7.2.** Gas production measured on-line and  $GE_C$ .

## 7.4 Analysis of the liquid effluents

In Figure 7.3, the low TOC content of the reactor effluent ( $< 400 \text{ mg L}^{-1}$ ) recorded during 50 h demonstrates the high catalytic activity of the catalyst for converting the microalgae from the liquid to the gas phase. As a result, a clean water phase was obtained (see Figure 7.5), in which a TOC reduction of 98.5-98.8% was calculated. After 60 h, the sudden change of the reactor effluent color (to yellow-brownish) and the appearance of a small amount of solid particles (coke) coincided with the higher TOC content measured. The presence of a higher amount of organic carbon shows the incapacity of the catalyst for breaking efficiently the C-C bonds due to a deactivation of the catalyst. The TIC values were relatively high (up to  $2900 \text{ mg L}^{-1}$ ) and can be attributed to the dissolved  $\text{CO}_2$ . Interestingly, the sample collected after 63 h was composed of an aqueous phase and an oily phase. As shown in Table 7.4, the oily phase was mainly composed of carbon, with some nitrogen and sulfur (and very likely also hydrogen and oxygen, which were not determined). The appearance of that oily phase occurred after having processed the concentrated feed (15 wt %). In fact, it seems that the salt separator was not able to heat up such a high concentration of microalgae, resulting in an insufficient liquefaction. The feed went through the salt separator without having being fully degraded. Hence, the ZnO bed and the catalyst bed may have been contaminated with the non- or partially liquefied feed, accelerating the deactivation of the catalyst. In Figure 7.6, the appearance of tars

and coke in the sample of the brine effluent taken after 50.1 h confirmed that the salt separator did not work properly when fed with the concentrated feed. As an explanation regarding the incapacity of the salt separator for heating up the concentrated feed, the precipitation and deposition at the wall of the salt separator of a high amount of minerals may be likely. In fact, the minerals may act as a resistance to the heat transfer from the heater to the fluid. Consequently, less heat was available for ensuring a proper liquefaction. The presence of sulfur reflects the incapacity of the adsorbent for the sulfur removal and indicates that the catalyst bed was contaminated with sulfur.

**Table 7.4.** Chemical composition of the oily phase of the sample taken at 63 h.

Sample	C wt % <sup>a</sup>	N wt % <sup>a</sup>	S wt % <sup>a</sup>
Oily phase	82.3 ± 3.5	1.7 ± 0.1	0.06 ± 0.01

[a] Determined with CNS elemental analysis.

Concerning the brine effluent, the TC and the TOC contents were both similar and significantly higher than those of the reactor effluent, showing the presence of a higher concentration of organic compounds in the brine effluent. By comparing the TC of the two effluents with the one of the feed, the higher values of the latter show that the carbon was either converted to the gas phase and/or accumulated in the plant.

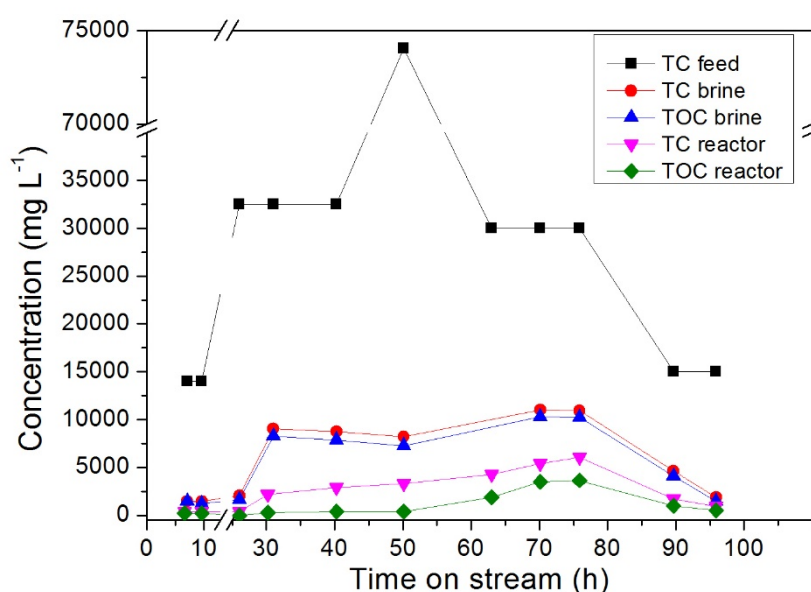


**Figure 7.3.** Evolution of the TC and TOC concentration of the feed, the reactor, and the brine effluents. Note that the TC of the feed was calculated based on a dry matter basis.

The carbon recovery, which did not exceed 63% (see Figure 7.4), confirms that a considerable amount of carbon was lost. Presumably, most of it left the plant as tars through the brine effluent, which was not collected as a whole. Some carbon also accumulated in the process. Similarly to the  $GE_c$  values, during the first 10 h of the experiment, the low carbon recovery can be attributed to the precipitation of the microalgae suspension inside the Slurry feeder. After 70 h, due to a high standard deviation of  $m_{\text{Reactor}}$ , a high standard error of the mean was calculated.

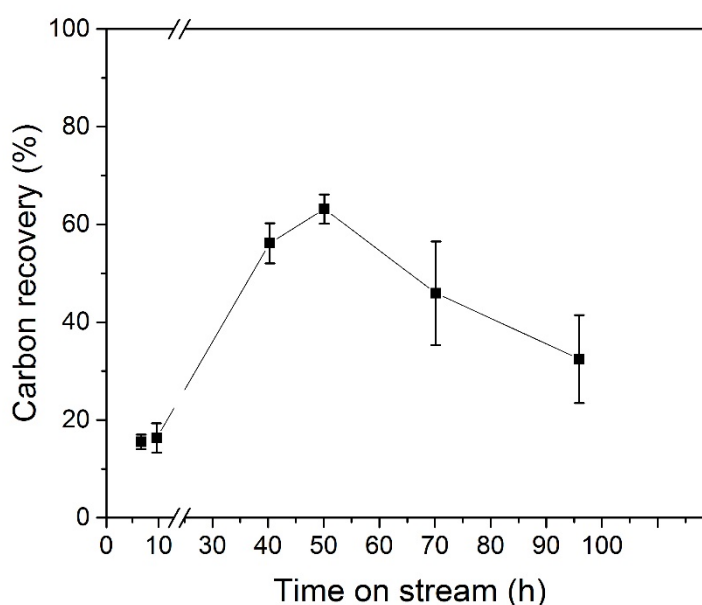


**Figure 7.4.** Evolution of the carbon recovery.

In Table 7.5, an overall carbon mass balance is depicted. Note that due to a lack of harvested samples (at time on stream: 83-84 h and 96-99 h) and problem encountered with the microGC (at time on stream: 18-19 h), the carbon mass balance is just a rough estimation and the calculated carbon recovery is slightly underestimated.

**Table 7.5.** Overall carbon mass balance.

$m_{C,\text{Feed}}$	$m_{C,\text{Brine}}$	$m_{C,\text{Reactor}}$	$m_{C,\text{Gas}}$	$m_{C,\text{Loss}}$	Recovery <sub>c</sub>
g	g	g	g	g	%
3217	209	289	873	1844	42.7

According to the plant capacity, *i.e.* volume of process units, such a high carbon loss could not have accumulated in the process. In fact, as already mentioned (see section 7.2), after 45 h, a high amount



of tarry products leaving the salt separator via the brine effluent was observed demonstrating that the salt separator was saturated with carbonaceous materials. The high quantity of tars caused also a severe accumulation of carbon in the phase separator of the brine effluent. Moreover, some tars left the phase separator at the top and spread outside of the plant. Unfortunately, the total amount of tar, which has left the plant, was not quantified and thus not taken into account for the overall carbon mass balance. Consequently, a high fraction of the estimated carbon loss comes from the tarry products, which have left the salt separator.

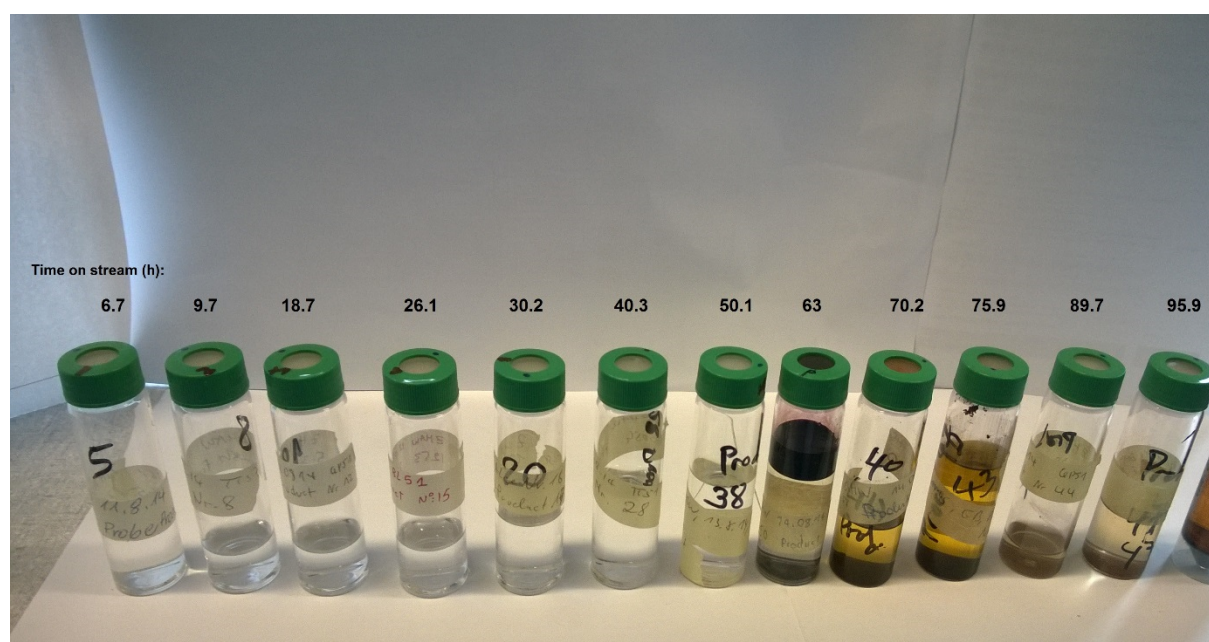


**Figure 7.5.** Visual aspect of the samples collected from the reactor effluent.

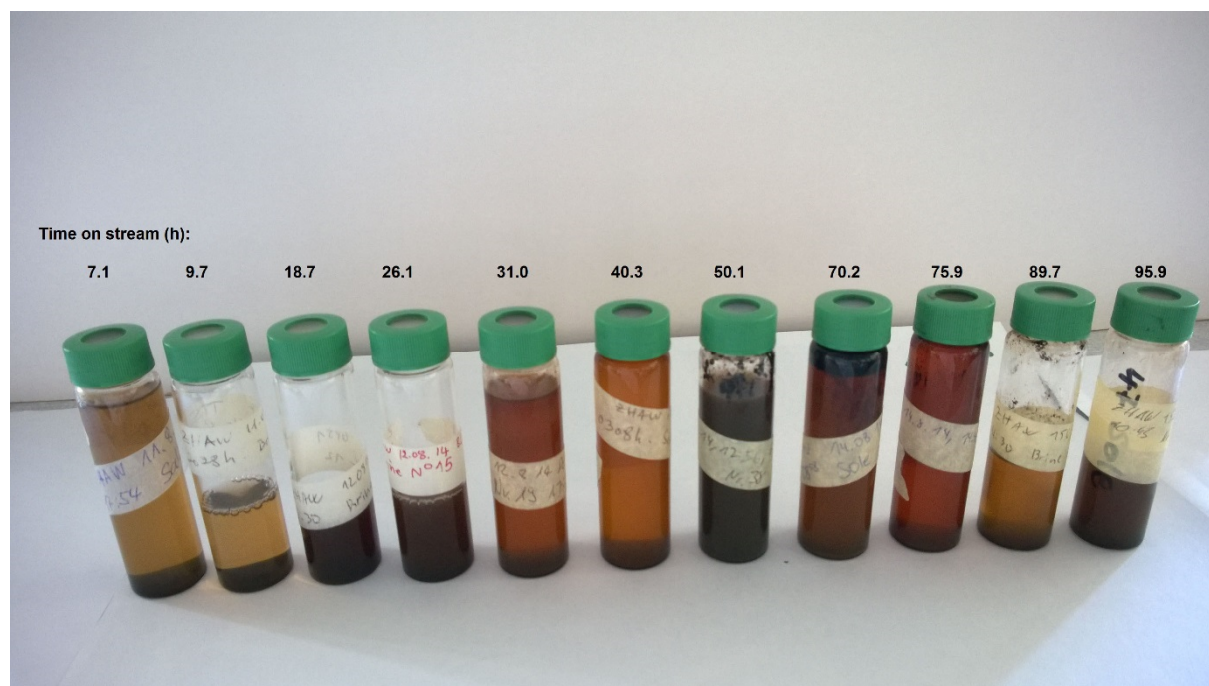


**Figure 7.6.** Visual aspect of the samples collected from the brine effluent.

As it can be seen in Figure 7.7, a significant difference between the ammonium and the nitrogen concentration was measured after 30 h in the reactor effluent. The higher total nitrogen content in comparison to the ammonium content suggests that other N-containing compounds such as nitrates or Maillard products (melanoidins) were formed. The pH of the reactor effluent was slightly basic (pH = 8.5-9) and can be explained by the presence of ammonium/ammonia [17,94]. Although the brine effluent contained a higher concentration of ammonium than the one of the reactor effluent, the pH was in the range of 6. This is likely due to the presence of higher concentrations of organic acids. As observed in the reactor effluent, a higher nitrogen concentration in comparison to the ammonium concentration was found in the brine effluent, suggesting the presence of other N-compounds (e.g. nitrates, pyridines, Maillard products) as mentioned by Brandenberger [17]. According to the nitrogen recovery, except for the first 10 h, most of the nitrogen contained in the feed was recovered in the liquid effluents (see Figure 7.8). Christensen et al. [26] also observed that most of the nitrogen was recovered in the aqueous phase during hydrothermal liquefaction of *Phaeod. tric.*. Note that due to a high standard deviation of  $\dot{m}_{\text{Reactor}}$ , especially at 70 h and 96 h, a high standard error of the mean was calculated.

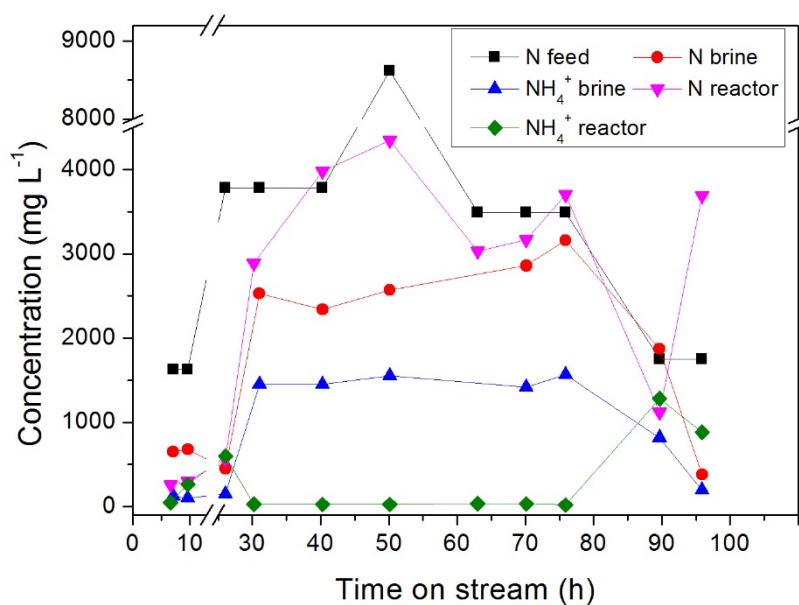


**Figure 7.7.** Evolution of the nitrogen and  $\text{NH}_4^+$  concentration of the feed, the reactor, and the brine effluents. Note that the nitrogen of the feed was calculated based on a dry matter basis.

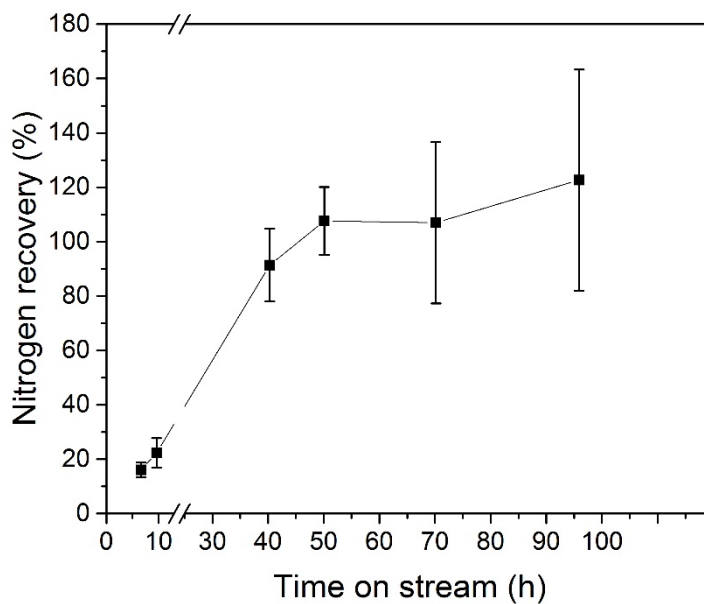


**Figure 7.8.** Evolution of the nitrogen recovery.

As shown in Figure 7.9, no sulfur was detected in the reactor effluent (aqueous phase) during 70 h demonstrating the good sulfur adsorption performance of the ZnO adsorbent. As previously discussed, sulfur was first detected in the oily phase of the sample collected after 63 h.

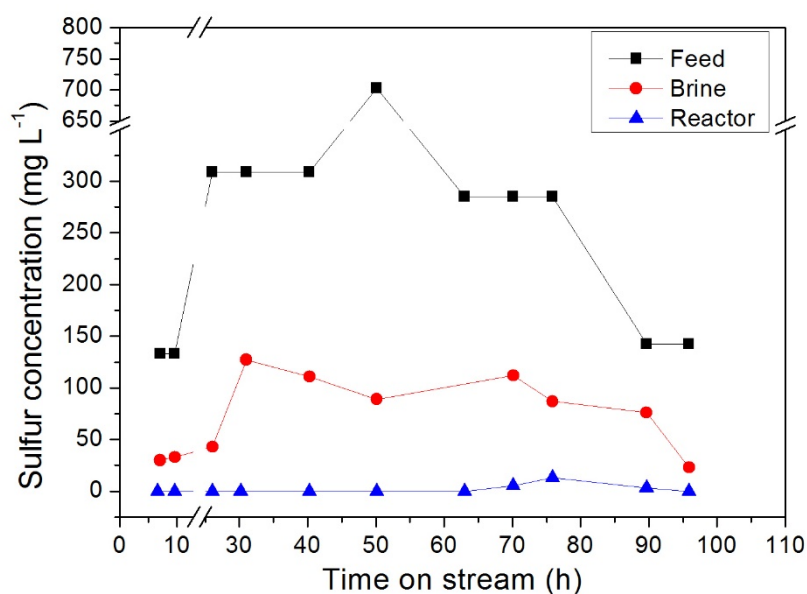


**Figure 7.9.** Evolution of the sulfur concentration of the feed, the reactor, and the brine effluents. Note that the sulfur of the feed was calculated based on a dry matter basis.

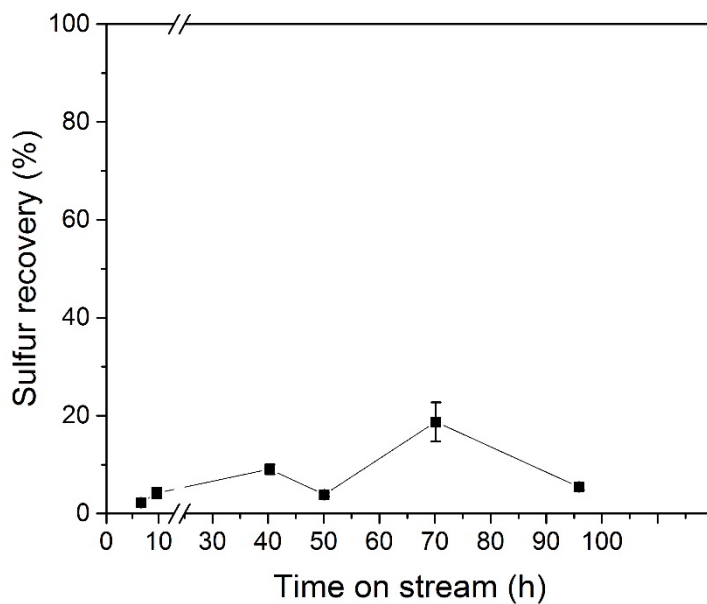


**Figure 7.10.** Evolution of the sulfur recovery.

According to Figure 7.10, a low sulfur recovery was calculated. As no sulfur was detected in the reactor effluent, except at 70 h, the standard error of the mean was small since only the errors on  $\dot{m}_{\text{Feed}}$  and  $\dot{m}_{\text{Brine}}$  were taken into account. In Table 7.6, the overall sulfur mass balance confirms that

most of the sulfur was accumulated in the process. It remains unclear if sulfur was fully adsorbed on the ZnO adsorbent or the catalyst or even deposited at the wall. By assuming that all the Zn and Ru would react to ZnS and RuS, the total amount of adsorbed sulfur would be ca. 281 g on the ZnO bed and ca. 8 g on the catalyst bed. Therefore according to that estimation, most of the ZnO bed would not have reacted with sulfur. Concerning the sulfur distribution along the ZnO bed and the catalyst bed, due to the relatively low ratio between the reactor diameter ( $d_{\text{reactor}} = 36 \text{ mm}$ ) and the particle diameter of ZnO ( $d_p = 2.8\text{-}4.8 \text{ mm}$ ) which was 8-13, some channeling at the reactor wall might be expected. In fact, it is reported to be significant for ratio below 30 and mass transfer rates are also reported to be lower in presence of large particles [163]. As a consequence, it is unlikely that all the accumulated sulfur has reacted solely with the ZnO bed and most probably that a fraction of sulfur passed through the ZnO bed to the catalyst bed.

**Table 7.6.** Overall sulfur mass balance.

$m_{\text{S,Feed}}$ g	$m_{\text{S,Brine}}$ g	$m_{\text{S,Reactor}}$ g	$m_{\text{S,Accumulation}}$ g	Recovery %
30.77	2.29	0.02	28.46	7.51

According to the ICP-OES analysis (see Figure 7.11), mainly highly soluble alkali metals such as K and Na were detected in the reactor effluent. A similar result was reported by Elliott et al. [94] although another microalgae specie (*Nannochloropsis salina*) was processed. No Ru and Zn were found confirming that Ru and Zn leaching did not occur to a significant extent. By contrast Elliott et al. [94] detected some traces of Ni in the reactor effluent showing that Raney Ni, which was used as a sulfur adsorbent, tends to solubilize from the adsorbent bed. In Figure 7.12, ICP-OES analysis of the brine effluent shows, as expected, a higher minerals content (K, P, and Na) than the reactor effluent. According to the chemical analysis, the performance of the salt separator was effective for the mineral recovery. Therefore the recycling of such a minerals-rich effluent for the microalgae growth seems promising. However, more toxicity studies (e.g. toxicity of N-compounds on the microalgae growth) are needed prior to ensuring direct recycling of the brine and reactor effluents to the microalgae cultivation system.

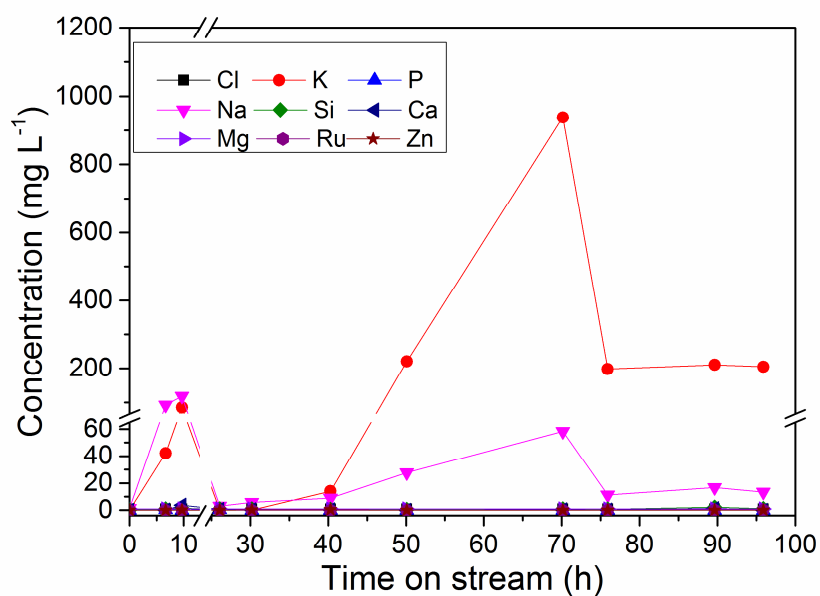


Figure 7.11. ICP-OES analysis of the reactor effluent.

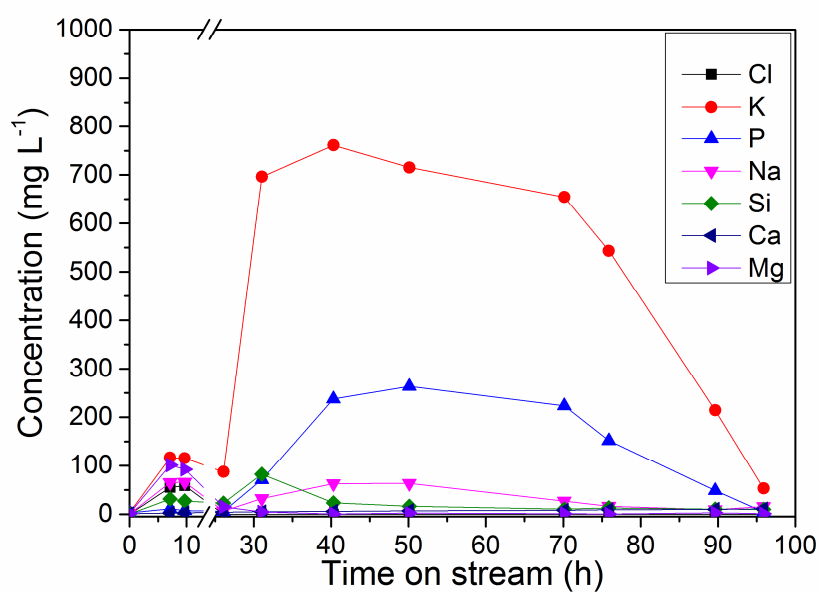


Figure 7.12. ICP-OES analysis of the brine effluent.

## 7.5 Analysis of the solid residue

At the end of the gasification campaign, the process was cooled down with DI water and the salt separator was opened for investigation. A solid residue was found inside the salt separator and was

harvested. In Table 7.7, the chemical analysis shows that the residue was mainly composed of carbon and ash. These results were similar to those reported by Elliott et al. [94] where the average of the solid residue was 35 wt % carbon, 4 wt % nitrogen, and 41 wt % ash. The ash content was high and consisted of minerals (e.g. P, Ca, Mg). The presence of a high amount of ash is explained by the minerals, which have precipitated under SCW conditions. In fact, the presence of these minerals is in good agreement with Elliott's results since Ca and Mg were also observed on the solid residue and were proposed to precipitate as sulfate or phosphate [94]. In agreement with the analysis of the reactor effluent, the absence of highly soluble alkali metals such as K and Na was expected. The fact that phosphorus was detected in the aqueous phase (brine effluent) and on the solid residue shows that the latter was distributed in both phases. Such a distribution was observed during hydrothermal liquefaction of *Phaeod. tric.* (275-420 °C, 28 MPa) where a transition of phosphorus from the aqueous phase to the solid residue was found to increase when increasing the reaction temperature [26].

**Table 7.7.** Chemical composition of the solid residue.

Composition, wt %	Solid residue
Ash content	55.07 ± 0.72
C <sup>a</sup>	33.16 ± 0.13
H <sup>a</sup>	2.13 ± 0.01
N <sup>a</sup>	2.65 ± 0.00
O <sup>a</sup>	14.55 ± 0.24
S <sup>a</sup>	0.03 ± 0.00
P <sup>a</sup>	12.16 ± 0.02
Cl <sup>a</sup>	0.16 ± 0.00
Ca <sup>b</sup>	4.92 ± 0.01
Mg <sup>b</sup>	2.92 ± 0.12
Fe <sup>b</sup>	0.50 ± 0.01
Mn <sup>b</sup>	0.16 ± 0.00
K <sup>b</sup>	0.03 ± 0.00
Cu <sup>b</sup>	0.06 ± 0.00
Zn <sup>b</sup>	0.13 ± 0.00

[a] Determined with elemental analysis [b] determined with WDXRF analysis.

The accumulation of minerals shows that the salt separator is not optimal yet and some improvements need to be undertaken (e.g. a better understanding of fluid dynamic and salt precipitation

under SCW conditions). However, due to the different conditions occurring inside the salt separation during all the campaign, it is not clear at what moment the solid residue was formed.

In order to identify the chemical compounds present on the solid residue, GC-MS analysis after extraction of the solid residue with toluene, was carried out. Mainly alkyl benzene compounds such as benzeneacetaldehyde, 1-ethyl-3-methylbenzene, 1-ethyl-2-methylbenzene, 1,2,3-trimethylbenzene, cyclopropylbenzene, butylbenzene, and 1,2,8-p-mentatriene were found. The presence of such aromatic compounds is typically what is referred as tars [167,168]. Besides, the improvement of the salt separation, it is also required to better understand tar and coke formation in the salt separator in order to improve the GE<sub>C</sub>.

## 7.6 Characterization of the spent catalyst

Three different fractions of the spent catalysts were harvested after the gasification campaign. The bottom fraction corresponds to the lower part of the bed, which was located after the ZnO bed, whereas the top fraction was located at the reactor outlet. As shown in Table 7.8, the physical structure was significantly affected at the bottom fraction since almost all the BET SSA was lost. The BET SSA at the middle and top fractions were both slightly reduced with a loss of 15% and 11% in comparison to the fresh catalyst.

**Table 7.8.** Characteristics of the fresh and spent 5% Ru/C<sub>BASF</sub> catalysts.

Catalyst	BET SSA m <sup>2</sup> g <sup>-1</sup>	V <sub>microp.</sub> cm <sup>3</sup> g <sup>-1</sup>	V <sub>mesop.</sub> cm <sup>3</sup> g <sup>-1</sup>	D <sub>CO</sub> - <sup>a</sup>	D <sub>STEM</sub> - <sup>b</sup>	d <sub>p,CO</sub> nm <sup>a</sup>	d <sub>p,STEM</sub> nm <sup>b</sup>
Fresh Ru/C	1254	0.42	0.21	0.23	0.47	4	2.2 ± 0.1
Spent Ru/C bottom	56	0.00	0.11	0.01	N.A	139	N.A
Spent Ru/C middle	1064	0.33	0.28	0.03	N.A	34	N.A
Spent Ru/C top	1110	0.36	0.27	0.01	0.10	79	13.5 ± 0.4

[a] Determined by CO pulse chemisorption [b] determined by HAADF-STEM.

Such a decrease of the BET SSA was also observed by Brandenberger [17]. The catalyst support used by the authors was the same as the one used in this work, and any changes of its physical structure caused by the harsh conditions of SCW was excluded since its robustness was already proved [63]. According to them, coking and salt deposits on the catalyst were the main reasons. In chapter 3 (section 3.4), the stability of a Ru/C catalyst was studied during continuous CSCWG of 10 wt % IPA



(400 °C, 30 MPa) and it was shown that the pores of the catalyst were progressively filled by carbon deposits resulting in a complete loss of the porosity.

The CO-chemisorption results show that the Ru dispersion dropped considerably for the spent catalyst in comparison to the fresh catalyst. The dispersion was similar for the three fractions and close to zero proving that the catalyst bed was fully deactivated. These results are in good agreement with those reported by Brandenberger who reported a total loss of the Ru dispersion [17]. The incapacity of Ru for adsorbing CO reflects the loss of the methanation. Several deactivation mechanisms may be responsible: (i) leaching of Ru, (ii) sintering of the Ru NPs, (iii) physical blockage of the pores, and/or (iv) irreversible chemical bonding on the Ru NPs. In order to elucidate the causes of the deactivation of the catalyst, other characterization methods are required. In Figure 7.13, HAADF-STEM measurements were performed for assessing the Ru NPs size. As illustrated in Figure 7.13 (a), small Ru NPs (2 nm) highly dispersed were observed on the fresh catalyst. The histogram shows a narrow distribution of the NPs size (1-3.5 nm). Although the top fraction of the catalyst bed was weakly affected by coking and salt deposits, the Ru NPs size has considerably increased with a wider distribution (2-34 nm) (see Figure 7.13 (c)). Hence, sintering of the Ru NPs appears to be another possible mechanism for the loss of the catalytic activity. However, it remains still unclear what were the causes for the growth of the Ru NPs. It is likely that either the exposure in the harsh environment of SCW and/or the chemical bonding of some contaminants coming from the feed (*e.g.* sulfur) were responsible. In Figure 7.13 (b) and (d), the secondary electron images reveal the presence of some spheres on the spent catalyst having a high electron density. EDX analysis confirmed that these spheres corresponded solely to Ru NPs. The middle fraction of the spent catalyst was analyzed with SEM-EDX (see Figure 7.14). Some particles having a well-defined shape were deposited on the catalyst surface. Elemental mapping showed that these particles were constituted by minerals such as Na, Ca, S, and Zn. Thus, it seems that catalyst fouling caused by the precipitation of minerals also contributed to the deactivation of the catalyst. Although the SEM-EDX mapping did not show any sulfur species bonded on Ru NPs, an interesting trend between Zn, S, and Na was observed. The fact that these three elements were located on the same particles suggests that sulfur was adsorbed by Zn. In addition, the presence of Na indicates that the particles were likely  $\text{Na}_2\text{SO}_{4(s)}$  which is known to have a low solubility in SCW [42].

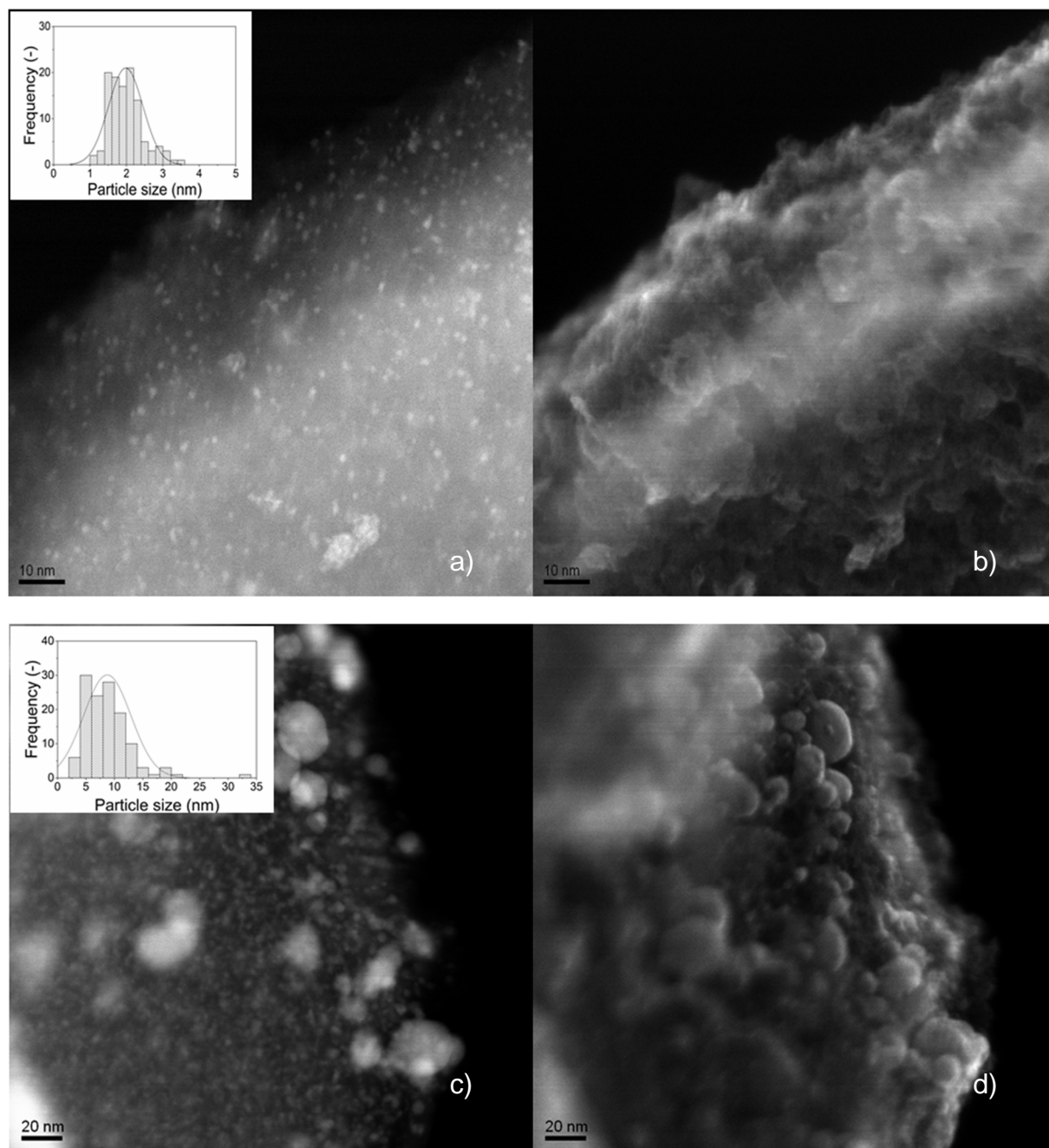


**Figure 7.13.** HAADF-STEM images of the (a), (b) fresh and (c), (d) spent (top fraction) 5% Ru/C<sub>BASF</sub> catalysts. The images (a) and (c) were acquired by Z contrast, whereas the images (b) and (d) by secondary electron.

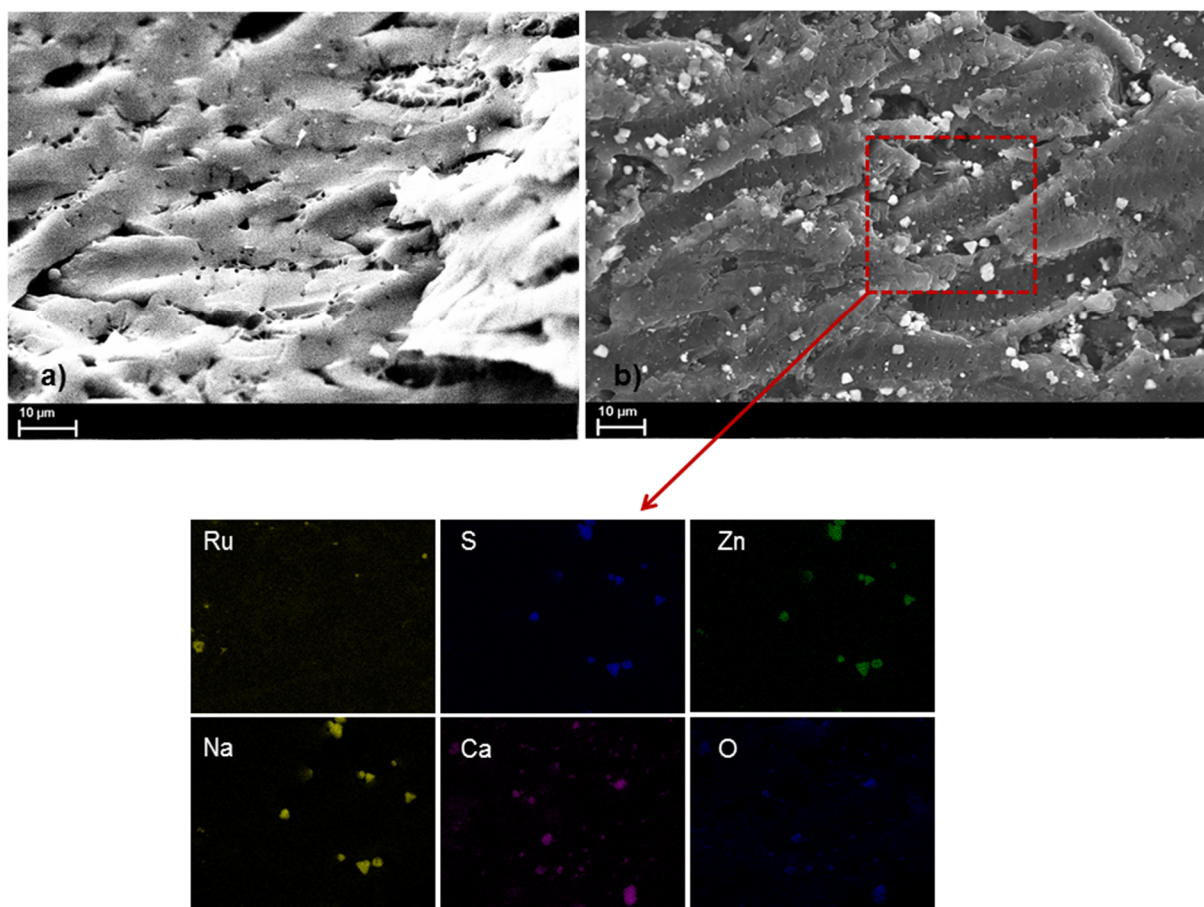


**Figure 7.14.** SEM-EDX of the (a) fresh and (b) spent (middle fraction) 5% Ru/C<sub>BASF</sub> catalysts.

As shown by the WDXRF analysis, the sulfur concentration on the spent catalyst was found to be 8–11 times higher in comparison to the fresh catalyst (see Table 7.9). Hence, the catalyst bed was contaminated with sulfur. By assuming that all the surface Ru atoms would react with sulfur according to the sulfur-saturated catalyst phase which was reported to be RuS<sub>0.33</sub> [58], the quantity of sulfur would be ca. 0.6 g. By comparing that value with the amount of sulfur detected in the catalyst bed, which was 0.7 g, most of the catalyst bed would be contaminated with sulfur. Hence, the deactivation of the catalyst can be explained by sulfur poisoning. The Ru content was found to be lower for the spent catalyst compared to the fresh. The fact that a concentration gradient (increasing from the bottom to the top of the bed) was measured might be due to Ru leaching and/or dilution of Ru by either carbon deposits and/or minerals. A similar concentration gradient of Ru along the catalyst bed was observed on the spent catalysts by Elliott et al. [94]. As no Ru leaching was detected in the reactor effluent, it seems that the dilution of Ru by either carbon deposits and/or minerals was the reason. In fact, the dilution can be explained by the concentration gradient of Zn, which decreases from the bottom to the top of the bed. The presence of Zn in the catalyst bed was also observed

with SEM-EDX analysis and was likely due to some slight attritions of the ZnO adsorbent. Other deposited minerals coming from the feed such as Ca, Fe, Cu, and Mg were detected along the catalyst bed. Note that these elements were also observed on the solid residue. Interestingly, some minerals (e.g. Na, P, K, and Cl) were found at a lower concentration and might be washed out from the catalyst bed during the campaign.

**Table 7.9.** WDXRF analysis of the fresh and spent 5% Ru/C<sub>BASF</sub> catalysts.

Elements	Fresh Ru/C	Spent Ru/C bottom	Spent Ru/C middle	Spent Ru/C top
Ru, wt %	5.0 ± 0.1	2.0 ± 0.1	3.6 ± 0.1	4.1 ± 0.2
Zn, wt %	0.1 ± 0.0	7.7 ± 0.4	3.8 ± 0.6	0.9 ± 0.0
S, mg kg <sup>-1</sup>	151 ± 4	1156 ± 65	1697 ± 34	1690 ± 76
Ca, mg kg <sup>-1</sup>	107 ± 2	403 ± 17	311 ± 6	325 ± 15
P, mg kg <sup>-1</sup>	796 ± 5	780 ± 48	673 ± 1	299 ± 3
Fe, mg kg <sup>-1</sup>	162 ± 2	332 ± 12	310 ± 8	176 ± 0
Cu, mg kg <sup>-1</sup>	300 ± 4	647 ± 19	463 ± 13	309 ± 6
Mg, mg kg <sup>-1</sup>	110 ± 0	88 ± 5	222 ± 12	153 ± 9
Na, mg kg <sup>-1</sup>	1396 ± 27	174 ± 4	145 ± 3	102 ± 1
K, mg kg <sup>-1</sup>	284 ± 2	226 ± 2	161 ± 3	148 ± 8
Cl, mg kg <sup>-1</sup>	224 ± 3	173 ± 3	158 ± 3	157 ± 5

## 7.7 Characterization of the spent ZnO adsorbent

Like for the spent catalyst, three different fractions of the spent ZnO adsorbent were harvested after the gasification campaign. The main objectives of the *ex situ* analysis were to evaluate its macro-/microscopic stability and its sulfur adsorption performance. In Figure 7.15, the visual aspect of the fresh and spent ZnO adsorbents is shown. The macroscopic structure of the spent ZnO and its mechanical properties (e.g. hardness) were well preserved. Only a noticeable change of its color from white to gray was observed, suggesting that some chemical modifications occurred.

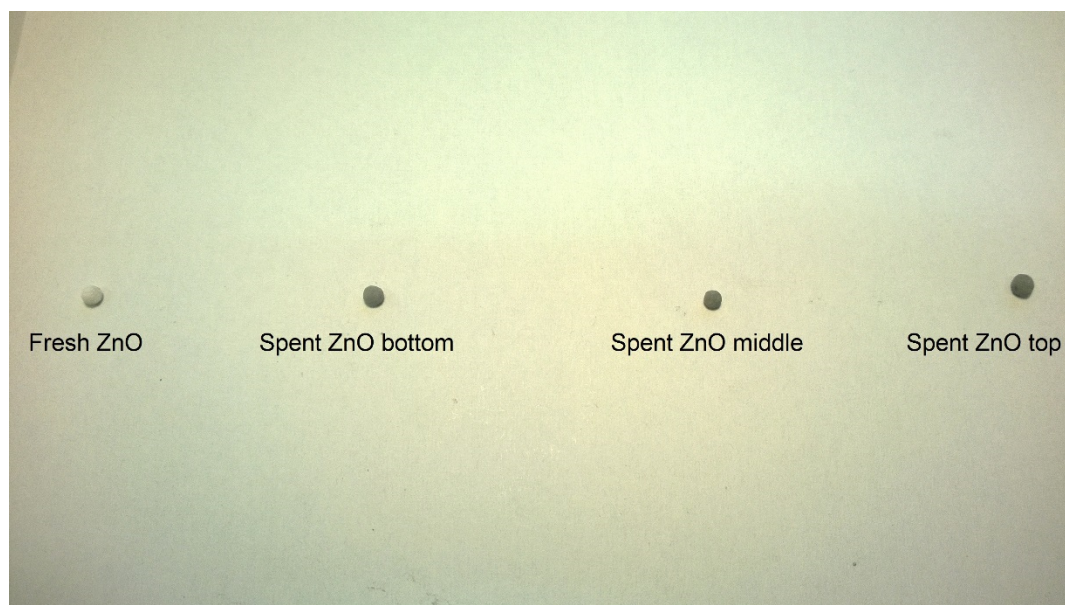


**Figure 7.15.** Picture of the fresh and spent ZnO adsorbents.

In order to determine the nature of these changes,  $N_2$ -physisorption, XRD,  $SO_2/CO_2$ -TPO, and carbon and sulfur elemental analysis were performed. As shown in Table 7.10, the physical structure of the spent adsorbent was affected in a similar manner for the three fractions. The BET SSA was close to the one of the adsorbent pre-treated in SCW (400 °C, 30 MPa) (see chapter 5, section 5.2). Hence, the evolution of the physical structure was caused by the harsh conditions of SCW.

**Table 7.10.** Physical structure of the fresh and spent ZnO adsorbents.

Sample	BET SSA $m^2 g^{-1}$	$V_{total}$ $cm^3 g^{-1}$	$d_p$ Å
Fresh ZnO	23	0.17	151
Spent ZnO bottom	6	0.05	179
Spent ZnO middle	5	0.05	204
Spent ZnO top	6	0.05	163

According to the XRD analysis, the crystalline structure of ZnO was well preserved since the diffraction peaks of ZnO were unchanged during CSCWG (see Figure 7.16). The apparition of a new diffraction peak at 28.7 ° can be attributed to the formation of ZnS suggesting that sulfur was chemically bonded to the adsorbent.

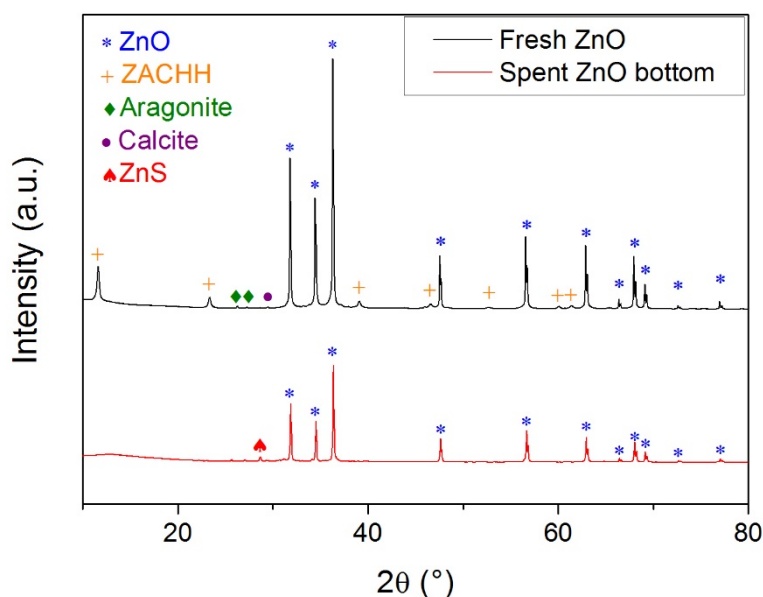


**Figure 7.16.** X-ray diffractograms of the fresh and spent ZnO (bottom fraction) adsorbents.

In Figure 7.17,  $\text{SO}_2$ -TPO analysis shows a unique  $\text{SO}_2$  desorption peak at ca. 700 °C for the three fractions, whereas no desorption peak occurred for the fresh ZnO. The peak intensity differed according to the fraction and diminished with the length of the ZnO bed. This qualitative analysis demonstrated that ZnO was able to adsorb sulfur under SCW conditions. The concentration gradient of sulfur along the bed indicates that the mass transfer zone already reached the end of the ZnO bed meaning that sulfur was likely in contact with the catalyst.

In Figure 7.18, several  $\text{CO}_2$  desorption peaks were observed for the fresh and spent ZnO. The desorption peaks above 650 °C may be related to carbon species coming from the binders of the ZnO adsorbent which contained  $\text{CaCO}_3$ . Whereas the desorption peaks at lower temperatures corresponded rather to carbon deposits coming from the liquefied feed. Astonishingly, the top fraction of the ZnO bed contained more carbon deposits than the lower fractions. It is not excluded that the higher residence time formed a larger amount of tars and/or coke.



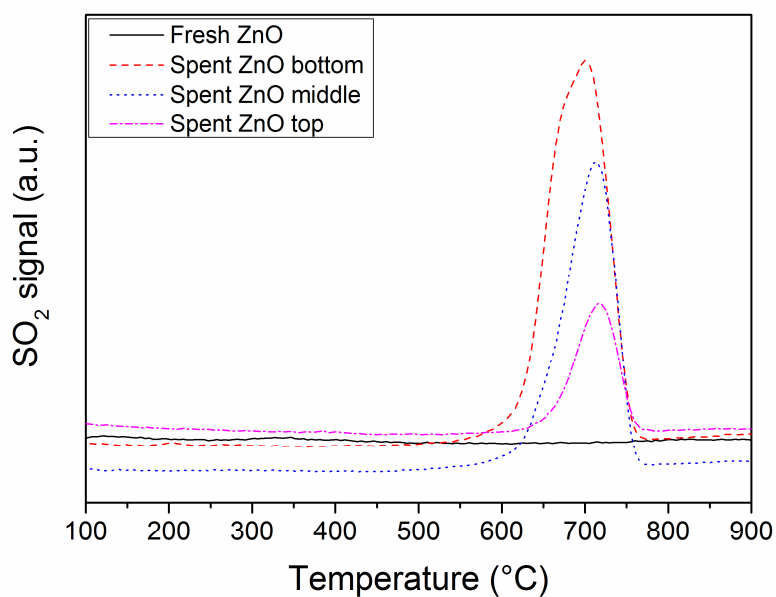


**Figure 7.17.** SO<sub>2</sub>-TPO analysis of the fresh and spent ZnO adsorbents.

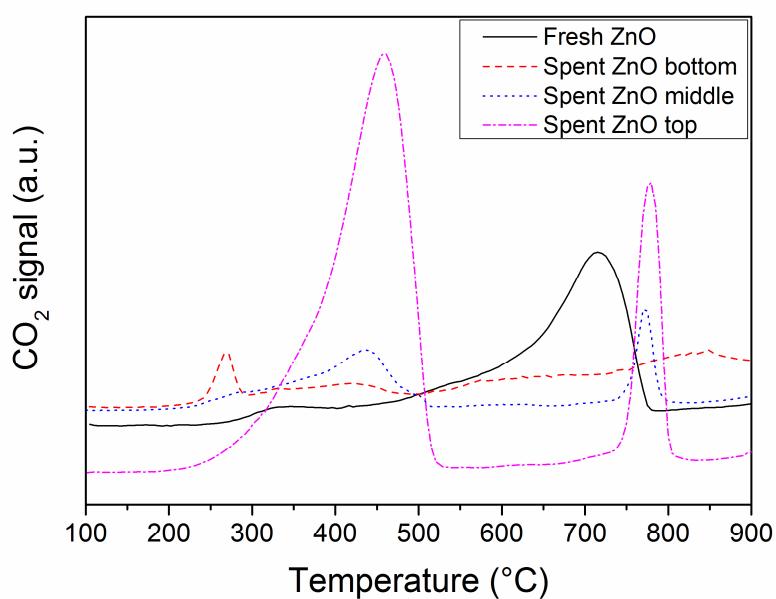


**Figure 7.18.** CO<sub>2</sub>-TPO analysis of the fresh and spent ZnO adsorbents.

The fresh and spent ZnO adsorbents were analyzed by carbon and sulfur elemental analysis in order to determine quantitatively their carbon and sulfur content (see Table 7.11). The sulfur analysis showed a good correlation with the SO<sub>2</sub>-TPO analysis since a concentration gradient of sulfur along

the ZnO bed was measured. The fact that the sulfur concentration did not reach the saturation concentration (see Table 5.4) may be caused either by channeling at the reactor wall or by the deposited minerals which have diluted the adsorbed sulfur. Additionally, as also observed by CO<sub>2</sub>-TPO, the top fraction contained a higher carbon content.

**Table 7.11.** Carbon and sulfur elemental analysis of the fresh and spent ZnO adsorbents.

Sample	C wt %	S wt %
Fresh ZnO	0.75 ± 0.01	0.04 ± 0.01
Spent ZnO bottom	0.27 ± 0.04	1.90 ± 0.08
Spent ZnO middle	0.52 ± 0.02	0.57 ± 0.03
Spent ZnO top	0.86 ± 0.04	0.52 ± 0.01

## 7.8 Temperature and pressure profiles

In Figure 7.19, the temperature profile at the inner wall of the salt separator is shown. As wished, a temperature gradient increasing from the bottom to the top of the salt separator was measured. At the bottom, a subcritical region ( $T < 374\text{ °C}$ ) was formed whereas at the top, a supercritical region ( $T > 374\text{ °C}$ ) was obtained. Hence, the conditions were optimal for favoring a good salt separation since the salts could be precipitated in the supercritical region and solubilized in the subcritical region. Note that the abrupt decrease of the temperature after 15 h, 80 h, and 85 h was caused by an urgent cooling of the process. In Figure 7.20, a similar behavior of the temperature profile at the lance of the salt separator was recorded. However, the temperature along the lance was instable with a lot of variation. The fact that the lance was only fixed at the top of the salt separator and not at the bottom as well, may be the reason. In fact, due to the nozzle exiting the standpipe, the lance might swing considerably. Note that the loss of signal occurred between 38 h and 52 h was caused by a freezing of the thermocouples (TLTR 2-9-TLTR 2-16).



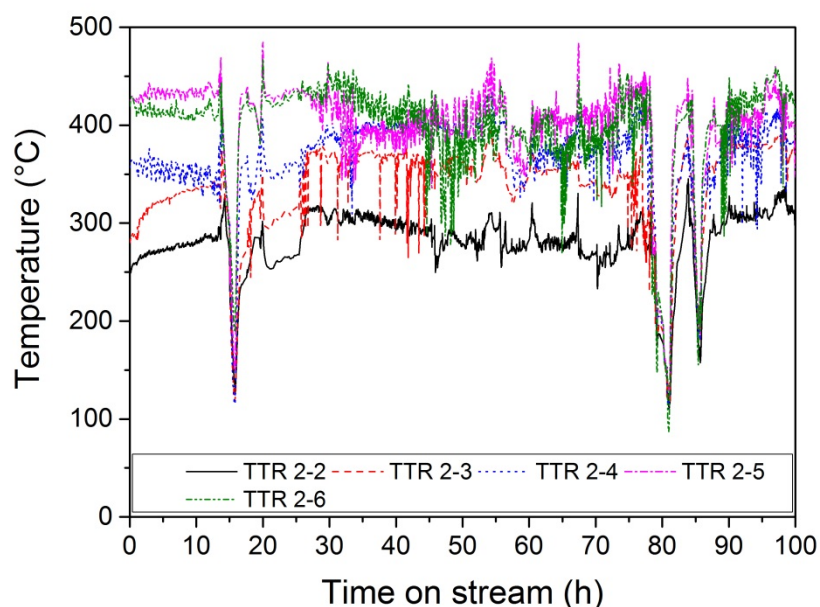


**Figure 7.19.** Temperature profile of the five thermocouples located at the inner wall of the salt separator, starting from the bottom (TTR 2-2) to the top (TTR 2-6) during the experiment KT10.

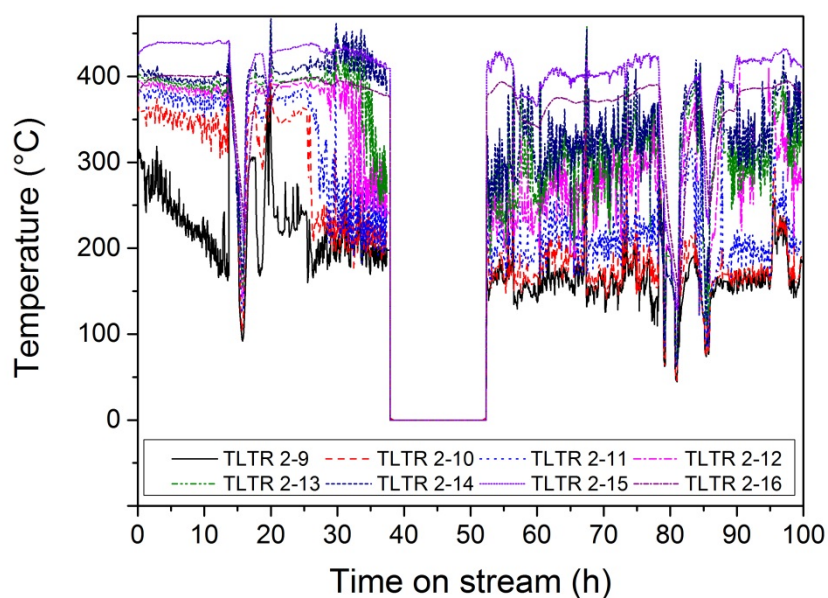


**Figure 7.20.** Temperature profile of the six thermocouples located on the lance of the salt separator starting from the bottom (TLTR 2-9) to the top (TLTR 2-16) during the experiment KT10.

In Figure 7.21, the temperature profile recorded at the inner wall of the reactor exhibited a relatively stable profile during the campaign. Except to the three cooled down emergencies of the process (15 h, 80 h, and 85 h), SCW conditions were achieved over the 100 h. A similar trend was recorded at

the lance of the reactor (see Figure 7.22). Similarly to the lance of the salt separator, the loss of signal was caused by a freezing of the thermocouples occurred in the same period (TLTR 4-5-TLTR 4-20).

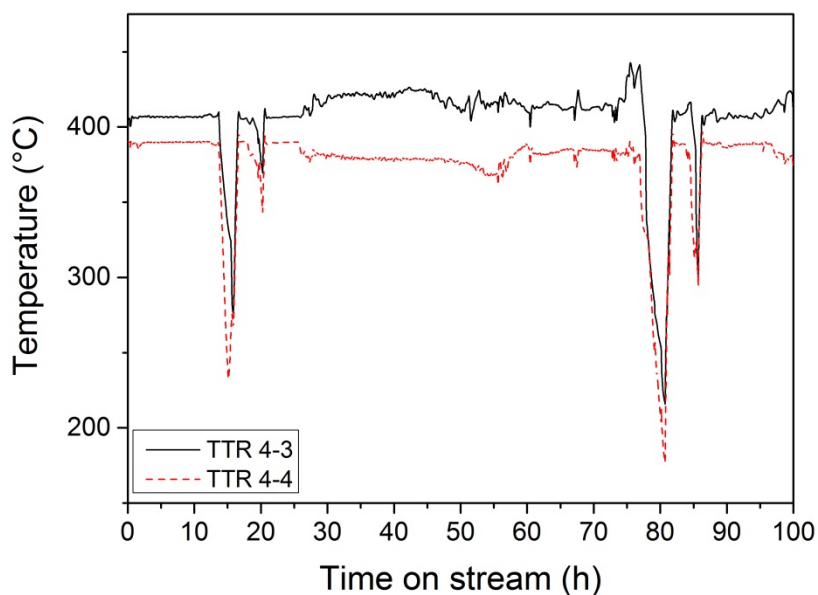


**Figure 7.21.** Temperature profile of the two thermocouples located at the inner wall of the reactor starting from the bottom (TTR 4-3) to the top (TTR 4-4) during the experiment KT10.

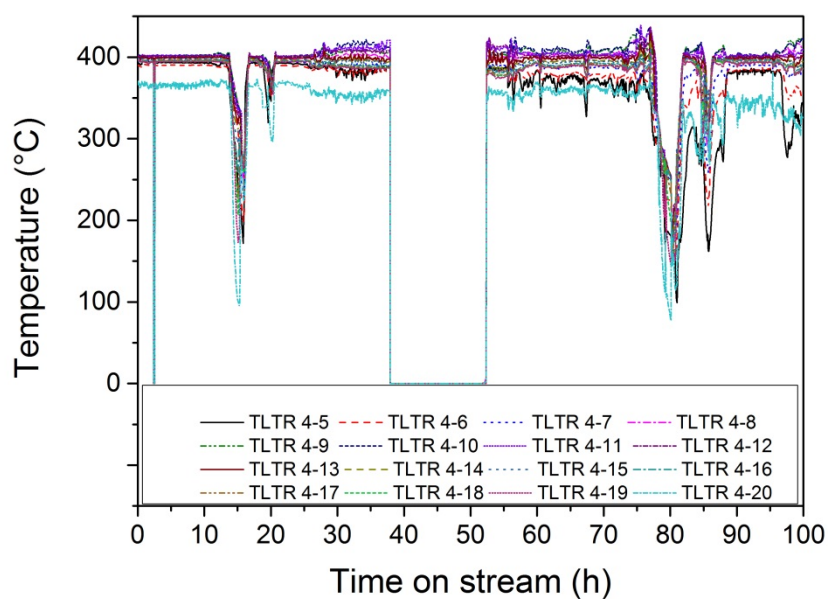


**Figure 7.22.** Temperature profile of the sixteen thermocouples located on the lance of the reactor starting from the bottom (TLTR 4-5) to the top (TLTR 4-20) during the experiment KT10.

In Figure 7.23, the pressure profile is depicted. Although some high decreases of the pressure were recorded after 13 h, 60 h, and 84 h, the latter remained quite stable during the campaign. As previously discussed, due to some increases of the pressure caused by plugging ( $P > 30$  MPa), for safety reasons, it was necessary to cool down the process with DI water. According to the pressure sensors, the plugging was located rather upstream of the reactor. A better view of the sudden increase of the pressure is shown in Figures 7.24-7.26. After 13 h, plugging took place upstream of the salt separator since only the pressure sensors ( $P_{\text{sensor 1-3}}$ ,  $P_{\text{sensor 1-5}}$ , and  $P_{\text{sensor 2-2}}$ ) indicate a high augmentation of the pressure. The most likely reason was a blocking (e.g. microalgae precipitation, solid particles) of the filter located between the Slurry feeder and the salt separator. The fact that this overpressure issue did not occur afterwards was likely due to the addition of xanthan gum in the feed which has helped to stabilize the microalgae suspension. Interestingly, after 60 h and 80 h, plugging occurred rather in the salt separator since the pressure sensor located at the middle of the salt separator ( $P_{\text{sensor 2-3}}$ ) indicates a high increase of the pressure, too. Therefore it is not excluded that plugging caused by cokes and/or salt precipitation were responsible.

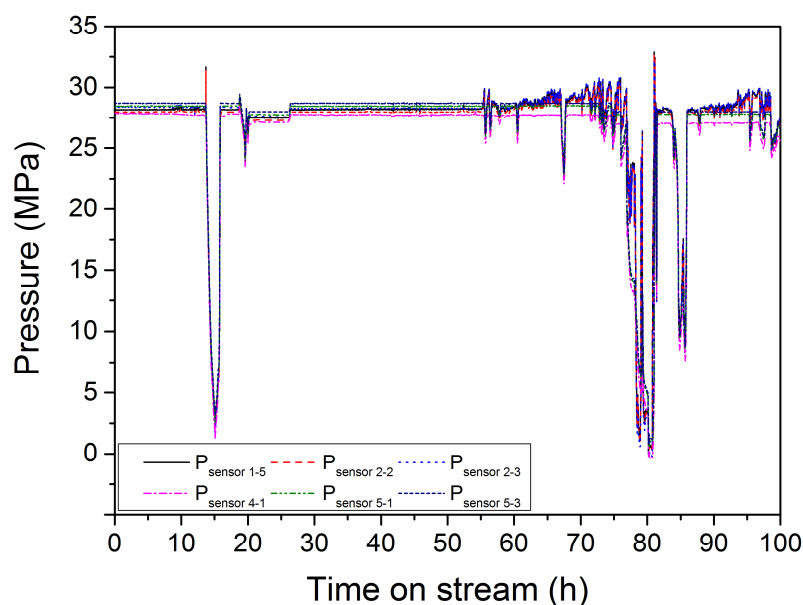


**Figure 7.23.** Pressure profile during the experiment KT10.  $P_{\text{sensor 1-5}}$  is located at the slurry feeder,  $P_{\text{sensor 2-2}}$  is located before the salt separator,  $P_{\text{sensor 2-3}}$  is located in the middle of the salt separator,  $P_{\text{sensor 4-1}}$  is located in the reactor,  $P_{\text{sensor 5-1}}$  is located upstream of the reactor effluent filter, and  $P_{\text{sensor 5-3}}$  is located downstream of the reactor effluent filter.

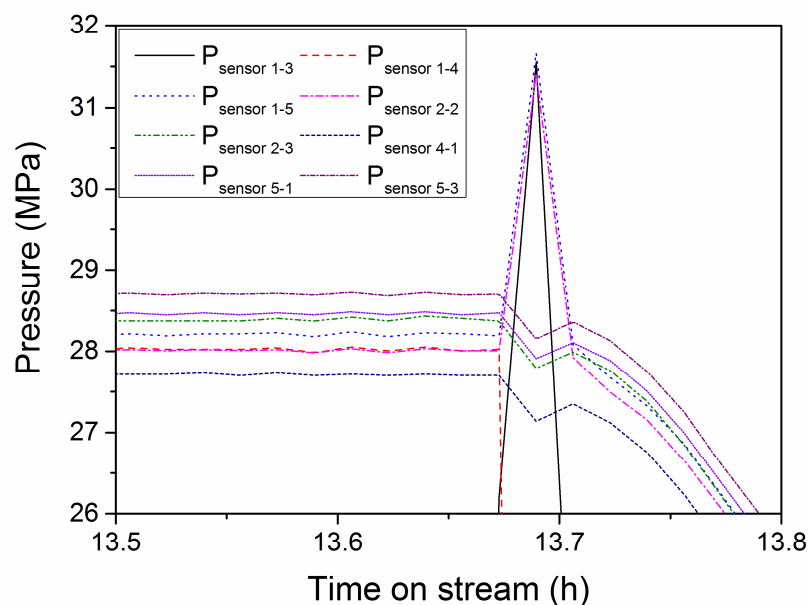


**Figure 7.24.** Plugging of the process after 13 h.  $P_{\text{sensor 1-3}}$ ,  $P_{\text{sensor 1-4}}$ , and  $P_{\text{sensor 1-5}}$  are located at the slurry feeder,  $P_{\text{sensor 2-2}}$  is located before the salt separator,  $P_{\text{sensor 2-3}}$  is located in the middle of the salt separator,  $P_{\text{sensor 4-1}}$  is located in the reactor,  $P_{\text{sensor 5-1}}$  is located upstream of the reactor effluent filter, and  $P_{\text{sensor 5-3}}$  is located downstream of the reactor effluent filter.

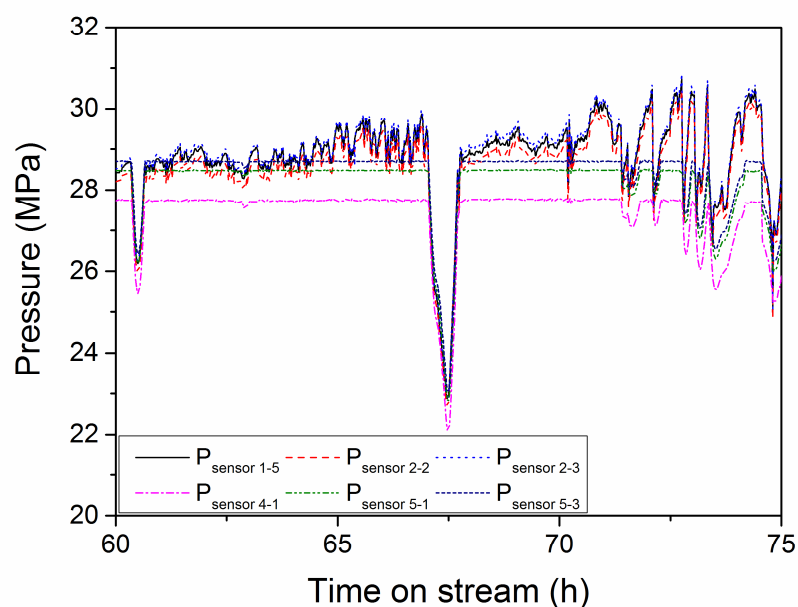


**Figure 7.25.** Plugging of the process after 60 h.  $P_{\text{sensor 1-5}}$  is located at the slurry feeder,  $P_{\text{sensor 2-2}}$  is located before the salt separator,  $P_{\text{sensor 2-3}}$  is located in the middle of the salt separator,  $P_{\text{sensor 4-1}}$  is located in the reactor,  $P_{\text{sensor 5-1}}$  is located upstream of the reactor effluent filter, and  $P_{\text{sensor 5-3}}$  is located downstream of the reactor effluent filter.

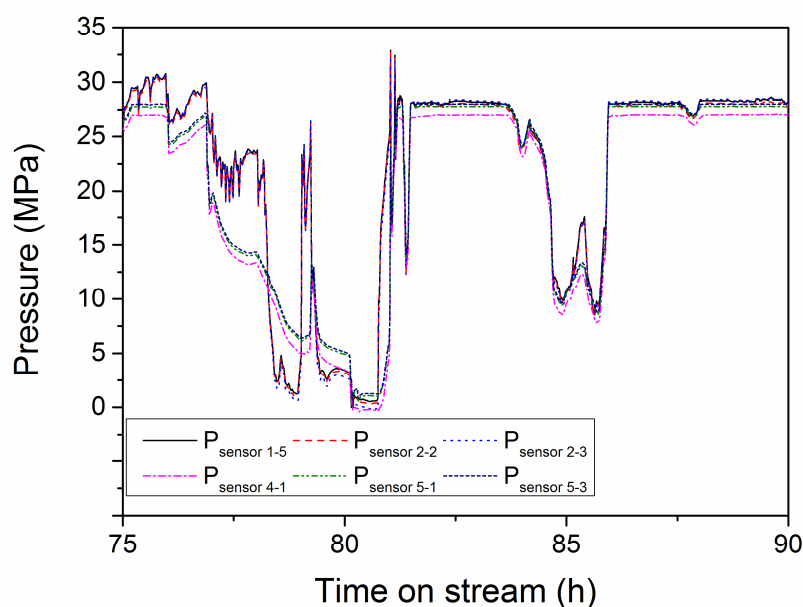


**Figure 7.26.** Plugging of the process after 80 h.  $P_{\text{sensor 1-5}}$  is located at the slurry feeder,  $P_{\text{sensor 2-2}}$  is located before the salt separator,  $P_{\text{sensor 2-3}}$  is located in the middle of the salt separator,  $P_{\text{sensor 4-1}}$  is located in the reactor,  $P_{\text{sensor 5-1}}$  is located upstream of the reactor effluent filter, and  $P_{\text{sensor 5-3}}$  is located downstream of the reactor effluent filter.

## 7.9 Summary

In this chapter, the results of the gasification campaign performed on the microalgae production site of ZHAW in Wädenswil (CH) were presented. The most relevant outcomes are summarized below:

- Microalgae (*Chlorella vul.*) were successfully gasified to methane (55-60 vol %) over a period of 55 h.
- A low TOC in the reactor effluent ( $< 400 \text{ mg L}^{-1}$ ) was recorded during this period demonstrating the high catalytic activity of the 5% Ru/C<sub>BASF</sub> catalyst.
- The  $GE_C$  was 45-50% revealing a relatively high tar and coke formation. The high amount of tarry products (not taken into account in the  $GE_C$  calculation), which has left the salt separator via the brine effluent, has significantly reduced the  $GE_C$ .
- A brine effluent rich in nutrients (N, K, S, P, and Na) was obtained showing the good performance of the salt separator when processing microalgae.

- The commercial ZnO adsorbent (*Katalco 32-5*) removed efficiently sulfur since no sulfur was detected in the reactor effluent during 60 h.
- The ZnO adsorbent exhibited a high mechanical stability (hardness) under SCW conditions.
- When the concentrated feed (15 wt %) was processed (50-56 h) some technical problems occurred. In fact, the salt separator was not able to liquefy such a high concentration of microalgae. Consequently, the ZnO bed and the catalyst bed were likely contaminated with the non- or partially liquefied feed.
- A part from sulfur poisoning, coking, catalyst fouling by salt deposits, and Ru sintering might contribute to the deactivation of the catalyst.
- After the campaign, a solid residue was found in the salt separator. The latter was mainly composed with carbon (tars and/or cokes) and minerals.



# Chapter 8 Concluding Remarks and Recommendations for Further Research

## 8.1 Achieved results

This doctoral thesis showed the relevance of studying systematically and separately the process units (*e.g.* catalytic reactor, salt separator, and sulfur removal unit) of the CSCWG process. Although the performance of these process units were assessed and optimized with model compounds, the new acquired knowledge were determinant for the development of KONTI-C.

During continuous CSCWG with IPA over Ru/C catalysts, coking was found to be a serious issue and led to a progressive deactivation of the catalyst. The decomposition of IPA over the carbon surface to coke and H<sub>2</sub> was the reason. In presence of organic acids or even more complex molecules (*e.g.* glycerol, lignin, microalgae), coking was already reported to deactivate Ru/C catalysts but it was the first time that coking was observed during CSCWG of a relatively simple organic alcohol. The progressive loss of the catalytic activity could solely be observed and studied when operating at a high WHSV, *i.e.* with  $X_c < 100\%$  and over a few days. To this aim, many efforts were done for selecting carefully the process parameters and for ensuring the stability of the process under these harsh conditions. By testing the catalytic performance of our standard commercial catalyst (2% Ru/C<sub>BASF</sub>), the results showed its poor stability, contradicting the observations reported previously by Waldner [65]. In fact, Waldner has evaluated the stability of this catalyst by working at a low WHSV (with  $X_c = 100\%$ ) over a period of 220 h during CSCWG of SLW, thus a deactivation of the catalyst could not be observed. Surprisingly, when the Ru loading of the 2% Ru/C<sub>BASF</sub> was increased from 2 wt % to 5 wt %, the stability was significantly improved. It was proposed that a higher decoration of the carbon surface with Ru may minimize the decomposition of IPA to coke since more Ru would be available for facilitating its conversion to gaseous products. This new finding was a key point in the process development since the improved catalyst (5% Ru/C<sub>BASF</sub>) was implemented in KONTI-C. The optimization of the catalytic performance was also performed with prepared Ru/C catalysts. Many synthe-



sis factors such as the Ru dispersion, the solvent used during the catalyst preparation, the salt precursor, and the carbon surface functional groups were systematically assessed. The results showed that the performance can be significantly improved by: achieving highly dispersed Ru NPs; using acetone instead of water during the catalyst synthesis; by preparing the catalyst with a chloride free salt precursor ( $\text{Ru}(\text{NO})(\text{NO}_3)_3$ ). Interestingly, the catalytic performance of a 2%Ru/C prepared with  $\text{Ru}(\text{NO})(\text{NO}_3)_3$  was higher in comparison to the 2% Ru/C<sub>BASF</sub>. The main reason for such a high catalytic activity was the absence of residual chlorides. Although  $\text{RuCl}_3$  remains a salt precursor of choice due to its low price, it was shown that this salt precursor should be avoided. By comparing the catalytic performance of a Ru/C catalyst with other Ru catalysts supported on metal oxides ( $\text{Ru}/\text{TiO}_2$ ,  $\text{Ru}/\text{ZrO}_2$ , and  $\text{Ru}/\text{Al}_2\text{O}_3$ ), Ru/C exhibited the highest catalytic activity and stability over a period of 50 h. A trend between the Ru dispersion and the coking resistance was observed where a higher Ru dispersion enhanced the catalyst stability. These results are of relevance because they demonstrate that among the tested catalysts, Ru/C is the most suitable catalyst.

Regarding the salt separator, a major improvement was achieved by modifying the feed entrance from the top to the bottom. This new design significantly improved the salt recovery and the inorganic sulfur ( $\text{SO}_4^{2-}$ ) was entirely removed from the reactor when processed with a model salt solution. The formation of a supercritical region (low salt solubility) at top of the salt separator and a subcritical region (high salt solubility) at the bottom was essential since the salts could precipitate at top and be recovered in the subcritical region. This amelioration was a crucial step for demonstrating the technical viability of the process since the catalyst located downstream can be protected from the inorganic sulfur ( $\text{SO}_4^{2-}$ ). However, the results showed that a salt fraction still accumulated in the process revealing that further progress is needed.

For the removal of reduced sulfur species (*e.g.*  $\text{H}_2\text{S}$ ), a new sulfur adsorption unit was implemented between the salt separator and the catalytic reactor. Preliminary experiments carried out with a fixed-bed PFR demonstrated the high stability and the good sulfur adsorption performance of a commercial ZnO adsorbent (*Katalco 32-5*) under SCW conditions. As this absorbent was exclusively designed for gas cleaning applications ( $\text{H}_2\text{S}$  removal) at low temperatures, such a good stability under SCW conditions was hardly expected. Moreover, its capacity for adsorbing sulfur to form ZnS when processed with a  $\text{Na}_2\text{S}\cdot 9\text{H}_2\text{O}$  solution was a major achievement for the process. Indeed, for the first time sulfur was adsorbed continuously and efficiently in the harsh environment of SCW. When working at a high pH (11.5), corrosion in the reactor was problematic for the reproducibility

of the breakthrough curves. A reactor of Inconel 625 was unsuitable for performing sulfur adsorption experiments due to the high activity of Ni with sulfur. By contrast, no reactivity with sulfur was observed with a reactor of AISI 316L revealing its better suitability.

Although the development of KONTI-C was based on the existing PDU (KONTI-2), several key modifications were performed: use of a 5% Ru/C<sub>BASF</sub>; construction of a new salt separator; and addition of a sulfur removal unit. The first experiments carried out with KONTI-C confirmed the good performance of the new salt separator as well as the high stability of the process when fed with a model salt solution. By contrast, when microalgae (*Phaeod. tric.*) were liquefied the stability of the process was affected by plugging. Many attempts were done prior to reaching stable process conditions by varying the process parameters (feed rate, Liquiflow, temperature of the salt separator) and by replacing the filter located upstream of the salt separator. Thereby, continuous processing of microalgae requires a certain experience regarding the tuning of the process parameters. During continuous liquefaction of microalgae, tar and coke formation in the process occurred since more than half of the carbon contained in the feed was recovered neither in the brine nor in the reactor effluents. Nevertheless, this result reveals that more efforts are still needed for ensuring a higher GE<sub>c</sub>, which would further improve the efficiency of the process. The good sulfur adsorption capacity of the ZnO adsorbent was also proved during continuous liquefaction of microalgae since no sulfur was detected in the reactor effluent. The impact of this result is considerable since it was demonstrated that sulfur can be fully removed from the reactor effluent prior to reaching the catalyst bed. As a result, when a 5% Ru/C<sub>BASF</sub> catalyst was added downstream of the ZnO bed, microalgae were successfully gasified to methane over a period of 7 h where no sign of deactivation of the catalyst was observed. Since the development of this technology at PSI, it was the first time that a stable gas composition close to the thermodynamic chemical equilibrium was obtained when gasifying wet biomass in a continuous test rig.

The gasification campaign carried out on the microalgae production site of ZHAW in Wädenswil (CH) was determinant for the demonstration of the technical feasibility. In fact, the stable gas composition recorded over a period of 55 h with the simultaneous achievement of a reactor effluent containing a low TOC showed the good catalytic performance of the catalyst. Up to now, no studies have reported such a long gasification period with a gas composition similar to the thermodynamic chemical equilibrium during continuous CSCWG of microalgae. The improvement of the separation

units achieved during this doctoral thesis was determinant for protecting the catalyst from contaminants. In contrast with Brandenberger's work [17], who carried out one continuous CSCWG of microalgae without having assessed and optimized the different process units, this work has shown the necessity for improving the process units prior to performing continuous CSCWG of microalgae. As a result, microalgae were successfully gasified from a few minutes (by Brandenberger) up to 55 h. In addition to methane production, a brine effluent rich in minerals was produced revealing the good performance of the new salt separator. Due to the low price of methane, the coproduction of nutrients, especially phosphorus may significantly improve the economics of the process. In the frame of the SunCHem, the coproduction of methane and nutrients were both two key goals to achieve. According to the carbon recovery, a carbon loss of ca. 40% was estimated. It seems that the high amount of tarry products, which has left the plant through the brine effluent and not collected as a whole, was responsible for the low  $GE_c$  values. Hence, tar and coke formation remains an issue to be solved in order to improve further the efficiency. On the other hand, processing concentrated feeds (> 14 wt %) remains a challenge for the present plant mainly due to the limited capacity of the salt separator to liquefy such concentrated streams. Furthermore, a practical strategy for removing organic sulfur compounds before the catalyst bed must still be developed to ensure industrially relevant processing times of several thousand hours.

## 8.2 Recommendations for further research

The improvement of the catalytic performance of Ru/C catalysts remains an ongoing work and some challenges such as the development of sulfur-resistant catalysts have still to be overcome. For instance, doping of supported Ru catalysts with phosphorus ( $Ru_2P$  and  $RuP$ ) was found to improve the sulfur-resistance of the catalyst during hydrodesulfurization [169]. Moreover, it would be interesting to evaluate the activity of these catalysts for hydrodesulfurization under SCW conditions. In fact, this reaction has been widely used in the industry for the removal of organic sulfur compounds and may be an effective strategy for their removal during CSCWG of microalgae. Further optimization of other synthesis factors that were not investigated in this doctoral dissertation is of interest. As an example, the graphitization degree of the carbon support which was shown to improve the activity of Ru/C catalysts during catalytic decomposition of  $NH_3$  [170]. The comparison of different catalyst preparation methods (*e.g.* sol-gel methods, hydrothermal synthesis) is also relevant since in the thesis only wet impregnation was investigated.

Although significant improvements regarding the salt separator were achieved, further optimization is still required. The salt precipitation inside the salt separation remains the main issue to solve. A better understanding of the fluid dynamic and salt separation under SCW conditions are both the key towards a salt recovery of 100%.

Continuous sulfur removal under SCW conditions was found to be possible with a commercial ZnO adsorbent. However, its quantitative adsorption capacity ( $\text{g}_{\text{Sulfur}}/\text{g}_{\text{Adsorbent}}$ ) has still to be determined when processing microalgae in order to develop a proper design of the sulfur removal unit. To this aim, further continuous liquefaction experiments with microalgae performed solely over ZnO are needed to determine sulfur breakthrough curves. The effect of channeling at the wall of the reactor remains still unclear. Therefore these experiments would help to optimize the design of the adsorbent, *i.e.* ratio  $d_{\text{reactor}}/d_p$ . The acquired data would also allow to develop sulfur adsorption models. The development of other metal oxide adsorbents (*e.g.* CuO, CaO, Fe<sub>2</sub>O<sub>3</sub>) and by comparing their respective sulfur adsorption capacity with *Katalco 32-5* would be of interest since only a few studies dedicated to sulfur removal under SCW conditions. Moreover, the long-term stability of the adsorbents is not known and need to be studied in detail.

Tar and coke formation when processing microalgae are still problematic. Hence, a better knowledge of tar and coke formation under continuous processing of microalgae would be helpful. For that, other continuous liquefaction experiments in KONTI-C are required where the effects of the process parameters (*e.g.* temperature, feed rate) on the carbon recovery are investigated systematically. Therefore the installation of a mass flow meter for recording the feed rate is a priority in order to calculate accurately carbon mass balances.

Although a brine effluent rich in nutrients was achieved during the gasification campaign, more toxicology studies regarding the effect of unconverted compounds (*e.g.* N-compounds, heavy metals) on the microalgae growth should be done prior to recycling it. In fact, the recycling of the nutrients to the microalgae cultivation system is a major objective of the SunCHem process since it aims at working as a closed loop system.



## A. Appendix

### A.1 Screenshots of the LabVIEW based software for KONTI-C

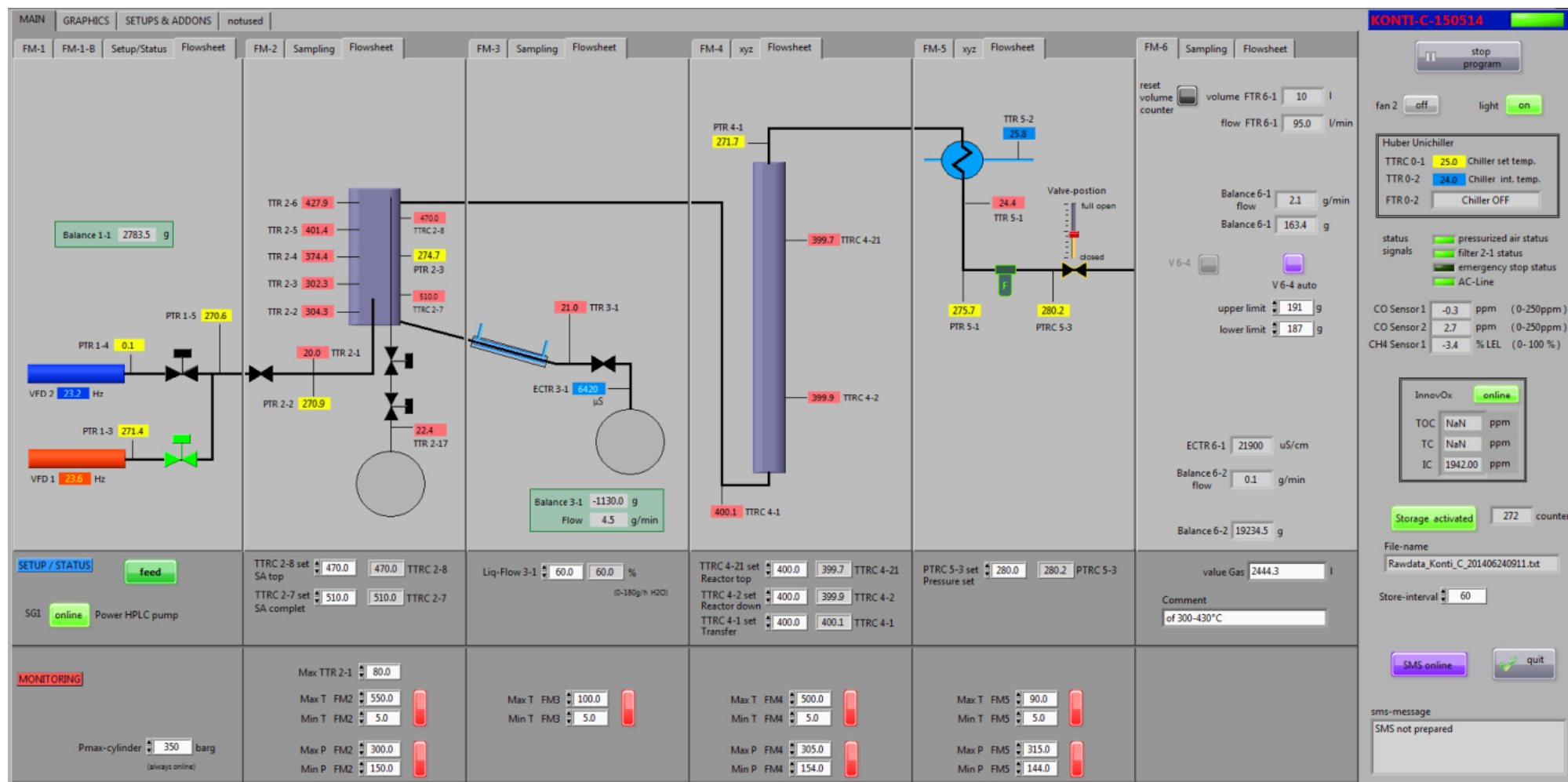


Figure A.1. LabVIEW-main screen.

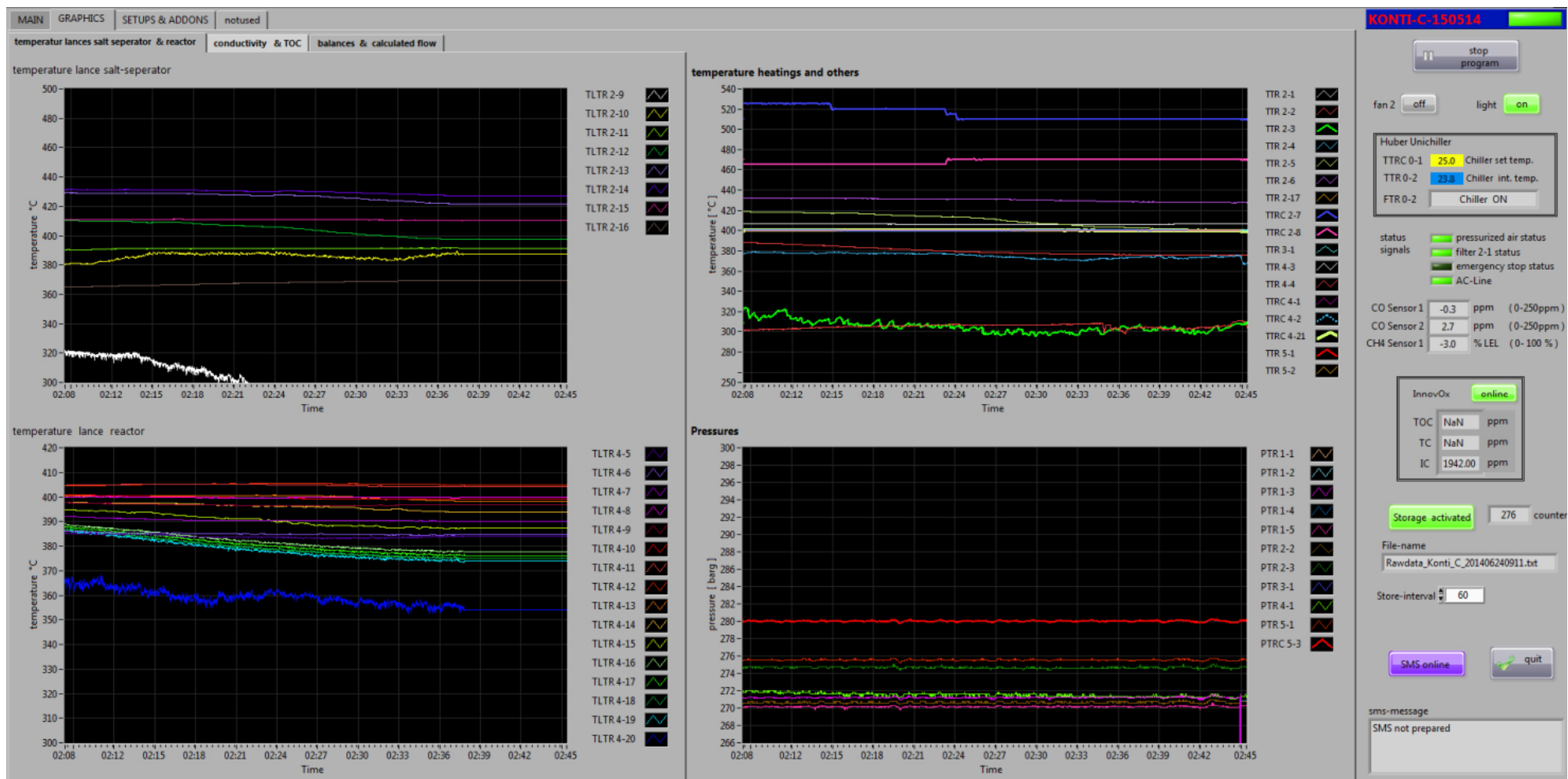


Figure A.2. LabVIEW-monitoring of temperature and pressure.

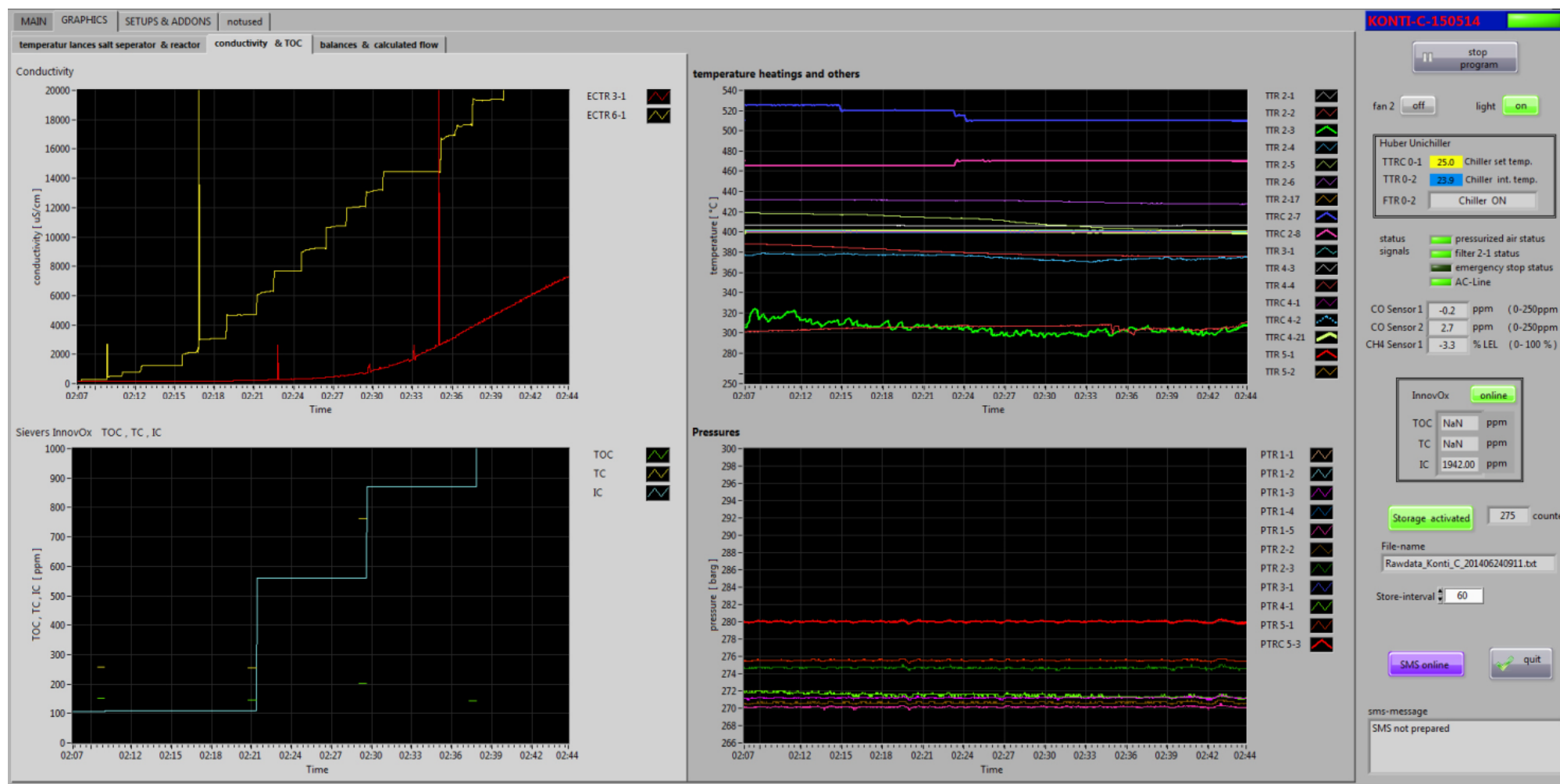


Figure A.3. LabVIEW-monitoring of conductivity, TOC/TIC, temperature, and pressure.



## A.2 Process flow sheet of KONTI-C

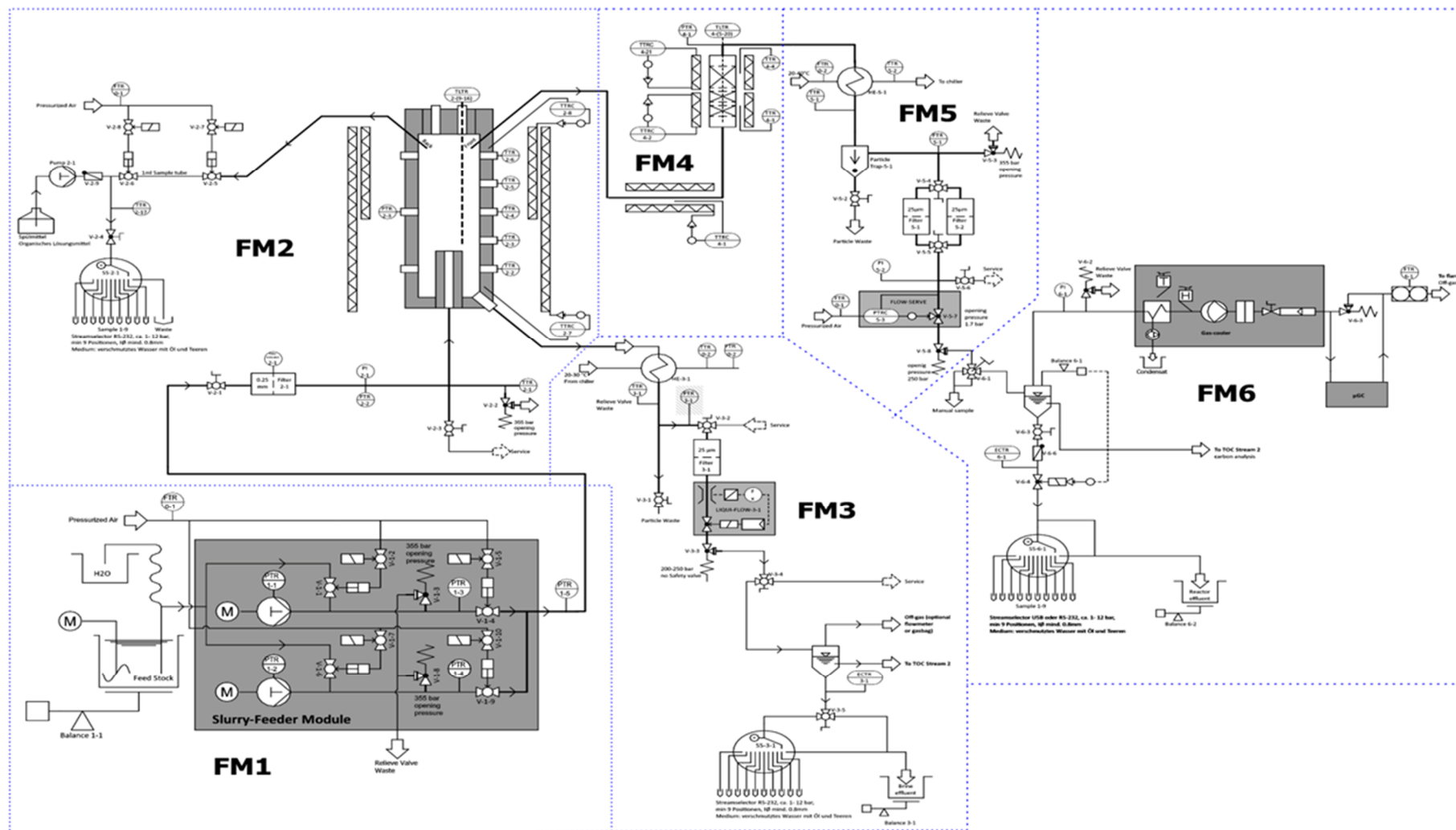


Figure A.4. All sections of the process.

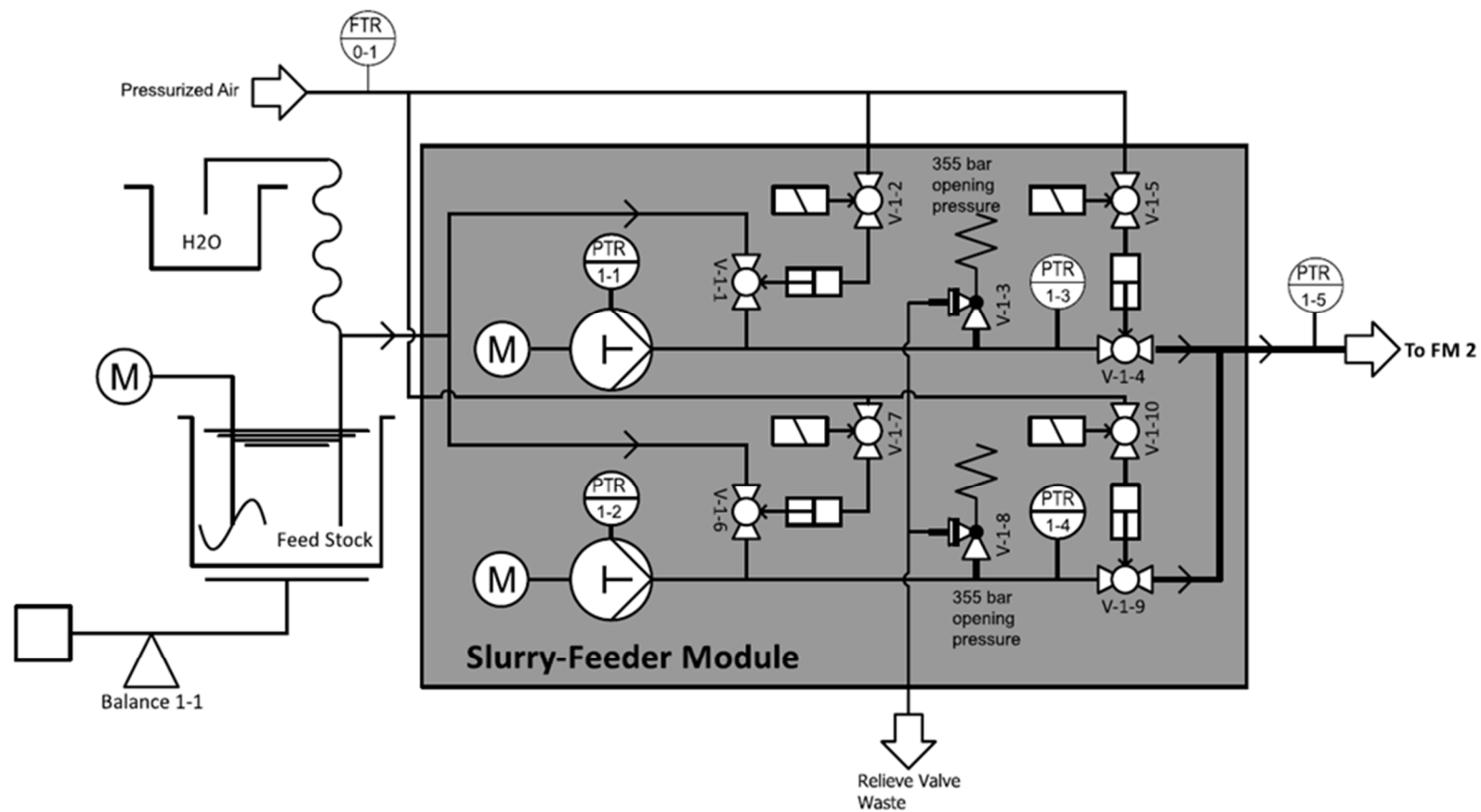


Figure A.5. Section FM1 of the process.

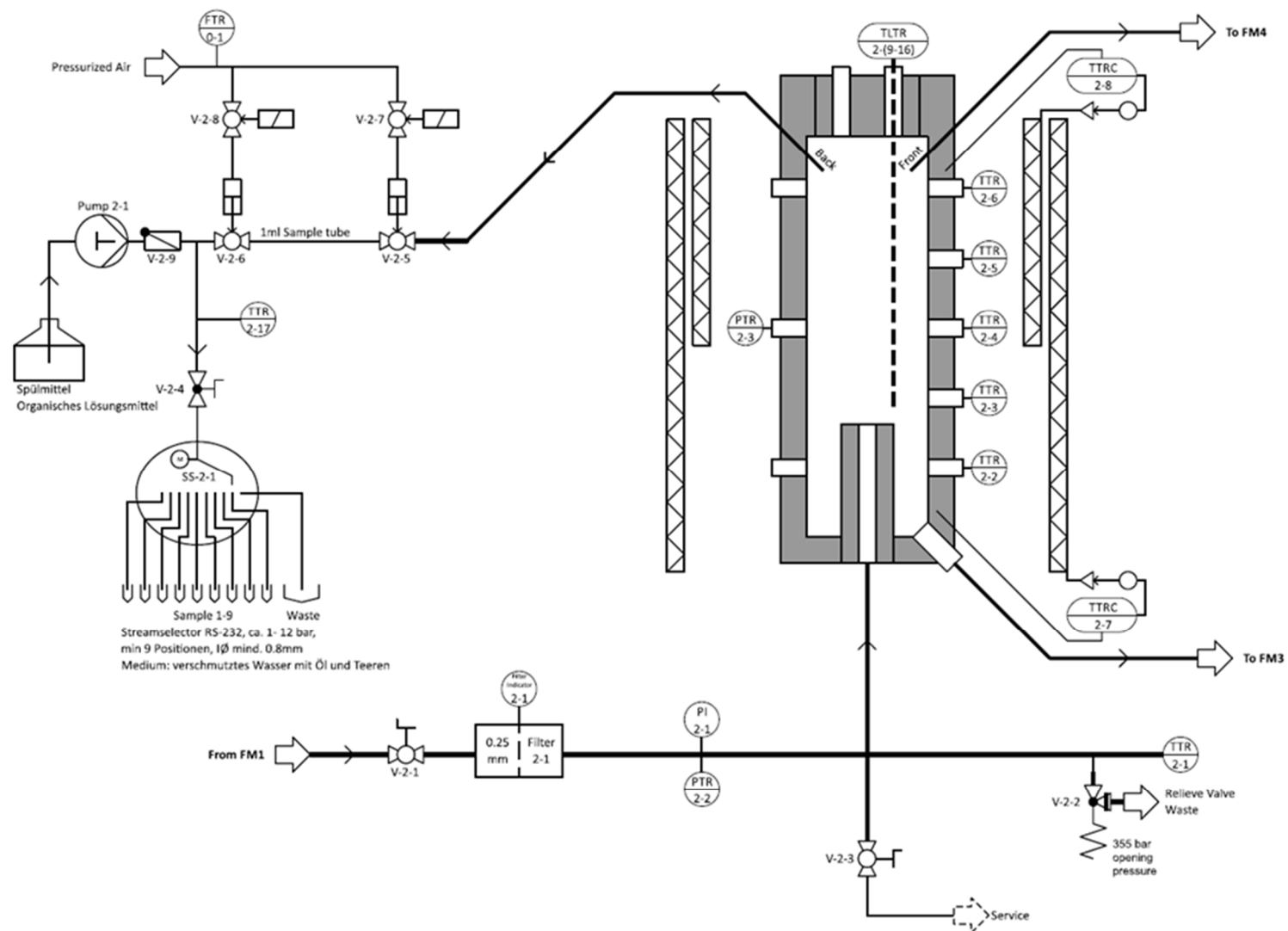


Figure A.6. Section FM2 of the process.

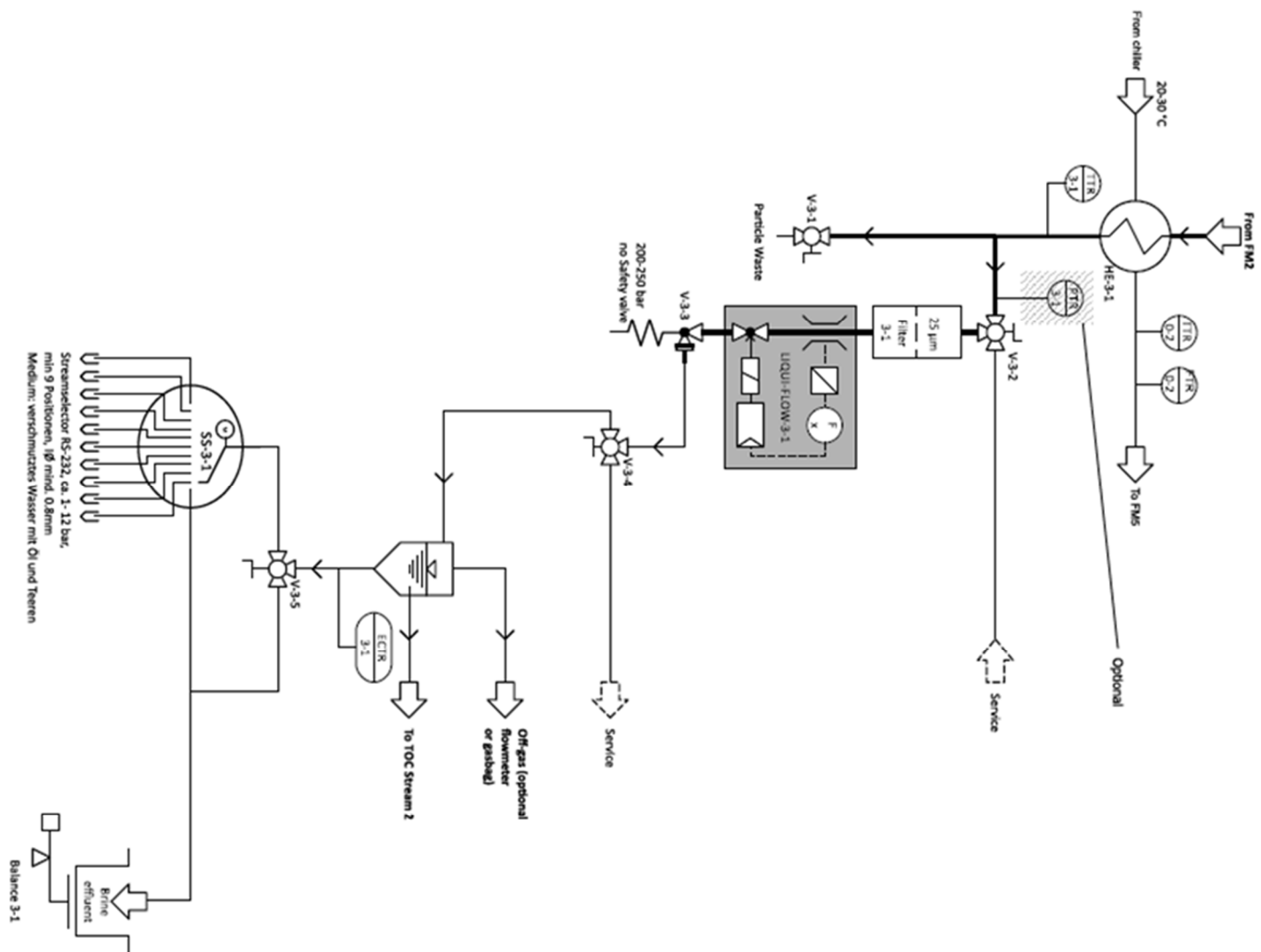


Figure A.7. Section FM3 of the process.

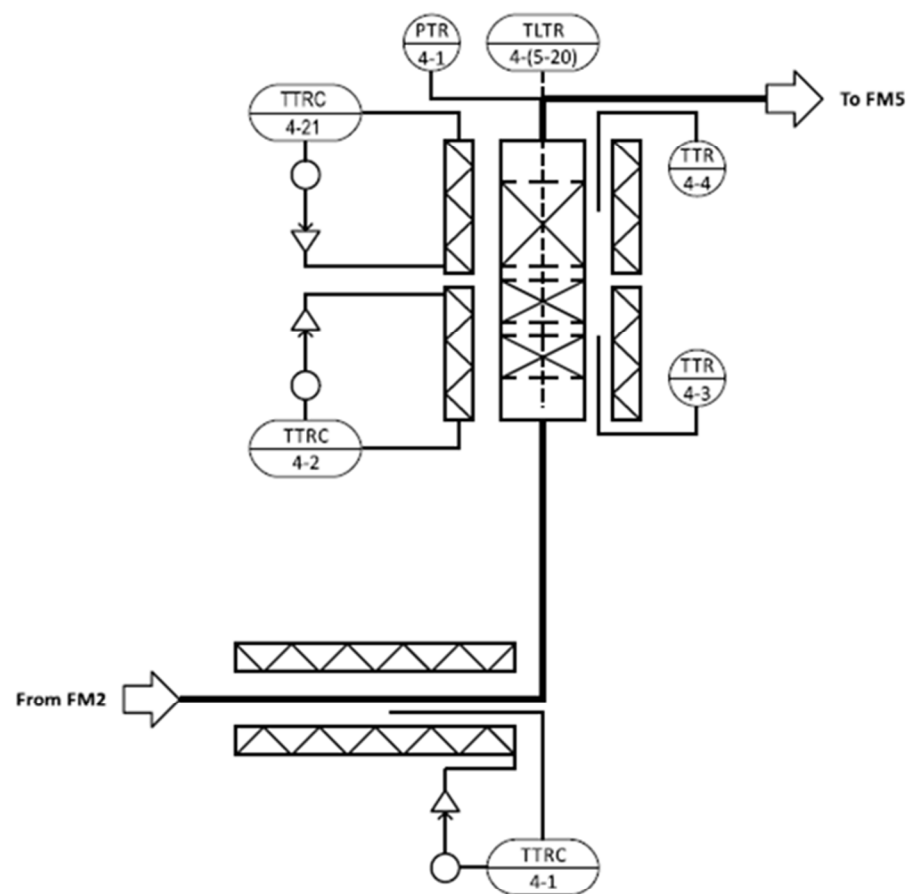


Figure A.8. Section FM4 of the process.

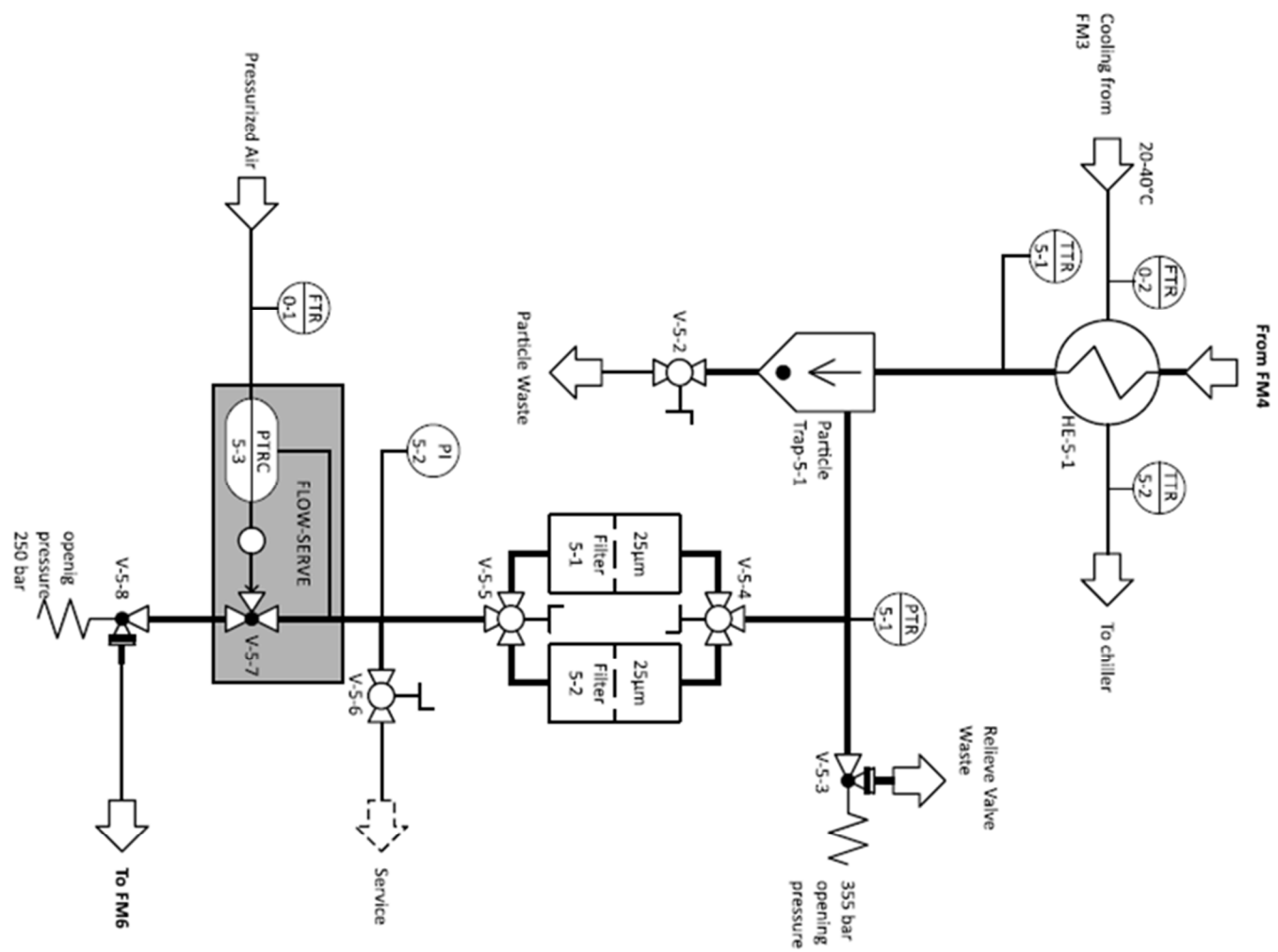


Figure A.9. Section FM5 of the process.

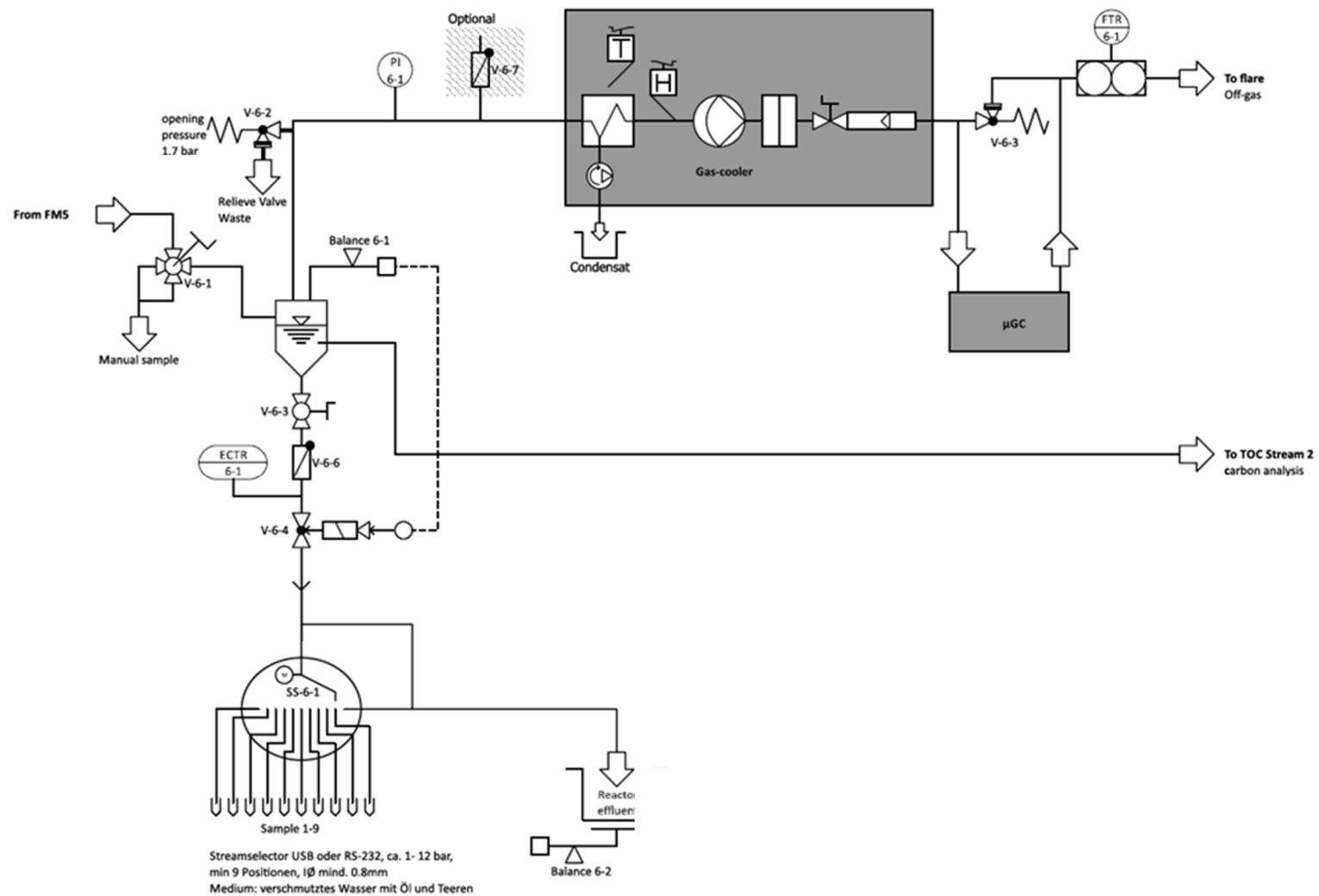


Figure A.10. Section FM6 of the process.

### A.3 List of all the experiments performed in this doctoral thesis

**Table A.1.** List of the experiments performed in mini-batch reactor (chapter 3).

Exp.	Sample	m g	Feed	Reaction time h	T °C	P MPa
BT1	Fresh C	1.5	water	5	420	35
BT2	C after exp. BT1	1.5	water	5	420	35

**Table A.2.** List of the CSCWG experiments of IPA performed in PFR (chapter 3).

Exp.	Catalyst	m <sub>Cat.</sub> mg	Feed	WHSV <sub>gRu</sub> g <sub>Org</sub> g <sub>Ru</sub> <sup>-1</sup> h <sup>-1</sup>	Time on stream h	Feed rate g min <sup>-1</sup>	T °C	P MPa	X <sub>C</sub> % <sup>a</sup>	GE <sub>C</sub> % <sup>a</sup>	Gas composition, vol % <sup>a</sup>					
											CH <sub>4</sub>	CO <sub>2</sub>	H <sub>2</sub>	CO	C <sub>2</sub> H <sub>6</sub>	C <sub>3</sub> H <sub>x</sub>
CS0	N.A.	0	10 wt % IPA	N.A.	3	3	450	30	1	N.A.	N.A.	N.A.	N.A.	N.A.	N.A.	N.A.
CS1	Fresh C	N.A.	10 wt % IPA	N.A.	24	3	450	30	11	4	3.3	0.5	96.1	0.2	< 0.1	5.0
CS2	2% Ru/C <sub>a</sub>	780	10 wt % IPA	1228	96	3	450	30	90	100	64.4	23.2	12.4	< 0.1	< 0.1	< 0.1
CS3	0.5% Ru/C <sub>w</sub>	597	10 wt % IPA	5202	6	3	450	30	25	17	46.7	16.5	36.2	0.2	< 0.1	< 0.1
					24	3	450	30	10	3	3.2	0.6	96.3	0.2	< 0.1	3.7
CS4	2% Ru/C <sub>w</sub>	149	10 wt % IPA	5202	6	3	450	30	15	5	22.1	9.5	68.1	0.2	< 0.1	2.9
CS5	2% Ru/C <sub>a</sub>	166	10 wt % IPA	5202	6	3	450	30	62	49	56.0	22.1	21.6	0.3	< 0.1	< 0.1
CS6	2% Ru/C <sub>nitro</sub>	173	10 wt % IPA	5202	6	3	450	30	99	101	66.9	24.5	8.7	0.0	< 0.1	< 0.1
CS7	2% Ru/C <sub>nitro</sub>	173	10 wt % IPA	5202	50	3	450	30	99	101	64.9	20.8	14.3	< 0.1	< 0.1	< 0.1
CS8	2% Ru/C <sub>BASF</sub>	173	10 wt % IPA	5202	50	3	450	30	16	5	25.4	12.6	62.0	0.0	N.A.	N.A.
CS9	5% Ru/C <sub>BASF</sub>	69	10 wt % IPA	5202	50	3	450	30	29	21	44.8	28.9	24.1	0.0	N.A.	N.A.
CS10	5% Ru/C <sub>BASF</sub>	139	10 wt % IPA	2586	50	3	450	30	56	57	55.1	24.4	20.3	0.0	< 0.1	0.1
CS11	4% Ru/C	214	10 wt % IPA	1972	50	3	450	30	96	102	65.8	24.3	9.9	< 0.1	< 0.1	< 0.1
CS12	4% Ru/C <sub>HNO3</sub>	233	10 wt % IPA	1972	50	3	450	30	95	101	65.0	20.6	14.1	0.3	< 0.1	< 0.1
CS13	4% Ru/C <sub>HT</sub>	223	10 wt % IPA	1972	50	3	450	30	96	102	66.2	22.3	11.2	0.4	< 0.1	< 0.1



Exp.	Catalyst	m <sub>Cat.</sub> mg	Feed	WHSV <sub>gRu</sub> g <sub>Org</sub> g <sub>Ru</sub> <sup>-1</sup> h <sup>-1</sup>	Time on stream h	Feed rate g min <sup>-1</sup>	T °C	P MPa	X <sub>C</sub> % <sup>a</sup>	GE <sub>C</sub> % <sup>a</sup>	Gas composition, vol % <sup>a</sup>					
											CH <sub>4</sub>	CO <sub>2</sub>	H <sub>2</sub>	CO	C <sub>2</sub> H <sub>6</sub>	C <sub>3</sub> H <sub>x</sub>
CS14	2% Ru/TiO <sub>2</sub>	192	10 wt % IPA	5202	50	3	450	30	21	14	46.1	18.5	35.4	< 0.1	< 0.1	0.3
CS15	2% Ru/ZrO <sub>2</sub>	281	10 wt % IPA	5202	50	3	450	30	38	27	48.2	21.0	30.7	< 0.1	< 0.1	0.4
CS16	2% Ru/Al <sub>2</sub> O <sub>3</sub>	281	10 wt % IPA	5202	50	3	450	30	22	22	43.5	18.0	38.5	< 0.1	< 0.1	< 0.1

[a] Calculated at the end of the experiment.

**Table A.3.** List of the salt separation experiments performed in KONTI-2 (chapter 4).

Exp.	Salt 1	Salt 2	C <sub>Salt 1</sub> mol kg <sup>-1</sup>	C <sub>Salt 2</sub> mol kg <sup>-1</sup>	Solvent	Feed rate g min <sup>-1</sup>	Brine rate g min <sup>-1</sup>	Reactor rate g min <sup>-1</sup>	T <sub>Salt top</sub> °C	T <sub>Salt bottom</sub> °C	P MPa	Sulfur concentration, mg kg <sup>-1</sup>		
												Feed effl.	Brine effl. <sup>b</sup>	Reactor effl. <sup>b</sup>
SP1	Na <sub>2</sub> SO <sub>4</sub>	K <sub>2</sub> SO <sub>4</sub>	0.1	0.05	water	12.9 ± 0.1	3.7 ± 0.1	9.2 ± 0.1	450	450	28	5103 ± 146	2917 ± 149	355 ± 6
SP2	Na <sub>2</sub> SO <sub>4</sub>	K <sub>2</sub> SO <sub>4</sub>	0.1	0.05	10 wt % IPA	18 <sup>a</sup>	3.2 <sup>a</sup>	15.6 ± 0.3	450	450	28	5103 ± 146	404 ± 5	3949 ± 241
SP3	Na <sub>2</sub> SO <sub>4</sub>	K <sub>2</sub> SO <sub>4</sub>	0.1	0.05	10 wt % IPA	14.8 ± 0.5	3.3 ± 0.1	13.8 ± 0.1	450	450	28	5103 ± 146	12743 ± 402	73 ± 6
SP4	Na <sub>2</sub> SO <sub>4</sub>	K <sub>2</sub> SO <sub>4</sub>	0.1	0.05	10 wt % IPA	9.0 ± 0.2	3.6 ± 0.0	5.3 ± 0.1	450	450	28	5103 ± 146	9749 ± 406	33 ± 4
SP5	Na <sub>2</sub> SO <sub>4</sub>	K <sub>2</sub> SO <sub>4</sub>	0.05	0.05	10 wt % IPA	8.8 ± 0.1	1.9 ± 0.0	6.9 ± 0.1	450	450	28	3219 ± 21	18385 ± 788	29 ± 4

[a] Corresponds to the set value [b] sample harvested at the end of the experiment.

**Table A.4.** List of the sulfur adsorption experiments performed in PFR (chapter 5).

Exp.	Feed	pH	C <sub>Sulfur, feed</sub> mg L <sup>-1a</sup>	m <sub>ZnO</sub> g	Feed rate g min <sup>-1</sup>	T °C	P MPa	C <sub>sulfur</sub> /C <sub>Sulfur,0</sub> - <sup>b</sup>
SA1	water	7	N.A.	5	3	400	30	N.A.
SA2	water	7	N.A.	5	3	400	30	N.A.
SA3	4 mM Na <sub>2</sub> S·9H <sub>2</sub> O	10.5	127	N.A.	3	400	30	1.01
SA4	4 mM Na <sub>2</sub> S·9H <sub>2</sub> O	10.5	133	2	3	400	30	0.49
SA5	4 mM Na <sub>2</sub> S·9H <sub>2</sub> O	10.5	120	1	3	400	30	0.73
SA6	4 mM Na <sub>2</sub> S·9H <sub>2</sub> O + 10 wt % IPA	10.5	121	1	3	400	30	0.69

Exp.	Feed	pH	C <sub>Sulfur, feed</sub> mg L <sup>-1a</sup>	m <sub>ZnO</sub> g	Feed rate g min <sup>-1</sup>	T °C	P MPa	C <sub>sulfur</sub> /C <sub>sulfur,0</sub> - <sup>b</sup>
SA7	24 mM Na <sub>2</sub> S·9H <sub>2</sub> O	11.5	750	2	3	400	28	0.77
SA8	24 mM Na <sub>2</sub> S·9H <sub>2</sub> O	11.5	750	2	3	400	28	N.A.
SA9	3 mM NaHS·xH <sub>2</sub> O	9.0	100	N.A.	5	400	28	0.0
SA10	3 mM NaHS·xH <sub>2</sub> O	9.0	100	N.A.	10	400	28	0.91

[a] Determined with ICP-OES [b] calculated at the end of the experiment.

**Table A.5.** List of the salt separation experiments performed in KONTI-C (chapter 6).

Exp.	Salt 1	Salt 2	C <sub>Salt 1</sub> mol kg <sup>-1</sup>	C <sub>Salt 2</sub> mol kg <sup>-1</sup>	Solvent	Feed rate g min <sup>-1</sup>	Brine rate g min <sup>-1</sup>	T <sub>Salt top</sub> °C	T <sub>Salt bottom</sub> °C	P MPa	Sulfur concentration, mg kg <sup>-1</sup>		
											Feed effl.	Brine effl. <sup>a</sup>	Reactor effl. <sup>a</sup>
KT1	Na <sub>2</sub> SO <sub>4</sub>	K <sub>2</sub> SO <sub>4</sub>	0.1	0.05	water	18 ± 0.2	2.8 ± 0.1	430	240	28	4283 ± 14	11994 ± 97	61 ± 7
KT2	Na <sub>2</sub> SO <sub>4</sub>	K <sub>2</sub> SO <sub>4</sub>	0.1	0.05	10 wt % IPA	18.9 ± 0.6	4.4 ± 0.2	430	240	28	6530 ± 77	25870 ± 67	100 ± 5
KT3	Na <sub>2</sub> SO <sub>4</sub>	K <sub>2</sub> SO <sub>4</sub>	0.1	0.05	10 wt % IPA	17.9 ± 0.3	4.2 ± 0.3	430	240	28	5704 ± 169	21825 ± 987	111 ± 3

[a] sample harvested at the end of the experiment.

**Table A.6.** List of the continuous liquefaction and CSCWG experiments of microalgae performed in KONTI-C (chapter 6 and 7).

Exp.	Feed	Dry matter wt %	m <sub>ZnO</sub> g	m <sub>Cat.</sub> g	Slurry f. freq., Hz	Liquiflow <sub>Brine</sub> %	T <sub>Salt top</sub> °C	T <sub>Salt bottom</sub> °C	T <sub>Reactor top</sub> °C	T <sub>Reactor bottom</sub> °C	P MPa	TOC <sub>Reactor effl.</sub> mg L <sup>-1a</sup>	Gas composition, vol % <sup>a</sup>			
													CO <sub>2</sub>	CH <sub>4</sub>	H <sub>2</sub>	CO
KT4	<i>Phaeod. tric.</i>	13	N.A.	N.A.	23	100	430	230	N.A.	N.A.	28	N.A.	N.A.	N.A.	N.A.	N.A.
KT5	<i>Phaeod. tric.</i>	8	N.A.	N.A.	25	100	400	200	N.A.	N.A.	28	N.A.	92	5	0	3
KT6	<i>Phaeod. tric.</i>	9	1944	N.A.	24	90	410	230	400	400	28	N.A.	N.A.	N.A.	N.A.	N.A.
KT7	<i>Phaeod. tric.</i>	6	1944	N.A.	23	80	410	250	400	400	28	N.A.	50	1	49	0
KT8	<i>Phaeod. tric.</i>	11	529	444	23	90	430	300	400	400	28	N.A.	N.A.	N.A.	N.A.	N.A.
KT9	<i>Phaeod. tric.</i>	9	529	444	23	60	430	300	400	400	28	< 1700	36	57	7	0
KT10	<i>Chlorella vul.</i>	3-15	713	493	16-21	40-100	370-440	265-325	360-390	390-420	25-30	< 400	36	57	7	0

---

[a] Determined at the steady state.

## References

- [1] F. Rosillo-Calle, P. De Groot, S. L. Hemstock, and J. Woods, *The biomass assessment handbook - bioenergy for a sustainable environment*, Earthscan (2007).
- [2] A. Zervos, C. Lins, and O. Schafer, "Tomorrow's world: 50% renewables scenarios for 2040," *Renew. Energy World* **7**, 238–245 (2004).
- [3] P. McKendry, "Energy production from biomass (part 2): conversion technologies," *Bioresour. Technol.* **83**, 47–54 (2002).
- [4] A. G. Haiduc, M. Brandenberger, S. Suquet, F. Vogel, R. Bernier-Latmani, and C. Ludwig, "SunCHem: an integrated process for the hydrothermal production of methane from microalgae and CO<sub>2</sub> mitigation," *J. Appl. Phycol.* **21**, 529–541 (2009).
- [5] Sustainable energy authority of Ireland, "The process and techniques of anaerobic digestion," 2010.
- [6] L. Gouveia, *Microalgae as a feedstock for biofuels*, Springer (2011).
- [7] J. Singh and S. Gu, "Commercialization potential of microalgae for biofuels production," *Renew. Sustain. Energy Rev.* **14**, 2596–2610 (2010).
- [8] U.S. Department of Energy, "National algal biofuels technology roadmap," 2010.
- [9] P. McKendry, "Energy production from biomass (part 1): overview of biomass," *Bioresour. Technol.* **83**, 37–46 (2002).
- [10] L. Brennan and P. Owende, "Biofuels from microalgae—A review of technologies for production, processing, and extractions of biofuels and co-products," *Renew. Sustain. Energy Rev.* **14**, 557–577 (2010).
- [11] A. Hirano, K. Hon-Nami, S. Kunito, M. Hada, and Y. Ogushi, "Temperature effect on continuous gasification of microalgal biomass: theoretical yield of methanol production and its energy balance," *Catal. Today* **45**, 399–404 (1998).
- [12] M. Gassner, F. Vogel, G. Heyen, and F. Maréchal, "Optimal process design for the polygeneration of SNG, power and heat by hydrothermal gasification of waste biomass: Thermo-economic process modelling and integration," *Energy Environ. Sci.* **4**, 1726 (Royal Society of Chemistry, 2011).
- [13] A. A. Peterson, F. Vogel, R. P. Lachance, M. Froeling, M. J. Antal Jr., and J. W. Tester, "Thermochemical biofuel production in hydrothermal media: A review of sub- and supercritical water technologies," *Energy Environ. Sci.* **1**, 32–65 (2008).

- 
- [14] D. C. Elliott, "Catalytic hydrothermal gasification of biomass," *Biofuels, Bioprod. Biorefining* **2**, 254–265 (2008).
- [15] F. Vogel, "Handbook of Green Chemistry, Volume 2: Heterogeneous Catalysis," in *Handb. Green Chem.* **2**, WILEY-VCH, R. H. Crabtree, Ed. (Weinheim, 2009).
- [16] A. Kruse, "Supercritical water gasification," *Biofuels, Bioprod. Biorefining* **2**, 415–437 (2008).
- [17] M. Brandenberger, "Process development for catalytic supercritical water gasification of algal feedstocks" (PhD Thesis, ETH Lausanne, No. 6165, 2014).
- [18] P. Biller and A. B. Ross, "Potential yields and properties of oil from the hydrothermal liquefaction of microalgae with different biochemical content.," *Bioresour. Technol.* **102**, 215–225 (2011).
- [19] Y. Dote, S. Sawayama, S. Inoue, T. Minowa, and S. Yokoyama, "Recovery of liquid fuel from hydrocarbon-rich microalgae by thermochemical liquefaction," *Fuel* **73**, 1855–1857 (1994).
- [20] T. M. Brown, P. Duan, and P. E. Savage, "hydrothermal liquefaction and gasification of *Nannochloropsis* sp.," *Energy & Fuels* **24**, 3639–3646 (2010).
- [21] P. Duan and P. E. Savage, "Hydrothermal liquefaction of a microalga with heterogeneous catalysts," *Ind. Eng. Chem. Res.* **50**, 52–61 (American Chemical Society, 2011).
- [22] U. Jena, K. C. Das, and J. R. Kastner, "Effect of operating conditions of thermochemical liquefaction on biocrude production from *Spirulina platensis*," *Bioresour. Technol.* **102**, 6221–6229 (2011).
- [23] A. B. Ross, P. Biller, M. L. Kubacki, H. Li, A. Lea-Langton, and J. M. Jones, "Hydrothermal processing of microalgae using alkali and organic acids," *Fuel* **89**, 2234–2243 (2010).
- [24] J. Zhang, W.-T. Chen, P. Zhang, Z. Luo, and Y. Zhang, "Hydrothermal liquefaction of *Chlorella pyrenoidosa* in sub- and supercritical ethanol with heterogeneous catalysts.," *Bioresour. Technol.* **133**, 389–397 (2013).
- [25] T. Minowa, S. Yokoyama, M. Kishimoto, and T. Okakura, "Oil production from algal cells of *Dunaliella tertiolecta* by direct thermochemical liquefaction," *Fuel* **74**, 1735–1738 (1995).
- [26] P. S. Christensen, G. Peng, F. Vogel, and B. B. Iversen, "Hydrothermal liquefaction of the microalgae *Phaeodactylum tricornutum* : impact of reaction conditions on product and elemental distribution," *Energy & Fuels* **28**, 5792–5803 (2014).
- [27] D. López Barreiro, W. Prins, F. Ronsse, and W. Brilman, "Hydrothermal liquefaction (HTL) of microalgae for biofuel production: State of the art review and future prospects," *Biomass and Bioenergy* **53**, 113–127 (2013).

- 
- [28] S. M. Heilmann, H. T. Davis, L. R. Jader, P. A. Lefebvre, M. J. Sadowsky, F. J. Schendel, M. G. von Keitz, and K. J. Valentas, "Hydrothermal carbonization of microalgae," *Biomass and Bioenergy* **34**, 875–882 (2010).
  - [29] W.-H. Chen, B.-J. Lin, M.-Y. Huang, and J.-S. Chang, "Thermochemical conversion of microalgal biomass into biofuels: A review.," *Bioresour. Technol.* **184**, 314–327 (2014).
  - [30] X. Miao, Q. Wu, and C. Yang, "Fast pyrolysis of microalgae to produce renewable fuels," *J. Anal. Appl. Pyrolysis* **71**, 855–863 (2004).
  - [31] A. Demirbaş, "Oily products from mosses and algae via pyrolysis," *Energy Sources, Part A Recover. Util. Environ. Eff.* **28**, 933–940 (Taylor & Francis Group, 2006).
  - [32] Y. Ueno, N. Kurano, and S. Miyachi, "Ethanol production by dark fermentation in the marine green alga, *Chlorococcum littorale*," *J. Ferment. Bioeng.* **86**, 38–43 (1998).
  - [33] A. Baiker, "Supercritical fluids in heterogeneous catalysis," *Chem. Rev.* **99**, 453–473 (1999).
  - [34] "NIST Chemistry webbook, <http://webbook.nist.gov>," 2011.
  - [35] A. V. Bandura, "The ionization constant of water over wide ranges of temperature and density," *J. Phys. Chem. Ref. Data* **35**, 15 (2006).
  - [36] H. Zöhrer, "Hydrothermal gasification of fermentation residues for SNG-production" (PhD Thesis, ETH Zurich, No. 21316, 2013).
  - [37] A. Kruse and E. Dinjus, "Hot compressed water as reaction medium and reactant," *J. Supercrit. Fluids* **39**, 362–380 (2007).
  - [38] J. W. Tester, P. A. Marrone, M. M. DiPippo, K. Sako, M. T. Reagan, T. Arias, and W. A. Peters, "Chemical reactions and phase equilibria of model halocarbons and salts in sub- and supercritical water (200–300 bar, 100–600°C)," *J. Supercrit. Fluids* **13**, 225–240 (1998).
  - [39] M. Modell, "Gasification and liquefaction of forest products in supercritical water," in *Fundam. Thermochem. Biomass Convers.* (1985).
  - [40] M. Schubert, "Catalytic hydrothermal gasification of biomass - salt recovery and continuous gasification of glycerol solutions" (PhD Thesis, ETH Zurich, No. 19039, 2010).
  - [41] M. Schubert, J. W. Regler, and F. Vogel, "Continuous salt precipitation and separation from supercritical water. Part 2. Type 2 salts and mixtures of two salts," *J. Supercrit. Fluids* **52**, 113–124 (2010).
  - [42] M. Schubert, J. W. Regler, and F. Vogel, "Continuous salt precipitation and separation from supercritical water. Part 1: Type 1 salts," *J. Supercrit. Fluids* **52**, 99–112 (2010).

- 
- [43] M. Schubert, J. Aubert, J. B. Müller, and F. Vogel, "Continuous salt precipitation and separation from supercritical water. Part 3: Interesting effects in processing type 2 salt mixtures," *J. Supercrit. Fluids* **61**, 44–54 (2012).
- [44] H. Weingärtner and E. U. Franck, "Überkritisches Wasser als Lösungsmittel," *Angew. Chemie* **117**, 2730–2752 (2005).
- [45] W. Buhler, Dinjus, E., Ederer, H. J., Kruse, A., Mas, C., "Ionic reactions and pyrolysis of glycerol as competing reaction pathways in near- and supercritical water," *J. Supercrit. Fluids* **22**, 37–53 (2002).
- [46] V. M. Valyashko, *Aqueous Systems at Elevated Temperatures and Pressures*, in *Aqueous Syst. Elev. Temp. Press.* (Elsevier, 2004).
- [47] G. W. Morey, "The solubility of solids in gases," *Econ. Geol.* **52**, 225–251 (1957).
- [48] V. M. Valyashko, "Phase equilibria in water-salt systems: some problems of solubility at elevated temperature and pressure," *high Temp. high Press. Electrochem. aqueous Solut.* **4**, 153–157 (1976).
- [49] S. S. Toor, L. Rosendahl, and A. Rudolf, "Hydrothermal liquefaction of biomass: A review of subcritical water technologies," *Energy* **36**, 2328–2342 (2011).
- [50] M. Nagamori and T. Funazukuri, "Glucose production by hydrolysis of starch under hydrothermal conditions," *J. Chem. Technol. Biotechnol.* **79**, 229–233 (2004).
- [51] P. J. le B. Williams and L. M. L. Laurens, "Microalgae as biodiesel & biomass feedstocks: Review & analysis of the biochemistry, energetics & economics," *Energy Environ. Sci.* **3**, 554 (Royal Society of Chemistry, 2010).
- [52] D. Klingler, Berg, J., Vogel, H., "Hydrothermal reactions of alanine and glycine in sub- and supercritical water," *J. Supercrit. Fluids* **43**, 112–119 (2007).
- [53] T. Rogalinski, S. Herrmann, and G. Brunner, "Production of amino acids from bovine serum albumin by continuous sub-critical water hydrolysis," *J. Supercrit. Fluids* **36**, 49–58 (2005).
- [54] A. Kruse, P. Maniam, and F. Spieler, "Influence of proteins on the hydrothermal gasification and liquefaction of biomass. 2. Model compounds," *Ind. Eng. Chem. Res.* **46**, 87–96 (2007).
- [55] M. Giordano, A. Norici, S. Ratti, and J. A. Raven, *Sulfur metabolism in phototrophic organisms*, R. Hell, C. Dahl, D. Knaff, and T. Leustek, Eds. (Springer Netherlands, Dordrecht, 2008).
- [56] S. Changi, A. J. Matzger, and P. E. Savage, "Kinetics and pathways for an algal phospholipid (1,2-dioleoyl-sn-glycero-3-phosphocholine) in high-temperature (175–350 °C) water," *Green Chem.* **14**, 2856 (2012).

- 
- [57] P. Azadi, E. Afif, F. Azadi, and R. Farnood, "Screening of nickel catalysts for selective hydrogen production using supercritical water gasification of glucose," *Green Chem.* **14**, 1766 (2012).
- [58] M. Dreher, "Catalysis under extreme conditions: in situ studies of the reforming of organic key compounds in supercritical water" (PhD Thesis, ETH Zurich, No. 21531, 2013).
- [59] D. J. M. De Vlieger, A. G. Chakinala, L. Lefferts, S. R. A. Kersten, K. Seshan, and D. W. F. Brilman, "Hydrogen from ethylene glycol by supercritical water reforming using noble and base metal catalysts," *Appl. Catal. B-Environmental* **111**, 536–544 (2012).
- [60] R. R. Davda, J. W. Shabaker, G. W. Huber, R. D. Cortright, and J. A. Dumesic, "Aqueous-phase reforming of ethylene glycol on silica-supported metal catalysts," *Appl. Catal. B-Environmental* **43**, 13–26 (2003).
- [61] R. D. Cortright, R. R. Davda, and J. A. Dumesic, "Hydrogen from catalytic reforming of biomass-derived hydrocarbons in liquid water.," *Nature* **418**, 964–967 (2002).
- [62] M. Osada, O. Sato, M. Watanabe, K. Arai, and M. Shirai, "water density effect on lignin gasification over supported noble metal catalysts in supercritical water," *Energy & Fuels* **20**, 930–935 (2006).
- [63] M. H. Waldner, F. Krumeich, and F. Vogel, "Synthetic natural gas by hydrothermal gasification of biomass selection procedure towards a stable catalyst and its sodium sulfate tolerance," *J. Supercrit. Fluids* **43**, 91–105 (2007).
- [64] P. Azadi and R. Farnood, "Review of heterogeneous catalysts for sub- and supercritical water gasification of biomass and wastes," *Int. J. Hydrogen Energy* **36**, 9529–9541 (2011).
- [65] M. H. Waldner, "Catalytic hydrothermal gasification of biomass for the production of synthetic natural gas" (PhD Thesis, ETH Zurich, No. 17100, 2007).
- [66] D. C. Elliott, E. G. Baker, R. S. Butner, and L. J. Sealock, "Bench-scale reactor tests of low temperature, catalytic gasification of wet industrial wastes," *J. Sol. Energy Eng.* **115**, 52 (1993).
- [67] D. C. Elliott Phelps, M. R., Sealock, L. J., Baker, E. G., "Chemical-processing in high-pressure aqueous environments. 4. continuous-flow reactor process-development experiments for organics destruction," *Ind. Eng. Chem. Res.* **33**, 566–574 (1994).
- [68] D. C. Elliott, T. R. Hart, and G. G. Neuenschwander, "Chemical processing in high-pressure aqueous environments. 8. Improved catalysts for hydrothermal gasification," *Ind. Eng. Chem. Res.* **45**, 3776–3781 (2006).
- [69] H. Zöhrer, F. Mayr, and F. Vogel, "Stability and performance of ruthenium catalysts based on refractory oxide supports in supercritical water conditions," *Energy Fuels* **27**, 4739–4747 (2013).



- 
- [70] M. Osada, O. Sato, K. Arai, and M. Shirai, "Stability of supported ruthenium catalysts for lignin gasification in supercritical water," *Energy & Fuels* **20**, 2337–2343 (American Chemical Society, 2006).
- [71] A. Yamaguchi, N. Hiyoshi, O. Sato, K. K. Bando, M. Osada, and M. Shirai, "Hydrogen production from woody biomass over supported metal catalysts in supercritical water," *Catal. Today* **146**, 192–195 (2009).
- [72] K. C. Park and H. Tomiyasu, "Gasification reaction of organic compounds catalyzed by RuO<sub>2</sub> in supercritical water," *Chem. Commun.*, 694–695 (2003).
- [73] A. Yamaguchi, N. Hiyoshi, O. Sato, M. Osada, and M. Shirai, "EXAFS study on structural change of charcoal-supported ruthenium catalysts during lignin gasification in supercritical water," *Catal. Letters* **122**, 188–195 (2008).
- [74] S. Rabe, M. Nachttegaal, T. Ulrich, and F. Vogel, "Towards understanding the catalytic reforming of biomass in supercritical water," *Angew. Chemie* **49**, 6434–6437 (2010).
- [75] M. Dreher, M. Steib, M. Nachttegaal, J. Wambach, and F. Vogel, "On-stream regeneration of a sulfur-poisoned ruthenium–carbon catalyst under hydrothermal gasification conditions," *ChemCatChem* **6**, 626–633 (2014).
- [76] M. Osada, N. Hiyoshi, O. Sato, K. Arai, and M. Shirai, "Effect of sulfur on catalytic gasification of lignin in supercritical water," *Energy & Fuels* **21**, 1400–1405 (2007).
- [77] M. Osada, N. Hiyoshi, O. Sato, K. Arai, and M. Shirai, "Reaction pathway for catalytic gasification of lignin in presence of sulfur in supercritical water," *Energy & Fuels* **21**, 1854–1858 (2007).
- [78] M. Dreher, B. Johnson, A. A. Peterson, M. Nachttegaal, J. Wambach, and F. Vogel, "Catalysis in supercritical water: Pathway of the methanation reaction and sulfur poisoning over a Ru/C catalyst during the reforming of biomolecules," *J. Catal.* **301**, 38–45 (2013).
- [79] Q. Guan, C. Wei, and P. E. Savage, "Hydrothermal gasification of *Nannochloropsis* sp. with Ru/C," *Energy & Fuels* **26**, 4575–4582 (2012).
- [80] E. Afif, P. Azadi, and R. Farnood, "Catalytic hydrothermal gasification of activated sludge," *Appl. Catal. B Environ.* **105**, 136–143 (2011).
- [81] M. Osada, N. Hiyoshi, O. Sato, K. Arai, and M. Shirai, "Subcritical water regeneration of supported ruthenium catalyst poisoned by sulfur," *Energy & Fuels* **22**, 845–849 (2008).
- [82] D. C. Elliott, K. L. Peterson, D. S. Muzakto, E. V. Alderson, T. R. Hart, and G. G. Neuenschwander, "Effects of trace contaminants on catalytic processing of biomass-derived feedstocks," *Appl. Biochem. Biotechnol.* **113-116**, 807–825 (2004).

- 
- [83] A. Kruse and A. Gawlik, "Biomass conversion in water at 330–410 °C and 30–50 MPa. Identification of key compounds for indicating different chemical reaction pathways," *Ind. Eng. Chem. Res.* **42**, 267–279 (2003).
- [84] Y. Matsumura, T. Minowa, B. Potic, S. Kersten, W. Prins, W. Vanswaaij, B. Vandebeld, D. Elliott, G. Neuenschwander, et al., "Biomass gasification in near- and super-critical water: Status and prospects," *Biomass and Bioenergy* **29**, 269–292 (2005).
- [85] Z. Fang and C. Fang, "Complete dissolution and hydrolysis of wood in hot water," *AIChE J.* **54**, 2751–2758 (2008).
- [86] A. Sinač, A. Kruse, and V. Schwarzkopf, "Formation and degradation pathways of intermediate products formed during the hydrolysis of glucose as a model substance for wet biomass in a tubular reactor," *Eng. Life Sci.* **3**, 469–473 (2003).
- [87] M. Watanabe, H. Inomata, M. Osada, T. Sato, T. Adschiri, and K. Arai, "Catalytic effects of NaOH and ZrO<sub>2</sub> for partial oxidative gasification of n-hexadecane and lignin in supercritical water," *Fuel* **82**, 545–552 (2003).
- [88] H. Schmieder, J. Abeln, N. Boukis, E. Dinjus, A. Kruse, M. Kluth, G. Petrich, E. Sadri, and M. Schacht, "Hydrothermal gasification of biomass and organic wastes," *J. Supercrit. Fluids* **17**, 145–153 (2000).
- [89] D. Cordell, J.-O. Drangert, and S. White, "The story of phosphorus: Global food security and food for thought," *Glob. Environ. Chang.* **19**, 292–305 (2009).
- [90] M. J. Antal, S. G. Allen, D. Schulman, X. D. Xu, and R. J. Divilio, "Biomass gasification in supercritical water," *Ind. Eng. Chem. Res.* **39**, 4040–4053 (2000).
- [91] A. Kruse, A. Krupka, V. Schwarzkopf, C. Gamard, and T. Henningsen, "Influence of proteins on the hydrothermal gasification and liquefaction of biomass. 1. comparison of different feedstocks," *Ind. Eng. Chem. Res.* **44**, 3013–3020 (2005).
- [92] M. Bagnoud-Velásquez, M. Brandenberger, F. Vogel, and C. Ludwig, "Continuous catalytic hydrothermal gasification of algal biomass and case study on toxicity of aluminum as a step toward effluents recycling," *Catal. Today* **223**, 35–43 (2014).
- [93] N. Boukis, U. Galla, H. Müller, and E. Dinjus, "Biomass gasification in supercritical water, experimental process achieved with the VERENA plant," in *15th Eur. Biomass Conf. Exhib. Berlin, Ger.*, (2007).
- [94] D. C. Elliott, T. R. Hart, G. G. Neuenschwander, L. J. Rotness, M. V. Olarte, and A. H. Zacher, "Chemical processing in high-pressure aqueous environments. 9. process development for catalytic gasification of algae feedstocks," *Ind. Eng. Chem. Res.* **51**, 10768–10777 (2012).

- 
- [95] J. B. Müller, "Hydrothermal gasification of biomass - investigation on coke formation and continuous salt separation with pure substrates and real biomass" (PhD Thesis, ETH Zurich, 2012).
- [96] T. Karayildirim, A. Sinağ, and A. Kruse, "Char and coke formation as unwanted side reaction of the hydrothermal biomass gasification," *Chem. Eng. Technol.* **31**, 1561–1568 (2008).
- [97] Y. Matsumura, M. Harada, K. Nagata, and Y. Kikuchi, "Effect of heating rate of biomass feedstock on carbon gasification efficiency in supercritical water gasification," *Chem. Eng. Commun.* **193**, 649–659 (2006).
- [98] A. May, J. Salvado, C. Torras, and D. Montane, "Catalytic gasification of glycerol in supercritical water," *Chem. Eng. J.* **160**, 751–759 (2010).
- [99] D. J. M. De Vlieger, B. L. Mojet, L. Lefferts, and K. Seshan, "Aqueous phase reforming of ethylene glycol - role of intermediates in catalyst performance," *J. Catal.* **292**, 239–245 (2012).
- [100] D. J. M. De Vlieger, L. Lefferts, and K. Seshan, "Ru decorated carbon nanotubes - a promising catalyst for reforming bio-based acetic acid in the aqueous phase," *Green Chem.* **16**, 864–874 (2014).
- [101] S. Kudo, Y. Hachiyama, Y. Takashima, J. Tahara, S. Idesh, K. Norinaga, and J. Hayashi, "Catalytic hydrothermal reforming of lignin in aqueous alkaline medium," *Energy & Fuels* **28**, 76–85 (2014).
- [102] S. Stucki, F. Vogel, C. Ludwig, A. G. Haiduc, and M. Brandenberger, "Catalytic gasification of algae in supercritical water for biofuel production and carbon capture," *Energy Environ. Sci.* **2**, 535 (2009).
- [103] Q. Guan, P. E. Savage, and C. Wei, "Gasification of alga *Nannochloropsis* sp. in supercritical water," *J. Supercrit. Fluids* **61**, 139–145 (2012).
- [104] A. G. Chakinala, D. W. F. Brilman, W. P. M. van Swaaij, and S. R. A. Kersten, "Catalytic and non-catalytic supercritical water gasification of microalgae and glycerol," *Ind. Eng. Chem. Res.* **49**, 1113–1122 (2010).
- [105] S. Elsayed, N. Boukis, and J. Sauer, "Hydrothermal gasification of microalgae – Prospects and challenges," in *DGMK-Fachbereichstagung Konversion von Biomassen Rotenbg. a. d. Fulda*, (2014).
- [106] D. J. Patzelt, S. Hindersin, S. Elsayed, N. Boukis, M. Kerner, and D. Hanelt, "Hydrothermal gasification of *Acutodesmus obliquus* for renewable energy production and nutrient recycling of microalgal mass cultures," *J. Appl. Phycol.* (2014).
- [107] [Http://www.micromeritics.com/](http://www.micromeritics.com/), "AutoChem II 2920 TECHNIQUE pulse chemisorption analysis."

- 
- [108] A. Borodzinski and M. Bonarowska, "Relation between crystallite size and dispersion on supported metal catalysts," *Langmuir* **13**, 5613–5620 (1997).
- [109] S. L. Goertzen, K. D. Theriault, A. M. Oickle, A. C. Tarasuk, and H. A. Andreas, "Standardization of the Boehm titration. Part I. CO<sub>2</sub> expulsion and endpoint determination," *Carbon* **48**, 1252–1261 (2010).
- [110] A. M. Oickle, S. L. Goertzen, K. R. Hopper, Y. O. Abdalla, and H. A. Andreas, "Standardization of the Boehm titration: Part II. Method of agitation, effect of filtering and dilute titrant," *Carbon* **48**, 3313–3322 (2010).
- [111] J. Breinl, "Catalytic hydrothermal gasification of microalgae: Start-up of a new process demonstration unit" (Vienna, 2014).
- [112] D. C. Elliott, M. R. Phelps, L. J. Sealock, and E. G. Baker, "Chemical processing in high pressure aqueous environments . 4. Continuous flow reactor process development experiments for organics destruction," *Ind. Eng. Chem. Res.* **33**, 566–574 (1994).
- [113] X. D. Xu Matsumura, Y., Stenberg, J., Antal, M. J., "Carbon-catalyzed gasification of organic feedstocks in supercritical water," *Ind. Eng. Chem. Res.* **35**, 2522–2530 (1996).
- [114] X. D. Xu and M. J. Antal, "Gasification of sewage sludge and other biomass for hydrogen production in supercritical water," *Environ. Prog.* **17**, 215–220 (1998).
- [115] I. G. Lee and S. K. Ihm, "Catalytic gasification of glucose over Ni/activated charcoal in supercritical water," *Ind. Eng. Chem. Res.* **48**, 1435–1442 (2009).
- [116] G. W. Huber, J. W. Shabaker, and J. A. Dumesic, "Raney Ni-Sn catalyst for H<sub>2</sub> production from biomass-derived hydrocarbons," *Science* **300**, 2075–2077 (2003).
- [117] Y. Li, L. Guo, X. Zhang, H. Jin, and Y. Lu, "Hydrogen production from coal gasification in supercritical water with a continuous flowing system," *Int. J. Hydrogen Energy* **35**, 3036–3045 (2010).
- [118] A. Sharma, H. Nakagawa, and K. Miura, "Uniform dispersion of Ni nano particles in a carbon based catalyst for increasing catalytic activity for CH<sub>4</sub> and H<sub>2</sub> production by hydrothermal gasification," *Fuel* **85**, 2396–2401 (2006).
- [119] B. Yan, J. Wu, C. Xie, F. He, and C. Wei, "Supercritical water gasification with Ni/ZrO<sub>2</sub> catalyst for hydrogen production from model wastewater of polyethylene glycol," *J. Supercrit. Fluids* **50**, 155–161 (2009).
- [120] T. Yoshida and Y. Oshima, "Partial oxidative and catalytic biomass gasification in supercritical water: A promising flow reactor system," *Ind. Eng. Chem. Res.* **43**, 4097–4104 (2004).

- 
- [121] K. Pinkwart, T. Bayha, W. Lutter, and M. Krausa, "Gasification of diesel oil in supercritical water for fuel cells," *J. Power Sources* **136**, 211–214 (2004).
- [122] A. J. Byrd, S. Kumar, L. Kong, H. Ramsurn, and R. B. Gupta, "Hydrogen production from catalytic gasification of switchgrass biocrude in supercritical water," *Int. J. Hydrogen Energy* **36**, 3426–3433 (2011).
- [123] A. J. Byrd, K. K. Pant, and R. B. Gupta, "Hydrogen production from glycerol by reforming in supercritical water over Ru/Al<sub>2</sub>O<sub>3</sub> catalyst," *Fuel* **87**, 2956–2960 (2008).
- [124] G. van Rossum, B. Potic, S. R. A. Kersten, and W. P. M. van Swaaij, "Catalytic gasification of dry and wet biomass," *Catal. Today* **145**, 10–18 (2009).
- [125] P. Azadi, J. Otomo, H. Hatano, Y. Oshima, and R. Farnood, "Hydrogen production by catalytic near-critical water gasification and steam reforming of glucose," *Int. J. Hydrogen Energy* **35**, 3406–3414 (2010).
- [126] A. G. Chakinala, S. Kumar, A. Kruse, S. R. A. Kersten, W. P. M. van Swaaij, and D. W. F. Brilman, "Supercritical water gasification of organic acids and alcohols: The effect of chain length," *J. Supercrit. Fluids* **74**, 8–21 (2013).
- [127] Z. Y. Ding, M. A. Frisch, L. X. Li, and E. F. Gloyna, "Catalytic oxidation in supercritical water," *Ind. Eng. Chem. Res.* **35**, 3257–3279 (1996).
- [128] Y. C. Chiang, W. H. Lin, and Y. C. Chang, "The influence of treatment duration on multi-walled carbon nanotubes functionalized by H<sub>2</sub>SO<sub>4</sub>/HNO<sub>3</sub> oxidation," *Appl. Surf. Sci.* **257**, 2401–2410 (2011).
- [129] J. Wambach, M. Schubert, M. Doebeli, and F. Vogel, "Characterization of a spent Ru/C catalyst after gasification of biomass in supercritical water," *Chimia (Aarau)*. **66**, 706–711 (2012).
- [130] F. Masini, C. E. Strebel, D. N. McCarthy, A. U. F. Nierhoff, J. Kehres, E. M. Fiordaliso, J. H. Nielsen, and I. Chorkendorff, "Methanation on mass-selected Ru nanoparticles on a planar SiO<sub>2</sub> model support: The importance of under-coordinated sites," *J. Catal.* **308**, 282–290 (2013).
- [131] S. B. Vendelbo, M. Johansson, D. J. Mowbray, M. P. Andersson, F. Abild-Pedersen, J. H. Nielsen, J. K. Nørskov, and I. Chorkendorff, "Self blocking of CO dissociation on a stepped ruthenium surface," *Top. Catal.* **53**, 357–364 (2010).
- [132] M. P. Andersson, F. Abild-Pedersen, I. N. Remediakis, T. Bligaard, G. Jones, J. Engbæk, O. Lytken, S. Hørch, J. H. Nielsen, et al., "Structure sensitivity of the methanation reaction: H<sub>2</sub>-induced CO dissociation on nickel surfaces," *J. Catal.* **255**, 6–19 (2008).

- 
- [133] S. F. Yin, B. Q. Xu, W. X. Zhu, C. F. Ng, X. P. Zhou, and C. T. Au, "Carbon nanotubes-supported Ru catalyst for the generation of CO<sub>x</sub>-free hydrogen from ammonia," *Catal. Today* **93-5**, 27–38 (2004).
- [134] M. Cerro-Alarcon, A. Maroto-Valiente, I. Rodriguez-Ramos, and A. Guerrero-Ruiz, "Further insights into the Ru nanoparticles-carbon interactions and their role in the catalytic properties," *Carbon* **43**, 2711–2722 (2005).
- [135] Y. Li, C. Pan, W. Han, H. Chai, and H. Liu, "An efficient route for the preparation of activated carbon supported ruthenium catalysts with high performance for ammonia synthesis," *Catal. Today* **174**, 97–105 (2011).
- [136] I. Rossetti, N. Pernicone, and L. Forni, "Characterisation of Ru/C catalysts for ammonia synthesis by oxygen chemisorption," *Appl. Catal. a-General* **248**, 97–103 (2003).
- [137] A. Guerrero-Ruiz, P. Badenes, and I. Rodriguez-Ramos, "Study of some factors affecting the Ru and Pt dispersions over high surface area graphite-supported catalysts," *Appl. Catal. a-General* **173**, 313–321 (1998).
- [138] E. Gallegos-Suarez, M. Perez-Cadenas, A. Guerrero-Ruiz, I. Rodriguez-Ramos, and A. Arcoya, "Effect of the functional groups of carbon on the surface and catalytic properties of Ru/C catalysts for hydrogenolysis of glycerol," *Appl Surf Sci* **287**, 108–116 (2013).
- [139] A. Yamaguchi, N. Hiyoshi, O. Sato, M. Osada, and M. Shirai, "Lignin gasification over supported ruthenium trivalent salts in supercritical water," *Energy & Fuels* **22**, 1485–1492 (2008).
- [140] Y. Yang, K. Chiang, and N. Burke, "Porous carbon-supported catalysts for energy and environmental applications: A short review," *Catal. Today* **178**, 197–205 (2011).
- [141] A. E. Aksoylu, M. Madalena, A. Freitas, M. F. R. Pereira, and J. L. Figueiredo, "The effects of different activated carbon supports and support modifications on the properties of Pt/AC catalysts," *Carbon* **39**, 175–185 (2001).
- [142] X. Wang, N. Li, J. A. Webb, L. D. Pfefferle, and G. L. Haller, "Effect of surface oxygen containing groups on the catalytic activity of multi-walled carbon nanotube supported Pt catalyst," *Appl Cat B Env.* **101**, 21–30 (2010).
- [143] H. Zhu, W. Han, and H. Liu, "Influence of oxidation on heat-treated activated carbon support properties and metallic dispersion of Ru/C catalyst," *Catal. Letters* **115**, 13–18 (2007).
- [144] X. M. Wang, N. Li, L. D. Pfefferle, and G. L. Haller, "Pt-Co bimetallic catalyst supported on single-walled carbon nanotubes: Effect of alloy formation and oxygen containing groups," *J Phys Chem C* **114**, 16996–17002 (2010).

- 
- [145] A. Boyano, C. Herrera, M. A. Larrubia, L. J. Alemany, R. Moliner, and M. J. Lázaro, "Vanadium loaded carbon-based monoliths for the on-board no reduction: Influence of temperature and period of the oxidation treatment," *Chem Eng J* **160**, 623–633 (2010).
- [146] S. Hermans, C. Diverchy, O. Demoulin, V. Dubois, E. M. Gaigneaux, and M. Devillers, "Nanostructured Pd/C catalysts prepared by grafting of model carboxylate complexes onto functionalized carbon," *J Cat* **243**, 239–251 (2006).
- [147] P. Chingombe, B. Saha, and R. J. Wakeman, "Surface modification and characterisation of a coal-based activated carbon," *Carbon* **43**, 3132–3143 (2005).
- [148] J. L. Figueiredo, M. F. R. Pereira, M. M. A. Freitas, and J. J. M. Orfao, "Modification of the surface chemistry of activated carbons," *Carbon* **37**, 1379–1389 (1999).
- [149] Salame I.I. and T. J. Bandoz, "Surface chemistry of activated carbons: Combining the results of temperature-programmed desorption, boehm, and potentiometric titrations," *J. Colloid Interface Sci.* **240**, 252–258 (2001).
- [150] R. R. A. Rios, D. E. Alves, I. Dalmázio, S. F. V. Bento, C. L. Donnici, and R. M. Lago, "Tailoring activated carbon by surface chemical modification with O, S, and N containing molecules," *Mat Res* **6**, 129–135 (2003).
- [151] A. Stein, Z. Wang, and M. A. Fierke, "Functionalization of porous carbon materials with designed pore architecture," *Adv. Mater.* **21**, 265–293 (2009).
- [152] G. Peng, M. Steib, F. Gramm, C. Ludwig, and F. Vogel, "Synthesis factors affecting the catalytic performance and stability of Ru/C catalysts for supercritical water gasification," *Catal. Sci. Technol.* **4**, 3329 (2014).
- [153] W. Zheng, J. Zhang, H. Xu, and W. Li, "NH<sub>3</sub> decomposition kinetics on supported Ru clusters: morphology and particle size effect," *Catal. Letters* **119**, 311–318 (2007).
- [154] T. Abe, S. Inoue, and K. Watanabe, "XRD and electrochemical measurements of RuO<sub>2</sub> powder treated by using a mechanical grinding method," *J. Alloys Compd.* **358**, 177–181 (2003).
- [155] N. Li, G. A. Tompsett, T. Zhang, J. Shi, C. E. Wyman, and G. W. Huber, "Renewable gasoline from aqueous phase hydrodeoxygenation of aqueous sugar solutions prepared by hydrolysis of maple wood," *Green Chem.* **13**, 91–101 (2011).
- [156] I. Rossetti, N. Pernicone, and L. Forni, "Graphitised carbon as support for Ru/C ammonia synthesis catalyst," *Catal. Today* **102-103**, 219–224 (2005).
- [157] Z. Kowalczyk, S. Jodzis, W. Rarog, J. Zielinski, J. Pielaszek, and A. Presz, "Carbon-supported ruthenium catalyst for the synthesis of ammonia. The effect of the carbon support and barium promoter on the performance," *Appl. Catal. a-General* **184**, 95–102 (1999).

- 
- [158] J. Reimer and F. Vogel, "High pressure differential scanning calorimetry of the hydrothermal salt solutions  $K_2SO_4$ – $Na_2SO_4$ – $H_2O$  and  $K_2HPO_4$ – $H_2O$ ," *RSC Adv.* **3**, 24503 (2013).
- [159] M. Roth, "Continuous adsorption of sulfur in supercritical water: Optimization of the process parameters; research and modeling of mass transfer and reaction kinetics" (Master Thesis, Dresden, 2015).
- [160] J. E. Parker, S. P. Thompson, A. R. Lennie, J. Potter, and C. C. Tang, "A study of the aragonite-calcite transformation using Raman spectroscopy, synchrotron powder diffraction and scanning electron microscopy," *CrystEngComm* **12**, 1590 (2010).
- [161] O. N. Fedyaeva and A. A. Vostrikov, "Hydrogenation of bitumen in situ in supercritical water flow with and without addition of zinc and aluminum," *J. Supercrit. Fluids* **72**, 100–110 (2012).
- [162] A. Ates, G. Azimi, K.-H. Choi, W. H. Green, and M. T. Timko, "The role of catalyst in supercritical water desulfurization," *Appl. Catal. B Environ.* **147**, 144–155 (2014).
- [163] W. J. Thomas and B. Crittenden, *Adsorption technology & design*, Elsevier (1998).
- [164] J. B. Müller and F. Vogel, "Tar and coke formation during hydrothermal processing of glycerol and glucose. Influence of temperature, residence time and feed concentration," *J. Supercrit. Fluids* **70**, 126–136 (2012).
- [165] A. Sinağ, T. Yumak, V. Balci, and A. Kruse, "Catalytic hydrothermal conversion of cellulose over  $SnO_2$  and  $ZnO$  nanoparticle catalysts," *J. Supercrit. Fluids* **56**, 179–185 (2011).
- [166] A. H. Mohammadi, R. Anderson, and B. Tohidi, "Carbon monoxide clathrate hydrates: Equilibrium data and thermodynamic modeling," *AIChE J.* **51**, 2825–2833 (2005).
- [167] A. Adegoroye, N. Paterson, X. Li, T. Morgan, A. . Herod, D. . Dugwell, and R. Kandiyoti, "The characterisation of tars produced during the gasification of sewage sludge in a spouted bed reactor," *Fuel* **83**, 1949–1960 (2004).
- [168] A. Kruse, P. Bernolle, N. Dahmen, E. Dinjus, and P. Maniam, "Hydrothermal gasification of biomass: consecutive reactions to long-living intermediates," *Energy Environ. Sci.* **3**, 136 (2010).
- [169] R. H. Bowker, M. C. Smith, B. A. Carrillo, and M. E. Bussell, "Synthesis and hydrodesulfurization properties of noble metal phosphides: ruthenium and palladium," *Top. Catal.* **55**, 999–1009 (2012).
- [170] L. Li, Z. H. Zhu, Z. F. Yan, G. Q. Lu, and L. Rintoul, "Catalytic ammonia decomposition over Ru/carbon catalysts: The importance of the structure of carbon support," *Appl. Catal. A Gen.* **320**, 166–172 (2007).





## List of publications

### **Peer Reviewed Journal Publications**

- Peng G., Ludwig C., Vogel F., "Ru dispersion: a key parameter for the stability of supported Ru catalysts during catalytic supercritical water gasification", submitted.
- Peng G., Gramm F., Ludwig C., Vogel F., "Effect of carbon surface functional groups on the synthesis of Ru/C catalysts for supercritical water gasification", *Catalysis Science & Technology*, 2015, **5**, 3658 – 3666.
- Bagnoud-Velásquez M., Schmid-Staiger U., Peng G., Vogel F., Ludwig C., "First developments towards closing the nutrient cycle in a biofuel production process", *Algal Research*, 2015, **8**, 76-82.
- Christensen P.S., Peng G., Vogel F., Iversen B.B., "Hydrothermal liquefaction of the microalgae *Phaeodactylum tricornutum*: Impact of reaction conditions on product and elemental distribution", *Energy & Fuels*, 2014, **28** (9), 5792-5803.
- Peng G., Steib M., Gramm F., Ludwig C., Vogel F., "Synthesis factors affecting the catalytic performance and stability of Ru/C catalysts for supercritical water gasification", *Catalysis Science & Technology*, 2014, **4**, 3329 – 3339.

### **Patent**

- Patent Nr. 14159871.4-1352 "Salzabscheider und Verfahren zur Erzeugung eines methanhaltigen Gasgemisches aus Biomasse unter Einsatz eines Salzabscheiders", Paul Scherrer Institut, Inventors: Deboni E., Reimer J., Peng G., Zöhrer H., Vogel F., 2014.

### **Conference talks**

- Peng G., Vogel F., Ludwig C., 2015. *Continuous catalytic supercritical water gasification of microalgae for methane production (SunCHem project)*. 23<sup>rd</sup> European Biomass Conference and Exhibition, Vienna, Austria.

- 
- Peng G., Ludwig C., Vogel F., 2014. *Ru/C as a catalyst for supercritical water gasification of IPA for methane production*. 8<sup>th</sup> International Conference on Environmental Catalysis, Asheville NC, USA.
  - Peng G., Vogel F., Ludwig C., 2014. *Ru/C catalysts for catalytic supercritical water gasification (CSCWG) of microalgae for bio-methane production (SunCHem project)*. 22<sup>nd</sup> European Biomass Conference and Exhibition, Hamburg, Germany.
  - Peng G., Ludwig C., Vogel F., 2013. *Carbon as a catalyst support for catalytic supercritical water gasification (CSCWG) of microalgae for bio-synthetic natural gas (Bio-SNG) production (SunCHem project)*. Annual World Conference on Carbon (Carbon 2013), Rio de Janeiro, Brazil.

#### **Other talks**

- Peng G., Vogel F., Ludwig C., 2014. *Hydrothermal gasification of microalgae for methane production (SunCHem process)*. Frontiers in Energy Research (ETHZ), Zurich, Switzerland.
- Peng G., Vogel F., Ludwig C., 2012. *SunCHem-hydrothermal gasification of microalgae*. Romande Energie, Morges, Switzerland.

#### **Conference posters**

- Peng G., Vogel F., Refardt D., Ludwig C., 2014. *Continuous catalytic hydrothermal gasification of microalgae*. SCCER BIOSWEET conference, Villigen PSI, Switzerland
- Peng G., Steib M., Gramm F., Ludwig C., Vogel F., 2014. *Synthesis factors affecting the catalytic performance of Ru/C catalysts for supercritical water gasification*. SCS Fall Meeting, Zürich, Switzerland
- Peng G., Steib M., Gramm F., Ludwig C., Vogel F., 2014. *Synthesis factors affecting the catalytic performance of Ru/C catalysts for supercritical water gasification*. 6<sup>th</sup> International Symposium on Carbon for Catalysis (CARBOCAT-VI), Trondheim, Norway.

# Curriculum Vitae

## PERSONAL INFORMATION

NAME

GAËL PENG

DATE/PLACE OF BIRTH

NOVEMBER 9, 1984, IN MOUTIER (BE), SWITZER-  
LAND

NATIONALITY

SWISS

## EMPLOYMENT HISTORY

July 2011 – July 2015

PhD studies in Catalytic Process Engineering  
Group at Paul Scherrer Institut (PSI) and  
Ecole Polytechnique Fédérale de Lausanne  
(EPFL)

April 2011 – July 2011

Research assistant in automotive catalysis  
within the Laboratory of Solid State Chemis-  
try and Catalysis at EMPA in Dübendorf (ZH)

September 2008 – February 2010

MSc studies in Chemical & Biochemical Engi-  
neering at EPFL

September 2005 – July 2008

BSc studies in Chemistry & Chemical Engi-  
neering at EPFL

January 2005 – March 2005

Ski and Snowboard instructor at Swiss Ski  
School in Zinal (VS)

August 2004 – December 2004

Support of the surveyor in the fieldwork, Of-  
fice Aeschlimann & Waelti, St-Imier (BE)

AUGUST 2001 – JUNE 2004

HIGH SCHOOL AT GYMNASSE FRANÇAIS DE BIENNE  
(BE)